

# **Dissolved oxygen-based annual biological production from glider observations at the Porcupine Abyssal Plain (North Atlantic)**

Umberto Binetti

A thesis submitted in partial fulfilment of the requirements for the degree of  
Doctor of Philosophy

University of East Anglia,  
Centre for Ocean and Atmospheric Sciences,  
School of Environmental Sciences

April 2016

Supervised by: Professor Jan Kaiser and Professor Karen Heywood

© This copy of the thesis has been supplied on condition that anyone who consults it is understood to recognise that its copyright rests with the author and that use of any information derived there from must be in accordance with current UK Copyright Law. In addition, any quotation or extract must include full attribution.



Breathe;



# Abstract

The OSMOSIS project used a fleet of gliders to survey at the Porcupine Abyssal Plain (North Atlantic) from September 2012 to September 2013. Different physical and biogeochemical parameters (salinity, temperature, oxygen concentration, chlorophyll fluorescence) were measured in the top 1000 m of the water column. The present study focused on calibrating and analysing the oxygen concentration data.

The mixing layer depth was defined as the depth where oxygen concentration varied by more than 0.5% from its value at 5 m. The mixing layer was shallower than the mixed layer, defined by density and temperature. In cases of low turbulence, the mixing layer described the vertical extent of the biologically productive layer (except deep chlorophyll maximums).

Net community production was calculated over a year-cycle with an oxygen-budget approach. Net autotrophy was found at the site with a net production of  $(6.4 \pm 1.9)$  mol m<sup>-2</sup> in oxygen equivalents. The period exhibiting a deep chlorophyll maximum contributed  $(1.5 \pm 0.5)$  mol m<sup>-2</sup> to the total production. The results were higher than most of the previous estimates and the productive season longer than that considered in previous studies. Increased net community production was related to the decrease in water turbulence and mixing layer shoaling, confirming the validity of the mechanism proposed by the model of Enriquez and Taylor (2015).

Gross primary production was calculated from the difference between rate of oxygen increase during the day and decrease during the night, diel cycle shown by *in situ* data in the top 20 m of the column. Physical processes often disrupted the biological diel cycle and restricted the analysis to four periods during the year. The gross primary production ranged between 6 mmol m<sup>-2</sup> d<sup>-1</sup> and 13 mmol m<sup>-2</sup> d<sup>-1</sup>. Results suggest an enhancement of the gross primary production when the mixing layer shoals.



# Table of Contents

<b>Abstract</b>	<b>5</b>
<b>Table Of Contents</b>	<b>7</b>
<b>List Of Figures</b>	<b>11</b>
<b>List Of Tables</b>	<b>21</b>
<b>Acknowledgments</b>	<b>23</b>
<b>Chapter 1 Introduction</b>	<b>25</b>
1.1 Quantification Of Biological Production In The Ocean	25
1.2 North Atlantic And Its Phytoplankton Bloom	27
1.3 Deep Chlorophyll Maximum	31
1.4 Oxygen As A Proxy To Estimate Biological Activity	32
1.5 Gliders: A Platform For High Frequency Measurements	33
1.6 Pap Site	34
1.7 Open questions about productivity in the North Atlantic	37
1.8 Thesis Outline	39
<b>Chapter 2 Data calibration</b>	<b>41</b>
2.1 Data acquisition	41
2.2 Calibration of CTD casts	42
2.3 Calibration of the gliders - methodology	45
2.3.1 TCPhase – Response time correction	46
2.3.2 CalPhase – computation and calibration	48
2.3.3 Oxygen concentration – calculation	49
2.4 Data quality control	50
2.5 Calibration of CTD casts – results	51
2.5.1 CTD calibration through Winkler titration of water samples	51
2.5.2 Comparison of O <sub>2</sub> concentrations with historical data	57
2.6 Calibration of the gliders – results	60
2.6.1 Calibration of gliders through calibrated ship-CTD casts	60

2.6.2	Detection of the biofouling during calibration	65
2.7	Data quality control – results	70
2.7.1	Despiking	70
2.7.2	Correction for clogged salinity sensor	72
2.8	Conclusions	74
<b>Chapter 3 Hydrographic analysis</b>		<b>75</b>
3.1	Oxygen parameters	75
3.2	Layers in the water column	76
3.3	Oxygen analysis in layer A	80
3.4	Oxygen in layer B	83
3.4.1	Correlation between oxygen concentration and temperature	83
3.4.2	Oxygen Subsurface Increases (OSIs)	84
3.5	Oxygen in layer C	88
3.6	Biofouling	90
3.7	Conclusions	93
<b>Chapter 4 Mixed and mixing layer</b>		<b>95</b>
4.1	Introduction	95
4.2	Methods	97
4.2.1	Calculation of ocean surface boundary layer depth	93
4.2.2	Simulation of lower frequency	101
4.3	Results and discussion	101
4.3.1	Smoothing process and oxygen reference concentration	101
4.3.2	Mixed layer calculation	102
4.3.3	Comparison between 0.5% and higher thresholds	105
4.3.4	Comparison among mixed layer estimates	107
4.3.5	Profiles without mixed and mixing layer	111
4.3.6	End-February Event (EFE)	112
4.3.7	Estimation of mixing layer depth based on density	115
4.3.8	Simulation of lower frequency	117
4.4	Differences between ascents and descents	119

4.5	General discussion	120
4.6	Conclusions	122

## **Chapter 5 Net Community Production** **123**

5.1	Introduction	123
5.2	Ancillary data and methodology	125
	5.2.1 Separation of descents and ascents	125
	5.2.2 Inventory calculation	125
	5.2.3 Air-sea O <sub>2</sub> flux calculation	128
	5.2.4 Entrainment	133
	5.2.5 Net community production calculation	135
	5.2.5 Average light in mixing layer	136
5.3	Results	138
	5.3.1 Year-long dataserries of net community production	138
	5.3.2 Autumn bloom	139
	5.3.3 Heterotrophic period	141
	5.3.4 Spring	143
	5.3.5 Summer bloom and deep chlorophyll maximum	149
	5.3.6 Method sensitivity	150
5.4	Discussion	153
	5.4.1 Autumn	153
	5.4.2 Heterotrophic period	155
	5.4.3 Spring	155
	5.4.4 Summer and deep chlorophyll maximum	156
	5.4.5 Production estimates	158
	5.4.6 Revisiting the Sverdrup hypothesis	160
5.5	Future work	162
5.6	Conclusions	163

## **Chapter 6 Gross primary production** **165**

6.1	Introduction	165
6.2	Method description	166

6.3	Results	167
6.4	Discussion and Conclusions	174
<b>Chapter 7 Conclusions</b>		<b>177</b>
7.1	Findings and estimates	177
	7.1.1 Biofouling	177
	7.1.2 Dataset	177
	7.1.3 Mixed and mixing layer depth	178
	7.1.4 Net community production	179
	7.1.5 Gross primary production	182
7.2	Considerations and suggestions	183
7.3	Future work	184
	7.1.5 Development of this dataset	184
	7.1.5 Development of glider-based surveys	185
7.4	Summary	186
<b>Abbreviations</b>		<b>189</b>
<b>Mathematical annotations</b>		<b>191</b>
<b>References</b>		<b>193</b>
<b>Appendix I Alternative net community production calculation</b>		<b>I</b>
<b>Appendix II Damerell et al. (2016) [manuscript]</b>		<b>V</b>
<b>Appendix III Oxygen data collection and calibration Best Practice Protocol</b>		<b>XXVII</b>
III.1	CTD data collection	XXVII
III.2	Glider data calibration	XXVIII

# List of figures

- Figure 1.1 Annual rates of net community production integrated from the surface to the base of the mixed layer as measured by Lee et al. (2001). Globally integrated net community estimate is  $9.1 \text{ Gt a}^{-1}$  in C equivalents. (figure from Lee, 2001) \_\_\_\_\_ 29
- Figure 1.2 Comparison of bloom hypotheses: (a) the critical depth hypothesis (CDH), (b) the critical turbulence hypothesis (CTH), and (c) the disturbance-recovery hypothesis (DRH). The seasonal cycle begins with summer on the left. Thick black line is the mixed-layer depth (MLD). Green phytoplankton cells and green shading above the MLD are proportional to phytoplankton concentration. Gray ciliates represent all phytoplankton grazers. Arrows above each panel indicate changes in phytoplankton abundance. In panel c, the blue arrows at the top correspond first to increasing water-column-integrated phytoplankton biomass (but not concentration) and then, once the mixed layer begins to shoal, to increasing phytoplankton concentration. (figure from Behrenfeld and Boss, 2014). \_\_\_\_\_ 30
- Figure 1.1 Bathymetry of the east Porcupine Abyssal Plain (North Atlantic) with the position of the Sustained Observatory marked with a white mark. Bathymetric colour legend is in meters. \_\_\_\_\_ 35
- Figure 1.4 Trajectories leading to PAP site computed from altimetry-derived geostrophic velocities. Each trajectory lasts for 90 days and ends at the PAP-OS (white cross) in the period January to March of the indicated years. In (a) PB indicates the Porcupine Bank and the Mid-Atlantic Ridge is also highlighted. (from Hartman et al., 2010). \_\_\_\_\_ 36
- Figure 2.1 Surfacing locations of gliders SG566 (blue), SG502 (red) and SG599 (yellow) showing the butterfly-shaped transects that they followed at the PAP site during the three consecutive missions. \_\_\_\_\_ 42
- Figure 2.2 Oxygen concentration profiles from CTD upcasts of cruise JC085 (blue) with the depths at which Niskin bottles were fired during a mission (red). \_\_\_\_\_ 43
- Figure 2.3 (a) Concentrations from btl files for each Winkler sample collected during the cruise against the relative concentrations measured by Winkler titration. The black line is the linear regression between valid data-points (red); samples disregarded are in grey; (b) residual difference between concentrations measured by Winkler titration and btl values after calibration. The difference increases with depth because of uncorrected pressure hysteresis. Winkler samples used for the calibration are shown in red. Values are from JC085. \_\_\_\_\_ 44
- Figure 2.4 Oxygen concentration profiles from the upcasts of CTD casts performed during cruise JC085 before (blue) and after (black) the calibration. In red are the oxygen

concentrations measured in the .btl file at the depths where the Niskin bottles were fired. In green are the values measured by Winkler titration. \_\_\_\_\_ 45

Figure 2.5 Example of potential density versus depth in an ascent and a descent paired to find the optimum  $\tau$ . Identical potential density values are found at different depths in the two profiles, biasing the RMS computation through equation 2.3. \_\_\_\_\_ 48

Figure 2.6 Cruise D381 - (a) Oxygen concentration profiles from CTD before (blue) and after calibration (black). In red are depths and oxygen concentrations of Niskin bottles fired above 1000 m and in green are the relative concentrations measured with Winkler titration; (b) concentrations from btl files for each Winkler sample collected during the cruise against the relative concentrations measured by Winkler titration; the black lines are the linear regressions of valid points used as calibration equations for the oxygen concentration profiles of CTD casts. Red are valid points for CTD casts 1-12 and green are for CTD casts 14-21. \_\_\_\_\_ 53

Figure 2.7 Cruise CE13001 - (a) Oxygen concentration profiles from CTD upcasts before (blue) and after calibration (black). In red are depths and oxygen concentrations of Niskin bottles fired above 1000 m and in green are the relative concentrations measured with Winkler titration; (b) concentrations from btl files for each Winkler sample collected during the cruise against the relative concentrations measured by Winkler titration; black line is the linear regression of valid points (red) used as calibration equation for the oxygen concentration profiles of CTD casts. \_\_\_\_\_ 54

Figure 2.8 Cruise JC087 - (a) Oxygen concentration profiles from CTD upcasts before (blue) and after calibration (black). In red are depths and oxygen concentrations of Niskin bottles fired above 1000 m and in green are the relative concentrations measured with Winkler titration; (b) concentrations from btl files for each Winkler sample collected during the cruise against the relative concentrations measured by Winkler titration; black line is the linear regression of valid points (red) used as calibration equation for the oxygen concentration profiles of CTD casts. \_\_\_\_\_ 55

Figure 2.9 Cruise JC090 - (a) Oxygen concentration profiles from CTD upcasts before (blue) and after calibration (black). In red are depths and oxygen concentrations of Niskin bottles fired above 1000 m and in green are the relative concentrations measured with Winkler titration; (b) concentrations from btl files for each Winkler sample collected during the cruise against the relative concentrations measured by Winkler titration; black line is the linear regression of valid points (red) used as calibration equation for the oxygen concentration profiles of CTD casts. \_\_\_\_\_ 56

Figure 2.10 Linear regression between btl and Winkler values used as calibration equations for each cruise. \_\_\_\_\_ 57

Figure 2.11 (a) Comparison between oxygen concentrations of the calibrated CTDs casted during OSMOSIS and the ones from Winkler samples titrated during eWOCE cruises

- (black) versus depth; (b) comparison between Winkler samples titrated during OSMOSIS and Winkler samples titrated during eWOCE cruises (black) versus potential density. \_\_59
- Figure 2.12 Distribution of the frequency with which each value between 0 s and 50 s is the best  $\tau$  value (blue bars) within each mission. In red is the normal distribution fitted over the data whose central value  $\mu$  is used as  $\tau$  for the mission. Analysis is carried out for each individual mission: SG566 (a), SG502 (b) and SG599 (c). The latter is also repeated not considering the profiles measured after August 11<sup>th</sup> because of biofouling (d). \_\_\_\_\_ 60
- Figure 2.13 Maps of the surfacing locations of the Seaglider before and after each dive for (a) SG566, (b) SG502 and (c) SG599. For each mission are shown the location of the CTD casts and the surfacing locations of the calibrated dives. \_\_\_\_\_ 63
- Figure 2.14 Calibration linear equations for the beginning (blue) and the end (red) of each glider mission for (a) SG566, (b) SG502 and (c) SG599. In (c) a third calibration done in the middle of the mission is also shown in black. The name of the cruises of the calibrating CTD casts is also shown. \_\_\_\_\_ 64
- Figure 2.15 Calibration of SG566: (a – b) linear regression between the TCPhase of the glider dives and the back-calculated CalPhase of the calibrated CTD used to calibrate TPhaseCoef0 and TPhaseCoef1 (shown); (c – f) calibrated dives and CTD used for the calibration against pressure (c – d) and potential density at surface (e – f); (a – c – e) is the calibration at the beginning of the mission and (b – d – f) is the calibration at the end of the mission. \_\_\_\_\_ 66
- Figure 2.16 Calibration of SG502: (a – b) linear regression between the TCPhase of the glider dives and the back-calculated CalPhase of the calibrated CTD used to calibrate TPhaseCoef0 and TPhaseCoef1 (shown); (c – f) calibrated dives and CTD used for the calibration against pressure (c – d) and potential density at surface (e – f); (a – c – e) is the calibration at the beginning of the mission and (b – d – f) is the calibration at the end of the mission. \_\_\_\_\_ 67
- Figure 2.17 Calibration of SG599: (a – b) linear regression between the TCPhase of the glider dives and the back-calculated CalPhase of the calibrated CTD used to calibrate TPhaseCoef0 and TPhaseCoef1 (shown); (c – f) calibrated dives and CTD used for the calibration against pressure (c – d) and potential density at surface (e – f); (a – c – e) is the calibration at the beginning of the mission and (b – d – f) is the calibration in the middle of the mission. \_\_\_\_\_ 68
- Figure 2.18 Calibration of SG599 with JC090 at the end of the mission (a) Linear regression between the TCPhase of the glider dives and the back-calculated CalPhase of the calibrated CTD used to calibrate TPhaseCoef0 and TPhaseCoef1 (shown); (b – d) calibrated dives and CTD used for the calibration against pressure and potential density at surface; (c – e) comparison of the same dives as calibrated using JC090 (3 CTD casts calibration) and as calibrated using the drift between the first two calibrations of the mission to compute

TPPhaseCoef0 and TPhaseCoef1 disregarding JC090 because of biofouling (2 CTD cass calibration).	69
Figure 2.19 Example of consecutive profiles where the descending profile (blue) has a decreasing gradient in salinity in the top 20 m that result in anomalous values of oxygen concentrations, therefore flagged as spikes.	70
Figure 2.20 (a-c-e) Valid data-points in blue and spikes in black for SG566 (a), SG502 (c) and Sg599 (e) with a focus of the spikes closest to the valid data; (b-d-f) cumulative proportion of spikes versus depth. All spikes are all constrained above 40 m for all missions.	71
Figure 2.21 Oxygen concentrations measured with the same CalPhase profile and with fixed temperature using two salinity values ( $S = 34.5$ and $S = 35.5$ ). The comparison is done to show the effect of salinity on oxygen concentration calculation (mean difference is $(1.6 \pm 0.2) \mu\text{mol kg}^{-1}$ ).	72
Figure 2.22 Salinity profiles measured with clogged sensor during SG566 (a) and SG599 (b). Profiles flagged because of the clogging are in grey, profiles measured just before and just after them are in black, the range of good salinity values is in red and the profiles used to calculate oxygen concentrations for the flagged profiles is in blue.	73
Figure 3.1 Variance preserving spectra for (a) temperature (b) salinity ( $\times 10^{-3}$ ) and (c) dissolved oxygen concentration. The colours show the power spectral density $\times$ frequency. The inertial frequency (IN) and M2 tidal frequency are marked as black arrows on the upper axis (Damerell et al., 2016).	77
Figure 3.2 Distribution against pressure (left panel) and time series against pressure (right panel) for (a-b) oxygen concentration, (c-d) oxygen saturation and (e-f) Apparent Oxygen Utilization. The black line in (b) marks the start of the biofouling.	78
Figure 3.3 Distribution against pressure (left panel) and time series against pressure (right panel) for (a-b) temperature, (c-d) salinity, (e-f) potential density at surface and (g-h) chlorophyll <i>a</i> concentration. The black line in (b-d-f-h) marks the start of the biofouling.	79
Figure 3.4 (a) Mean conservative temperature in the top 20 m of the water column; (b) mean oxygen concentration (blue) and oxygen saturation concentration (red) in the top 20 m of the water column. Red line is above blue line during periods of undersaturation, vice versa for supersaturation.	81
Figure 3.5 Distribution of oxygen saturation against chlorophyll <i>a</i> concentration coloured by the date of measurements between mid-September 2012 and mid-December 2012 (a), mid-December 2012 and mid-March 2013 (b), mid-March 2013 and mid-June 2013 (c) and mid-June 2013 to mid-August 2013 (d).	83
Figure 3.6 Correlation coefficient between oxygen concentration and conservative temperature versus pressure. Data are gridded in pressure. Positive values are for correlated data, negative values for anti-correlated data.	84

- Figure 3.7 Sea level anomaly on 10<sup>th</sup> April 2013 at the OSMOSIS site from AVISO global allsat product. Velocity field (black arrows) is in  $\text{m s}^{-1}$  and the butterfly surveyed by gliders is in red. \_\_\_\_\_ 85
- Figure 3.8 (a) Time series of the position (latitude) of the glider between 6<sup>th</sup> and 23<sup>rd</sup> April; (b) Dissolved oxygen concentration against depth and time in  $\mu\text{mol kg}^{-1}$  with depth of the isopycnals  $\sigma=27.11 \text{ kg m}^{-3}$  in black and  $\sigma=27.16 \text{ kg m}^{-3}$  in red and euphotic depth in green for the same period as in (a); (c) apparent oxygen utilization (AOU) between  $\sigma=27.11 \text{ kg m}^{-3}$  and  $\sigma=27.16 \text{ kg m}^{-3}$  over time for the same period as in panel (a) in grey, AOU in the core of the OSIs in black with associated mean value and standard deviation per each profile in green and fitting regression line showing the linear increase of AOU calculated between 9<sup>th</sup> and 23<sup>rd</sup> April in red. \_\_\_\_\_ 86
- Figure 3.9 Sea level anomaly on 7<sup>th</sup> February 2013 at the OSMOSIS site from AVISO global allsat product. Velocity field (black arrows) is in  $\text{m s}^{-1}$  and the butterfly surveyed by gliders is in red. \_\_\_\_\_ 87
- Figure 3.10 (a) Dissolved oxygen concentration versus depth between January 30<sup>th</sup> and February 18<sup>th</sup> in  $\mu\text{mol kg}^{-1}$  with depth of the isopycnals  $\sigma=27.11 \text{ kg m}^{-3}$  (black),  $\sigma=27.16 \text{ kg m}^{-3}$  (red) and the euphotic depth (green); (b) same as (a) but for oxygen saturation; (c) mean apparent oxygen utilization (AOU) for each profile between  $\sigma=27.11 \text{ kg m}^{-3}$  and  $\sigma=27.16 \text{ kg m}^{-3}$  (red) with standard deviation (blue) and original data-points (grey) \_\_\_\_\_ 88
- Figure 3.11 Distribution of oxygen concentration against absolute salinity in layer C (below 700 m) coloured by pressure. \_\_\_\_\_ 89
- Figure 3.12 (a) Oxygen concentration at the 11 m horizon during the ascending phase (blue) and descending (red) phase of glider dives; (b) Minimum oxygen concentration (if measured within the boundaries of Intermediate Water). In both (a) and (b) the black vertical line marks the date of August 11<sup>th</sup>, when the bias due to biofouling is considered to start formally. (c) expanded section from panel (a) during the biofouling-affected period showing the difference between ascents and descents that mismatched during daytime and matched again at night. \_\_\_\_\_ 91
- Figure 3.13 Scheme of the position of the foil of the optode with respect to the surface and to the incident light in the ascents and descents of each dive \_\_\_\_\_ 92
- Figure 4.1 Comparison between smoothed versions of profiles number 2336 (a-b) and 3548 (c-d) and the original profiles. The ‘lowess’ algorithm (red dots in b-d) matches the shape of the original (blue line) better than its robust version ‘rflowess’ (green dots in a-c). \_\_\_\_\_ 99
- Figure 4.2 Top m of the 40 oxygen concentration profiles used for the calculation of the variability of values within the surface boundary layer. The depth of the layer (black horizontal lines) was visually identified as the maximum depth of the homogeneous values. Black profiles are measured during the night and red profiles during the day. \_\_\_\_\_ 100

Figure 4.3 Mean difference between oxygen concentrations and oxygen concentration reference within the ocean surface boundary layer of the 40 selected profiles. Error bars show $\pm$ standard deviation.	101
Figure 4.4 Oxygen reference concentration used as proxy for the oxygen concentration in the homogeneous ocean surface boundary layer.	102
Figure 4.5 Examples of profiles with their OSBL depth defined by oxygen concentration with the threshold of 0.5% (black horizontal lines). (a-f) shows profiles in which the homogeneous OSBL is obvious during the autumn (a-b), winter and early spring (c-d), late spring and summer (e-f). Panels (i-j) show examples of profiles with stratification spanning all the way to the surface. Please note different x and y axes for each panel.	104
Figure 4.6 Examples of profiles (1385 in a, 2097 in b) used for the validation of the thresholds used for the calculation of the OSBL depth.	106
Figure 4.7 (a) Time series of OSBL depth defined by oxygen with the threshold of 0.5% (black) and 1.5% (blue) over the timeseries of oxygen concentration; (b) difference between the two estimates measured per each profile.	107
Figure 4.8 Timeseries of $z_{\text{mix}}$ defined by oxygen concentration with the threshold of 0.5% (black) compared with (a) $z_{\text{mix}}$ defined by density and temperature (red) from Damerell et al. (2016) and (b) chlorophyll <i>a</i> concentration (green).	109
Figure 4.9 Root mean square difference calculated for each month between September 2012 and September 2013 between $z_{\text{mix}}$ defined by density/temperature and $z_{\text{mix}}$ defined by oxygen concentration with a threshold of 0.5% (blue line) and 1.5% (red line).	109
Figure 4.10 Timeseries of $z_{\text{mix}}$ defined by oxygen concentration with the threshold of 1.5% (blue) compared with (a) $z_{\text{mix}}$ defined by density and temperature (red) from Damerell et al. (2016) and (b) chlorophyll <i>a</i> concentration (green).	111
Figure 4.11 Profile 1861 as an example of (a) an oxygen concentration profile with a gradient spanning all the way to the surface with its mixing layer depth defined by oxygen concentration (black l) and (b) its potential density profile with visible mixing layer whose depth aligns with the mixing layer defined by oxygen concentration. Red line is the mixed layer depth defined by density from Damerell et al. (2016).	112
Figure 4.12 End February Event. (a) Wind speed at 10 m from the sea surface from ERA-Interim reanalysis; (b) oxygen concentration, (c) chlorophyll concentration and (d) potential density versus depth. The black line is the mixing layer depth defined by oxygen concentration with 0.5% threshold, the red line is the mixed layer depth defined by density/temperature according to Damerell et al. (2016), the blue line is the mixed layer depth defined by oxygen concentration with 1.5% threshold, the green line is the mixed layer depth defined by chlorophyll concentration and in bright blue is the mixing layer depth defined by density with 0.005 kg m <sup>-3</sup> threshold. Euphotic depth is in yellow in panel c.	113

Figure 4.13 Examples of (a-e) oxygen concentration profiles completely stratified with sign of a mixing layer defined by potential density and (f-j) oxygen concentration profiles with a mixing layer whose depth aligns to gradients in the physical parameters.	114
Figure 4.14 Time series of mixing layer depth defined by potential density with the threshold of $0.005 \text{ kg m}^{-3}$ (bright blue) superimposed to the time series of mixing layer depth defined by oxygen concentration with the threshold of 0.5% (black).	115
Figure 4.15 Example of (a-b) profile in which the mixing layer defined by oxygen (black line) and density (bright blue line) match and (c-d) profile in which they do not match and the mixing layer defined by oxygen match with euphotic depth (yellow line). Red line is the mixed layer defined by density/temperature by Damerell et al. (2016).	117
Figure 4.16 (a-e) Complete time series of mixing layer at PAP station in blue and subsample considering one profile sampled at midnight every (a) 1, (b) 3, (c) 5, (d) 7 and (e) 10 days in red over one year cycle.	118
Figure 4.17 (a) Correlation coefficient between the original mixing layer time series and each of the subsamples considering profiles measured at midnight every 1, 3, 5, 7 and 10 days; (b) root mean square difference between the original mixing layer time series and each of the subsamples considering profiles measured at midnight every 1, 3, 5, 7 and 10 days.	119
Figure 5.1 Euphotic depth measured before the start of the biofouling event with horizontal bar showing its mean value.	126
Figure 5.2 (a) oxygen concentration in $\mu\text{mol kg}^{-1}$ versus depth with mixing layer depth ( $z_{\text{mix}}$ , black line), euphotic depth ( $z_{\text{eup}}$ , green line) and $z_{\text{lim}}$ (red, 60 m); (b) mean concentration of oxygen above $z_{\text{lim}}$ calculated dividing the oxygen inventory by $z_{\text{lim}}$ ; (c) rate of change in oxygen inventory between consecutive profiles.	127
Figure 5.3 (a) Mean potential temperature in the top 10 m of the water column for each profile in $^{\circ}\text{C}$ ; (b) mean absolute salinity in the top 10 m of the water column for each profile in $\text{g kg}^{-1}$ ; (c) atmospheric pressure from ERA-Interim reanalysis during each surface event; (d) mean oxygen saturation concentration in the top 10 m for each profile calculated according to García and Gordon (1992). When $z_{\text{mix}} < 10 \text{ m}$ , values are the mean above $z_{\text{mix}}$ .	129
Figure 5.4 (a) Daily averages of wind speed at 10 m above sea-surface from ERA-Interim reanalysis; (b) $k_{600}$ as calculated based on wind speed plotted in (a).	130
Figure 5.5 Daily averages of (a) potential temperature used for Schmidt number calculation and (b) resultant Schmidt number time series.	131
Figure 5.6 Gas transfer velocities scaled for oxygen.	131
Figure 5.7 (a) Difference between daily mean oxygen concentration and daily mean oxygen saturation concentration in the top 10 m used in the air-sea oxygen flux calculation (in blue) and magnitude of the bubble correction (in red). Positive values indicate	

supersaturation and negative values indicate undersaturation; (b) bubble supersaturation parameterisation ( $\Delta$ ) according to Woolf and Thorpe (1991); (c) air-sea oxygen flux (in blue), air-sea oxygen flux without considering bubble correction (in red) and air-sea oxygen flux due to bubbles (in yellow). Positive values indicate outgassing of oxygen in the atmosphere and negative values indicate influx of oxygen into the water column. --- 133

Figure 5.8 (a) oxygen concentration versus depth with smoothed mixing layer depth (black line) and  $z_{lim} = 60$  m (red line); (b) entrainment flux, i.e. rate of change of oxygen inventory due to entrainment. ----- 135

Figure 5.9 (a) Time series of total amount of light intensity in einstein per unit surface and per day; mean light in mixed layer. Daily values (blue) and weekly values (red).----- 137

Figure 5.10 Time series of (a)  $\Delta I(z_{lim})/\Delta t$  in blue, air-sea oxygen flux in red, entrainment in yellow and net community production in purple. All values are 7-day averages. Note that the sign of the entrainment is here inverted in order to represent its contribution to  $N$ . -- 138

Figure 5.11 Time series of net community production divided in the four periods analysed separately.----- 139

Figure 5.12 (a) Net community production, (b) mixing layer and euphotic depths over oxygen concentration versus depth, (c) wind speed, (d) chlorophyll a concentration versus depth and (e) weekly mean light in the mixing layer during the autumn bloom. Black vertical lines indicate the end of wind speed increases (storms) after which there was an increase in biological productivity. The red vertical line marks a decrease in wind speed linked to the switch between net autotrophy and net heterotrophy during mixing layer depth shoaling. ----- 140

Figure 5.13 (a) Net community production during the heterotrophic period; (b) oxygen concentration versus depth with mixing layer depth (black line) and euphotic depth (green line); (c) wind speed at 10 m from sea surface from ERA-Interim reanalysis.----- 142

Figure 5.14 (a) Net community production, (b) oxygen concentration and (c) potential density measured during the spike in net community production at the end of the autumn bloom. The exact correlation between variations in  $c(O_2)$  and  $\sigma$  suggests the presence of geographical features in the area.----- 143

Figure 5.15 (a) Net community production, (b) mixing layer and euphotic depths over oxygen concentration versus depth, (c) wind speed, (d) chlorophyll a concentration versus depth, (e) net heat flux and (f) weekly averaged light in the mixed layer between 9<sup>th</sup> February and 12<sup>th</sup> April. Red vertical line indicates the start of the peak on 4<sup>th</sup> March and light blue line the start of the peak on 16<sup>th</sup> March. In panel (a) is also shown the peak associated to End-February Event (see chapter 4).----- 145

Figure 5.16 Parameters between April 19<sup>th</sup> and May 27<sup>th</sup>. (a) Net community production above 60 m; (b) mean chlorophyll a concentration above 60 m (courtesy of Anna Rumyantseva, NOC); (c) wind speed (Era-Interim reanalysis); (d) mean potential density above 10 m; (e)

mixing layer depth (in black), euphotic depth (in green) and oxygen concentration versus depth between 250  $\mu\text{mol kg}^{-1}$  and 275  $\mu\text{mol kg}^{-1}$ ; (f) mean temperature in the top 10 m; (g) air-sea flux including bubbles, (h) net surface heat flux (Era-Interim reanalysis) and (i) weekly mean light intensity in the mixed layer. Red line is the beginning of the peak (April 19<sup>th</sup>), black line is the beginning of the heterotrophic period (May 4<sup>th</sup>), pink line is the end of it (May 8<sup>th</sup>), light blue line is the deepening event replenishing the nutrients above  $z_{\text{mix}}$  (May 16<sup>th</sup>) and green line is the end of the productive peak (May 27<sup>th</sup>). The arrow in panel (h) marks the switch between a period of mean negative net surface heat flux and a period of mean positive net surface heat flux.----- 147

Figure 5.17 (a) Net community production, (b) mixing layer depth and euphotic depth over oxygen concentration versus depth, (c) wind speed, (d) potential density versus depth with mixing layer depth and (e) weekly mean light intensity in the mixing layer between 31<sup>st</sup> May and 21<sup>st</sup> June.----- 148

Figure 5.18 (a) Net community production during the summer bloom and the deep chlorophyll maximum; (b) oxygen concentration over depth and time above  $z_{\text{lim}}$  with  $z_{\text{mix}}$  (black line) and  $z_{\text{eup}}$  (green line); (c) wind speed at 10 m above sea-surface from ERA-Interim reanalysis and (d) chlorophyll *a* concentration versus depth.----- 150

Figure 5.19 Net community production time series measured above (a) 45 m, (b) 60 m and (c) 75 m using descents (blue lines) and ascents (red lines) from each glider dive----- 151

Figure 5.20 Net community production measured above 60 m and averaged over 7 days-bins with values recalculated (a) not considering air-sea O<sub>2</sub> flux (blue line) and (b) not considering entrainment flux (red line).----- 153

Figure 6.1 (a) Oxygen concentration timeseries between 4<sup>th</sup> and 13<sup>th</sup> October 2012 versus pressure and time. The mean mixed layer depth is also shown; (b) Oxygen concentration in the top 20 m (grey) with line fits calculated per each day (red) and night (black). The diel cycle is visible through the alternation of oxygen increase during the day and decrease during the night; (c) air-sea oxygen flux where positive values mean outgassing and negative ones mean ingassing. The median value for the period is also plotted. \_\_\_\_\_ 169

Figure 6.2 As figure 6.1 but for period between 19<sup>th</sup> and 27<sup>th</sup> March 2013. \_\_\_\_\_ 170

Figure 6.3 As figure 6.1 but for period between 14<sup>th</sup> and 21<sup>st</sup> April 2013. \_\_\_\_\_ 171

Figure 6.4 As figure 6.1 but for period between 14<sup>th</sup> and 22<sup>nd</sup> May 2013. \_\_\_\_\_ 172

Figure 6.5 Gross primary production estimated for the four periods using ascents and descents. The error bars are based on the standard deviations of the mean increase and decrease rates of oxygen concentration within each period. \_\_\_\_\_ 173

Figure 7.1 Model of the mechanism proposed to explain the start of the spring bloom. The mixing layer (dark blue layer) shoals above the euphotic depth (yellow line) (from  $t_1$  to  $t_2$ ).

This occurs when the turbulent mixing (circular arrows) decreases because the wind speed decreases (dark green arrow) and the net surface heat flux (red arrow) switches from cooling to warming of surface water. As a consequence, the net community production increases and this leads to the accumulation of biomass and, then, chlorophyll ( $t_3$ ). \_\_\_\_ 167

# List of tables

Table 1.1 Net community production in carbon equivalent,  $N_C$  (adapted and expanded from Alkire et al. 2014). In bold are the results from studies analysing  $N_C$  directly, while in normal characters are the estimates in oxygen unit converted to  $N_C$  using the photosynthetic quotient, PQ. In these cases the PQ value used for the conversion is indicated. \_\_\_\_\_ 27

Table 2.1 Number of CTD casts, number of Winkler samples collected and number of Winkler samples discarded for each cruise during OSMOSIS. Winkler samples discarded are divided according to the reason of flagging. \_\_\_\_\_ 52

Table 2.2 CTD casts and glider dives used per each calibration, spatial and temporal distance between them,  $r^2$  value of their regression, calibration equation using TPhaseCoef<sub>0</sub> and TPhaseCoef<sub>1</sub> obtained by the regression and uncertainty associated to the calibration. \_\_ 62

Table 2.3 CTD casts for each cruise with either the Seaglider mission they calibrated or the reason why they were disregarded. Cast 13 of D381 is not included because the wire holding the frame split. Dives 1 and 3 from JC090 were not used in the final calibration\_ 63

Table 5.1 Net community production mean, standard deviation and total sum calculated above 45 m, 60 m and 75 m. \_\_\_\_\_ 152

Table 5.2 Mean values of the net community production time series that were obtained averaging individual estimates between consecutive profiles over different bin lengths. 152

Table 5.3 Net community production in carbon equivalent,  $N_C$  (adapted and expanded from Alkire et al. 2014). In bold are the results from studies analysing  $N_C$  directly, while in normal characters are the estimates in oxygen unit converted to  $N_C$  using the photosynthetic quotient, PQ. In these cases the PQ value used for the conversion is indicated. \_\_\_\_\_ 159

Table 6.1 Rates of mean diurnal increase and mean nocturnal decrease in oxygen concentration for unit volume calculated for each of the four periods where a diel cycle is visible. Gross primary production per unit volume is measured as the difference between the mean increase and decrease. \_\_\_\_\_ 168

Table 6.2 Gross primary production per unit volume and unit surface measured in each period according to the depth of the mixed layer. The days in which the mixed layer shoals are also listed. Mixed layer depth is indicated and used for the conversion between gross primary production per unit volume and unit surface. \_\_\_\_\_ 173



# Acknowledgments

This thesis summarises more than three years of work. I want to thank my supervisors, Jan Kaiser and Karen Heywood, for their patience, suggestions, corrections, words, time, solace and trust. They have been precious professional and personal guides in this long (and sometimes hard) path.

The OSMOSIS dataset was big and complex and I'd like to thank Gillian Damerell, Anna Rumyantseva and Victoria Hemsley for their effort in analysing the other parameters that compose it. Their work provided useful data to realise important parts of this thesis. Thanks to the UEA glider piloting team for the priceless collective effort done in order to maintain the gliders operative without interruptions for an entire year. Thanks to Bastien Queste, Gareth Lee and Stephen Woodward for having shared with me their knowledge about gliders and for the fieldwork they carried out. Thank to Adrian Martin, Stuart Painter and Alex Forryan at NOC Southampton for their help to analyse (and re-analyse) the CTDs. Thanks also to the scientists, technicians, officers and crew on board of RRS Discovery, RV Celtic Explorer and RRS James Cook for their fundamental work.

This project was possible thanks to the NERC funding NE/I019905/1 and NSF award OCE 1155676.

My Ph.D. was a moment of significant personal growth. In these three years of my life, I came across many people. A bunch of them deserve some particular acknowledgment for their indirect contribution in finishing this project and in writing this thesis (and for their direct help in making me survive my Ph.D.).

Thanks to Céline, Chris, Chris, Dave, Denis, Honza, Karin, Laura, Louise, Luke, Marina, Michael, Osgur, Richard, Rihannon, Tahmeena and everybody else who laughing, chatting, counselling, correcting or even just being there made the office 3.17 much more than just a place to read and write.

Thanks to Anna and Chata for their cheering up emergency-coffees and thanks to Alida, Geoff, James, Matt, Oliver, and everybody else from Kaiser-Lab for the interesting and cake-fuelled meetings of the last 3 years.

Thanks to Audrey, Alex, Damian, Dan, Davie, G., Hussam, Isa, Markus, Mathew, Matthew, Michael, Nuno, Omar, Ossie, Seavly, Sergio, Steven and Stewart for making Norwich a place where I can say I have lived and not just studied.

And last but not least, thanks (but probably 'grazie' works better here) to my parents, my sisters and Andrea, Anna, Angela, Alessandro, Daniela, Daniele, Elena, Federico, Frediano, Luca, Luca, Manuel, Pietro, Rossana and Teresa. Their being so close even when they were so far was more important than they probably realise.



# Chapter 1

## Introduction

This study presents the analysis of oxygen concentration measured by gliders at the Porcupine Abyssal Plain (North Atlantic) from September 2012 to September 2013. The study aims to use the oxygen data for biological purposes. The interpretation of the results will be focused on revealing how physical processes affect biology and quantifying the magnitude of the plankton production.

### 1.1 Quantification of biological production in the ocean

In the open ocean, biological processes are related to the metabolic activity of the plankton community. This community has an autotrophic component (usually identified with the phytoplankton) that fixes inorganic carbon into organic compound through photosynthesis; and a heterotrophic component (usually identified with the zooplankton and the non-photosynthesizing bacterioplankton), which consumes the organic compounds to produce energy. The balance of these two activities in the plankton community is very important on the global-scale carbon cycle (Volk and Hoffert, 1985) because according to Field et al. (1998) half of the carbon fixation happening on the planet occurs in the ocean. Phytoplankton has the capacity to remove a large amount of dissolved carbon dioxide (inorganic carbon) from the ocean, locking it in the organic compounds that can be then exported in the deep sediments. The heterotrophic component of the plankton, on the other hand, can remobilize through respiration the inorganic carbon previously locked. This remineralisation of the organic carbon is particularly important at the top of the water column, since its rate decreases exponentially with depth ('Martin curve', Martin et al., 1987). This entire process (phytoplankton production and respiration) is called the 'biological carbon pump' and, removing carbon dioxide from the water, triggers an air-sea mass flux that makes the ocean absorb large quantities of this gas from the atmosphere. The organic carbon that escapes remineralisation is then stored in the deep, which acts as a long term carbon sink, stocking it in long-term reservoirs. Along with the biological carbon pump there is also a 'physical carbon pump' (or 'solubility pump') that stores inorganic carbon in the water column dissolving carbon dioxide from the atmosphere. The solubility pump has been enhanced in the past decades by the increase of carbon dioxide in the atmosphere due to fossil fuel combustion due to human activity (Doney et al., 2009). Sabine et

al. (2004) estimated that 48 % of the carbon dioxide produced by anthropogenic activity between 1800 and 1994 was absorbed by the ocean, most of which has been due to the solubility pump. Since carbon dioxide is transformed in carbonic acid once dissolved in water, the acidity of the ocean has increased. This creates creating problems to many biologic compartments, including phyto- and zooplankton (e.g. reduction in calcification) (Bijma 1991, Riebesell et al. 2000). In order to understand how these changes are affecting the carbon cycle, the magnitude of plankton production should be estimated as precisely as possible in order to assess its trends over long time periods. This is of great importance because carbon dioxide is a well-known greenhouse gas and understanding the dynamics of the global carbon cycle will permit to develop models that could forecast climate change and quantify the impact that human activities have on it (Houghton, 2007; Palevsky et al, 2013).

Due to its importance, the scientific community has made a huge effort to quantify plankton production (Robinson et al., 2009; Regaudie de-Gioux, 2014; Hull et al., 2016). The estimation of the rate at which phytoplankton fixes carbon ('gross primary production' or  $P$ ) and the rate at which the whole community exports organic carbon to the deep ('net community production' or  $N$ , i.e.  $P$  minus community respiration) have received particular attention. Many methods have been developed to calculate these rates and many models and observations have focused on the parameterisation of their magnitude (Robinson et al., 2009; Quay et al., 2010; Marra, 2012; Regaudie de-Gioux, 2014, Hull et al., 2016). However, despite the high number of calculations, the real values of  $P$  and  $N$  are still uncertain, such that there is still an open debate about the metabolic balance of some areas of the ocean (i.e., whether they are heterotrophic or autotrophic systems) (Duarte et al., 2013; Ducklow and Doney, 2013; Williams et al., 2013).

There is high variability in the estimates for  $P$  and  $N$  even when the same area and the same period of the year are considered. As an example, in Table 1.1 it is possible to see the range of  $N$  estimates from several studies focused on the same area analysed by this study. This uncertainty is linked to many factors, including interannual variability of biological activity, the technical limits in measuring the data or the influence of physical processes, which hide the biological signal in the observations. Different studies use different methods, producing estimates that are based on different assumptions and sometimes are quantifying different processes (e.g. Williams et al., 2013; Regaudie de-Gioux, 2014). The need for new estimates, based on coherent methods applied over a long time span, is therefore required to lower the uncertainty, parameterize the seasonal and interannual variability and quantify better the magnitude of  $P$  and  $N$ .

**Table 1.1 Net community production in carbon equivalent,  $N_C$  (adapted and expanded from Alkire et al. 2014). In bold are the results from studies analysing  $N_C$  directly, while in normal characters are the estimates in oxygen unit converted to  $N_C$  using the photosynthetic quotient, PQ. In these cases the PQ value used for the conversion is indicated.**

Study	Year	Period	$N_C$ mmol m <sup>-2</sup> d <sup>-1</sup>	PQ used	Notes
<b>Bender et al., 1992</b>	<b>1989</b>	<b>13 days between Apr and May</b>	<b>52</b>		<b>JGOFS - NABE</b>
<b>Robertson et al., 1992</b>	<b>1989</b>	<b>29 May – 5 Jun</b>	<b>42-34</b>		<b>JGOFS – NABE</b>
<b>Körtzinger et al., 2008a</b>	<b>2004</b>	<b>May –Aug</b>	<b>25</b>		<b>PAP station</b>
<b>Körtzinger et al., 2008b</b>	<b>2005</b>	<b>mid May -Jul</b>	<b>50-70</b>		<b>Labrador Sea</b>
Alkire et al. 2012	2008	Apr May (average)	66 115 (90)	1.5	Early Bloom Main Bloom
Alkire et al. 2014	2008	Apr-Jun 3-26 Jun	25 43	1.5	Considerind Alkire et al. 2012 +postbloom
Ostle et al., 2015	2012	Apr – Sep	16	0.8	Basin-wide, region 2 (see Ostle et al., 2015)
<b>Frigstad et al., 2015</b>	<b>2003- 2012</b>	<b>Feb – July</b>	<b>25 (72-6)</b>		<b>PAP site, MLD</b>

## 1.2 North Atlantic and its phytoplankton bloom

The magnitude of  $P$  and  $N$  is not temporally and geographically uniform in the ocean. It is influenced by a series of factors such as light, macro- and micronutrient concentrations, turbulence and the composition of the plankton community. The geographical heterogeneity of net community production (figure 1.1) makes some areas of the Earth Ocean particularly

important for the carbon cycle. The temporal heterogeneity, instead, leads to important seasonal features such as the ‘phytoplankton blooms’, periods of enhanced production usually defined by the high chlorophyll *a* concentration that accumulates at the surface.

Phytoplankton blooms happen worldwide and they are particularly common in polar and subpolar oceans, lakes and upwelling systems (Behrenfeld and Boss, 2014). The spring bloom occurring annually in the North Atlantic has been studied since the first half of the 20<sup>th</sup> century and it has become a model to study the plankton annual cycle. Milestone in this long-term study was the paper by Sverdrup (1953), who proposed his ‘Critical Depth Hypothesis’ to explain the phytoplankton bloom that occurred in the Norwegian Sea (North Atlantic) between March and May 1949. More recently, the North Atlantic Bloom Experiment (NABE) of the Joint Global Ocean Flux Study (JGOFS) was carried out in this region (47°N, 20°W) for 13 days between April and May 1989 in order to study the bloom and analyse the flux of carbon related to plankton community (see Table 1.1).

Starting from Sverdrup (1953), a series of papers tried to describe the dynamics that trigger the bloom. Sverdrup’s theory states that blooms are triggered when the mixed layer shoals above a critical depth, retaining plankton in the layer of the column where it produces more than it consumes (figure 1.2a). According to this theory, the turbulence is always strong enough to keep an even distribution of phytoplankton in the mixed layer and total light is the most important factor, which defines the vertical extent of the productive layer and the amount of phytoplankton growth. The theory has been debated since then, passing through a series of both confirmations and confutations. Other theories have been proposed to explain the triggering factors of the spring bloom. Huisman et al. (1999) took into account the possible mismatching between speed of growth and speed of mixing. They proposed that plankton would bloom before stratification because the fast production would accumulate instead of being mixed down (figure 1.2b). Taylor and Ferrari (2011) related the turbulence to the net surface heat flux, stating that the moment in which this flux increases from negative values (water cooling, mixing due to convection) to positive values (water warming, stratification) could be used as a proxy to predict the start of the spring bloom. Enriquez and Taylor (2015) also modelled the effects of reduced turbulence, linking the bloom to the shoaling of the mixing layer. Behrenfeld et al. (2010) proposed instead a different theory based on the decoupling between predation and production. According to this theory the production rate would be highest during winter, when the mixed layer deepens diluting phyto- and zooplankton and relaxing the predation rate (figure 1.2c).

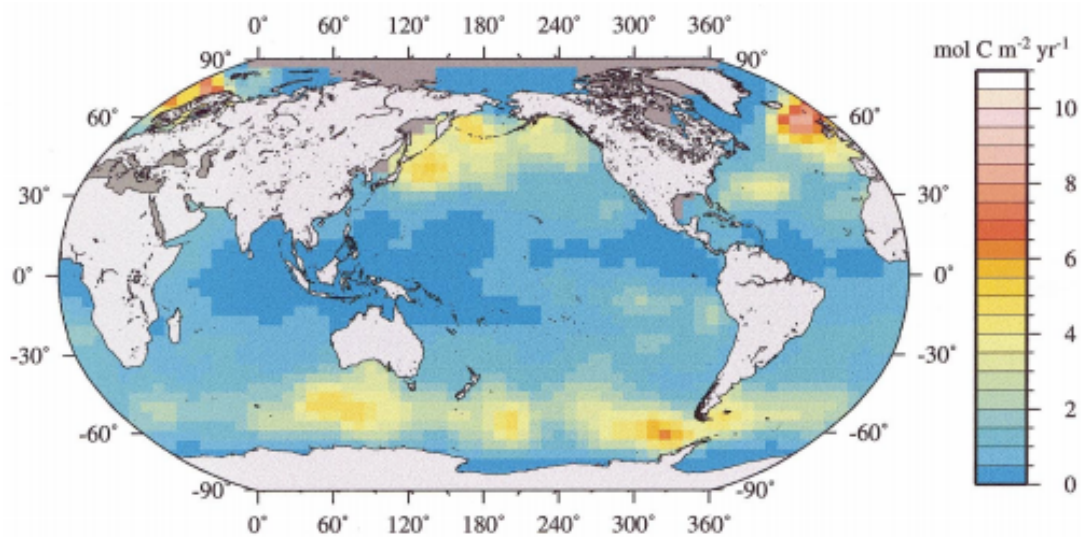


**Figure 1.1 Annual rates of net community production integrated from the surface to the base of the mixed layer as measured by Lee et al. (2001). Globally integrated net community estimate is  $9.1 \text{ Gt a}^{-1}$  in C equivalents. (figure from Lee, 2001)**

Testing these theories has faced many difficulties in the past. The absence of a clear definition of the bloom in the literature and the lack of a threshold to mark the start of blooms have created problems to constrain temporally these events. Furthermore, the use of proxies such as chlorophyll fluorescence has complicated the analysis due to the high number of assumptions made in interpreting the data. There are also small pre-bloom peaks in production such as the ones observed by Körtzinger et al. (2008) at the Porcupine Abyssal Plain (PAP) that have yet to be fully explained. A comparison between physical parameters measured at high frequency and direct estimates of net community production is therefore needed to reveal the possible triggering factors of the bloom and understand their initialisation dynamics.

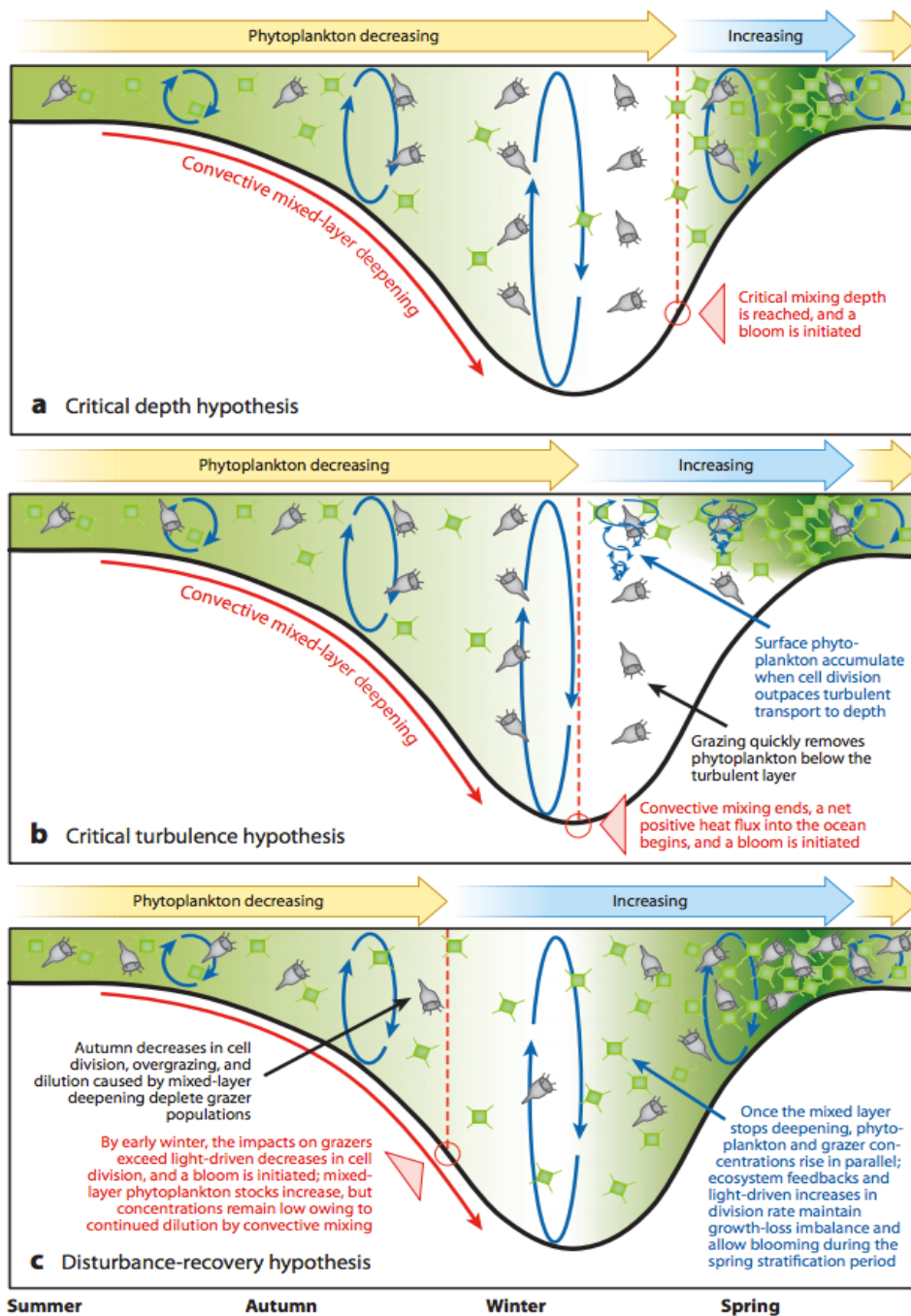


**Figure 1.2 Comparison of bloom hypotheses: (a) the critical depth hypothesis (CDH), (b) the critical turbulence hypothesis (CTH), and (c) the disturbance-recovery hypothesis (DRH). The seasonal cycle begins with summer on the left. Thick black line is the mixed-layer depth (MLD). Green phytoplankton cells and green shading above the MLD are proportional to phytoplankton concentration. Gray ciliates represent all phytoplankton grazers. Arrows above each panel indicate changes in phytoplankton abundance. In panel c, the blue arrows at the top correspond first to increasing water-column-integrated phytoplankton biomass (but not concentration) and then, once the mixed layer begins to shoal, to increasing phytoplankton concentration (figure from Behrenfeld and Boss, 2014).**

### 1.3 Deep chlorophyll maximum

Apart from spring blooms, another feature caused by the biological activity of the plankton is the Deep Chlorophyll Maximum (DCM) (Longhurst, 1998; Denaro et al., 2013), the accumulation of biologically produced oxygen and chlorophyll below the mixed layer. In the North Atlantic, this is a seasonal feature, as opposed to the year-round DCMs that can be found at lower latitudes (Mann and Lazier, 1996; Longhurst, 1998; Letelier et al., 2004). DCMs are the effect of the distribution of light and nutrients that control phytoplankton growth (Klausmeier and Litchman, 2001; Klausmeier et al., 2007, Denaro et al., 2013): when DCMs develop, the mixed layer has abundant light but low nutrient concentrations, while below the mixed layer depth there are enough light and nutrients. Phytoplankton therefore experiences the best growth conditions at the depths occupied by the DCM. This allows the thriving of bigger eukaryotic cells that would not outcompete bacterioplankton (e.g. *Prochlorococcus*) in the low-nutrients mixed layer. This modifies therefore the ecology and augments the biodiversity of the plankton (Veldhuis et Kraay, 2004; Brunet et al., 2008; Dimier et al., 2009b). In DCMs there is therefore a peak in biomass that influences the carbon cycle in the region.

DCMs have been shown to be very dynamic features, influenced by internal waves, Rossby waves, mesoscale events and wind shear on the surface. These processes can enhance production importing nutrients from below or exposing cells to more favourable light conditions (Wolanski et Deleersnijder, 1998; Cipollini et al., 2001; Uz et al., 2001; de Silva et al., 2002; Wang et al., 2007; Vázquez et al., 2009; Pan et al., 2012; Muacho et al., 2013), but they can also decrease production moving the cells away from the light (Chiarra et al., 2008; Evans et al., 2008). Strass and Woods (1991) also showed a deepening of the DCM after its formation, probably due to the consumption of nutrients where there was more light. This means that the nutricline is at the mixed layer depth when the DCM first appears and then deepens when the shallower nutrients are consumed (Strass and Woods, 1991).

The correct estimate of the production rates during the period exhibiting these DCMs is thus important to fully describe and quantify the biogeochemical cycles. However, remote-sensing of ocean colour (satellites) cannot resolve these features (Sathyendranath and Platt, 1989; Fernand et al., 2013), while plankton sampling for incubations might miss the community from these depths (Weston, 2005). The quantification of production in the periods with a DCM remains therefore a challenge for many methods and more investigation about their contribution to the total annual budget is needed.

## 1.4 Oxygen as a proxy to estimate biological activity

Many methods that are used to calculate production and respiration rates (and their balance) are based on the analysis of variations in oxygen-related parameters (concentration, saturation, isotopic composition). Oxygen is used to estimate these processes because of its stoichiometric relationship with the biologically-caused changes in inorganic carbon (Anderson and Sarmiento, 1994). Oxygen is produced as a by-product during photosynthesis and consumed in some of the catabolic reactions during respiration. Its increase and decrease can therefore be used as proxies for quantitative estimates of the plankton metabolic activity. The fact that oxygen does not chemically react with water molecules makes it also more easily measurable than inorganic carbon itself, which instead enters in the cycle of carbonates (Wikner et al., 2013; Hull et al., 2016). Due to its importance in biogeochemical analyses, oxygen has become the most measured parameter in the ocean after temperature and salinity (Boyer et al., 2009).

An array of different methods has been developed to measure biological activity through oxygen. Argon and oxygen have similar solubility and the physical fluxes of these two gases are similar. The O<sub>2</sub>/Ar method uses the imbalance between them in order to measure the biological signal because the biota does not produce or consume argon (e.g. Kaiser et al., 2005). The analysis of the isotopic composition of oxygen and the relative enrichment of <sup>17</sup>O/<sup>16</sup>O with respect to <sup>18</sup>O/<sup>16</sup>O has been also used as a tracer of the biological productivity (e.g. Luz et al., 1999, Luz and Barkan, 2000). The mass balance approach analyses instead the variation in oxygen concentration over time and, subtracting the influence of physical factors from the total variation, calculates the biological activity (e.g., Alkire et al., 2012; Alkire et al., 2014, Nicholson et al., 2015). Variations in oxygen concentration have been analysed both *in vitro* and *in situ*. Measurements *in vitro* are based on the calculation of  $c(\text{O}_2)$  produced and consumed by phytoplankton incubated in laboratory condition. These measurements have been considered affected by a series of biases: the not-natural absence of significant processes such as predation that can influence production (Robinson & Williams, 2005), the wavelength of the light used in the incubation (Godoy et al., 2012), the interaction with the material of the incubation vessels or the possible under-sampling of specific components of the community, for example when there are deep chlorophyll maxima (Weston, 2005). Measurements *in situ* are instead carried out in the natural environment, analysing  $c(\text{O}_2)$  variation in the water column of the ocean or in microcosms. Data can be collected by different This involves a big effort to split the biological and the physical signal contributing to the oxygen variations. The use of several assumptions has helped to overcome many of these biases and produce accurate estimates of the plankton activity. Robertson et al. (1992) for example analysed the diel cycle in  $c(\text{O}_2)$  in the North Atlantic when the mixed layer shoaled and following a drift floating in the same water mass. In

this way they could neglect advection and entrainment and calculate N more easily. Davies and Williams (1984) used instead enclosed ecosystem to reduce the effect of advection, which on the other hand reduced also vertical mixing. The use of several methods, as noted in section 1.1, result in a very high variability among estimates.

For long time, a major problem for oxygen analysis was the low accuracy with which concentrations could be resolved. Although the first study including oxygen dates back to 1927 (Gaarder and Gran, 1927), a more precise way of measuring oxygen with a precision comparable to modern standards was only obtained in the 1960s with the publication of new protocols for Winkler titrations (Carpenter 1965, Carrit and Carpenter, 1966). The complexity of this analysis, however, has slowed down the data collection process. Winkler titration is a time consuming process, which naturally led to studies based on few samples. In the past decades, however, sensors (e.g., pulsed sensor, optodes) have been developed for high precision measurements of oxygen (e.g., Langdon, 1984; Tengberg et al., 2006). These sensors have an adequate sensitivity to detect oxygen variations that are significant to calculate biological productivity (Williams and Jenkinson, 1982; Wikner et al., 2013; Hull et al., 2016). The first analysis *in situ* started during ship-based surveys with the analysis of water collected from the seawater supply of the ships (Robertson et al., 1992). The development of adequate platforms such as gliders, has allowed the creation of datasets of oxygen concentrations measured at high frequency that can be used for biological analysis.

## **1.5 Gliders: a platform for high frequency measurements**

Gliders are autonomous underwater vehicles (AUVs) developed thanks to the funding of the US Office of Naval Research. Three prototypes are the most widely used in oceanographic studies (Rudnick, 2016): Seagliders, used in this study and developed by the University of Washington (Eriksen et al., 2001), Slocum (Webb et al., 2001; Schofield et al., 2007) and Spray (Sherman et al., 2001).

Seagliders can profile the water column from surface to 1000 m using a suite of different sensors for physical and biogeochemical parameters. They move following a saw-tooth path in the water, moving vertically with 1:3 glide angle and a vertical speed of about 10 cm s<sup>-1</sup>. They stay at the surface for 5 to 15 minutes after each dive to communicate via satellite with a basestation on land, sending the data collected during the previous dive and obtaining commands for the following one. Surfacing are separated by 4-6 km for 1000 m deep dives and the actual distance depends on currents and density gradients encountered in the water column. Seagliders do not have propellers and move vertically thanks to buoyancy variations obtained by the displacement of oil between an internal reservoir and a bladder that changes the density

of the glider. The system is powered by lithium batteries that can make the Seaglidern operate up to several months depending on the frequency of the measurements and dive depth.

Gliders have caught the interest of the oceanographic community in recent years thanks to their capability of gathering huge datasets of observations covering large spatial (from 1000 km to cm) and temporal (years to minute) scales (Rudnick, 2016). They are also competitive for economic reasons, with a lower cost per data-point with respect to ship-based missions. The presence of wings and software for a directional horizontal movement also gives gliders an advantage with respect to similar technologies such as the floats used for the Argo program (Roemmich et al., 2009). The large number of measurable parameters and their high resolution also allow comparisons among different processes to understand how they are related in the ocean (e.g. Nicholson et al., 2008; Frajka-Williams et al., 2009; Briggs et al., 2011; Frajka-Williams et al., 2011; Martin et al., 2011; Alkire et al., 2012; Alkire et al., 2014, Nicholson et al., 2015; Damerell et al., 2016).

Problems related to gliders include the need to develop small sensors to study those parameters that are not measureable as yet. A second major problem is the difficulty in splitting temporal and geographical variability in the measurements. However, a big effort by companies and academia has led to the development of novel small, low-power sensors while the use of fleets of gliders has helped overcome the second problem. This has made gliders excellent platforms for biogeochemical studies despite their limitations.

## 1.6 PAP site

The Porcupine Abyssal Plain sustained observatory (PAP, figure 1.3) is the longest running deep ocean time-series observatory in Europe (<http://noc.ac.uk/ocean-watch/sustained-observations/porcupine-abyssal-plain/about>) started in 1989 with the JGOFS North Atlantic Bloom Experiment (NABE) (Ducklow and Harris, 1993, Lampitt et al., 2010, Painter et al., 2010b).

After an initial location at 48° N 19.5° W, the observatory was moved to an area with less complex benthic topography (Rice et al., 1991). The current nominal location of the station is therefore 49° N 16.5° W (figure 1.1) with a bottom depth of 4800 m (Körtzinger et al., 2008; Billet et al., 2010; Lampitt et al., 2010; Painter et al., 2010) in the province of the North Atlantic Drift (NADR) (Sathyendranath et al., 1995; Longhurst, 1998, Lampitt et al., 2010). In 2002, a full depth multidisciplinary mooring was added by the ANIMATE consortium (Körtzinger et al., 2008) to the sediment traps. In 2010 NERC and the UK Met Office started atmospheric measurements at PAP (<http://www.eurosites.info/pap.php>). Since the beginning, the PAP site has also been visited regularly by scientific cruises with the purpose of making *in situ*

measurements, calibrating and replacing instruments. The measurements at PAP were set up in order to study the North Atlantic Spring Bloom (Körtzinger et al., 2008) and the effect of the downward flux of carbon coming from the top layer to the abyssal benthic environment (Billet et al., 2010; Lampitt et al., 2010).

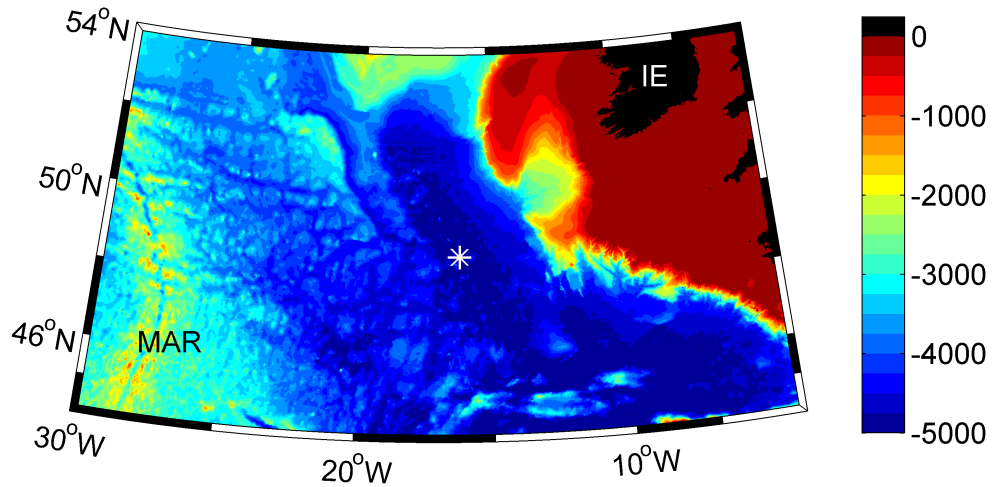


**Figure 1.3 Bathymetry of the east Porcupine Abyssal Plain (North Atlantic) with the position of the Sustained Observatory marked with a white mark. Bathymetric colour legend is in meters.**

Although the PAP site was supposed to be clear from major changes in water masses (Lampitt et al., 2001; Körtzinger et al., 2008; Lampitt et al., 2010), many studies have shown high variability in hydrography over long- and short-term that influenced the biological activity in the area. Considering the interannual variability first, Hartman et al. (2010) described a shift in the circulation of the North Atlantic Current (NAC) between 2003 and 2004 that brought water with different origin to the PAP site (figures 1.3a-b). They also showed an intrusion of the tropical flavour of the Eastern North Atlantic Central Water (ENACWt, Rios et al., 1992; and Castro et al., 1998) in the area during 2005 (figure 1.3c). The different nutrient concentrations of these water masses was connected to the decrease of new production of this bloom from  $6 \text{ mol m}^{-2} \text{ a}^{-1}$  to  $3 \text{ mol m}^{-2} \text{ a}^{-1}$  (carbon equivalents) between 2003 and 2005 (Hartman et al., 2010), showing the biological effects of the interannual variability.

Also the intraseasonal variability at the PAP site, on a temporal scale from days to weeks, has gained attention due to its biological relevance. Shoosmith et al. (2005) showed that during the World Ocean Circulation Experiment (WOCE) the area had a few stable eddies and that most of

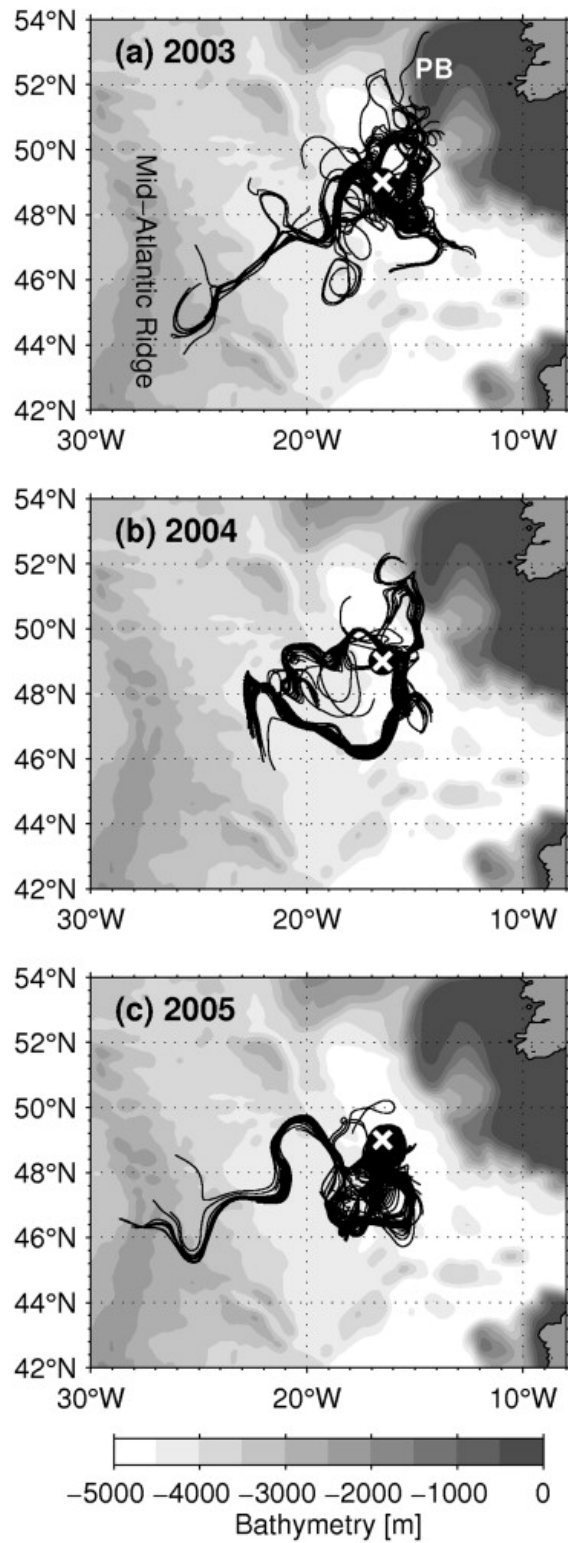


**Figure 1.4** Trajectories leading to PAP site computed from altimetry-derived geostrophic velocities. Each trajectory lasts for 90 days and ends at the PAP-OS (white cross) in the period January to March of the indicated years. In (a) PB indicates the Porcupine Bank and the Mid-Atlantic Ridge is also highlighted. (from Hartman et al., 2010).

them were anticyclonic. These eddies merged together and lasted longer than cyclonic eddies and this long duration made possible the formation of smaller features. These features have been proven to influence the productivity and enhance shear and nutrient fluxes (Allen and Smeed, 1996). Martin et al. (2010) used the different nutrient concentrations in the mesoscale features to explain the large gap (almost 2 orders of magnitude) between the nutrient uptake measured and the nutrient supply estimated. Painter et al. (2010a) showed that an eddy that crossed the area originated filaments associated with higher primary production and high chlorophyll concentration (Hartman et al., 2010; Painter et al., 2010a).

The PAP site is a suitable area to study the variability of biological activity at different time scales. The presence of several studies focusing on this area permits a comparison with previous estimates of production to appreciate the interannual variability. Observations spanning over long periods are also likely to detect the advection of mesoscale features to the area and observe their influence on production.

The importance of this site explains why PAP site was chosen as study area for the project OSMOSIS, which provided the frame for the realisation of the present study. OSMOSIS was a consortium of oceanographers working in different Universities and research centres around UK (University of Oxford, University of Southampton, University of East Anglia, University of Reading, University of Portsmouth, Bangor University, University of Liverpool, Met. Office, National Oceanographic Centre, SAMS) that aimed to study the top water column in the deep ocean. The Scientific goals of the project was the collection of detailed oceanographic and atmospheric data through an array of moorings, gliders and cruises in order to model the dynamics of the upper ocean. This was done in order to understand and quantify the fluxes of energy and matter in the ocean surface boundary layer, characterising its mixing processes due to internal and external factors acting at the surface. The presence of sensors on the gliders for the detection of chlorophyll *a* fluorescence and oxygen concentration allowed the development of a biogeochemical study within OSMOSIS whose results will be present in the following chapters.

## **1.7 Open questions about productivity in the North Atlantic**

The calculation of phytoplankton productivity from observations *in situ* has been historically calculated relying on datasets from ship-based surveys. This has produced many estimates of N and P during the productive season (spring/summer), when it is easier to reach the open ocean and carry out experiments. At the same time, this has produced a much lower number of studies that analyse productivity in the fall/winter period. Long-lasting time series, spanning over one or more annual cycles, have been produced using moorings, but this has produced dataset with low vertical resolution. Satellites have also produced annual time series

of productivity from the variations in chlorophyll *a* fluorescence, but these calculations rely on many assumptions to calculate productivity and use climatological data to characterise the water column. Furthermore, the chlorophyll-based calculations assume that variation in chlorophyll fluorescence can be attributed entirely to biomass growth, while it can be influenced by photoacclimation or by the different chlorophyll *a* content in different species that dominate the community over time. Argo floats and gliders have started to be involved in this kind of measurements only in the last years and gliders have been usually used for short-lasting missions. Observations at high frequency during the late fall and winter seasons in the North Atlantic are still scarce and a time series at high resolution spanning over an entire year is still missing. This means that the pattern of productivity over one annual cycle has never been produced. Thanks to three consecutive glider missions, this project aims to produce this time series. The use of oxygen for the calculation of *N* aims to produce *N* estimates more trustworthy than the ones from chlorophyll *a* fluorescence because less affected by other phenomena as discussed above.

The scarcity or the low resolution of time series of *N* and *P* has also slowed down the analysis of which factors trigger the blooms over the year. Often derived data are used, such as climatology for the mixed layer depth or variations in the chlorophyll *a* fluorescence rather than a direct calculation of productivity. Data are also sometimes collected at different resolution and with different platforms, which makes it difficult to compare different factors. In the present study, mixing layer depths calculated from *in situ* parameters will be used and *N* and *P* pattern will be compared with physical and biogeochemical parameters (temperature, salinity and chlorophyll *a*) measured at the same resolution and by the same platform as the oxygen concentration. This will give precious hints about what triggers the blooms. In particular, it will be possible to test the theories discussed in section 1.3. Once defined the bloom as an increase of *N* from autotrophy to heterotrophy, the pattern of *N* over time will be compared with the temporal patterns of other factors. According to Sverdrup's theory, *N* shall increase when mixing layer shoals and light intensity increases, which should be obvious by an increase of the mean light in the mixing layer. According to Behrenfeld et al. (2010), *N* shall increase during winter, along with the deepening of the mixing layer, and then decrease when the deepening stops. According to Huismann's theory, in case of slow turbulence *N* should increase at the top of the water column with accumulation of oxygen and chlorophyll *a* even without shoaling of the mixed layer. The theory proposed by Taylor and Ferrari (2011) and developed by Enriquez and Taylor (2015) focus on the effect of the heat flux. These theories can then be confirmed if *N* increases when the heat flux switches from a negative to positive values.

## 1.8 Thesis outline

This thesis aims to answer the open questions listed above. The calculation of N will be based on the variation in  $c(O_2)$  at the top of the water column. The biological signal will be calculated as the residual variation not related to any physical factor. In order to analyse the variations in  $c(O_2)$  related to physics, the thickness of the ocean surface boundary layer will be calculated using the homogeneity of parameters in the at the top of the water column. The high frequency of the measurements will be used at last to analyse the diel cycle in  $c(O_2)$  with the aim of calculate P.

In chapter 2, the calibration of the glider data against ship-CTD casts will be described. This includes the calibration of ship-CTD casts done through Winkler titrations of water samples.

In chapter 3, the time series of oxygen concentration, oxygen saturation and apparent oxygen utilization will be compared with the time series of the other parameters measured during the glider mission.

In chapter 4, the calculation of mixed and mixing layer depth defined by changes in oxygen concentration will be presented. The values will be then compared with estimates based on density/temperature and chlorophyll *a* concentration.

In chapter 5, the estimates of net community production over one year cycle will be presented. The magnitude of the estimates will be compared with previous studies and their temporal pattern will be used to infer the triggering causes of the variations in production.

In chapter 6, the gross primary production for some periods in the dataset will be computed using a new method based on the *in situ* increase and decrease of oxygen during day and night.

In chapter 7, the results will be summarised and future developments of the work will be suggested.



# Chapter 2

## Data calibration

In this chapter the protocols for the calibration of the oxygen concentrations in the ocean are explained. The first protocol is the one used to calibrate the CTD casts against water samples whose concentrations are measured by Winkler titration. A comparison with oxygen concentrations from literature for the area is carried out to validate the data. The calibrated CTD casts are then used in the second protocol to calibrate the glider profiles. This process includes the correction for the time response of the optode. The quality control of the data and the removal of spikes are also described.

### 2.1 Data acquisition

The OSMOSIS project included five cruises and three glider missions performed at Porcupine Abyssal Plain (PAP) between September 2012 and September 2013. The goal of the cruises was the deployment and recovery of the gliders and the collection of a suite of *in situ* parameters to be used for the calibration of the glider's data. The three glider missions were done in series with short overlapping periods when the cruises visited the area to swap them. The glider SG566 operated between September 2012 and January 2013, SG502 between January 2013 and April 2013 and SG566 a second time between April 2013 and September 2013. Since the glider SG566 was used during the first and the third mission, in this study it will be called SG599 when referred to the mission from April to September 2013 (i.e., third mission) in order to avoid confusion. Gliders followed butterfly- or hourglass-shaped transects centred around 48.7° N and 16.2° W with sides ~15 km long (figure 2.1).

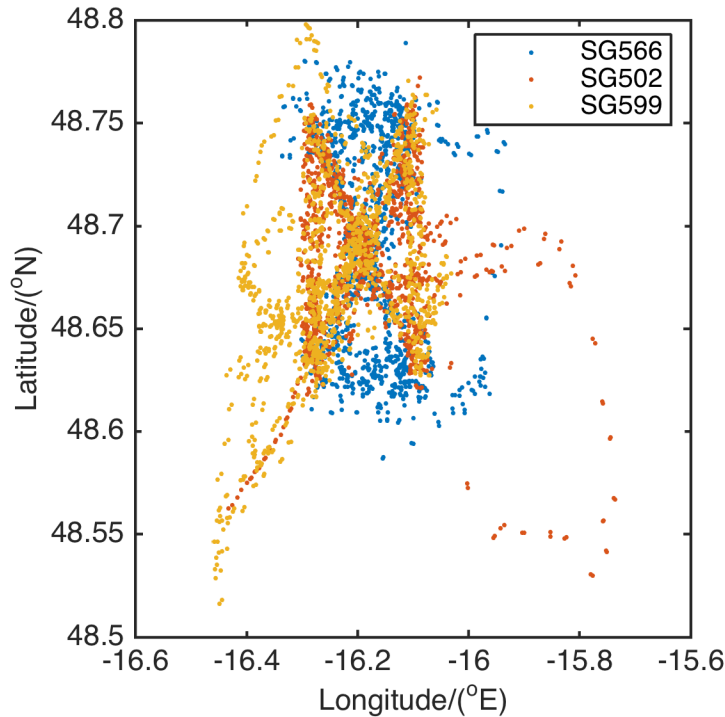


**Figure 2.1** Surfacing locations of gliders SG566 (blue), SG502 (red) and SG599 (yellow) showing the butterfly-shaped transects that they followed at the PAP site during the three consecutive missions.

## 2.2 Calibration of CTD casts

During the cruises, oxygen concentration,  $c(\text{O}_2)$ , was measured by a Clark-type electrode (Seabird SBE43) attached to the CTD frame. A rosette of Niskin bottles surrounded the CTD frame and was used for the collection of water from several depths during selected casts. Every CTD cast can be split into a downcast, when the CTD frame goes from the surface to the bottom, and an upcast, when the frame is pulled towards the surface. When water was sampled with Niskin bottles, the  $c(\text{O}_2)$  profile during the downcast was visually analysed in real time to check its shape and decide at which depths water parcels had to be collected during the following upcast. In general, it was chosen to sample layers with  $c(\text{O}_2)$  as stable as possible over several metres, while sharp gradients were avoided. This was done in order to reduce the noise in the data due to the vertical oscillations of the frame among waters with significant different  $c(\text{O}_2)$ . Furthermore, when more than one bottle was sealed (“fired”) at any depth in order to have replicates of the sampling, it was assumed that the two bottles were sampling the same water. This assumption is difficult to justify when the frame oscillates within a sharp gradient. Attention was also paid to spreading the samples through the whole water column during each CTD. Maxima and minima in oxygen concentrations were also sampled in order to expand the concentration range as much as possible. An example of the sampling depths with respect to the profile shape can be seen in figure 2.2.

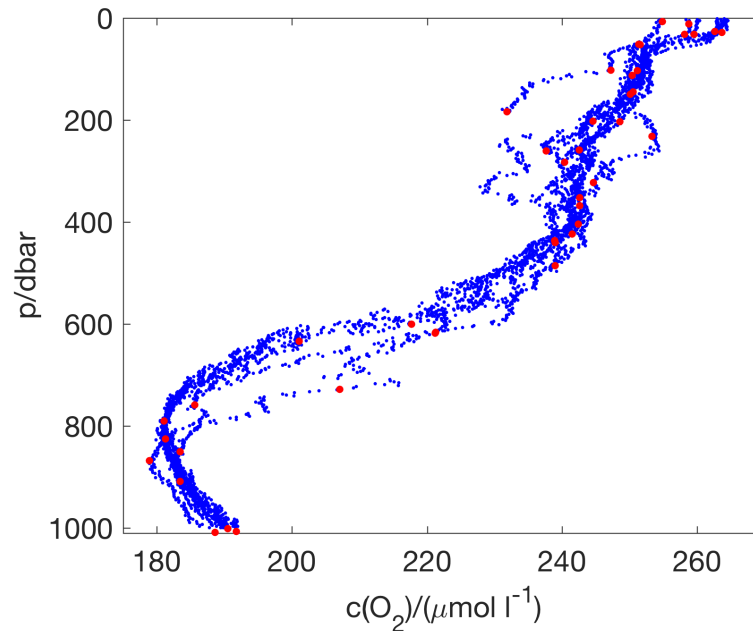


**Figure 2.2 Oxygen concentration profiles from CTD upcasts of cruise JC085 (blue) with the depths at which Niskin bottles were fired during a mission (red).**

For each upcast, the Seabird CTD software created a .btl file with all the parameters (including  $c(\text{O}_2)$ ) measured in the water column at the depths where each Niskin bottle had been fired. Once the CTD frame had been recovered, one or more Winkler samples were collected from selected Niskin bottles. The temperature of water flowing out from the Niskin bottles was checked to detect possible leaks: water coming out with a temperature different from the one recorded in the .btl file indicated a leak in the sealing system and the sample was thus considered contaminated by shallower water encountered during the upcast.  $c(\text{O}_2)$  of the Winkler samples was then analysed by Winkler titration following the WOCE protocol as described by Culberson (1991) and Dickson (1996).

For each Winkler sample there was therefore one  $c(\text{O}_2, \text{btl})$  and one  $c(\text{O}_2, \text{Winkler})$  – the first being the concentration in the .btl file matching the uncalibrated CTD value, and the second being the result of the titration, considered to be the best estimate of the real  $c(\text{O}_2)$ . All the Winkler samples collected from the same Niskin bottle had the same  $c(\text{O}_2, \text{btl})$ , but  $c(\text{O}_2, \text{Winkler})$  was unique for each Winkler sample. All the concentrations were expressed in units of  $\mu\text{mol l}^{-1}$  ( $= \text{mmol m}^{-3}$ ).

Each  $c(\text{O}_2, \text{Winkler})$  was plotted against the corresponding  $c(\text{O}_2, \text{btl})$  (figure 2.3a). After a visual analysis of this scatter plot, a few of these concentrations were flagged as biased (grey points in figure 2.3a). In particular, samples from deeper than 1500 m were ignored because the sensor was affected by pressure hysteresis, as visible from the increasing residual difference between  $c(\text{O}_2, \text{Winkler})$  and  $c(\text{O}_2, \text{btl})$  (figures 2.4b). Other data-points were ignored because standard deviation of the replicates was  $> 2 \mu\text{mol l}^{-1}$ ; this was attributed to errors during titration

of the individual Winkler samples. In other cases all the replicates from the same Niskin bottle were ignored because they were considered outliers with respect to the whole dataset, perhaps because of previously undetected leaks in the Niskin bottles. A linear regression was fitted through the remaining points obtaining the slope and the offset of the linear calibration equation. The calibration was then applied to the  $c(\text{O}_2)$  profiles of the CTD casts (figure 2.4).

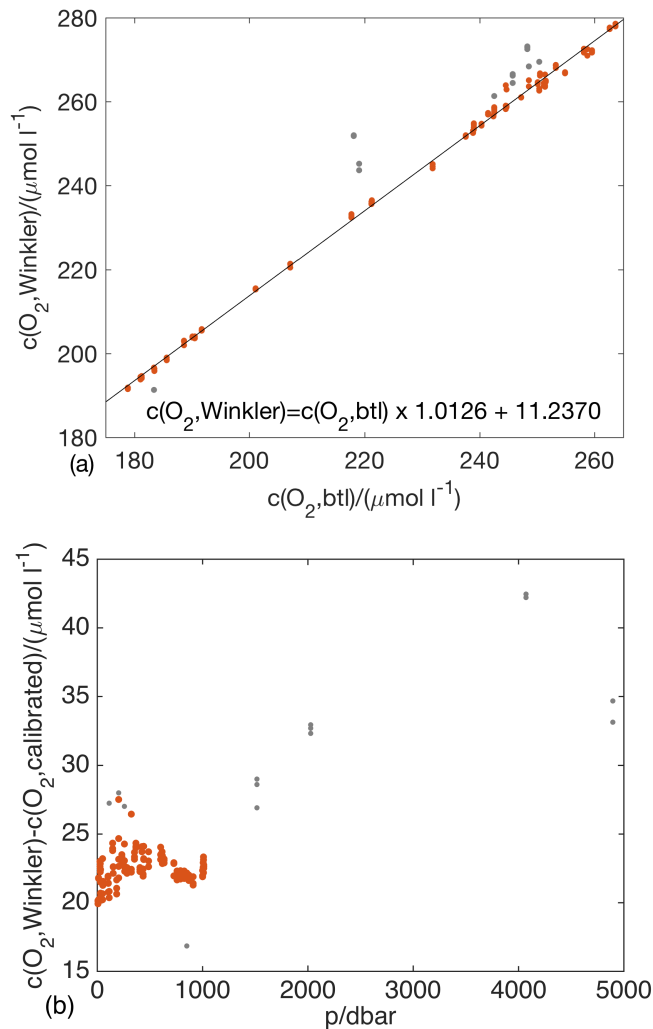


**Figure 2.3 (a) Concentrations from btl files for each Winkler sample collected during the cruise against the relative concentrations measured by Winkler titration. The black line is the linear regression between valid data-points (red); samples disregarded are in grey; (b) residual difference between concentrations measured by Winkler titration and btl values after calibration. The difference increases with depth because of uncorrected pressure hysteresis. Winkler samples used for the calibration are shown in red. Values are from JC085.**

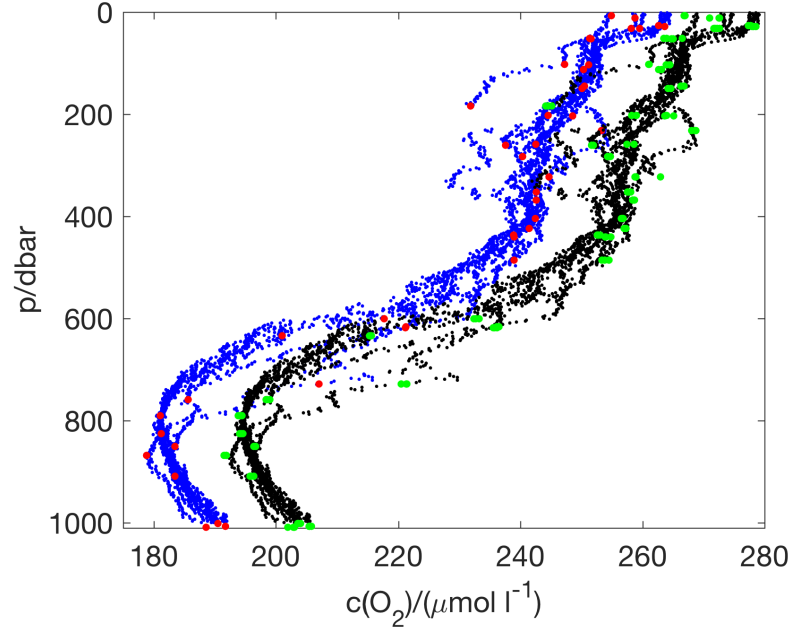


**Figure 2.4** Oxygen concentration profiles from the upcasts of CTD casts performed during cruise JC085 before (blue) and after (black) the calibration. In red are the oxygen concentrations measured in the .btl file at the depths where the Niskin bottles were fired. In green are the values measured by Winkler titration.

In order to be used for the calibration of Seagliders data,  $c(\text{O}_2)/(\mu\text{mol l}^{-1})$  from CTD casts were converted from in  $c(\text{O}_2)/(\mu\text{mol kg}^{-1})$  using equation 2.1:

$$c(\text{O}_2)/(\mu\text{mol kg}^{-1}) = c(\text{O}_2)/(\mu\text{mol l}^{-1}) * 1000 / \rho_0/(\text{kg m}^{-3}) \quad (2.1)$$

where  $\rho_0/(\text{kg m}^{-3})$  is the potential density corresponding to each  $c(\text{O}_2)$  data-point.

### 2.3 Calibration of the gliders - methodology

Gliders measured two  $c(\text{O}_2)$  profiles per each dive (a descent and an ascent) by means of optodes (Aanderaa Data Instruments; Tengberg et al., 2003) mounted near their wings. These probes work by analysing the decay of platinum porphyrin compounds excited by blue-green light. The porphyrins are embedded in silicon foils and they decay from the excited state to the ground one emitting red light. However, when oxygen is present in the environment, some of the energy released during the decay is transferred to  $\text{O}_2$  instead of being emitted as light. This is called “quenching reaction” and reduces both the intensity and the duration of the red emission. The optode measures the lifetime of the red emission in terms of a phase difference  $T\text{CPhase } (\phi_{TC})$ , which is correlated to  $c(\text{O}_2)$  in the environment.

### 2.3.1 TCPhase – Response time correction

The distribution of  $\phi_{TC}$  versus pressure (and depth) is affected by a delay caused by the response time of the sensor. This is the time that it takes for  $O_2$  to diffuse through the silicon foil in the process of equilibrating  $c(O_{2, \text{internal}})$  within the optode with  $c(O_{2, \text{external}})$  in the water column – i.e., equilibrating the concentration that is actually measured by the sensor with the concentration that is meant to be quantified. This equilibration takes time because the diffusion of gases across membranes is not an instantaneous process and is influenced by factors such as membrane boundary layer thickness and temperature. An optode that moves up and down in a physically stable water column and had a response time of zero would measure two identical profiles. However, the delay caused by the response time causes each variation in  $c(O_2)$  to be measured later than when it actually happens. The profile of an optode going towards the deep is therefore shifted deeper with respect to the real distribution of  $c(O_2)$  versus depth, while the profile of an optode going towards the surface is shifted shallower. At the end, the two profiles of the same water column measured in opposite phases do not match as they should. This is particularly visible in the presence of strong gradients, where variations are more rapid and the delay of the sensor is more obvious. The delay is called  $\tau$  and is used to shift the  $\phi_{TC}$  profiles using the equation 2.2

$$\phi_{TC, \text{time-shifted}}(t) = \phi_{TC, \text{original}}(t + \tau) \quad (2.2)$$

where  $t$  is time since the beginning of the dive.

The response time is different for each individual sensor and depends on the structure, thickness, age and frequency of use of its foil (McNeil and D'Asaro, 2014). Furthermore, oscillations in temperature, water flux and the natural noise of  $c(O_2)$  in the external environment affect the speed of diffusion of the gas through the membrane, causing  $\tau$  to vary constantly. There should be therefore a different  $\tau$  for each data-point collected during the mission. Because this continuously changing  $\tau$  is impossible to quantify, only one value was chosen for each glider and mission.

The determination of the  $\tau$  value to use for each optode was based on the comparison between consecutive profiles. Each dive was split into an ascent and a descent, which were the profiles measured when the glider was in its ascending or descending phase respectively. Between the end of an ascent and the beginning of the following descent, gliders stayed at the surface just for  $(17 \pm 15)$  min. Thanks to this proximity in time and space, the top part of the ascent (its end) could be considered a replicate of the top part of the following descent (its beginning). The comparison of these two profiles was limited to the top 300 dbar. In this pressure-range, the profiles were supposed to match when the right  $\tau$  value was applied to the dataset. Since gliders move horizontally during the dive, the deep parts of the same ascent and descent (pressure > 300 dbar) could not be considered replicates because they are too far apart

from each other. Furthermore, deeper in the water column the conditions are more stable, giving more time to the optodes to equilibrate  $c(\text{O}_2, \text{internal})$  with  $c(\text{O}_2, \text{external})$ . This makes the shift less obvious and the estimation of  $\tau$  less precise. The deep part of the profiles (below 300 dbar) was therefore not used at all for the comparison. The limit of 300 dbar was used also because its depth was below the mixing layer depth (see chapter 4). The rapid gradient (oxycline) at the bottom of the mixing layer could then be used to check how effective the application  $\tau$  was.

The comparison between each ascent and its following descent followed a criterion that used pressure as binning parameter and potential density as matching parameter. Pressure was used for the binning because its range for all the deep profiles is nominally always the same (0 – 1000 dbar). Binning in pressure therefore gave the possibility to use the same number of bins with the same width throughout the whole year, giving coherence to the comparison. However, the distribution of the water masses (i.e., potential density) with respect to pressure was different even between consecutive profiles due to processes such as internal waves or because of natural heterogeneity in altimetry (e.g., geostrophic currents). Since similar  $\phi_{\text{TC}}$  (i.e., similar  $c(\text{O}_2)$ ) in consecutive profiles were supposed to be found in the same water mass, potential density was used as the matching parameter between the profiles.

The comparison was done dividing in non-overlapping 2-dbar bins the top 300 dbar of each ascent  $\phi_{\text{TC}}$  profiles. Each bin was centred on the pressure  $p_i$  between 9 dbar and 299 dbar. the mean  $\phi_{\text{TC}}$  of the bin  $i$ ,  $\phi_{\text{TC,asc}}(i)$ , was then calculated. The  $\phi_{\text{TC}}$  value measured in the following descent at the mean potential density of the bin  $i$  was identified as the correspondent  $\phi_{\text{TC,des}}(i)$ . For each pair of profiles (i.e., ascent and following descent), the root mean square difference of  $\phi_{\text{TC,asc}}$  and correspondent  $\phi_{\text{TC,des}}$  ( $\phi_{\text{TC,rms}}$ ) was then measured as in equation 2.3.

$$\phi_{\text{TC,rms}} = \sqrt{\frac{1}{n} \sum_{i=1}^n (\phi_{\text{TC,asc}}(i) - \phi_{\text{TC,des}}(i))^2} \quad (2.3)$$

where  $n = 146$  (number of bins between 9 m and 299 m). Ascent and descent of each pair were shifted using  $\tau$  from 0 s to 50 s. The optimum  $\tau$  for each pair was the one that yielded the lowest  $\phi_{\text{TC,rms}}$ . Within one mission, it was then calculated the number of pairs for which each value between 0 s and 50 s had been found to be the optimum  $\tau$ . Values were plotted in a histogram and were fitted to a normal distribution. The normality was assumed because  $\tau$  is expected to vary randomly around its nominal value, which is determined by the foil characteristics. The normal fit was obtained using the function ‘histfit’ built in Matlab 2014b. The central value of this normal distribution was used as  $\tau$  values to shift the whole mission.

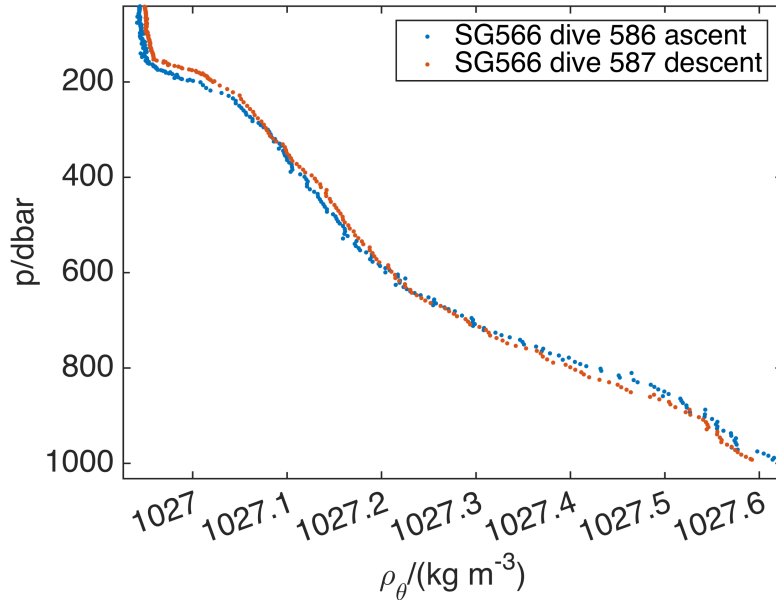


**Figure 2.5 Example of potential density versus depth in an ascent and a descent paired to find the optimum  $\tau$ . Identical potential density values are found at different depths in the two profiles, biasing the RMS computation through equation 2.3.**

### 2.3.2 CalPhase – computation and calibration

Once shifted using  $\tau$ ,  $\phi_{TC}$  profiles had to be transformed in  $\phi_{cal}$  through a linear transformation as in equation 2.4

$$\phi_{cal} = TPhaseCoef_0 + \phi_{TC} \times TPhaseCoef_1 \quad (2.4)$$

This was the step when the glider profiles were calibrated against ship-CTD casts. Calibrated values of  $TPhaseCoef_0$  and  $TPhaseCoef_1$  were determined every time a cruise was close to a profiling glider calculating the linear regression between  $\phi_{TC}$  profiles of selected glider dives and the back-calculated  $\phi_{cal}$  profiles of selected CTD casts. CTDs and dives shallower than 1000 m were not used for the calibration in order to use the whole range of values recorded during any dive. Only the downcasts of the CTD casts were used. CTD casts were chosen based on their geographical and temporal proximity to the glider that they had to calibrate: a CTD cast should have started within 4 km and 3 hours from the surfacing location and time of the glider dive that they had to calibrate. Once a CTD cast had been chosen, its  $\phi_{cal}$  profile,  $\phi_{cal}(CTD, backcalculate)$ , was back-calculated starting from its calibrated  $c(O_2)$  profile.

The back-calculation of  $\phi_{cal}(CTD, backcalculate)$  profiles followed five steps:

- calculation of water vapour pressure  $p(vap)$  profiles, computed using potential temperature from the ship CTD;

- calculation of oxygen saturation concentration  $c_{\text{sat}}(\text{O}_2)$  profiles obtained from potential temperature and calibrated salinity from the ship CTD using the solubility coefficients from Benson and Krause (1984) for the output in  $\mu\text{mol kg}^{-1}$ ;
- calculation of air saturation  $s(\text{air})$  profiles equivalent to the atmospheric pressure of 1013.25 hPa.  $s(\text{air})$  was based on  $c(\text{O}_2)$  and  $c_{\text{sat}}(\text{O}_2)$  as in equation 2.5;

$$s(\text{air}) = c(\text{O}_2) / c_{\text{sat}}(\text{O}_2) \quad (2.5)$$

- calculation of profiles of partial pressure of oxygen,  $\Delta p(\text{O}_2)$ , using  $s(\text{air})$  and  $p(\text{vap})$  profiles;
- calculation of  $\phi_{\text{cal}}(\text{CTD,backcalculate})$  through a polynomial that used the potential temperature from the ship CTD,  $\Delta p(\text{O}_2)$  and 21 coefficients (FoilCoefA0 to FoilCoefA13 and FoilCoefB0 to FoilCoefB6) specified by the manufacturer and characteristic of each individual optode.

Ascent and descent  $\phi_{\text{TC}}$  profiles of each dive close to the CTD cast were then binned in potential density using bins  $0.02 \text{ kg m}^{-3}$  wide centred around the potential density  $\rho_\theta$  correspondent to each  $\phi_{\text{cal},i}(\text{CTD,backcalculated})$ . In this way  $\phi_{\text{TC,asc},i}(\rho_\theta)$  and  $\phi_{\text{TC,des},i}(\rho_\theta)$  were obtained. A linear regression was drawn between  $\phi_{\text{TC,asc}}(\rho_\theta)$ ,  $\phi_{\text{TC,des}}(\rho_\theta)$  and their respective  $\phi_{\text{cal}}(\text{CTD,backcalculated},\rho_\theta)$ . In order not to use portions of the glider profiles that were particularly variable between ascent and descent of the same dive, the difference between  $\phi_{\text{TC,asc},i}(\rho_\theta)$  and  $\phi_{\text{TC,des},i}(\rho_\theta)$  was calculated as in equation 2.6:

$$\Delta\phi_{\text{TC},i}(\rho_\theta) = \phi_{\text{TC,asc},i}(\rho_\theta) - \phi_{\text{TC,des},i}(\rho_\theta) \quad (2.6)$$

If any  $\Delta\phi_{\text{TC},i}(\rho_\theta)$  was bigger than twofold the standard deviation of all the  $\Delta\phi_{\text{TC}}(\rho_\theta)$  of the dive, then  $\phi_{\text{TC,asc},i}(\rho_\theta)$  and  $\phi_{\text{TC,des},i}(\rho_\theta)$  were flagged and not used to calculate the regression.  $\phi_{\text{TC}}$  profiles from several dives of a glider and  $\phi_{\text{cal}}(\text{CTD,backcalculated})$  profiles from several CTD casts of a cruise could be used as long as the glider and the ship were within the limits of proximity defined above. The offset and the slope of the linear regression were respectively the calibrated TPhaseCoef<sub>0</sub> and TPhaseCoef<sub>1</sub> and were used in equation 2.4 to obtain calibrated  $\phi_{\text{cal}}$  profiles of the glider.

### 2.3.3 Oxygen concentration – calculation

The calculation of  $c(\text{O}_2)$  profiles from the calibrated  $\phi_{\text{cal}}$  profiles included five steps that retraced backwards the steps seen in section 2.3.2 for the calculation of  $\phi_{\text{cal}}(\text{CTD,backcalculate})$ :

- calculation of  $\Delta p(\text{O}_2)$  profiles through a polynomial that used potential temperature from the CTD mounted on the glider, the calibrated  $\phi_{\text{cal}}$  profile and 21 coefficients (FoilCoefA0 to FoilCoefA13 and FoilCoefB0 to FoilCoefB6) specified by the manufacturer and characteristic of each individual optode;
- calculation of  $p(\text{vap})$  profiles using potential temperature from the CTD mounted on the glider;
- calculation of  $s(\text{air})$  profiles equivalent to the atmospheric pressure of 1013.25 hPa based on  $\Delta p(\text{O}_2)$  and  $p(\text{vap})$  profiles;
- calculation of  $c_{\text{sat}}(\text{O}_2)$  profiles from potential temperature and calibrated salinity from the CTD mounted on the glider using the solubility coefficients from Benson and Krause (1984) for the output in  $\mu\text{mol kg}^{-1}$ ;
- calculation of  $c(\text{O}_2)$  profiles using  $c_{\text{sat}}(\text{O}_2)$  and  $s(\text{air})$  profiles with the equation 2.6

$$c(\text{O}_2) = c_{\text{sat}}(\text{O}_2) \times s(\text{air}) \quad (2.7)$$

This calculation was done at first for the selected dives that were close to the CTD casts and whose TPhaseCoef<sub>0</sub> and TPhaseCoef<sub>1</sub> had been calculated as described in section 2.3.2. The  $c(\text{O}_2)$  profiles of these glider dives were then compared with the  $c(\text{O}_2)$  profiles of the CTD casts used for their calibration. If these profiles obviously mismatched in some part of the water column, the calibration of TPhaseCoef<sub>0</sub> and TPhaseCoef<sub>1</sub> was repeated disregarding these highly variable parts of the water column.

The linear calibration equations obtained at the beginning and at the end of each mission were then compared. In case of drift between two calibrations, it was assumed a linear shift between the initial and the final value for both TPhaseCoef<sub>0</sub> and TPhaseCoef<sub>1</sub>. A different TPhaseCoef<sub>0</sub> and TPhaseCoef<sub>1</sub> was then calculated for each dive temporally interpolating the values.

## 2.4 Data quality control

Spikes in a profile are isolated data-points with anomalous values with respect to the rest of the distribution. Spotting and flagging these spikes in  $c(\text{O}_2)$  was a complicated process. There were several profiles whose  $c(\text{O}_2)$  at surface had data-points that required a quality check. In some profiles there were single data-points with anomalous  $c(\text{O}_2)$ , while in others profiles several points were monotonically aligned to unreal values or scattered near to the surface. The causes of these spikes at the surface are several: light that hits the foil of the sensor; waves that expose the sensor to the air; a real  $\tau$  of the profile very different from the  $\tau$  applied to the whole mission (see section 2.3.1) that uncoupled density and  $c(\text{O}_2)$ . Spikes in salinity had been flagged using thresholds too sensitive with respect to their influence on  $c(\text{O}_2)$  computation. Data-points

whose salinity had been flagged were therefore not disregarded, but in case flagged on the base of their  $c(\text{O}_2)$  values.

The despiking process was based on the automatic identification based on few criteria:

- 1) unrealistic  $c(\text{O}_2)$ , like values  $<0 \mu\text{mol kg}^{-1}$  or  $>1000 \mu\text{mol kg}^{-1}$ ;
- 2) significant increase in the standard deviation of a  $c(\text{O}_2)$  profile due to a spike;
- 3) single points with anomalous  $c(\text{O}_2)$  within water masses with constant concentrations (homogeneous ocean surface boundary layer in the autumn for example);
- 4)  $c(\text{O}_2)$  measured above 0 m (where a few data-points had been shifted due to correction for the response time described in 2.3.1).

Due to the high number of false positives in the output of the automatic identification, the candidate spikes were analysed one by one to assess their quality. The shape of each profile was taken into account and, in case of uncertainty about the validity of a data-point, the profile was compared with previous and following profiles. Suspect features visible in a few consecutive profiles were considered real, while odd  $c(\text{O}_2)$  in only one profile were flagged as spikes.

## **2.5 Calibration of CTD casts – results**

### **2.5.1 CTD calibration through Winkler titration of water samples**

Each cruise was treated and calibrated as an individual dataset, apart from the first cruise (D381) because during its 13<sup>th</sup> CTD cast the wire split and the CTD frame was lost. Casts 1-12 were then performed with different sensors than casts from number 14 onwards. The casts from D381 were then divided in two datasets that were calibrated separately. In figures from 2.6 to 2.9 are shown profiles before and after the calibration (panels a) and the linear equation used for the calibration (panels b). Each cruise is in a different figure. The equivalent figures for JC085 that have been already shown in section 2.2.

Table 2.1 shows the number of CTD casts in each cruise, how many Winkler samples were collected and how many were disregarded in the calibration of the CTD casts (grey points in figure 2.6b-2.9b). The main cause why Winkler samples were not considered was that they had been collected deeper than 1500 m and were affected by hysteresis (similar to what shown in figure 2.3b). The number of Winkler samples collected per each cruise varied with the number of CTD casts and also according to the operator carrying out the fieldwork. The standard deviation of the replicate Winkler samples from the same Niskin bottles was used to measure the uncertainty associated with the titration. Winkler samples that had been flagged and Niskin bottles with only one valid replicate were not used in this calculation. The mean uncertainty for the five cruises is  $0.42 \mu\text{mol l}^{-1}$  and the values per each cruise are listed in table 2.1.

**Table 2.1 Number of CTD casts, number of Winkler samples collected and number of Winkler samples discarded for each cruise during OSMOSIS. Winkler samples discarded are divided according to the reason of flagging.**

Cruise	Date	CTD casts	Winkler samples	Winkler samples discarded				Uncertainty <i>titration</i> calibration ( $\mu\text{mol l}^{-1}$ )
				Deep	Odd Niskin	Odd Winkler	Total	
D381 (casts 1-12)	28 <sup>th</sup> Aug – 3 <sup>rd</sup> Oct 2012	12	212	25	4	14	43 (20.28 %)	0.53 <u>2.49</u>
D381 (casts 14-21)	28 <sup>th</sup> Aug – 3 <sup>rd</sup> Oct 2012	9	138	0	8	18	26 (18.84 %)	0.46 <u>1.89</u>
CE13001	5 <sup>th</sup> – 11 <sup>th</sup> Jan 2013	4	52	12	0	2	14 (26.92 %)	0.40 <u>0.89</u>
JC085	14 <sup>th</sup> – 29 <sup>th</sup> Apr 2013	5	140	11	0	4	15 (10.71 %)	0.48 <u>1.19</u>
JC087	31 <sup>st</sup> May – 18 <sup>th</sup> Jun 2013	24	291	45	10	2	57 (19.59 %)	0.46 <u>2.34</u>
JC090	30 <sup>th</sup> Aug – 17 <sup>th</sup> Sep 2013	9	83	0	0	1	1 (1.20 %)	0.18 <u>0.63</u>

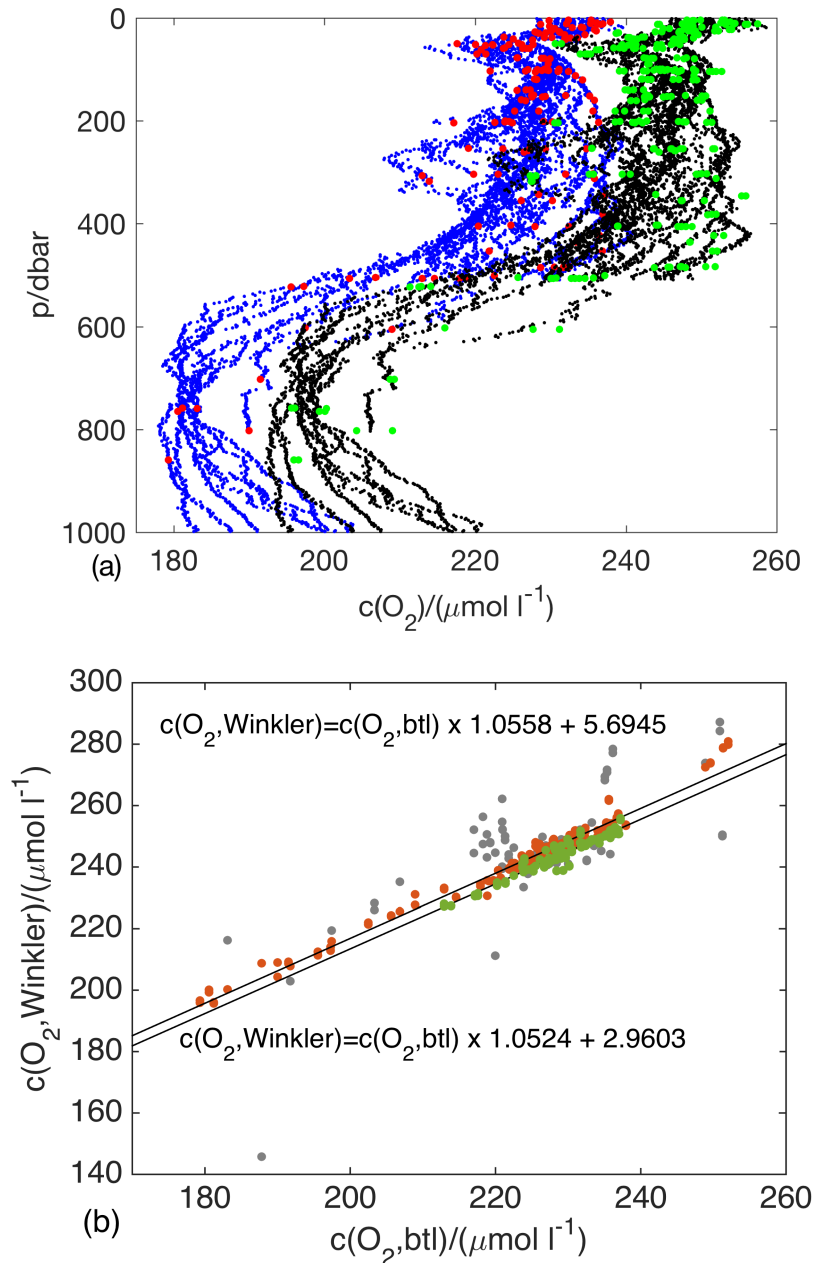


**Figure 2.6 Cruise D381 - (a) Oxygen concentration profiles from CTD before (blue) and after calibration (black). In red are depths and oxygen concentrations of Niskin bottles fired above 1000 m and in green are the relative concentrations measured with Winkler titration; (b) concentrations from btl files for each Winkler sample collected during the cruise against the relative concentrations measured by Winkler titration; the black lines are the linear regressions of valid points used as calibration equations for the oxygen concentration profiles of CTD casts. Red are valid points for CTD casts 1-12 and green are for CTD casts 14-21.**

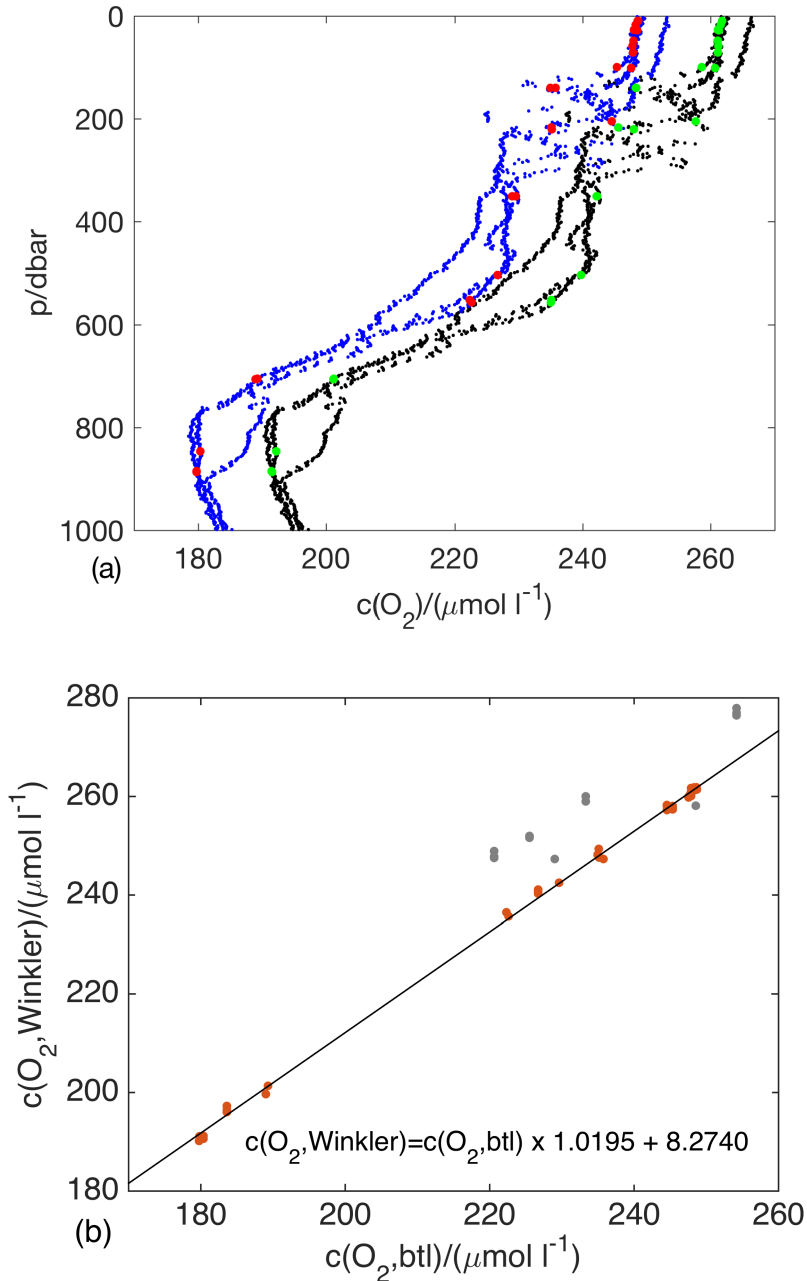
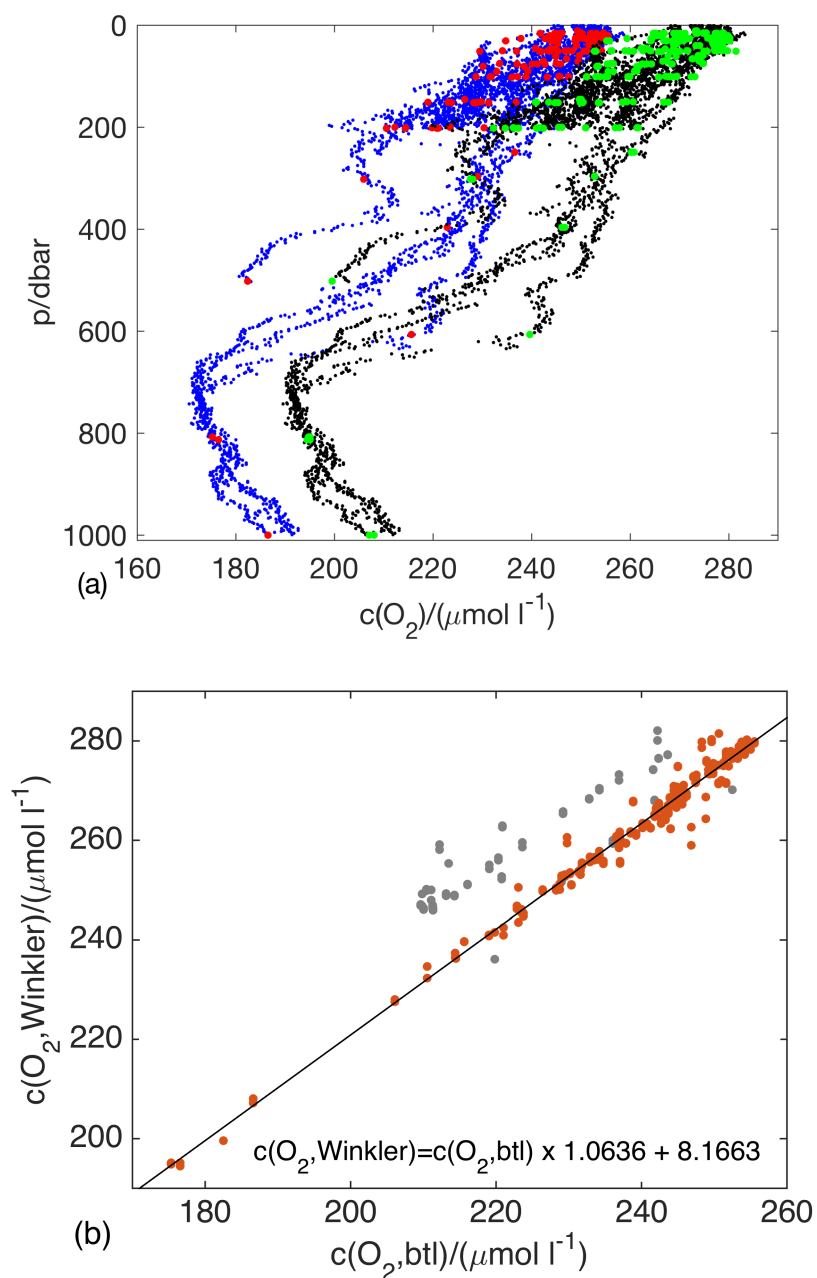


Figure 2.7 Cruise CE13001 - (a) Oxygen concentration profiles from CTD upcasts before (blue) and after calibration (black). In red are depths and oxygen concentrations of Niskin bottles fired above 1000 m and in green are the relative concentrations measured with Winkler titration; (b) concentrations from btl files for each Winkler sample collected during the cruise against the relative concentrations measured by Winkler titration; black line is the linear regression of valid points (red) used as calibration equation for the oxygen concentration profiles of CTD casts.

JC087



**Figure 2.8** Cruise JC087 - (a) Oxygen concentration profiles from CTD upcasts before (blue) and after calibration (black). In red are depths and oxygen concentrations of Niskin bottles fired above 1000 m and in green are the relative concentrations measured with Winkler titration; (b) concentrations from btl files for each Winkler sample collected during the cruise against the relative concentrations measured by Winkler titration; black line is the linear regression of valid points (red) used as calibration equation for the oxygen concentration profiles of CTD casts.

JC090

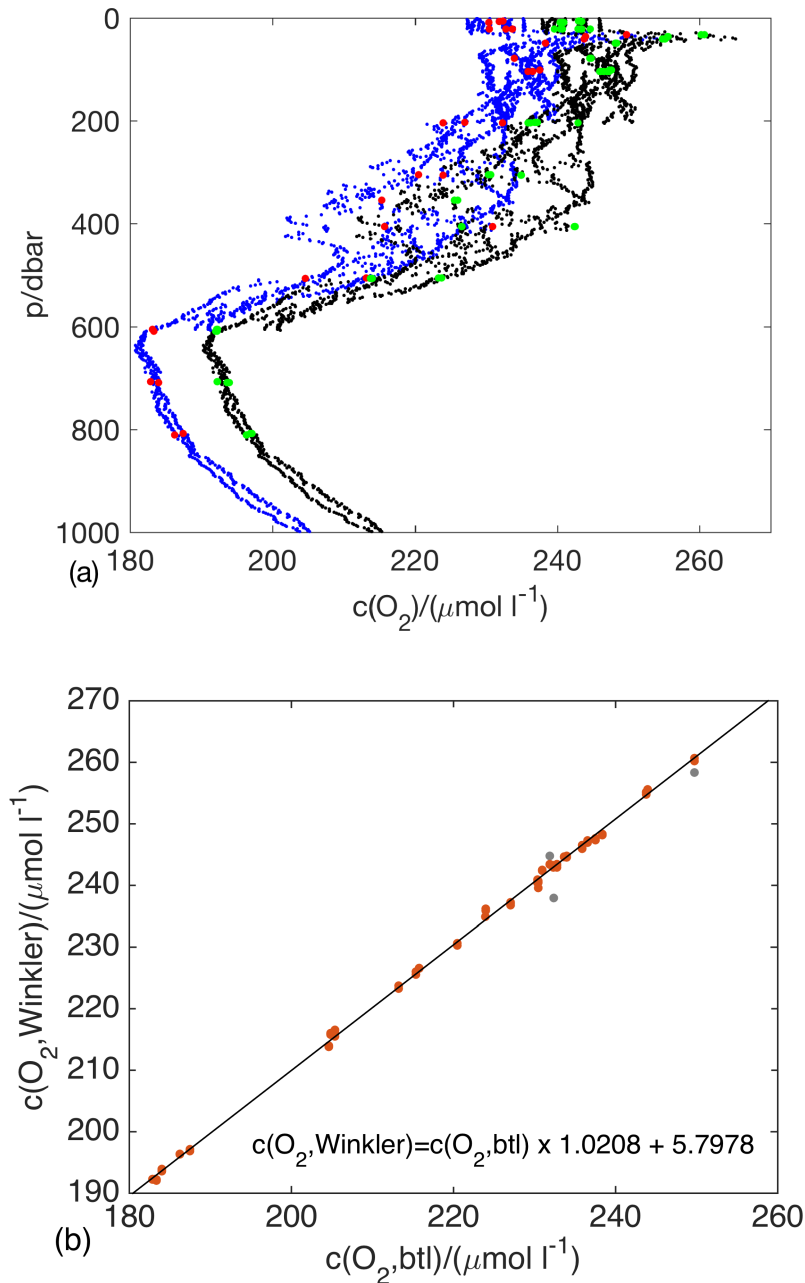


**Figure 2.9** Cruise JC090 - (a) Oxygen concentration profiles from CTD upcasts before (blue) and after calibration (black). In red are depths and oxygen concentrations of Niskin bottles fired above 1000 m and in green are the relative concentrations measured with Winkler titration; (b) concentrations from btl files for each Winkler sample collected during the cruise against the relative concentrations measured by Winkler titration; black line is the linear regression of valid points (red) used as calibration equation for the oxygen concentration profiles of CTD casts.

The CTD calibration uncertainty was estimated from the standard deviation of the residuals between  $c(\text{O}_2, \text{Winkler})$  and  $c(\text{O}_2, \text{btl})$  after the calibration. The uncertainty varied according to the cruise as can be seen in table 2.1. The mean value was  $1.57 \mu\text{mol l}^{-1}$ . The combined uncertainty of Winkler titration and CTD calibration was  $1.62 \mu\text{mol l}^{-1}$ . All the uncalibrated CTD casts underestimate the real  $c(\text{O}_2)$  in the water column. The different calibration curves are plotted together in figure 2.10. JC087 has the biggest correction increasing the values of  $22.9 \mu\text{mol l}^{-1}$  (figure 2.8a), while the correction for the other cruises is between  $10.5 \mu\text{mol l}^{-1}$  and  $16.4 \mu\text{mol l}^{-1}$  (figures 2.6a, 2.7a and 2.9a).

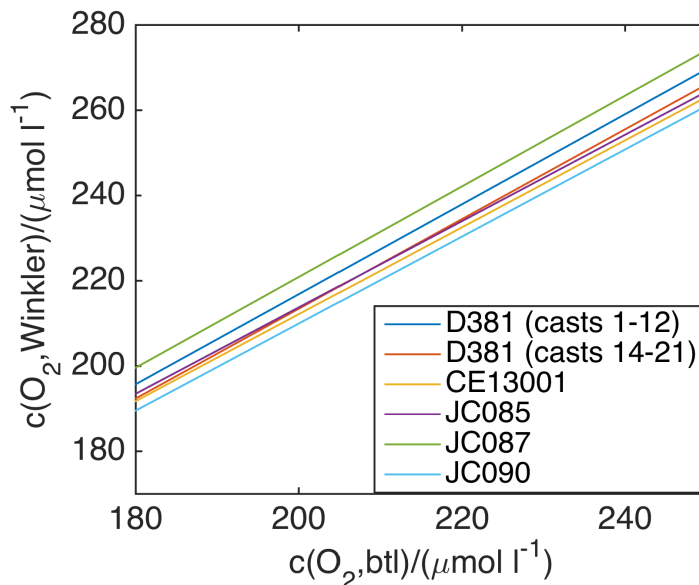


**Figure 2.10 Linear regression between btl and Winkler values used as calibration equations for each cruise.**

### 2.5.2 Comparison of $\text{O}_2$ concentrations with historical data

$c(\text{O}_2)$  from calibrated CTD casts was compared with historical data obtained from the Electronic Atlas of the World Ocean Circulation Experiment (WOCE) Data ([www.ewoce.org](http://www.ewoce.org)). These data will therefore be referred as WOCE dataset. The first comparison was carried out between the WOCE data and the calibrated  $c(\text{O}_2)$  of the CTD casts (figure 2.11a). WOCE data are the results of Winkler titrations performed during seven cruises (A02\_06MT030\_2, A02\_06MT039\_3, A24\_316\_N\_151\_2, AR19\_06GA350\_1, HUDSON82, AR19\_06GA276\_2 and AR19\_06GA226\_2) in a period spanning from 1981 to 2000. The results of the Winkler samples titrated during the present study were then compared directly with the ones titrated during WOCE cruises at the same potential densities (figure 2.11b).

There is an overall good agreement between the data from WOCE and the data from the present study. The higher variability of  $c(\text{O}_2)$  shown in this study is explainable by the time of the year in which data were collected: WOCE cruises were performed only between May and September, with just one cruise in November. The CTD casts used in this study, instead, span through the whole year, detecting variability not measured in the previous dataset.

A mismatch between the data analysed in the present study and the historical data is instead expected in some part of the water column due to multi-decadal decrease in  $c(\text{O}_2)$  shown by Stendardo and Gruber (2012). In particular, lower  $c(\text{O}_2)$  with respect to WOCE data is observed in the present study between 600 and 900 m (i.e., between  $\rho_0 \approx 1027.2 \text{ kg m}^{-3}$  and  $\rho_0 \approx 1027.5 \text{ kg m}^{-3}$  in figure 2.11b) and this confirm the magnitude of the de-oxygenation that has been observed at these densities. The loss of  $(-15 \pm 6.6) \mu\text{mol kg}^{-1}$  in the Intermediate Water and  $(-1.6 \pm 4.3) \mu\text{mol kg}^{-1}$  in the Mediterranean Outflow Water reported between 1993 and 2011 in the eastern North Atlantic (Stendardo and Gruber, 2012, Stendardo et al., 2015) match the magnitude of the difference between present and historical  $c(\text{O}_2)$ .

The results of the Winkler titration and CTD calibration generally agreed with the WOCE dataset. The values were in the typical range for this area and therefore the titrations were considered valid. This comparison was then used a validation of the whole CTDs calibration process.

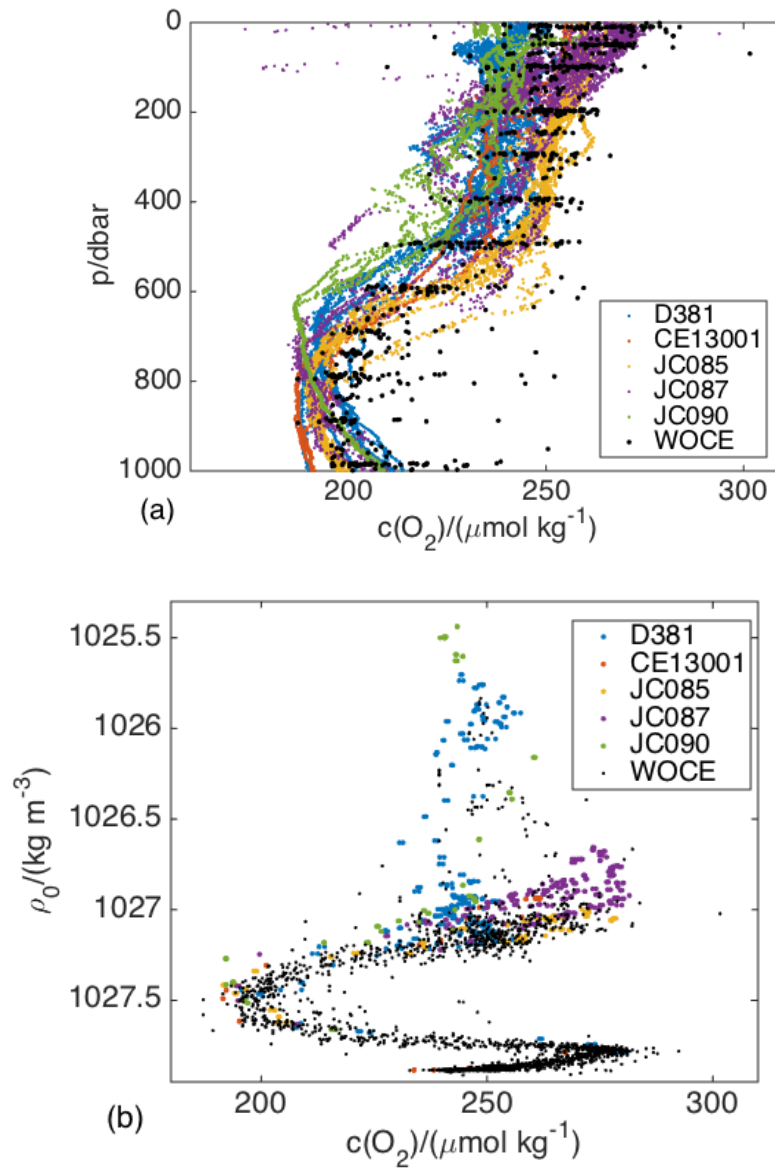


**Figure 2.11 (a) Comparison between oxygen concentrations of the calibrated CTDs casted during OSMOSIS and the ones from Winkler samples titrated during WOCE cruises (black) versus depth; (b) comparison between Winkler samples titrated during OSMOSIS and Winkler samples titrated during WOCE cruises (black) versus potential density.**

## 2.6 Calibration of the gliders – results

### 2.6.1 Calibration of gliders through calibrated ship-CTD casts

The determination of the  $\tau$  value to be applied to each mission was based on the normal distribution that fitted the frequencies with which each  $\tau$  between 0 s and 50 s was found to be the optimum within the mission (see section 2.3.1). SG566 and SG599 used the same optode and therefore they were expected to have similar  $\tau$  values (around 12 s for both these missions, figures 2.12a and 2.12c). The reason for the shorter  $\tau$  in SG502 ( $\tau = 8$  s, figure 2.12b) reflects different sensing foil characteristics.

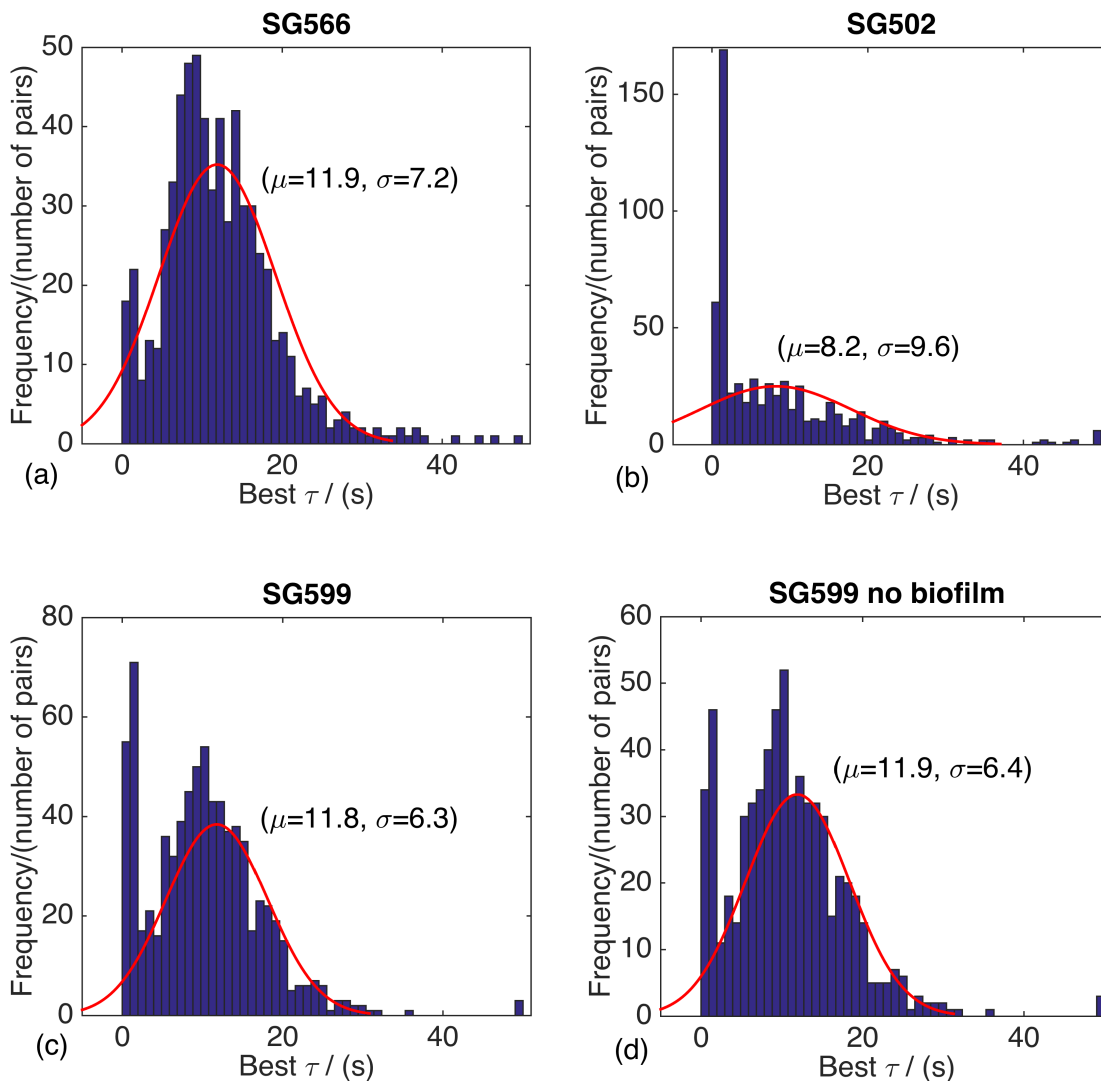


**Figure 2.12** Distribution of the frequency with which each value between 0 s and 50 s is the best  $\tau$  value (blue bars) within each mission. In red is the normal distribution fitted over the data whose central value  $\mu$  is used as  $\tau$  for the mission. Analysis is carried out for each individual mission: SG566 (a), SG502 (b) and SG599 (c). The latter is also repeated not considering the profiles measured after August 11<sup>th</sup> because of biofouling (d).

SG566 and SG502 were calibrated using CTD casts from the cruises that visited the site to deploy and recover the gliders. These casts were performed when the ship was close to the profiling gliders (figure 2.13a-b). SG599 was instead calibrated using CTD casts from three different cruises. Apart from the deployment and recovery cruises, another one (JC087) visited the site in the middle of the mission (locations in figure 2.13c). Seven different calibrations were then performed during the study and their details are listed in table 2.2. Three calibrations were done during a long-lasting proximity between the glider and the ship, which allowed the use of more than one CTD cast and more than one glider dive. In table 2.3 are listed the CTD casts performed during each cruise and which casts were used to calibrate the gliders. Two of the seven calibrations were done using CTD casts and glider dives that were far from each other in space (SG599 with JC087, figure 2.13c) and time (SG502 with JC085) with respect to the thresholds of “proximity” defined in section 2.3.2. However, these calibrations were done using the CTD casts that were the closest to the profiling gliders.

The linear calibration equations calculated are compared in figure 2.14. However, some of these lines are the results of a recalculation of the calibration equation. After the first calibration,  $c(\text{O}_2)$  from glider dives and CTD casts were plotted on top of each other. This was done in order to check if there were parts of the water column where they obviously mismatched. The calibrated dives of mission SG566 matched well the CTD casts from both D318 and CE13001 (figure 2.15c-d) against which they had been calibrated. These two calibrations were not repeated. The dive calibrated at the beginning of SG502 showed an obvious mismatch between 100 m and 280 m with the CTD cast from CE13001 (figure 2.16c), while the dive calibrated at the end of SG502 mismatched between 180 m and 320 m with the CTD cast from JC085 (figure 2.17d). These calibrations were therefore repeated not considering the portions of the column where the data mismatched. For the mission SG599, the dive calibrated against the CTD cast from JC087 mismatched with it between 160 m and 600 m (figure 2.17d). The calibration was repeated. The fact that such a wide portion of the water column had to be left out of the calibration is explainable with the large distance between the ship and the glider and the geographical heterogeneity in the area. The calibration of SG599 against CTD casts from JC085 was not repeated because the calibrated dive was considered in good agreement with the CTD cast throughout the whole column (figure 2.17c). The calibration of SG599 against the CTD casts from JC090 was not repeated despite mismatching (figure 2.18) because biofouling was detected (see section 2.6.2). These calibration equations are the ones listed in table 2.2.

**Table 2.2 CTD casts and glider dives used per each calibration, spatial and temporal distance between them,  $r^2$  value of their regression, calibration equation using  $TPhaseCoef_0$  and  $TPhaseCoef_1$  obtained by the regression and uncertainty associated to the calibration.**

Seaglider mission	Dive number	CTD	Cast	Spatial separation (km)	Temporal separation (h)	$r^2$	Calibration equation $C = \phi_{cal}, T = \phi_{TC}$ $\pm$ uncertainty ( $\phi_{cal}$ unit)	Uncertainty $\pm \mu\text{mol kg}^{-1}$
SG566	Dive 3	D381	Cast 3	1.43	6.72	0.998	$C = 0.9341 \times T - 0.0597$ $\pm 0.11$	1.84
	Dive 653	CE13001	Cast 1	1.80	2.48	0.998	$C = 0.9563 \times T - 1.3937$ $\pm 0.13$	2.80
	Dive 654		Cast 1	1.94	2.22			
Dive 655	Cast 3		0.46	0.95				
SG502	Dive 5	CE13001	Cast 3	3.16	2.12	0.996	$C = 0.9796 \times T - 1.4487$ $\pm 0.12$	2.23
	Dive 604	JC085	Cast 3	1.06	7.60	0.999	$C = 0.9464 \times T - 1.5059$ $\pm 0.10$	1.73
SG599	Dive 40	JC085	Cast 7	0.23	1.1	0.998	$C = 0.9122 \times T + 0.1628$ $\pm 0.14$	2.21
	Dive 40		Cast 8	0.40	0.39			
	Dive 41		Cast 9	2.02	0.18			
	Dive 342	JC087	Cast 24	4.11	2.99	0.999	$C = 0.9418 \times T - 1.1863$ $\pm 0.11$	2.30
	Dive 777	JC090	Cast 1	1.54	2.36	0.958	$C = .09109 \times T + 1.0022$ $\pm 0.26$	4.98
Dive 778	Cast 1		1.30	2.53				
Dive 782	Cast 3		1.52	0.08				

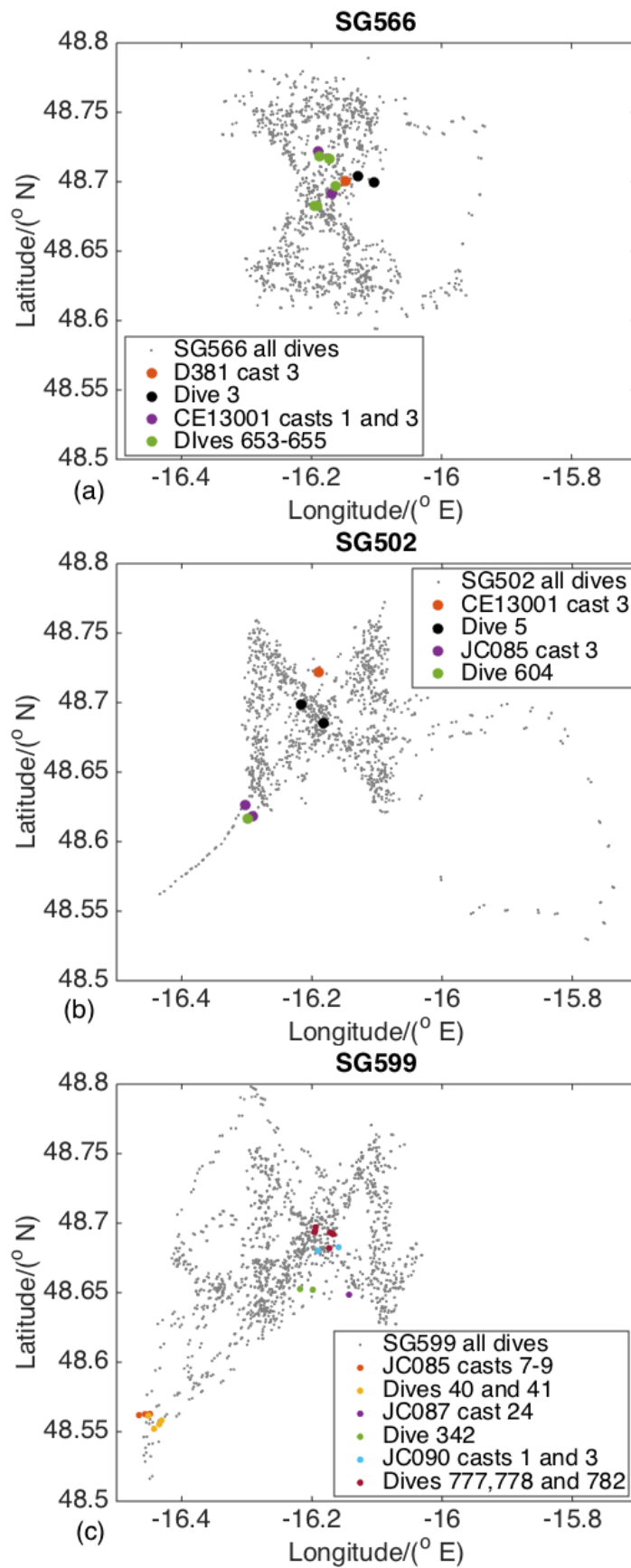


**Figure 2.13** Maps of the surfacing locations of the Seaglider before and after each dive for (a) SG566, (b) SG502 and (c) SG599. For each mission are shown the location of the CTD casts and the surfacing locations of the calibrated dives.

**Table 2.3 CTD casts for each cruise with either the Seaglider mission they calibrated or the reason why they were disregarded. Cast 13 of D381 is not included because the wire holding the frame split. Dives 1 and 3 from JC090 were not used in the final calibration**

CRUISE	DISREGARDED BECAUSE		USED TO CALIBRATE		
	FAR	SHALLOW	SG566	SG502	SG502
D381	1,2,4,6,9,14:22	5,7,8,10,11,12	3		
CE13001	-	2,4	1,3	3	
JC085	1,4,5,6	2		3	7,8,9
JC087	1,6	2:5, 7:23			24
JC090	2,4:9	-			<u>1,3</u>

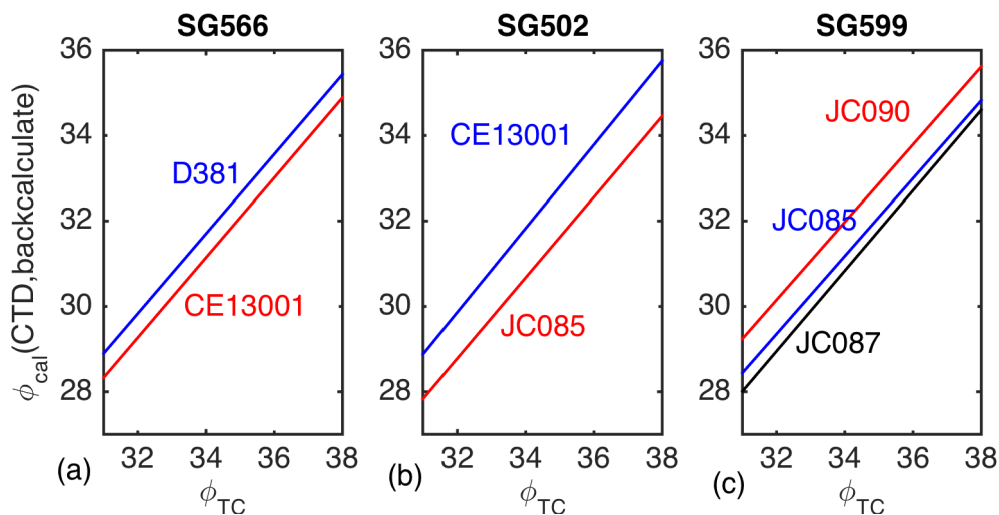


**Figure 2.14 Calibration linear equations for the beginning (blue) and the end (red) of each glider mission for (a) SG566, (b) SG502 and (c) SG599. In (c) a third calibration done in the middle of the mission is also shown in black. The name of the cruises of the calibrating CTD casts is also shown.**

The uncertainty associated with the calibration of  $c(\text{O}_2)$  values has been measured for each calibration as the standard deviation of the residual error between  $c(\text{O}_2, \text{CTD})$  and  $c(\text{O}_2, \text{glider})$  after the calibration. In case of recalculation of the calibration linear equation, the data-points in the disregarded portions of the water column were not used to calculate the uncertainty. In case of more CTD casts and/or more dives used for the same calibration, the mean values of the uncertainty of each couple CTD-dive was used. The uncertainty for the whole dataset was computed as the mean of the uncertainties of the six different calibrations ( $\pm 2.2 \mu\text{mol kg}^{-1}$ ). Considering the uncertainty in the CTD calibration of  $1.6 \mu\text{mol kg}^{-1}$  (transformed from  $\mu\text{mol l}^{-1}$  using the mean  $q_0$  of the dataset of  $1027.08 \text{ kg m}^{-3}$ ), the overall uncertainty associated with calibrated  $c(\text{O}_2)$  was  $2.7 \mu\text{mol kg}^{-1}$ .

## 2.6.2 Detection of biofouling during calibration

The  $TPhaseCoef_0$  and  $TPhaseCoef_1$  values for the seven calibrations were obtained through linear regressions between  $\phi_{TC}$  and  $\phi_{cal}$ . The r-values of these regressions were all above 0.99, apart for the calibration between SG599 and JC090 that had  $r = 0.958$  (table 2.2 and figures 2.15a-b, 2.16a-b, 2.17a-b, 2.18a).  $TPhaseCoef_0$  and  $TPhaseCoef_1$  increased between the beginning and the end for the missions SG566 and SG502 and the drift had the same direction towards lower  $c(O_2)$  (figure 2.14a-b). The drift has also the same direction in SG599 between the calibrations done at the beginning and in the middle of the mission (blue and black lines in figure 2.14c). However,  $TPhaseCoef_0$  and  $TPhaseCoef_1$  calculated at the end of SG599 in the calibration against JC090 showed a drift with inverse direction with respect to the other two calibrations for the same mission (red line in figure 2.14c being above the blue line rather than below it). The mission SG599 was then calibrated twice, the first time considering all the three CTD casts and the second time using only the first two CTD casts, disregarding the final one with the anomalous drift (data not shown). This second calibration revealed the presence of biofouling (see chapter 3) in the final part of the mission, with obviously biased data starting from 11<sup>th</sup> August 2013. The calibration between SG599 and JC090 was therefore considered not valid and only the first two calibrations were applied to this mission. The biofouling was more obvious in the top part of the water column, mismatching the concentrations measured in the ascents and descents. This means that the homogeneity at the top of consecutive profiles assumed for the calculation of  $\tau$  (see 2.3.1) was not valid during the period of the mission affected by the biofouling. The  $\tau$  calculation was then repeated accounting for this problem, not considering in the computation the biofouled profiles (all the ones measured after 11<sup>th</sup> August). The result confirmed  $\tau$  value reducing the number of odd profiles with the unrealistic optimum  $\tau$  of 0 s and 1 s (see figure 2.12d). This happened because the effect of the biofouling in decoupling the ascents with the following descents was bigger than the one deriving from the temporal lag of the optode, giving the unrealistically low optimum  $\tau$ . Higher values only increased the noise in the measurements without increasing the matching of the profiles, heavily affected by the difference due to the biofouling.

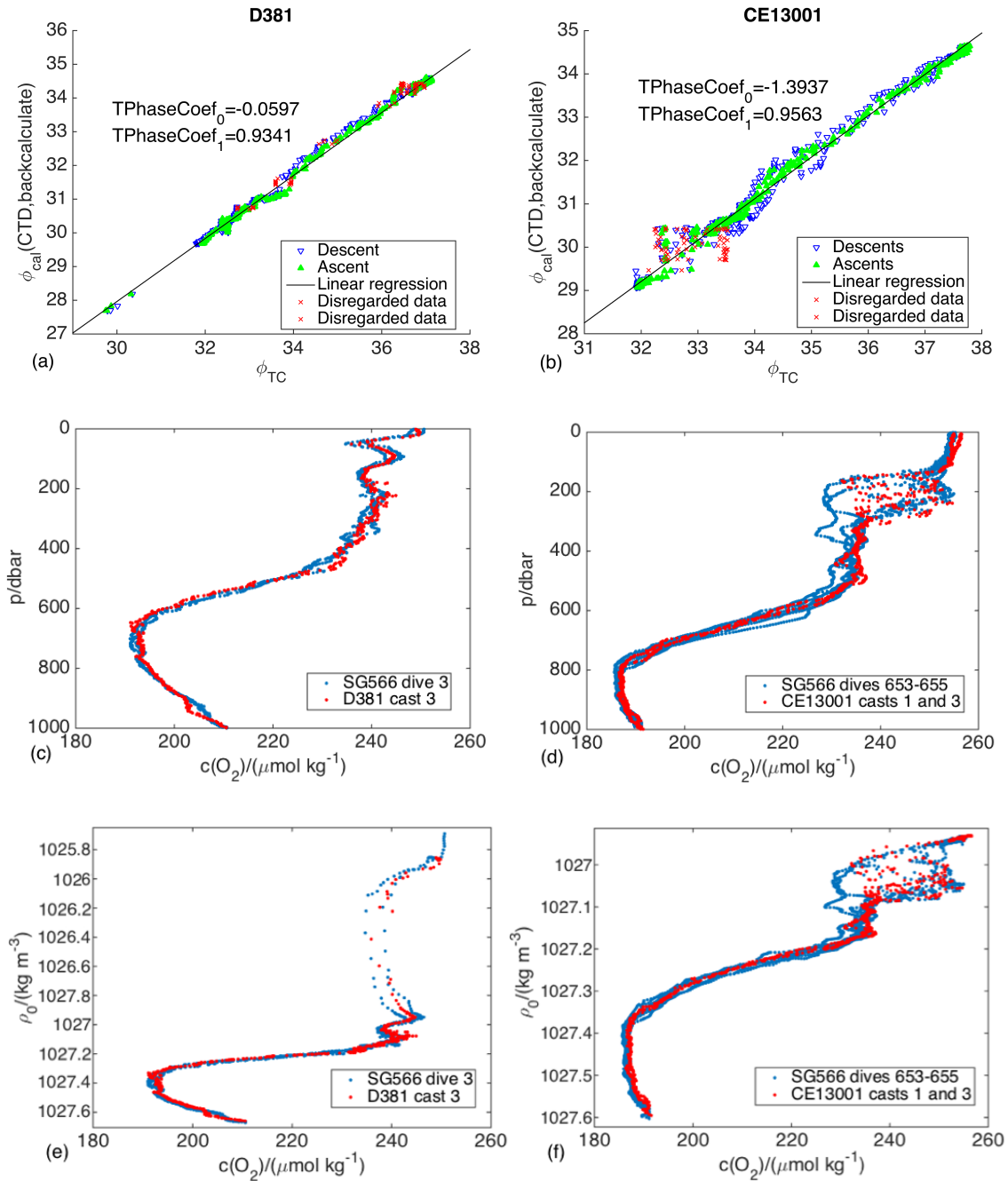


**Figure 2.15 Calibration of SG566: (a – b) linear regression between the TCPhase of the glider dives and the back-calculated CalPhase of the calibrated CTD used to calibrate TPhaseCoef0 and TPhaseCoef1 (shown); (c – f) calibrated dives and CTD used for the calibration against pressure (c – d) and potential density at surface (e – f); (a – c – e) is the calibration at the beginning of the mission and (b – d – f) is the calibration at the end of the mission.**

## SG502

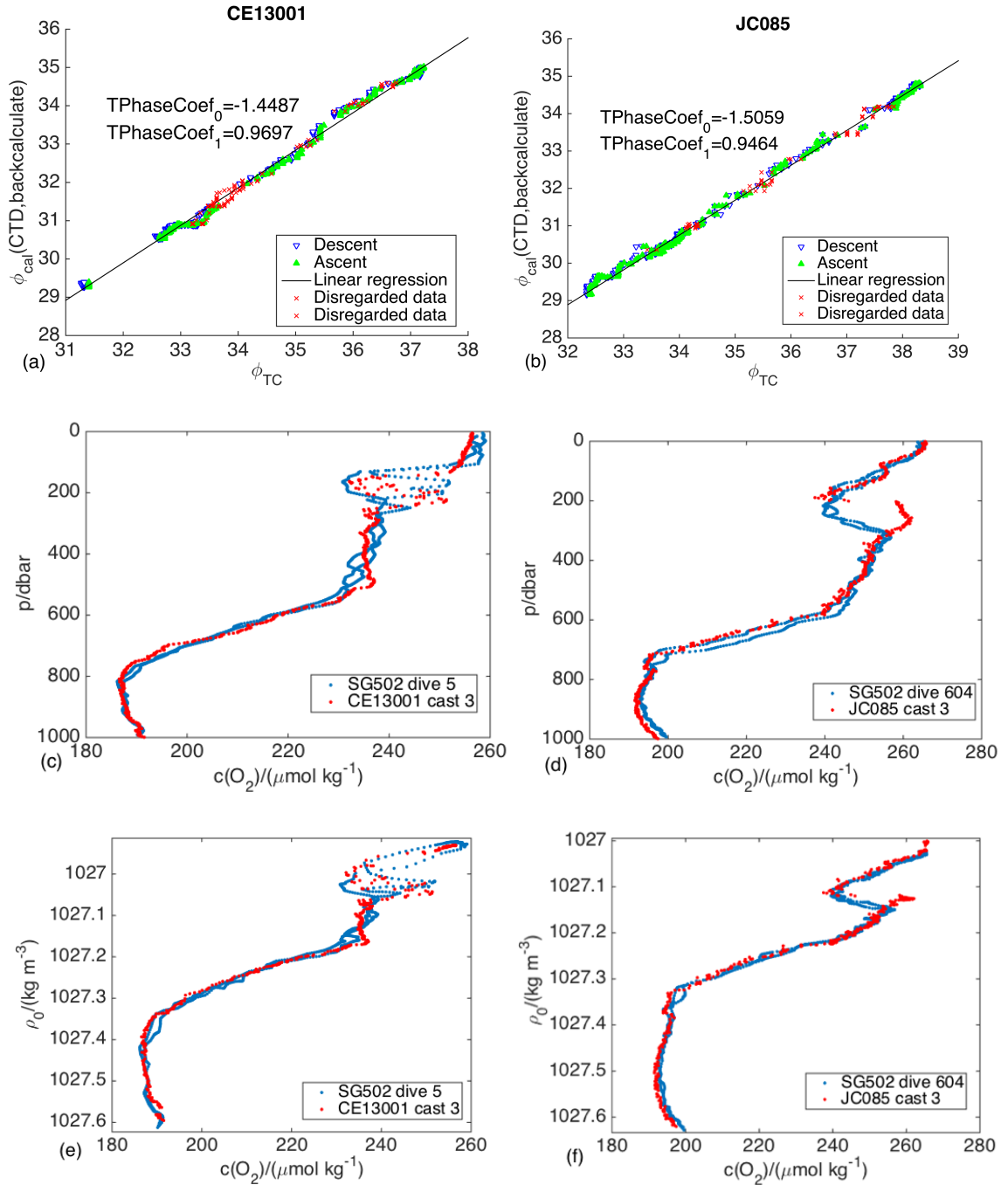


**Figure 2.16 Calibration of SG502: (a – b) linear regression between the TCPhase of the glider dives and the back-calculated CalPhase of the calibrated CTD used to calibrate TPhaseCoef0 and TPhaseCoef1 (shown); (c – f) calibrated dives and CTD used for the calibration against pressure (c – d) and potential density at surface (e – f); (a – c – e) is the calibration at the beginning of the mission and (b – d – f) is the calibration at the end of the mission.**

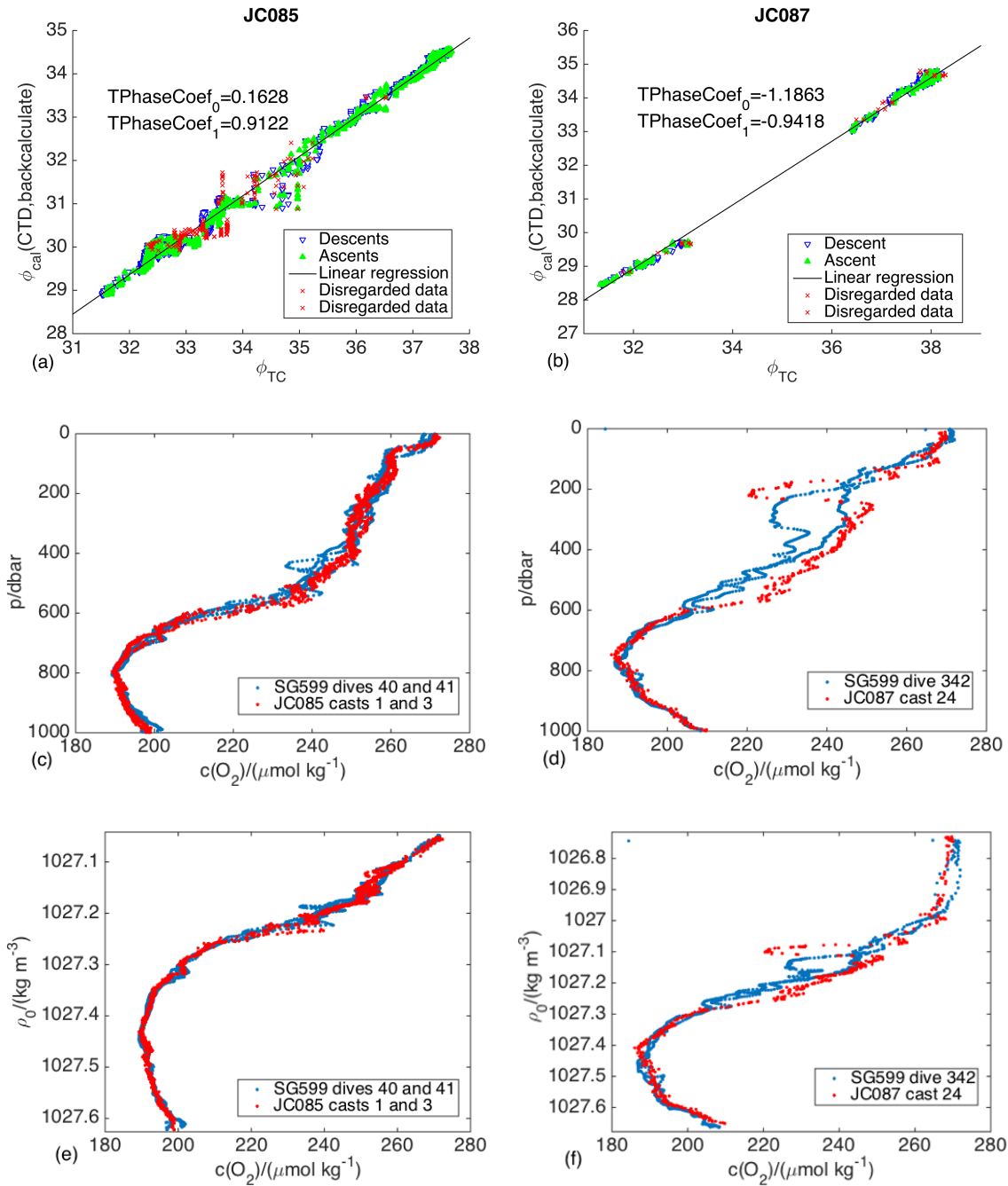


**Figure 2.17 Calibration of SG599: (a – b) linear regression between the TCPhase of the glider dives and the back-calculated CalPhase of the calibrated CTD used to calibrate TPhaseCoef0 and TPhaseCoef1 (shown); (c – f) calibrated dives and CTD used for the calibration against pressure (c – d) and potential density at surface (e – f); (a – c – e) is the calibration at the beginning of the mission and (b – d – f) is the calibration in the middle of the mission.**

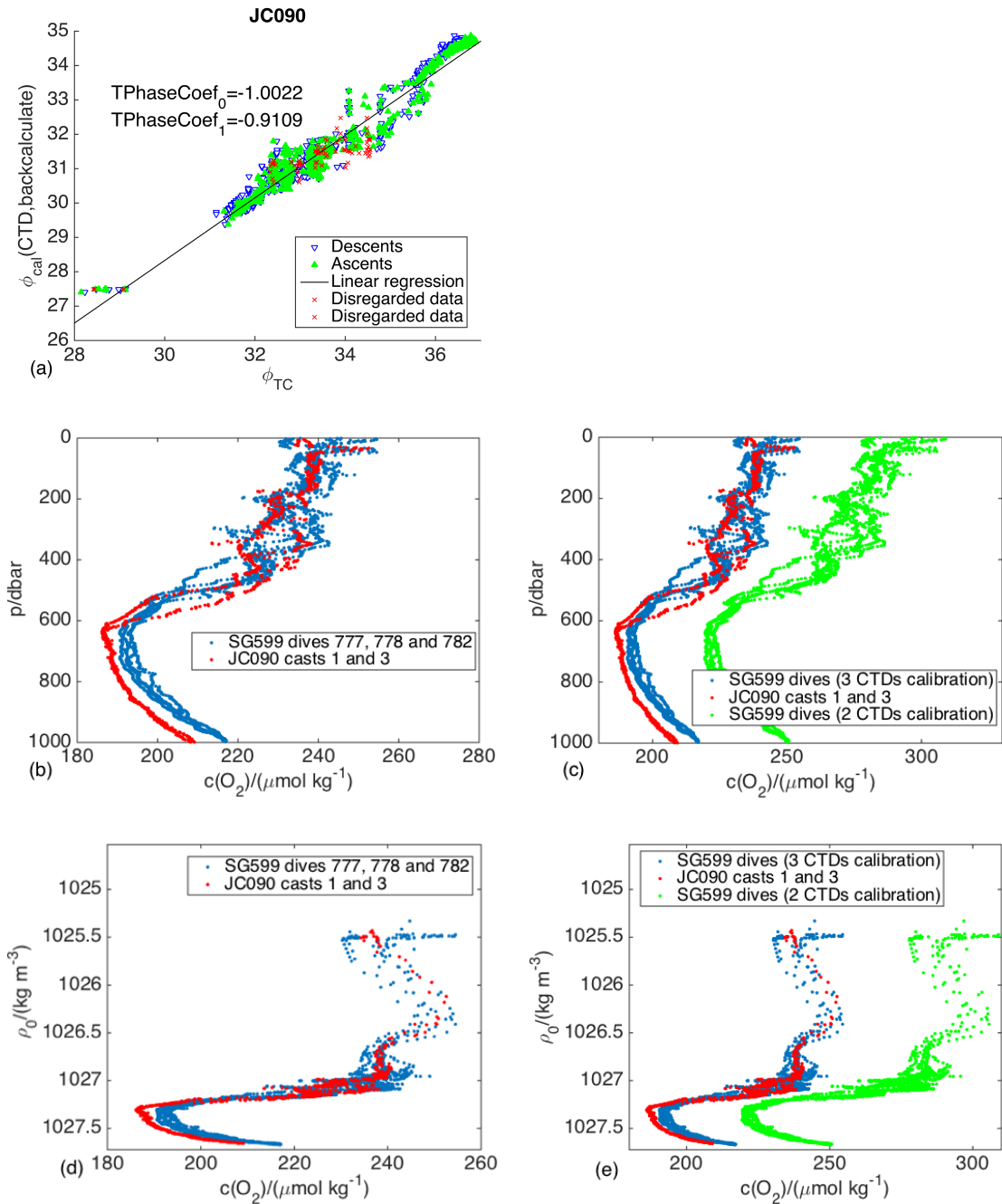


**Figure 2.18 Calibration of SG599 with JC090 at the end of the mission (a) Linear regression between the TCPhase of the glider dives and the back-calculated CalPhase of the calibrated CTD used to calibrate TPhaseCoef0 and TPhaseCoef1 (shown); (b – d) calibrated dives and CTD used for the calibration against pressure and potential density at surface; (c – e) comparison of the same dives as calibrated using JC090 (3 CTD casts calibration) and as calibrated using the drift between the first two calibrations of the mission to compute TPhaseCoef0 and TPhaseCoef1 disregarding JC090 because of biofouling (2 CTD cass calibration).**

## 2.7 Data quality control – results

### 2.7.1 Despiking

The identification of spikes involved a visual check of the individual profiles. Potential spikes were automatically detected, but there was high number of false positives. At the end of the process, 527 points were flagged as spikes in SG566 (0.14% of the total), 837 in SG502 (0.22 %) and 546 in SG599 (0.14%). These spikes were restricted in the first 40 m of the water column (figures 2.20b-d-f) and the majority of them were above 5 m.

The descents of some dives had a very steep decreasing gradient in salinity at the surface (figure 2.19b). This occurred at the same time as an anomalous feature of  $c(\text{O}_2)$  in the top m of the water column (figure 2.19a). Since this happened only in descents, and considering the concomitant anomaly in salinity, these data-points were considered as due to a fault of the sensors. They were therefore flagged and disregarded.

Two profiles from SG502 were also disregarded because of their anomalous shape (data not shown). It was also decided not to consider the shallow profiles that were at the beginning and at the end of each mission if they overlapped in time with deep profiles of another glider at the changeover between two consecutive missions.

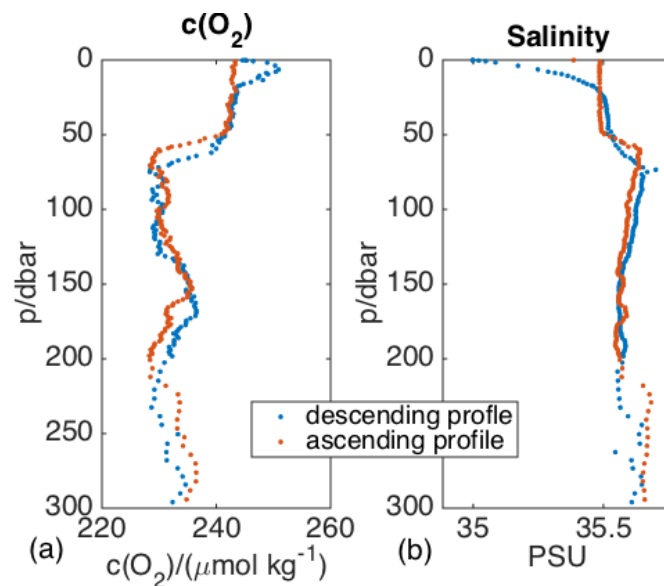


**Figure 2.19** Example of consecutive profiles where the descending profile (blue) has a decreasing gradient in salinity in the top 20 m that result in anomalous values of oxygen concentrations, therefore flagged as spikes.

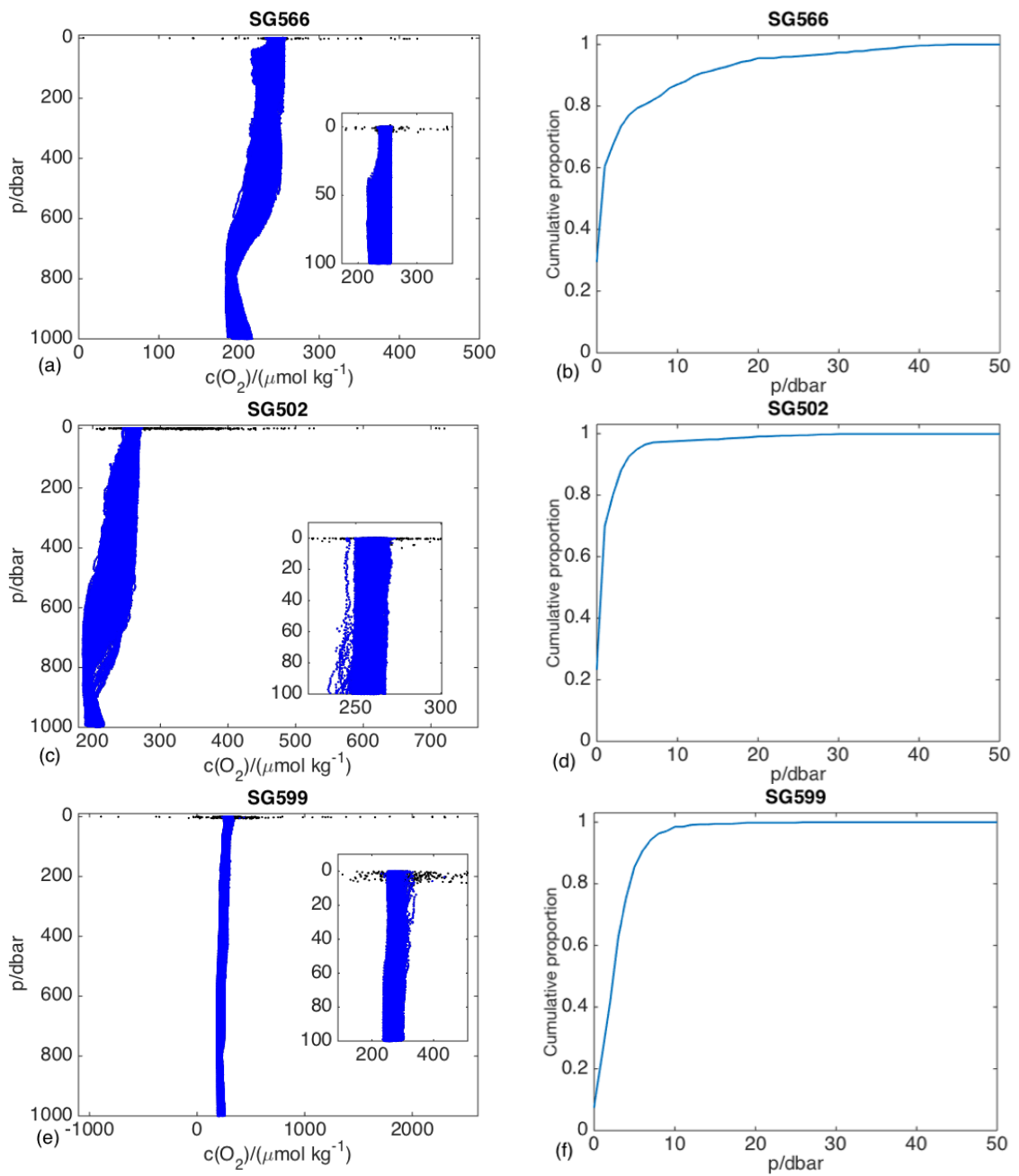


**Figure 2.20** (a-c-e) Valid data-points in blue and spikes in black for SG566 (a), SG502 (c) and Sg599 (e) with a focus of the spikes closest to the valid data; (b-d-f) cumulative proportion of spikes versus depth. All spikes are constrained above 40 m for all missions.

### 2.7.2 Correction for clogged salinity sensor

43 profiles during SG566 (from 7<sup>th</sup> to 10<sup>th</sup> September 2012) and 59 profiles during SG599 (from 25<sup>th</sup> to 30<sup>th</sup> June 2013) were considered bad data because the salinity sensor had been clogged during the mission and the salinity, which is used in the conversion from  $\phi_{\text{cal}}$  to  $c(\text{O}_2)$ , was obviously wrong (grey profiles in figure 2.22). Since the salinity of the whole profiles had been flagged as a spike (rather than having single spikes within good profiles),  $c(\text{O}_2)$  of these profiles was flagged in first instance as bad data. However, the problem in these calculations only arises in the transformation between  $\phi_{\text{cal}}$  and  $c(\text{O}_2)$ , where salinity is involved.  $\phi_{\text{TC}}$  were checked and recognised to be of good quality.

The calculation of  $c(\text{O}_2)$  is not very sensitive to salinity. Figure 2.21 shows the  $c(\text{O}_2)$  measured using the real  $\phi_{\text{cal}}$  profile of a dive from SG566 and a voluntarily exaggerated salinity change from 34.5 to 35.5 (temperature was maintained fixed for the entire profile to its mean value). The mean difference in values is  $(1.6 \pm 0.2) \mu\text{mol kg}^{-1}$ , lower than the uncertainty of  $c(\text{O}_2)$  values of  $2.7 \mu\text{mol kg}^{-1}$  and therefore not considered significant.

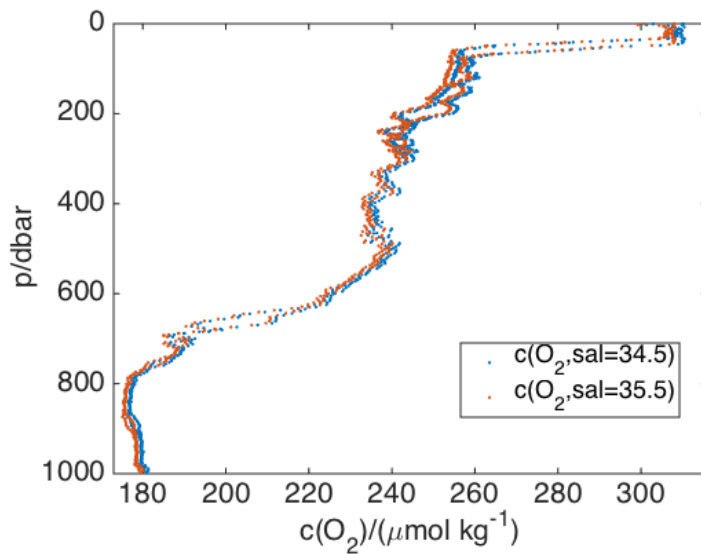


**Figure 2.21 Oxygen concentrations measured with the same CalPhase profile and with fixed temperature using two salinity values ( $S = 34.5$  and  $S = 35.5$ ). The comparison is done to show the effect of salinity on oxygen concentration calculation (mean difference is  $(1.6 \pm 0.2) \mu\text{mol kg}^{-1}$ ).**

For each of the two periods when the sensor was clogged, the salinity measured just before and just after the bad data (ten profiles before and ten profiles after) showed that the variations in salinity at any depth were  $< 1$  (Damerell et al., 2016). Salinity variations happening at any depth in these periods were therefore considered small enough not to cause significant ( $>$  uncertainty) errors in  $c(\text{O}_2)$  values. An averaged salinity profile was calculated using the good salinity profiles measured just before and just after the period with the clogged sensor. These

averaged profiles (figure 2.22a-b, blue lines) were therefore used for the calculation of  $c(\text{O}_2)$  instead of the bad salinity profiles. This was done not only for the two main periods when the salinity sensor was clogged (shown in figure 2.22), but also for some isolated profiles with wrong shape or with big part of the column flagged for salinity. This allowed the use of good  $\phi_{\text{TC}}$  profiles that had been previously discarded because of salinity.

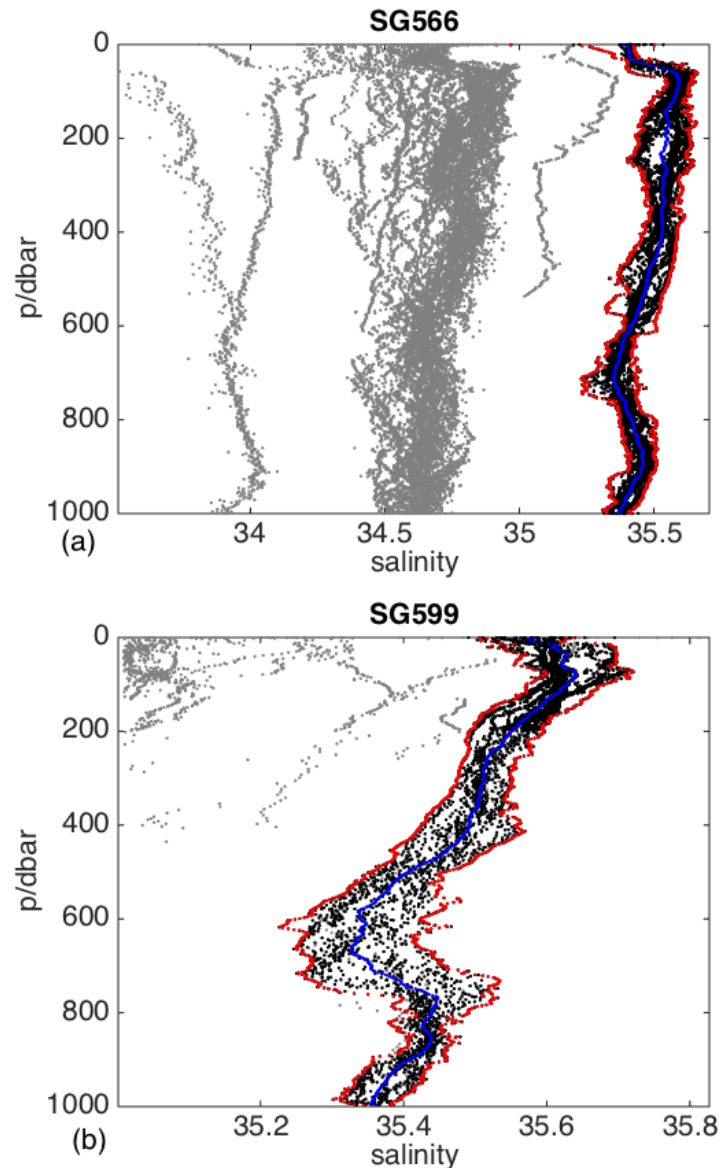


**Figure 2.22 Salinity profiles measured with clogged sensor during SG566 (a) and SG599 (b). Profiles flagged because of the clogging are in grey, profiles measured just before and just after them are in black, the range of good salinity values is in red and the profiles used to calculate oxygen concentrations for the flagged profiles is in blue.**

## 2.8 Conclusions

A big effort was made in the calibration of the  $c(\text{O}_2)$  values from the three glider missions from the OSMOSIS dataset to merge them into a coherent and unique dataset. This process had to account for the differences in the data collection due to several operators carrying out the fieldwork. The result is a time series of 4035  $c(\text{O}_2)$  glider profiles spanning continuously over one year from September 2012 to September 2013 near the PAP station plus CTD data from five cruises that visited the area in the same time.

The uncertainty associated with the absolute value of the glider data is  $2.7 \mu\text{mol kg}^{-1}$ . All the gliders were affected by drifting, in accordance to previous studies that used optodes (e.g., McNeil and D'Asaro, 2014; Bushunsky and Emerson, 2015; Hulle et al., 2016). This drift was corrected assuming a linear shift between the calibration equations done at the beginning and at the end of each mission. The despiking process showed the presence of spikes almost exclusively in the top 10 m of the water column. It is worth to spend a major effort for the implementation of the despiking process. The algorithm for the automatic detection of the odd values had in fact a high frequency of false positives which makes the process still rely on a time consuming visual check. It is also worth noticing that recent studies (e.g. Bittig and Körtzinger, 2015) have used only potential density (without using pressure) for the calculation of  $\tau$ . This could be used as an alternative method to the one used in the present study especially in regimes where variations of density at each depth are small such as where internal waves are negligible or tidal forcing is reduced or slow enough not to make density change between consecutive profiles.

# Chapter 3

## Hydrographic analysis

A relation between oxygen parameters (concentration, saturation and apparent oxygen utilization) and other variables (temperature, salinity, chlorophyll *a* concentration) are described for three separate layers in the water column (0-150 m, 150-700 m and 600-1000 m). The topmost layer comprises the euphotic zone and the surface boundary layer, the middle layer shows least stability in O<sub>2</sub> concentration and the bottommost layer shows O<sub>2</sub> minimum concentrations. Biofouling affecting the measurements in the last month of the last deployment is also described.

### 3.1 Oxygen parameters

The goal of this chapter is the hydrographic analysis of the 4035 oxygen concentration ( $c(\text{O}_2)$ ) profiles whose calibration has been described in chapter 2. The profiles were measured by the optodes mounted on three gliders operating over the period September 2012 – September 2013 in the framework of the project OSMOSIS. The gliders collected a suite of different physical and biogeochemical parameters in the top 1000 m of the water column sampling at high frequency. The resultant dataset is very detailed and allows a comparison of all these parameters to deduce possible correlations among them. The focus of the chapter is on the time series of  $c(\text{O}_2)$  and other two significant O<sub>2</sub>-related parameters such as the oxygen saturation ( $s(\text{O}_2)$ ) and the Apparent Oxygen Utilization (AOU).

$s(\text{O}_2)$  is the ratio between  $c(\text{O}_2)$  and the oxygen saturation concentration ( $c_{\text{sat}}(\text{O}_2)$ ) (equation 3.1).  $c_{\text{sat}}(\text{O}_2)$  parameterises the solubility of oxygen in the water and was calculated following Garcia and Gordon (1992), considering in situ potential temperature, absolute salinity and atmospheric pressure from ERA-Interim re-analysis (<http://www.ecmwf.int/en/research/climate-reanalysis/era-interim>):

$$s(\text{O}_2) = \frac{c(\text{O}_2)}{c_{\text{sat}}(\text{O}_2)} \quad (3.1)$$

Waters where  $s(\text{O}_2) > 1$  are supersaturated, while waters where  $s(\text{O}_2) < 1$  are undersaturated. Supersaturation is usually related to biological production, which only occurs above the euphotic depth ( $z_{\text{eup}}$ ), because photosynthesis needs light as energy source.

AOU is the difference between  $c_{\text{sat}}(\text{O}_2, 1013.25 \text{ hPa})$  and  $c(\text{O}_2)$  (equation 3.2) and can be used to calculate respiration rates ( $R$ ) in deep waters and to estimate the time elapsed since the most recent ventilation (Ogura et al., 1970; Doval and Hansell, 2000; Aristegui et al., 2002; Carlson et al., 2010; Stanley et al., 2012; Stendardo and Gruber, 2012).

$$\text{AOU} = c_{\text{sat}}(\text{O}_2) - c(\text{O}_2) \quad (3.2)$$

The AOU concept assumes that air-sea  $\text{O}_2$  flux is sufficiently fast to equilibrate atmosphere and ocean when a water parcel is at the surface. According to this concept, the water masses that leave the surface are therefore in a state of equilibrium ( $s(\text{O}_2) = 1$ ). The majority of water subduction at mid-high latitudes happens in winter when there is no supersaturation due to biological activity. Disregarding AOU changes due to mixing effects, the increase in AOU in subducted waters can be then related to  $R$  and can be used to estimate its magnitude.  $R$  estimates usually focus on AOU changes in the cores of the water masses, where there is a low influence of diapycnal mixing with other water bodies. AOU is therefore associated with the “age” of the water (i.e., the time elapsed since it was last at the surface) and  $R$ .

$c(\text{O}_2)$ ,  $s(\text{O}_2)$  and AOU were compared with the other parameters measured simultaneously by the gliders such as absolute salinity (from now on ‘salinity’), potential temperature (from now on ‘temperature’), potential density (from now on ‘density’) and chlorophyll  $a$  concentration ( $c(\text{Chl } a)$ ). The analysis of salinity, temperature and  $c(\text{O}_2)$  led to the definition of three layers in the column (section 3.2, figure 3.1). The whole time series of the  $\text{O}_2$ -related parameters are shown in figure 3.2, while physical parameters and  $c(\text{Chl } a)$  are shown in figure 3.3. Data measured after 11<sup>th</sup> August 2013 were disregarded because of the biofouling as explained in section 3.5.

## 3.2 Layers in the water column

The comparison among parameters was carried out taking into account the presence of three layers in the water column. These layers were identified by the hydrographic analysis presented by Damerell et al. (2016). In the present study, these three layers will be called A, B and C. Layer A was at the top of the column and was roughly 150 m deep (figure 3.1). This layer included the ocean surface boundary layer (see chapter 4) that had an obvious seasonal cycle in the temperature due to solar insolation. Salinity was more variable, it did not follow any seasonal cycle and varied at all time scales, probably due to advection or vertical mixing. Layer B lay between 150 m and 700 m and was characterised by a significant intraseasonal variability in temperature and salinity, which were also strongly correlated with each other. The variability was mostly related to gyre-scale and mesoscale dynamics, but not to the surface forcing. Layer C was at the bottom of the surveyed column between 700 and 1000 m and had high variability

at all timescales in temperature and salinity, strongly influenced by the Mediterranean Outflow Water (MOW) that appeared at these depths.

The three layers can be seen in figure 3.1 as depth ranges where parameters have different spectra of variation. Temperature and salinity in layer A and C varied over a broad range of frequencies, while  $c(\text{O}_2)$  had a strong signal at periods of about 3 months. In Layer B, instead, temperature and salinity did not show a particular periodicity, while  $c(\text{O}_2)$  had a strong signal on the period of 3 months and smaller significant variations at all time scales.

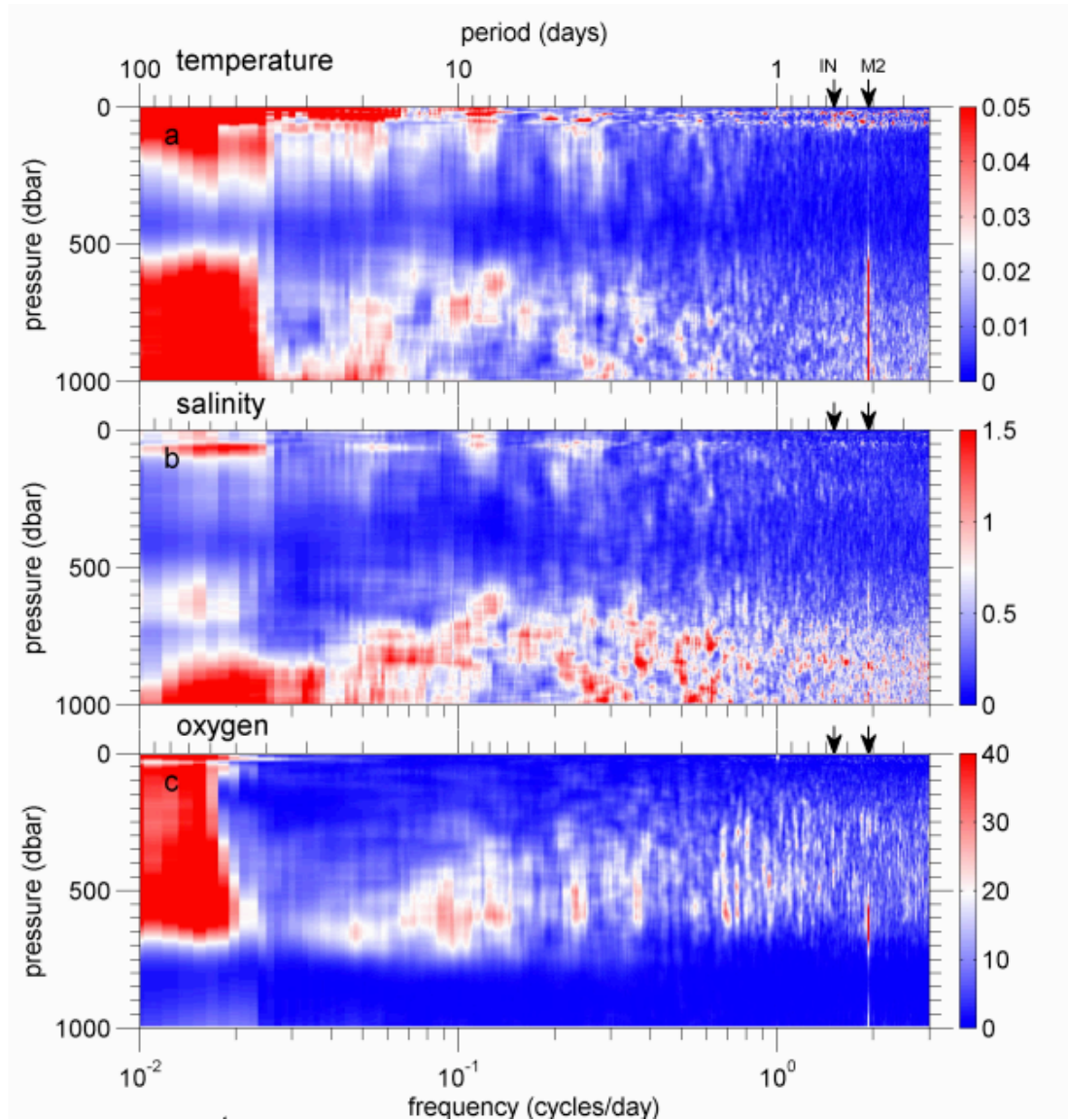


**Figure 3.1** Variance preserving spectra for (a) temperature (b) salinity ( $\times 10^{-3}$ ) and (c) dissolved oxygen concentration. The colours show the power spectral density  $\times$  frequency. The inertial frequency (IN) and M2 tidal frequency are marked as black arrows on the upper axis (Damerell et al., 2016).

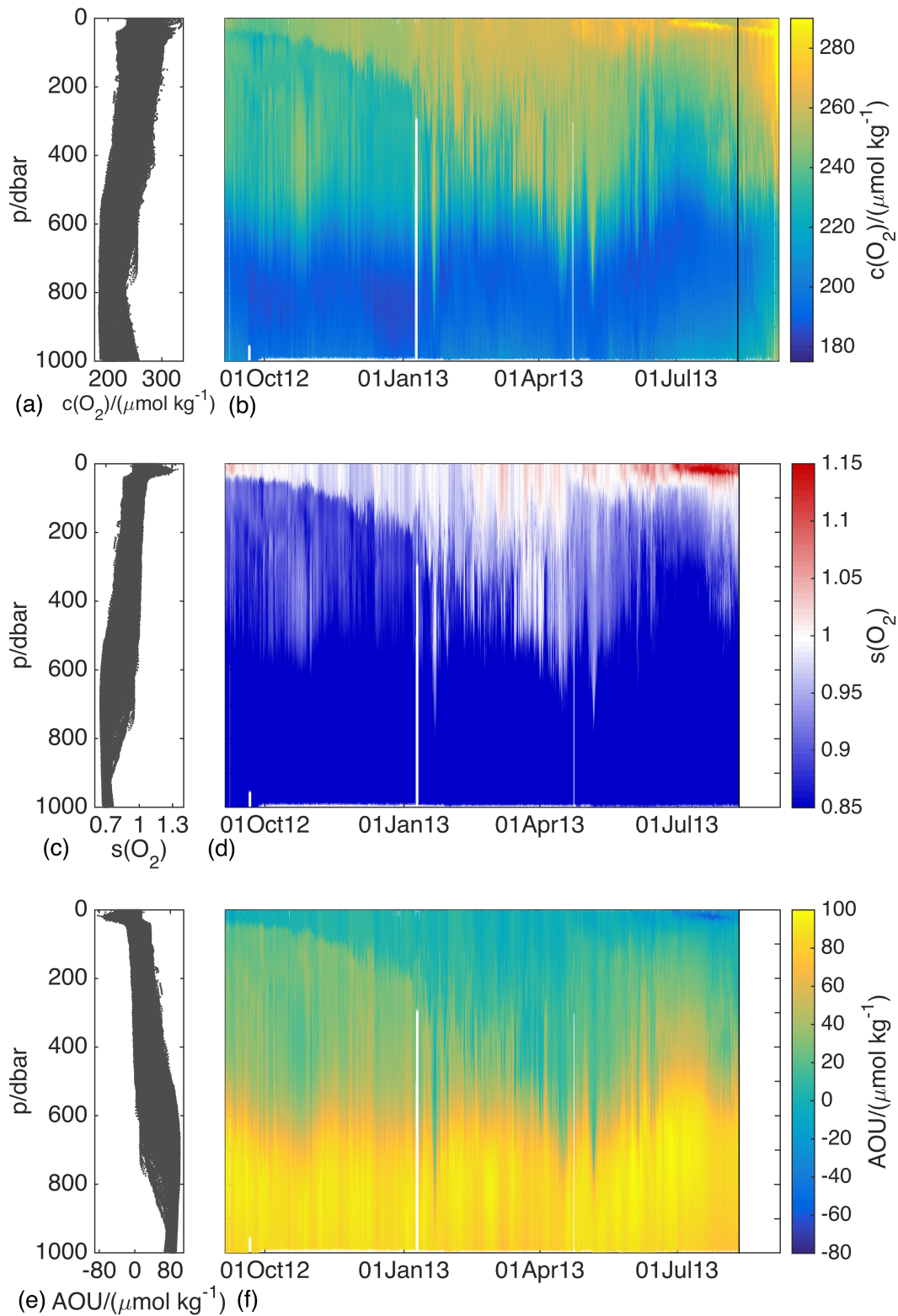


**Figure 3.2** Distribution against pressure (left panel) and time series against pressure (right panel) for (a-b) oxygen concentration, (c-d) oxygen saturation and (e-f) Apparent Oxygen Utilization. The black line in (b) marks the start of the biofouling.

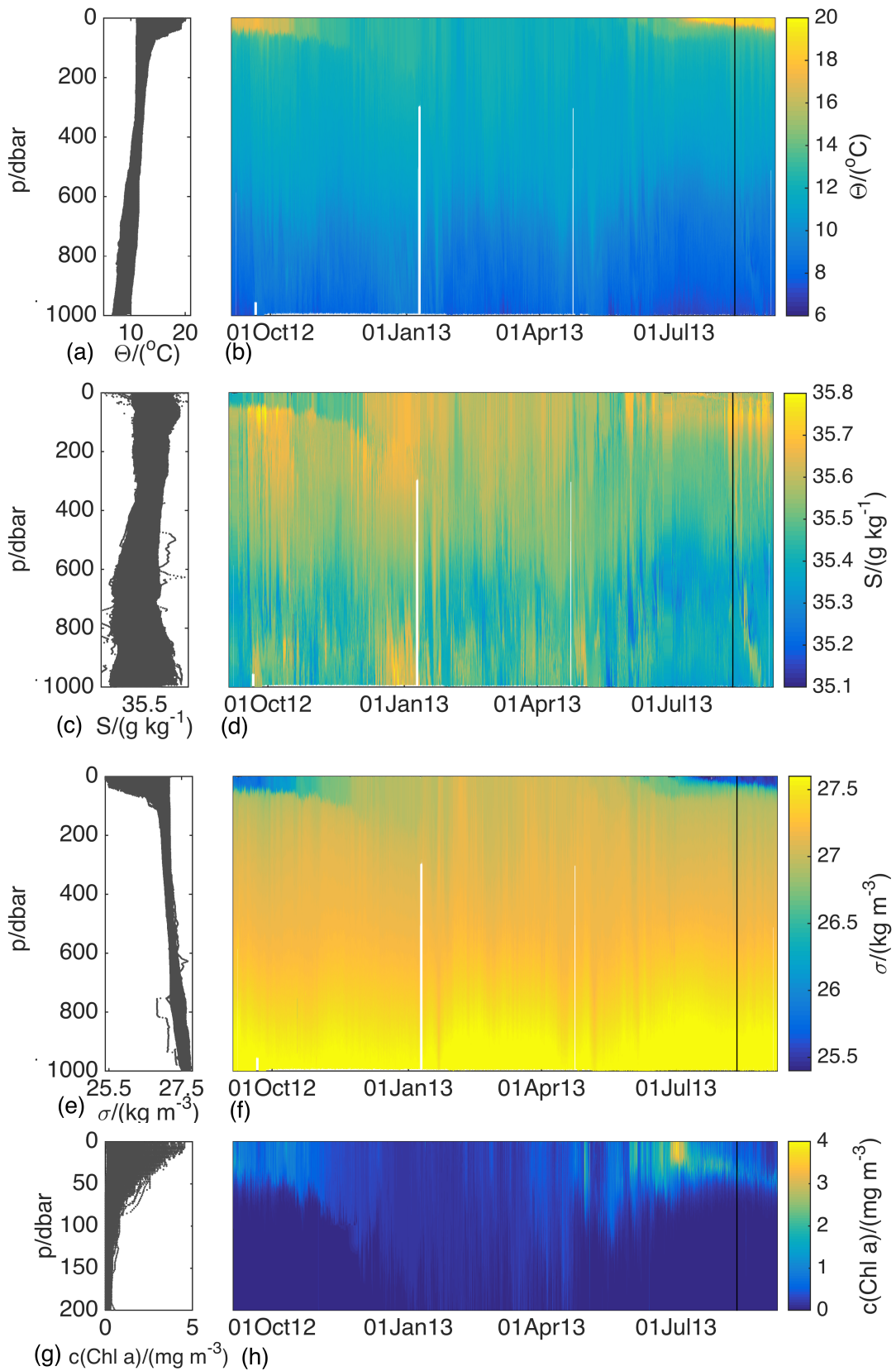


**Figure 3.3** Distribution against pressure (left panel) and time series against pressure (right panel) for (a-b) temperature, (c-d) salinity, (e-f) potential density at surface and (g-h) chlorophyll *a* concentration. The black line in (b-d-f-h) marks the start of the biofouling.

### 3.3 Oxygen analysis in layer A

The analysis of  $c(\text{O}_2)$  in layer A is important because waters at the surface acquire the characteristics that they will have once subducted, determining the amount of  $\text{O}_2$  that will be transported at depth. Layer A was in contact with the atmosphere, directly influenced by the air-sea fluxes (ventilation). The strong seasonal cycle in temperature due to the insolation caused a large variation in  $c_{\text{sat}}(\text{O}_2)$  that spanned between  $224 \mu\text{mol kg}^{-1}$  and  $273 \mu\text{mol kg}^{-1}$ . The plankton blooms also occurred in this layer because  $z_{\text{cup}}$  was always shallower than 100 m. The presence of several factors made it difficult to evaluate the signals related to each process in the determination of  $c(\text{O}_2)$ .

$c(\text{O}_2)$  had a very strong seasonal signal, varying between  $215 \mu\text{mol kg}^{-1}$  and  $315 \mu\text{mol kg}^{-1}$  (figures 3.2a-b). Water was undersaturated and supersaturated according to the time of the year when it was sampled as can be seen in figure 3.2d. During winter,  $c_{\text{sat}}(\text{O}_2)$  increased due to the temperature dependence of the solubility. The water-cooling process can be appreciated in figure 3.4a, where the mean temperature in the top 20 m of the water column is shown. The increased solubility (higher  $c_{\text{sat}}(\text{O}_2)$ ) triggered an influx of  $\text{O}_2$  from the atmosphere (see air-sea  $\text{O}_2$  flux in section 5.2.3). In this period the water was expected to be close to saturation at the surface (Broecker and Peng, 1982; Woolf and Thorpe, 1991; Chester, 2000; Ito et al., 2004) because biological rates should be near zero and gas exchange should be rapid due to high wind speeds. However, water at the surface was actually undersaturated for the majority of the winter (figure 3.2d). The air-sea  $\text{O}_2$  flux was not sufficient to saturate the water. These results confirm previous observations (e.g. Gordon and Huber, 1990; Körtzinger et al., 2001; Russell and Dickson, 2003; Körtzinger et al., 2004; Keeling et al., 2010; Duteil et al., 2013) and model output (Ito et al., 2004), which also reported undersaturation in surface waters. Between 7<sup>th</sup> October 2012 and 3<sup>rd</sup> March 2013 the mean  $s(\text{O}_2)$  at 5 m depth was 0.98. Compared with the mean  $s(\text{O}_2)$  of 0.90-0.97 found by Keeling et al. (2010) in polar waters, this result shows weaker undersaturation at these lower latitudes. Part of the undersaturation was due to the sporadic doming of isopycnals that brought deeper and less saturated water at the surface.

The majority of the supersaturated data-points in the dataset were expected in layer A, where the biological production happens. In particular, water was expected to become supersaturated in  $\text{O}_2$  during phytoplankton blooms, when biological production peaks (see chapter 5). Biological processes increased  $c(\text{O}_2)$  from mid February onwards (figure 3.2b), but supersaturation was not persistent. There was an alternation with periods of  $s(\text{O}_2) < 1$ , which is reflected in the alternation of red and blue areas near the surface in figure 3.2d. This suggests that instead of a continuous bloom, a series of minor blooms occurred from February onwards before the major spring bloom that started at the end of May, when  $c(\text{Chl } a)$  increased significantly (figure 3.3f). It can be argued that, since the air-sea flux was not sufficient to bring  $s(\text{O}_2)$  to equilibrium and the water was undersaturated for a long time, increases in  $c(\text{O}_2)$  due to

biological production might have been not always sufficient to give supersaturation. For this reason the analysis of the production should not be based only on the supersaturation pattern. A more detailed analysis of biological production is carried out in chapter 5 using the  $O_2$  budget method.

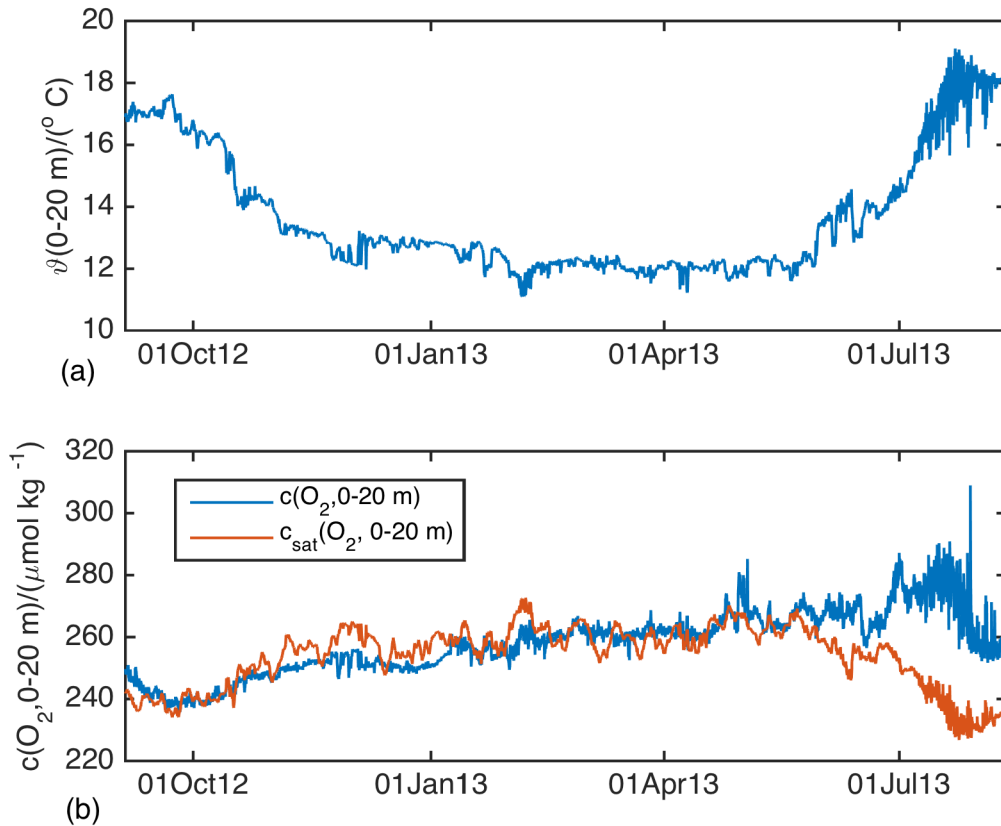


**Figure 3.4 (a) Mean potential temperature in the top 20 m of the water column; (b) mean oxygen concentration (blue) and oxygen saturation concentration (red) in the top 20 m of the water column. Red line is above blue line during periods of undersaturation, vice versa for supersaturation.**

Starting from the beginning of July (i.e., at the end of the main bloom),  $c(O_2)$  decreased at the surface, while a deep chlorophyll and oxygen maximum developed deeper (figures 3.2b and 3.3h). The high  $s(O_2)$  (up to 1.18) and the negative AOU ( $-44\ \mu\text{mol kg}^{-1}$ ) that were measured in this deep  $c(O_2)$  maximum from 14<sup>th</sup> to 28<sup>th</sup> July and between 10 m and 20 m show high biological production. A more detailed analysis of the period exhibiting the deep  $c(O_2)$  maximum is carried out in chapter 5 to estimate its production.

The  $s(O_2)$  and  $c(\text{Chl } a)$  are correlated for  $c(\text{Chl } a)$  higher than  $0.5\ \text{mg m}^{-3}$ . In figure 3.5 it is possible to see a tendency to higher  $s(O_2)$  when there was higher  $c(\text{Chl } a)$  (figures 3.5c-d).  $s(O_2)$  for  $c(\text{Chl } a)$  lower than  $0.5\ \text{mg m}^{-3}$  were influenced by physical rather than biological processes because the algal biomass was too low to produce significant quantities of  $O_2$ . This

was particularly obvious from September to March (figures 3.5a-b). Data from July and August showed higher  $s(\text{O}_2)$  with respect to March-June. This could be an indication of a possible community shift related to the formation of the deep chlorophyll maximum (DCM). The change in the dominant taxa within the phytoplankton community between spring and summer is well known, with diatoms blooming before dinoflagellates (Margalef, 1978; Leterme et al., 2005; McQuatters-Gollop et al., 2007, Barton et al., 2013). This is due to different factors such as their size, trophic strategy, light absorption efficiency, growth rate among the others (Barton et al., 2013). Furthermore, dimensional classes within the same group show a succession related to their ability of uptaking nutrients more efficiently in oligotrophic environments (Barton et al., 2013). Each taxon produces a different amount of oxygen per mole of chlorophyll *a* and, within the same species, this ratio can change because of photoacclimatation (Sakshaug et al. 1997; Goericke and Montoya 1998; Henriksen et al. 2002). This shift in species and/or in the physiology of the cells is influenced by many environmental factors such as light intensity, nutrient availability or the regime of turbulence (e.g., Huisman et al., 2004; Veldhuis et Kraay, 2004; Brunet et al., 2008; Dimier et al., 2009b, Barton et al., 2013). Considering that the formation of the summer deep chlorophyll maximum suggests a substantial attenuation of mixing forces and low nutrients, it is reasonable to induce that a shift in the phytoplankton community could be the cause of the differences observed. The community of the deep chlorophyll maximum seems able more efficient, being able to produce more  $\text{O}_2$  and super-saturate the water at lower  $c(\text{Chl } a)$  with respect to earlier periods of the year.

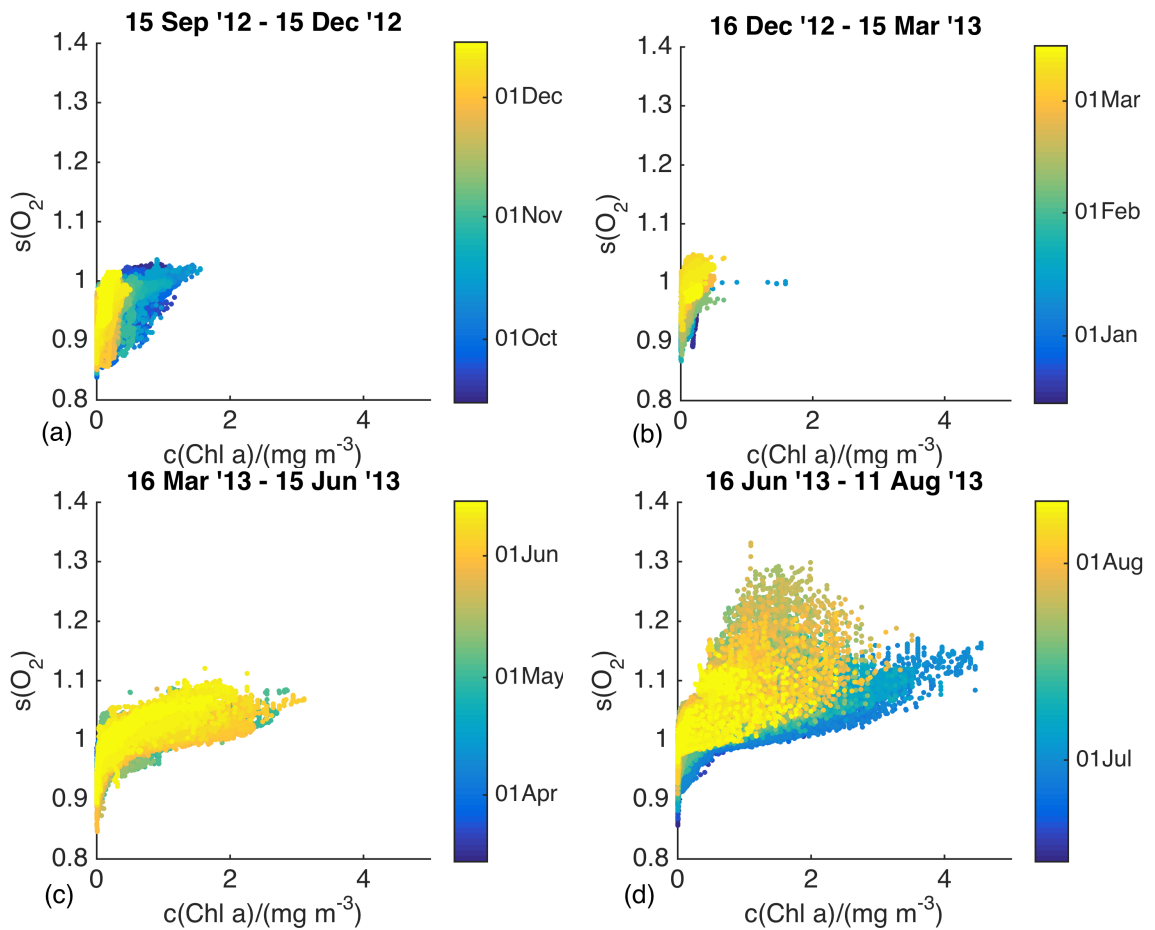


**Figure 3.5** Distribution of oxygen saturation against chlorophyll *a* concentration coloured by the date of measurements between mid-September 2012 and mid-December 2012 (a), mid-December 2012 and mid-March 2013 (b), mid-March 2013 and mid-June 2013 (c) and mid-June 2013 to mid-August 2013 (d).

### 3.4 Oxygen in layer B

#### 3.4.1 Correlation between oxygen concentration and temperature

In the absence of biological effects,  $c(\text{O}_2)$  should be anti-correlated with temperature because  $\text{O}_2$  solubility increases with decreasing temperature (higher  $c_{\text{sat}}(\text{O}_2)$  in colder water). However, in layer B, temperature and  $c(\text{O}_2)$  were positively correlated as can be seen by the positive values of the correlation coefficient shown in figure 3.6 below 400 dbar. The increase of AOU and the decrease of  $s(\text{O}_2)$  visible between 150 dbar and 700 dbar (figures 3.2c-e) show that deeper water had been subducted for longer and/or had higher respiration rates. Temperature also decreases with increasing pressure. This means that deeper and colder waters were more undersaturated because more oxygen had been consumed. This suggests that in layer B the magnitude of biological  $\text{O}_2$  consumption was more important than the temperature

dependence of  $O_2$  solubility in the determination of  $c(O_2)$ . This explained the positive correlation between temperature and  $c(O_2)$ .

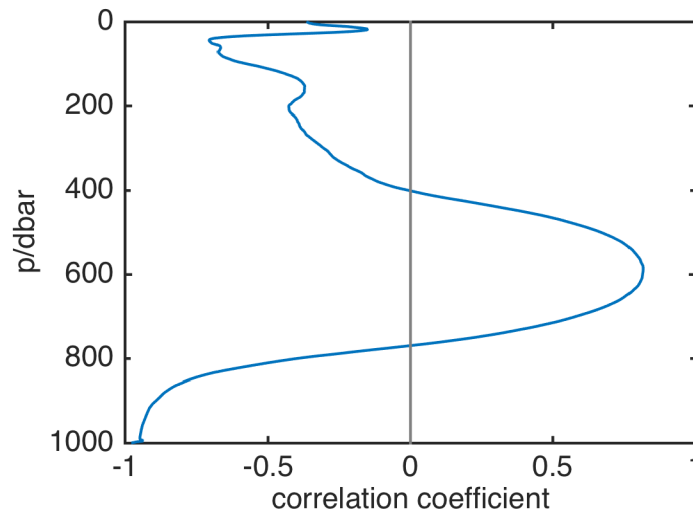


**Figure 3.6 Correlation coefficient between oxygen concentration and potential temperature versus pressure. Data are gridded in pressure. Positive values are for correlated data, negative values for anti-correlated data.**

### 3.4.2 Oxygen Subsurface Increases (OSIs)

Throughout the year, transient patches of water with high  $c(O_2)$  appeared in layer B. These Oxygen Subsurface Increases (OSIs) were deeper than  $z_{\text{eup}}$ . Their  $c(O_2)$  could therefore not be due to *in situ* biological production. Deep parcels of water with high  $c(O_2)$  have been observed in previous studies (e.g. Bairs and Ridgway, 2012, Omand et al., 2015) and predicted by models (Lee and Nurser, 2012). Their origin has been related to fields of sloping isopycnals that outcrop at surface and then steeply reach greater depths below the Ocean Surface Boundary Layer OSBL (Spall, 1995, Lee and Nurser, 2012). The downward isopycnal mixing created by the mesoscale features is in fact able to create injections of surface water at depth (Lévy et al., 2001, Mahadevan et al., 2006). Sometimes these OSIs were just below the OSBL, divided from it by a layer of low  $c(O_2)$  lying in between.

The presence of OSIs was related to the presence of mesoscale heterogeneity also in the present study. This was particularly obvious between the 7<sup>th</sup> and 23<sup>rd</sup> of April. Geographical heterogeneity in the area is visible in the altimetry data (figure 3.7), which show positive sea level anomaly in the northern part of the area and negative sea level anomaly in the southern part. Geographical heterogeneity is also visible in the  $c(\text{O}_2)$  distribution versus depth and time (figure 3.8a).

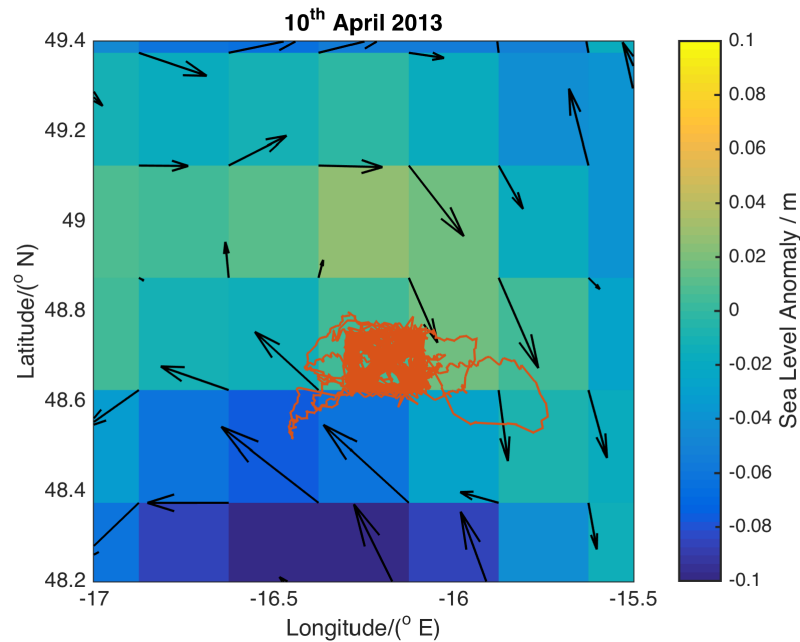


**Figure 3.7** Sea level anomaly on 10<sup>th</sup> April 2013 at the OSMOSIS site from AVISO global allsat product. Velocity field (black arrows) is in  $\text{m s}^{-1}$  and the butterfly surveyed by gliders is in red.

In figure 3.8a it is possible to see that between 7<sup>th</sup> and 10<sup>th</sup> April there was a fast change in  $c(\text{O}_2)$  across the isopycnal  $\sigma=27.11 \text{ kg m}^{-3}$ . This happened every time the glider was at the north side of the butterfly (latitude  $> 48.71^\circ \text{ N}$ , figure 3.8a). This water had higher  $c(\text{O}_2)$  and  $s(\text{O}_2) > 1$ , suggesting the presence of biological production in this water mass, in particular above the isopycnal  $\sigma=27.16 \text{ kg m}^{-3}$ . After 11<sup>th</sup> April, the isopycnal  $\sigma=27.11 \text{ kg m}^{-3}$  was no longer at surface, but OSIs were instead visible below 150 m (figure 3.8b). Each of these OSIs could be identified by an increase of  $c(\text{O}_2)$  at depth along with a weak doming of the isopycnal  $\sigma=27.11 \text{ kg m}^{-3}$ , not sufficient to make it outcrop at surface. These ‘trains’ of OSIs were the result of a single feature sampled several times by the glider as argued for similar features in previous studies (e.g. Omand et al., 2015). The gradual decrease in  $c(\text{O}_2)$  in the core of these OSIs was therefore the sign of oxygen consuming processes such as biological respiration. As an evidence for this assumption, following Omand et al. (2015), the change over time in AOU in the core of OSIs was followed, showing a linear increase over time from negative AOU at the surface to gradually more positive AOU within the OSIs at depth (figure 3.8c). The slope of this

linear increase was used for the calculation of the respiration rate in the feature originating the OSIs, which was estimated as  $1.6 \mu\text{mol kg}^{-1} \text{d}^{-1}$  ( $r^2=0.81$ ).

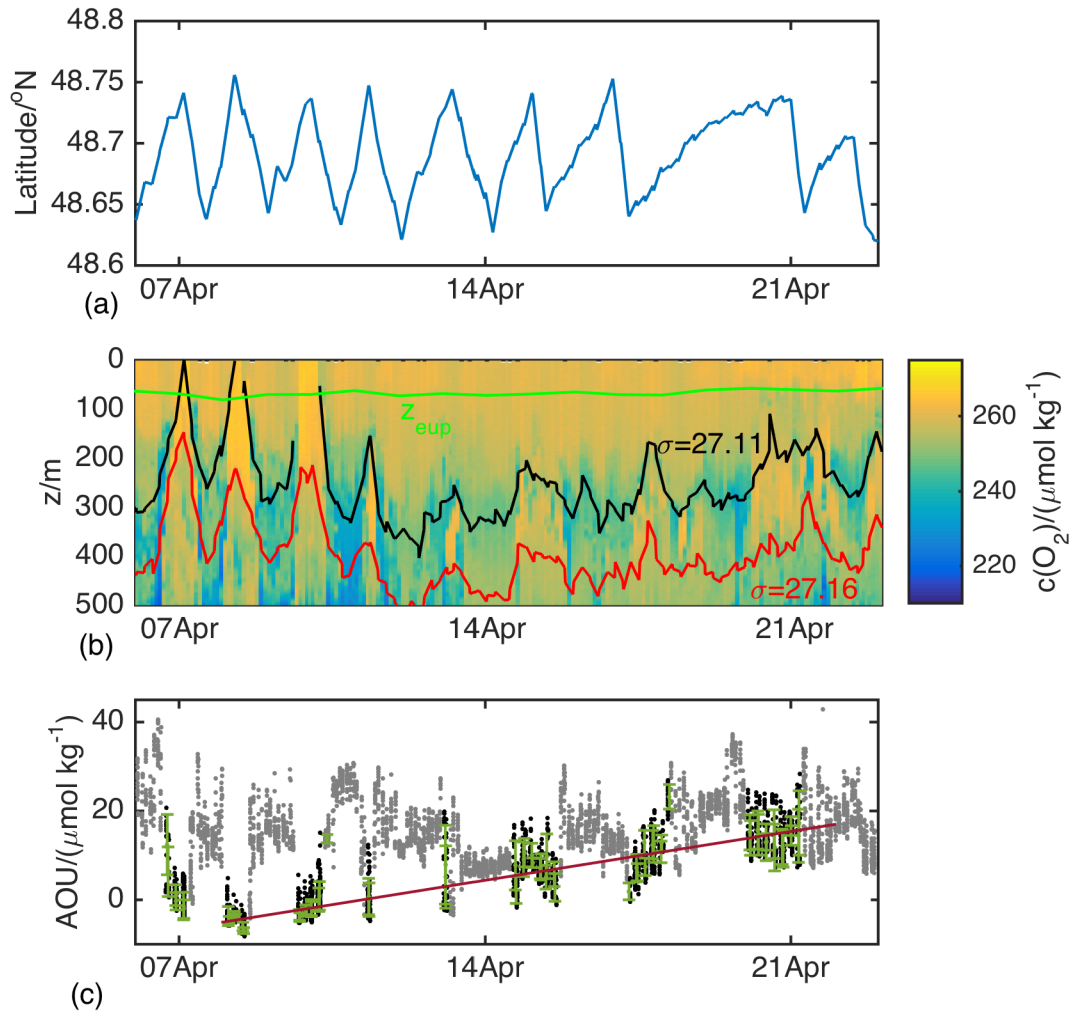


**Figure 3.8** (a) Time series of the position (latitude) of the glider between 6<sup>th</sup> and 23<sup>rd</sup> April; (b) Dissolved oxygen concentration against depth and time in  $\mu\text{mol kg}^{-1}$  with depth of the isopycnals  $\sigma=27.11 \text{ kg m}^{-3}$  in black and  $\sigma=27.16 \text{ kg m}^{-3}$  in red and euphotic depth in green for the same period as in (a); (c) apparent oxygen utilization (AOU) between  $\sigma=27.11 \text{ kg m}^{-3}$  and  $\sigma=27.16 \text{ kg m}^{-3}$  over time for the same period as in panel (a) in grey, AOU in the core of the OSIs in black with associated mean value and standard deviation per each profile in green and fitting regression line showing the linear increase of AOU calculated between 9<sup>th</sup> and 23<sup>rd</sup> April in red.

Another train of OSIs related to a mesoscale eddy was visible between 3<sup>rd</sup> and 9<sup>th</sup> February. The altimetry data showed that during these days the butterfly was crossed by the edge of a cyclonic eddy approaching from the north (figure 3.9). As for the OSIs in April discussed before, a difference in  $c(\text{O}_2)$  was visible across the isopycnal  $\sigma=27.11 \text{ kg m}^{-3}$  when it outcropped at surface and the  $\text{O}_2$ -rich layer was limited at the bottom by the isopycnal  $\sigma=27.16$

$\text{kg m}^{-3}$  (figure 3.10a). In this case the water at the surface, despite its higher  $c(\text{O}_2)$ , was not supersaturated (figure 3.10b). This suggests a weaker biological activity than in April. This weak activity could also explain the virtual absence of variation in AOU over time in the core of these OSIs. AOU remained always below  $20 \mu\text{mol kg}^{-1}$  as can be seen in figure 3.10c.

These two trains of OSIs are taken as evidence of the non-biological origin of the OSIs in layer B. These features are related to geographical heterogeneity and to the subduction of surface water at depth. It would therefore not be appropriate to include these features in the calculation of the biological production carried out in chapters 5 and 6.

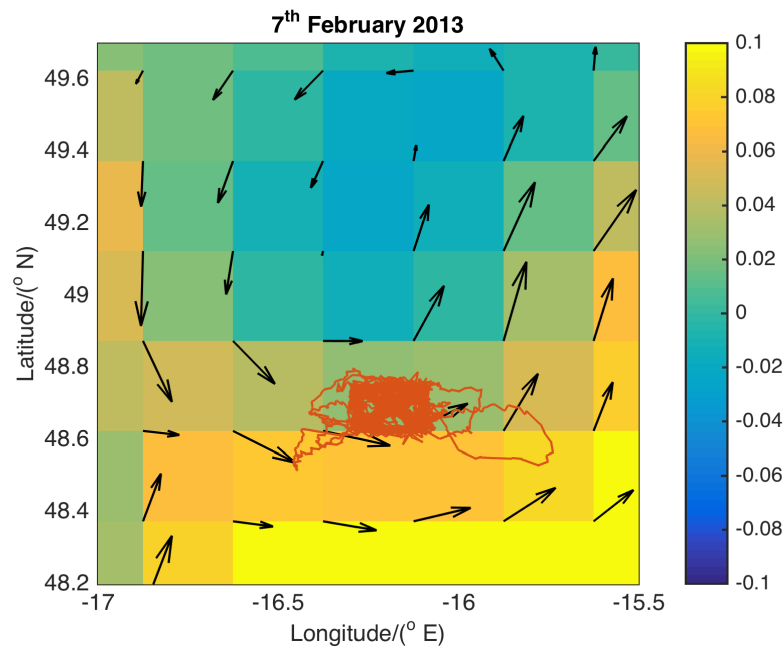


**Figure 3.9** Sea level anomaly on 7<sup>th</sup> February 2013 at the OSMOSIS site from AVISO global allsat product. Velocity field (black arrows) is in  $\text{m s}^{-1}$  and the butterfly surveyed by gliders is in red.

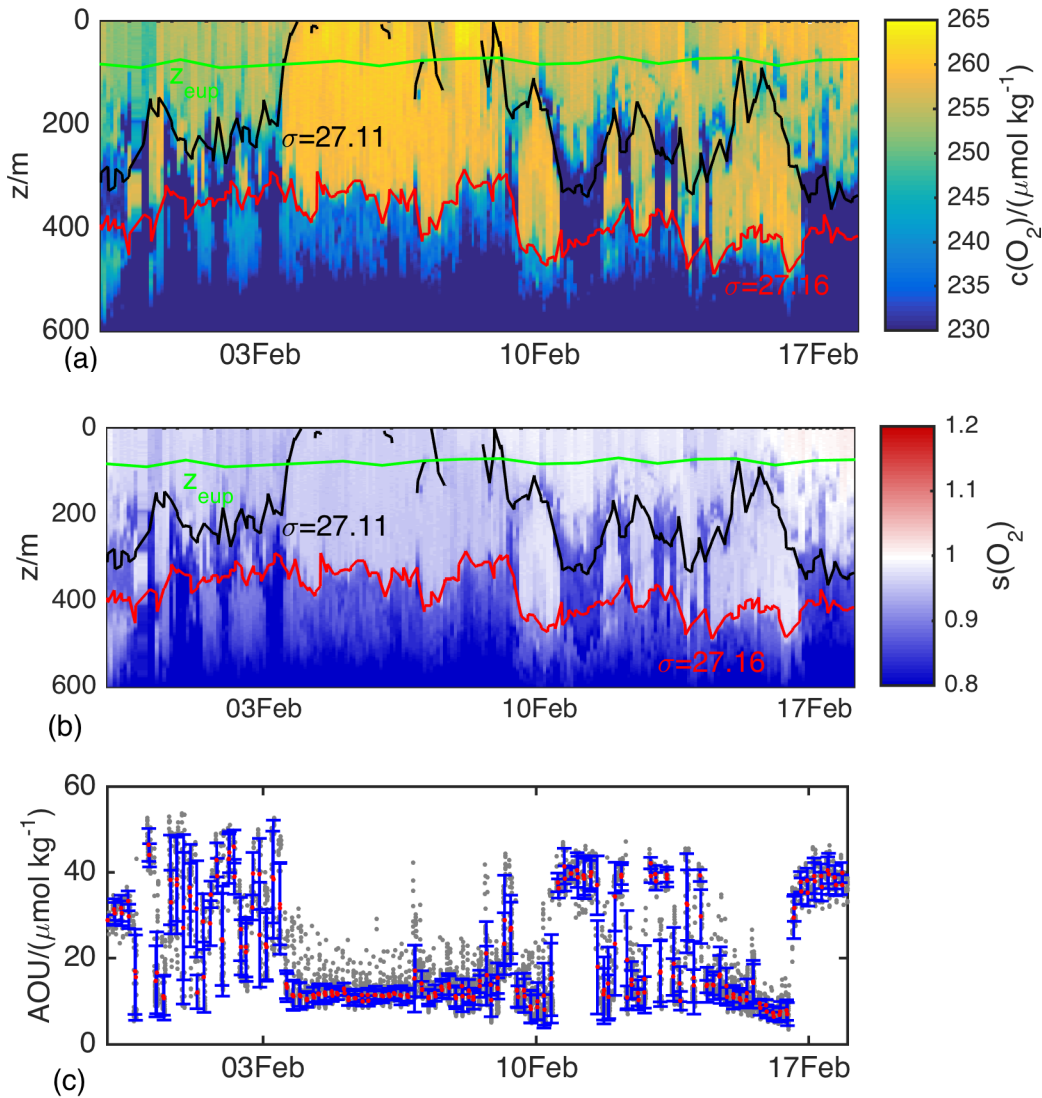


**Figure 3.10** (a) Dissolved oxygen concentration versus depth between January 30<sup>th</sup> and February 18<sup>th</sup> in  $\mu\text{mol kg}^{-1}$  with depth of the isopycnals  $\sigma=27.11 \text{ kg m}^{-3}$  (black),  $\sigma=27.16 \text{ kg m}^{-3}$  (red) and the euphotic depth (green); (b) same as (a) but for oxygen saturation; (c) mean apparent oxygen utilization (AOU) for each profile between  $\sigma=27.11 \text{ kg m}^{-3}$  and  $\sigma=27.16 \text{ kg m}^{-3}$  (red) with standard deviation (blue) and original data-points (grey).

### 3.5 Oxygen in layer C

The third and deepest layer lay below 700 m and had low  $c(\text{O}_2)$ , low  $s(\text{O}_2)$  and high AOU (oxygen-minimum layer). It showed the least variability in  $c(\text{O}_2)$  among the three layers (figure 3.1, Damerell et al., 2016). Part of this layer was occupied by the Mediterranean Outflow Water MOW, which is usually at the lower limit of the water column analysed here. The density range  $27.28 \text{ kg m}^{-3} - 27.5 \text{ kg m}^{-3}$  was identified as the Intermediate Water (IW) (van Aken and de Boer, 1995; van Aken and Becker, 1996, Johnson and Gruber, 2007; Sarafanov et al., 2008,

Stendardo and Gruber, 2012; Stendardo et al., 2015) as defined following Stendardo et al. (2015). According to Sarafanov et al. (2008), IW is a mix of Antarctic Intermediate Water (AAIW), Subarctic Intermediate Water (SAIW) with sporadic mixing of MOW.  $c(\text{O}_2)$  values were lower than  $220 \mu\text{mol kg}^{-1}$  and AOU was higher than  $70 \mu\text{mol kg}^{-1}$ , in the expected ranges for IW according to Stendardo et al. (2015).

The waters were colder than  $9 \text{ }^\circ\text{C}$  and had  $c(\text{O}_2)$  anti-correlated with temperature, as expected for a solubility-driven system (figure 3.6). In these deep waters the AOU and  $s(\text{O}_2)$  were more constant than in layer B (figures 3.2c and 3.2e), while temperature decreased at higher pressures (figure 3.3a). This suggest that in layer C the physical (i.e., temperature) differences among these water masses were more important in the determination of  $c(\text{O}_2)$  than the differences in biological respiration rates and/or age of the water since subduction. This explains why the intraseasonal variability in  $c(\text{O}_2)$  was coupled to the intraseasonal variability in temperature and salinity as shown by Damerell et al. (2016).

Low  $c(\text{O}_2)$  was linked to high salinity ( $> 36.5 \text{ g kg}^{-1}$ ) in waters when density was higher than  $1027.28 \text{ kg m}^{-3}$  (figure 3.11). Damerell et al. (2016) linked this signal of high salinity at high depths with pulses of MOW. Low  $c(\text{O}_2)$  here was not due to higher AOU or lower  $s(\text{O}_2)$ , but to the characteristics of the MOW that has a naturally lower  $c_{\text{sat}}(\text{O}_2)$  due to the high temperatures and salinities in the Mediterranean basin (Sarafanov et al., 2008; Stendardo and Gruber, 2012; Stendardo et al., 2015). Damerell et al. (2016) showed that MOW appeared intermittently throughout the year in the form of filaments in the deep part of the dataset, explaining the appearance of low  $\text{O}_2$  patches at these depths in the whole time series.

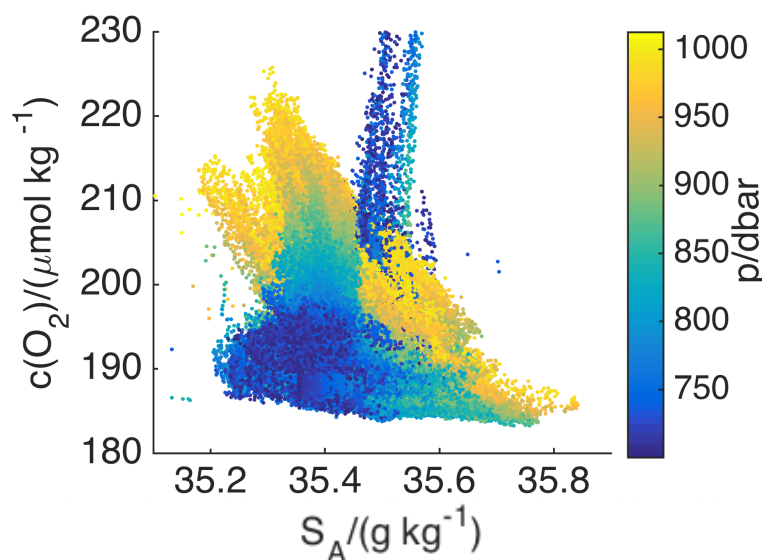


**Figure 3.11 Distribution of oxygen concentration against absolute salinity in layer C (below 700 m) coloured by pressure.**

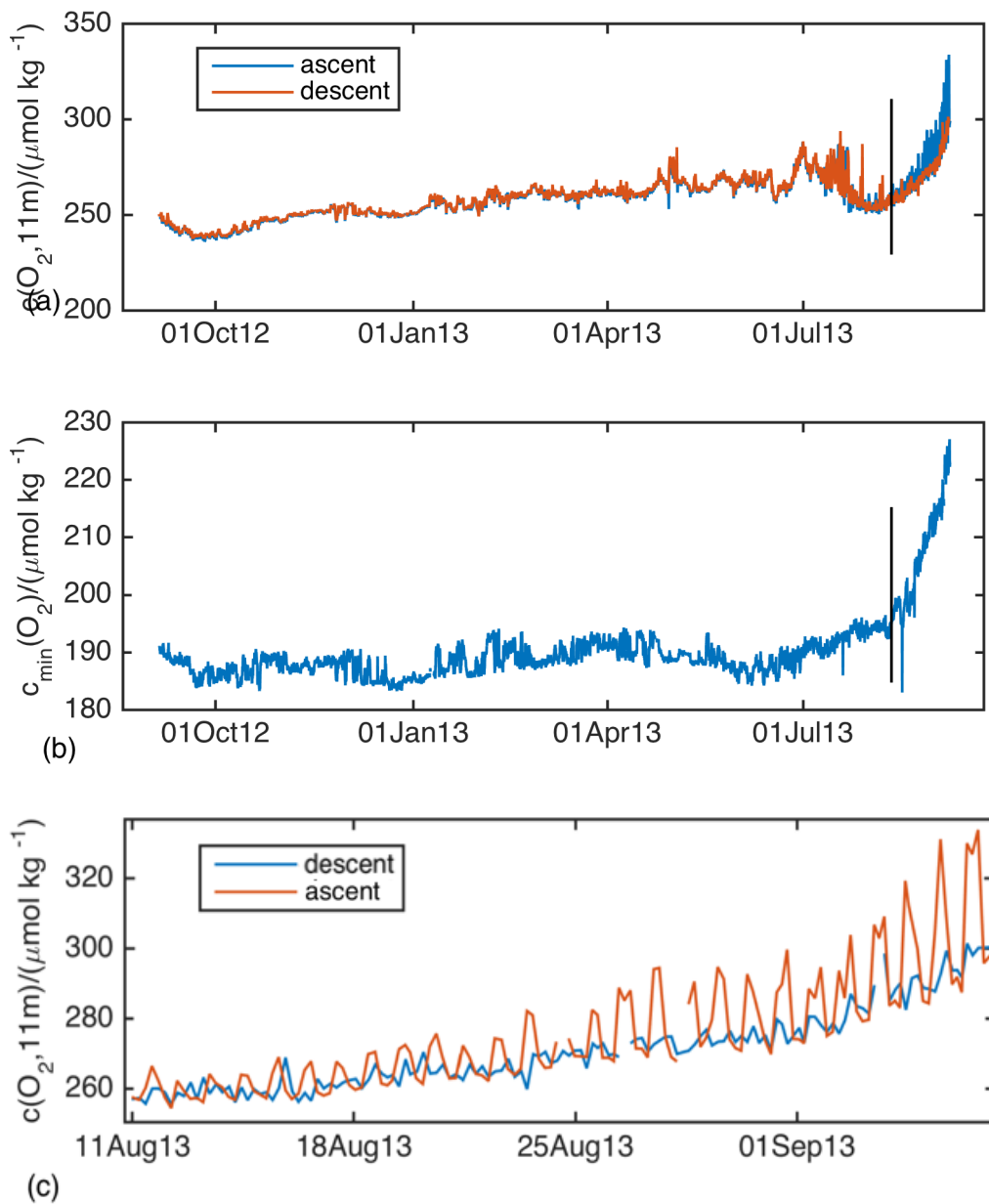
### 3.6 Biofouling

Figure 3.2b shows that  $c(\text{O}_2)$  increased throughout the water column in the last month of the time series (August-September 2013). At the surface,  $c(\text{O}_2)$  reached values that were higher than in the rest of the year, and  $c(\text{O}_2)$  increased also at depths where it had been stable for the rest of the year. A careful analysis of this period was therefore carried out in order to understand the reason for this phenomena.

The presence of high  $c(\text{O}_2)$  values near the surface was considered first. There were actually two phenomena visible at the top of the water column. The first was the anomalous increase in  $c(\text{O}_2)$  that was particularly visible near the deep chlorophyll maximum, where  $c(\text{O}_2)$  reached  $343 \mu\text{mol kg}^{-1}$  (figure 3.2a-b). The second phenomenon was a discrepancy between the data collected during the ascent and the descent of each glider dive. Figure 3.12a shows the concentration at 11 m as measured during descents and ascents. After 11<sup>th</sup> August,  $c(\text{O}_2, 11 \text{ m})$  in the ascents is higher than in the descents. The magnitude of this difference increased over time, especially in the first metres of the water column down to the deep chlorophyll maximum (data not shown). However, during the night  $c(\text{O}_2)$  values measured during the ascents and descents matched again (figure 3.12c).

Sunlight seems therefore to be a possible factor causing this difference. This was possibly related to the different angle that the optode had with respect to the incident light according to the direction of the glider (figure 3.13). The foil was virtually parallel to the surface in the ascents and more angled with respect to the incident light during the descents. This means that the probe was hit directly by the light when the glider went towards the surface, whereas it received less light when it went towards the deep. Sunlight, however, cannot be the only factor of this difference because, otherwise, this phenomenon would have been present throughout the whole time series. There must have been a new factor that, interacting with the foil and with the light, caused the difference between ascents and descents in this part of the year. The increasing mismatch between phases (figure 3.12 a-c) also showed that this new factor had a growing influence on the sensor over time.

In the last month of the dataset there was also an increase in  $c(\text{O}_2)$  in the otherwise overall stable IW, as can be seen analysing minimum  $c(\text{O}_2)$  values per each profile,  $c_{\min}(\text{O}_2)$  (figure 3.13b). Being distant from the surface and from  $z_{\text{eup}}$ , this deep water mass was expected not to vary because it was not exposed to the big perturbations due to air-sea exchange and biological production. After 11<sup>th</sup> August there was a fast and un-interrupted increase of  $c_{\min}(\text{O}_2)$  that reached  $226 \mu\text{mol kg}^{-1}$ . Considering that this sharp increase in  $c(\text{O}_2)$  at depth began at the same time as the discrepancy between ascents and descents (on 11<sup>th</sup> August), these events were considered to be caused by the same factor.



**Figure 3.12 (a) Oxygen concentration at the 11 m horizon during the ascending phase (blue) and descending (red) phase of glider dives; (b) Minimum oxygen concentration (if measured within the boundaries of Intermediate Water). In both (a) and (b) the black vertical line marks the date of August 11<sup>th</sup>, when the bias due to biofouling is considered to start formally. (c) expanded section from panel (a) during the biofouling-affected period showing the difference between ascents and descents that mismatched during daytime and matched again at night.**

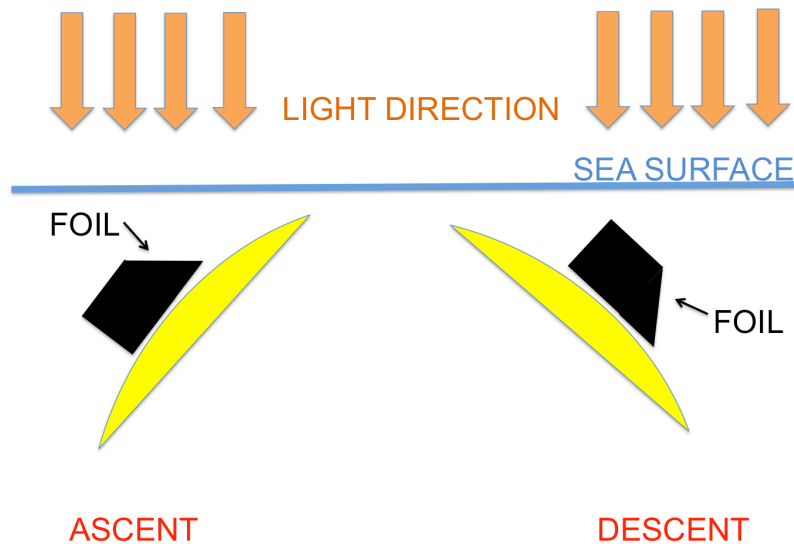


**Figure 3.13 Scheme of the position of the foil of the optode with respect to the surface and to the incident light in the ascents and descents of each dive**

Biofouling of the foil was the most likely factor behind the phenomena just described. It probably developed on top of the optode foil after the end of June, when  $c(\text{Chl } a)$  at the top of the water column was higher than in the rest of the year (figure 3.3h). This is usually a proxy for the presence of high phytoplankton biomass, which makes plausible that phytoplankton started to grow into a biofilm on the foil. The algae, producing more  $\text{O}_2$  when exposed to direct and stronger light (during ascents), would have caused the difference between profiles in different phases.  $\text{O}_2$  produced by the biofilm would have given high  $c(\text{O}_2)$  readings not reflecting the actual  $c(\text{O}_2)$  in the water column. Furthermore, the amount of gas released by the biofilm would have been proportional to its biomass – the growth of the biofilm would explain why there was an increase of the difference between phases, of  $c(\text{O}_{2,\text{surface}})$  and of  $c_{\text{min}}(\text{O}_2)$ . When the glider was recovered, all the sensors were covered by a green biofilm (Stephen Woodward, personal communication). The data collected after 11<sup>th</sup> August are therefore considered not valid for the scope of this study and are not analysed any further in the following chapters.

Biofouling is a well-known problem in oceanographic measurements (Tosteson et al., 1982; Manov et al., 2004; Delauney et al., 2010). It has been advocated in previous studies to be the cause of drift in optical sensors mounted on both moorings (e.g., Kinkade, 2001; Manov et al., 2004; Heupel et al., 2008) and gliders (e.g., Nicholson et al., 2008; Cetinić et al., 2009; Krahnmann et al., 2011). The interest of the scientific community in new solutions that can reduce the biofouling (e.g., Manov et al., 2004; Whelan and Regan, 2006; Delauney et al., 2010; Lobe et al., 2010) is clear evidence of the importance of this problem for oceanographic observations. The research is particularly active in the glider-users community since the biofouling can also affect the flight performance of these vehicles (Krahnmann et al., 2011; Moline and Went, 2011). The analysis of the different  $c(\text{O}_2)$  between ascents and descents could

be a proxy to identify the growth of a biofilm on the optode foils even before any correction or calibration.

### 3.7 Conclusions

In this chapter the variability of  $c(\text{O}_2)$ ,  $s(\text{O}_2)$  and AOU measured over the year September 2012 – September 2013 at the PAP site has been related with the other parameters measured simultaneously by the glider (chlorophyll *a* fluorescence, density). Biofouling covering the sensor has been identified in the last month of the mission (since 11<sup>th</sup> August) leading to anomalous values of  $c(\text{O}_2)$  in the whole water column. Data affected by biofouling have been disregarded.

The spectra of variability in temperature, salinity and  $c(\text{O}_2)$  in the water column have shown the presence of three layers influenced by different dynamics. The layer in contact with the atmosphere (layer A) had strong seasonality, being undersaturated from the end of October to mid-February and with a series of supersaturation events from mid-February to the end of the mission. The results show that two common ideas about the OSBL are wrong: it is not always close to saturation in winter time and the spring bloom is not a unique event. These findings suggest the need for future investigation in the upper water column with similar frequency to better constrain the undersaturation at the surface and to understand the triggering factors of the little blooms. Different relationships between the amount of chlorophyll *a* and the oxygen saturation in different periods of the year suggest changes in community or metabolic activity of the phytoplankton at different stages of the bloom.

The layer in the middle of the water column (layer B) was characterised by high variability in salinity, temperature and  $c(\text{O}_2)$ . This variability is linked by Damerell et al. (2016) to mesoscale features. Oxygen Subsurface Increases occurring in this layer are shown to be caused by the passage of mesoscale features at the surface.

The deepest layer (layer C) was the  $\text{O}_2$ -poor layer, identified as the IW described by Stendaro et al. (2015) with intrusions of underlying MOW. As expected, this water mass was the most stable, had low  $c(\text{O}_2)$  and high AOU. The presence of MOW in the IW horizon has been linked to low  $c(\text{O}_2)$  and to high salinity, confirming the appearance of MOW filaments in the area as shown by Damarell et al. (2016) with an independent parameter, namely  $c(\text{O}_2)$ .



# Chapter 4

## Mixed and mixing layer

In this chapter the depth of the surface boundary layer is calculated based on oxygen concentration profiles. The distinction between the depth of the mixed and mixing layer is attempted through the analysis of the differences between estimates defined by different parameters and thresholds. The importance of this distinction for the calculation of productivity carried out in the following chapters is shown through the analysis of a little bloom happening at the end of February 2013.

### 4.1 Introduction

The water in the ocean surface boundary layer (OSBL) at the top of the ocean is well mixed by the turbulence induced by surface winds (Lukas and Lindstrom, 1991; Brainerd and Gregg, 1995, Castro-Morales and Kaiser, 2012, Yoshikawa, 2015), by surface gravity waves and the loss of buoyancy due to the water-cooling (Sutherland et al., 2014). This layer has been historically called the surface “mixed layer” (ML) because parameters such as temperature, salinity and solute concentrations are quasi uniform due to the homogenising action of the mixing turbulence (de Boyer Montégut et al., 2004; Dong et al., 2008; Castro-Morales and Kaiser, 2012).

The best way to measure the thickness of the OSBL would be the direct measurement of the vertical turbulence that mixes the water, but detailed turbulence data are difficult to obtain due to the small signal of the vertical turbulence when compared to the big non-turbulent motion such as the one from surface and internal waves (D’Asaro, 2014). Microstructure profilers are also expensive, difficult to use and data are difficult to analyse. An operational definition of the boundary layer based on turbulence thresholds is also missing, which is a major obstacle for the creation of a robust protocol to use (Franks, 2014). Temperature (Kara et al., 2000), density (Lukas and Lindstrom, 1991, de Boyer-Montegut, 2004; Damerell et al, 2016) and oxygen concentration ( $c(\text{O}_2)$ ), Castro-Morales and Kaiser, 2012) have therefore been used as proxies for  $z_{\text{mix}}$  calculations. These calculations assumed that the extent of the homogeneity and active turbulence are linked by a causal correlation: the parameter in the water are constant when there is active mixing. The thickness of the boundary layer has been assumed therefore to be the depth  $z_{\text{mix}}$  where parameters start to deviate from the overlying homogeneity creating a

gradient (“cline”). The threshold over which this deviation from homogeneity is considered significant changes according to the system analysed, the parameter used as proxy and the resolution of measurements.

$z_{\text{mix}}$  is important in oceanographic studies and climatological models because it defines the amount of water that has direct interaction with the atmosphere at any given time (Dong et al., 2008). It is useful to calculate the inventories involved in the estimation of air-sea fluxes of momentum, heat, moisture and gases (Dong et al., 2008), for the quantification of the ocean interior ventilation through subduction of surface water masses (Le Quéré et al., 2003; Cisewski et al., 2008) and for the assessment of the magnitude of net community production happening at the top of the water column (see chapter 5). However, Brainerd and Gregg (1995) pointed out a key distinction in the causal relation between turbulence and homogeneity, showing that  $z_{\text{mix}}(\text{O}_2)$  had been (and is still) used to estimate the thickness of two distinct layers. They recognised in fact the presence of a “mixing layer” (XL) where the water is actively mixed by the turbulence at the moment of the measurements along with a “mixed layer” (ML) in which the water has been mixed in the recent past. Despite many studies assuming XL=ML, the difference between the two has been identified as the focus point to understand physical and biogeochemical dynamics related to the amount of turbulent energy acting in the water.

The problem of which layer (XL or ML) is described by  $z_{\text{mix}}(\text{O}_2)$  in each different study is related to which factors are influencing the parameter used for the calculation, to how strict is the definition of ‘homogeneity’ used every time (i.e., sensitivity), to which criterion is used in each protocol and to the stage of the annual cycle in which the analysis is carried out. In this respect, de Boyer Montégut et al. (2004) pointed out how the lack of a universally accepted proxy for  $z_{\text{mix}}$  has led to the use of several parameters, thresholds and protocols in the literature. This has created artificial heterogeneity in  $z_{\text{mix}}$  estimates, making the comparison among different papers difficult. Understanding in the first instance what each study is actually estimating with its  $z_{\text{mix}}$  has therefore become a crucial step for the correct use of this parameter in relation to the different processes happening in the water (Noh and Lee, 2008).

The difficult comparability when different parameters are used arises from the time scale with which different factors influence different quantities. As an example, heat is exchanged faster than gases (Fairall et al., 2000) and each gas has a specific solubility, with relative faster or slower air-sea fluxes (Castro-Morales and Kaiser, 2012). Furthermore gas as  $\text{O}_2$  and  $\text{CO}_2$  can be produced or consumed by the plankton community.  $z_{\text{mix}}$  calculated considering temperature or gas concentrations are therefore different, especially in regimes of low turbulence when the water is warming up or when there is high and patchy biological activity in the water. Therefore, in this example, the comparison between the two estimates is actually meaningless.

The choice of the criteria used for the  $z_{\text{mix}}$  computation is also a big source of variability that complicates the comparison. Some papers have focused on the shape of the profiles with a gradient-based method (Lukas and Lindstrom, 1991), looking for the sharpest gradient as the lower limit of the boundary layer. Other studies have instead used a difference-based method (Levitus, 1982) analysing the deviation of a parameter from a reference value measured near the surface. In the latter case, the sensitivity of the protocols used in different studies is also a problem: lower thresholds assume a strict homogeneity that is typical of the XL, while higher thresholds partially relax the assumption of homogeneity making  $z_{\text{mix}}$  a proxy of ML depth. This obviously complicates even more the comparison of results.

In this work  $z_{\text{mix}}$  is estimated based on  $c(\text{O}_2)$  using different thresholds. The relevance of this estimate as a proxy for XL rather than ML is analysed comparing it with  $z_{\text{mix}}$  defined by temperature/density and chlorophyll  $a$  concentration (from chlorophyll  $a$  fluorescence) for the same dataset. The results are then compared in an attempt to describe the coupling and decoupling dynamics between XL and ML and to decide the most appropriate  $z_{\text{mix}}$  to use for the productivity calculations used in the following chapters. Considering that gliders collect data with higher frequency than many other platforms (e.g. Argo floats and cruises), an experiment is also run to investigate how the  $z_{\text{mix}}$  would appear if it was sampled at lower frequencies ( $\leq 1$  profile per day).

## 4.2 Methods

### 4.2.1 Calculation of ocean surface boundary layer depth

The calculation of  $z_{\text{mix}}(\text{O}_2)$  was performed for each of the 4035  $c(\text{O}_2)$  profiles of the OSMOSIS time series. A difference-based criterion was preferred to a gradient-based one. This decision follows the conclusions of Dong et al. (2008) who show how changes in resolution along the profile, spikes and noisiness of the sensor can bias the output of gradient-based criterion, resulting in values of  $z_{\text{mix}}$  that are too shallow. In this study, in the first metres of the water column the resolution of oxygen profiles is quite variable depending on the speed of the glider and some spikes might still be present despite the despiking process described in chapter 2. The top part of the profile is therefore not “well-resolved” as needed for the gradient-based criteria (Brainerd and Gregg, 1995; Cisewski et al., 2008).

The first step of  $z_{\text{mix}}(\text{O}_2)$  computation was the calculation of the reference concentration ( $c_{\text{ref}}(\text{O}_2)$ ), considered an estimate of the homogeneous  $c(\text{O}_2)$  within the OSBL. The concentration at the depth of 5 m was chosen as reference. This depth is shallower than the one (10 m) chosen in previous studies (i.e. de Boyer Montégut et al., 2004, Castro-Morales and Kaiser, 2012), but it was chosen considering the availability of high-resolution data all the way to the surface. This

depth was picked as a compromise between the need to use a value as close to the surface as possible and the noisiness of the very first metres of the water column (Brainerd and Gregg, 1995, Castro-Morales and Kaiser, 2012). The noisiness in near-surface measurements in the present dataset is shown by the frequency of spikes in the profiles, mostly distributed above 10 m (figures 2.18b-d-f) with a very rapid increase above 5 m.

$c_{\text{ref}}(\text{O}_2)$  was obtained by linear interpolation between the  $c(\text{O}_2)$  immediately above and below 5 m. In case no interpolation at 5 m was possible because the shallowest data-point of the profile was deeper ( $z_1 > 5$  m), then the first depth below the shallowest data-point,  $c(\text{O}_2, z_1)$ , was used. If  $z_1 > 10$  m,  $c_{\text{ref}}(\text{O}_2)$  and  $z_{\text{mix}}$  were not computed. The shallowest possible value for  $z_{\text{mix}}$  is therefore assumed to be between 5 and 10 m at any time.

$c(\text{O}_2)$  profiles were smoothed using the algorithm ‘lowess’ built into Matlab ‘smooth’ function. The smoothing was meant to eliminate possible individual data-points whose values were significantly over the  $c(\text{O}_2)$  variability of all the other data-points within OSBL. This was done assuming that single points could not be considered the real signal of a significant deviation from  $c_{\text{ref}}(\text{O}_2)$ . The smoothing decreased therefore the variability of the values within OSBL, lowering the threshold that constrains the homogeneity increasing the sensitivity of the calculation. The algorithm ‘lowess’ was preferred to its version ‘rlowess’ because it performed better in preserving the shape of the profile after the smoothing both in the middle of the column (figure 4.1a-b) and at the top of the water column when gradients are near the surface (figure 4.1c-d).

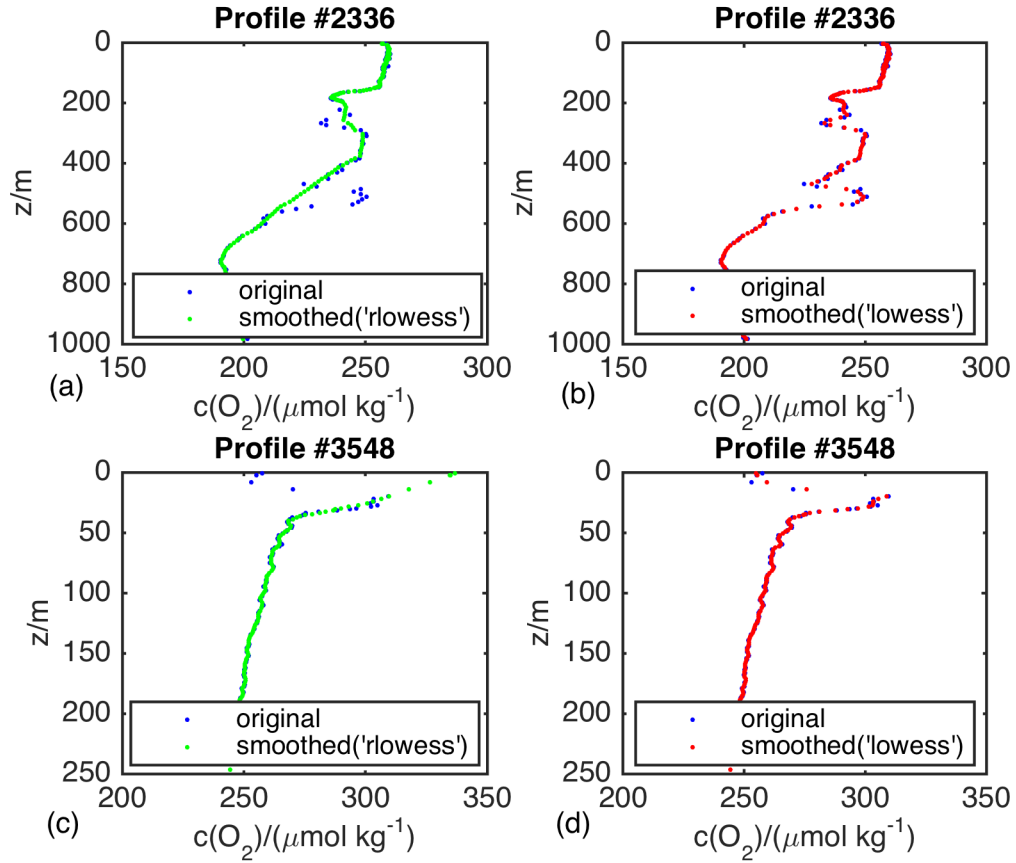


**Figure 4.1 Comparison between smoothed versions of profiles number 2336 (a-b) and 3548 (c-d) and the original profiles. The ‘lowess’ algorithm (red dots in b-d) matches the shape of the original (blue dots) better than its robust version ‘rloess’ (green dots in a-c).**

Smoothed  $c(\text{O}_2)$  profiles and  $c_{\text{ref}}(\text{O}_2)$  were used for the calculation of the percentage difference between  $c(\text{O}_2)$  and  $c_{\text{ref}}(\text{O}_2)$ ,  $\Delta c/c_{\text{ref}}$ , measured as in equation 4.1.

$$\Delta c/c_{\text{ref}} = \frac{(c(\text{O}_2) - c_{\text{ref}}(\text{O}_2))}{c_{\text{ref}}(\text{O}_2)} \times 100 \quad (4.1)$$

The shape of  $\Delta c/c_{\text{ref}}$  profiles was visually checked and a group of 40 profiles with an obvious OSBL was selected. These profiles are shown in figure 4.2 and their OSBL defined visually is marked with a horizontal black line. The mean and standard deviation of  $\Delta c/c_{\text{ref}}$  for each of these profiles were then measured in the surface homogeneous layer to estimate the variability of the values (figure 4.3). Data-points shallower than 5 m were not considered because they would not have been taken into account in the computation of  $z_{\text{mix}}(\text{O}_2)$  as shallower than the reference depth.

Considering that the maximum variability in the OSBL of these 40 profiles was  $(0.24 \pm 0.1) \%$  (see figure 4.3), using a precautionary approach, the value of  $\Delta c/c_{\text{ref}} = 0.5 \%$  was used as

the lowest and most sensitive possible threshold. This value was considered above the variability within the homogeneous OSBL of the 40 selected profiles. This threshold is also in accordance with the one used for similar calculations by Castro-Morales and Kaiser (2012). Lower thresholds would pick random  $z_{\text{mix}}(\text{O}_2)$  not corresponding to a significant difference from  $c_{\text{ref}}(\text{O}_2)$ . For each profile, the shallowest depth at which  $\Delta c/c_{\text{ref}}$  exceeded 0.5% was considered to be  $z_{\text{mix}}(\text{O}_2)$ .

Profiles whose  $z_{\text{mix}}(\text{O}_2)$  had not been calculated because their  $z_1 > 10$  m were re-checked. For each of these profiles it was assumed that if  $z_1$  was shallower than  $z_{\text{mix}}(\text{O}_2)$  calculated for both the previous and the following profile, then  $z_1$  was also above  $z_{\text{mix}}(\text{O}_2)$  of its own profile. In this case,  $c(\text{O}_2, z_1)$  was used as  $c_{\text{ref}}(\text{O}_2)$  and the  $z_{\text{mix}}(\text{O}_2)$  was measured.

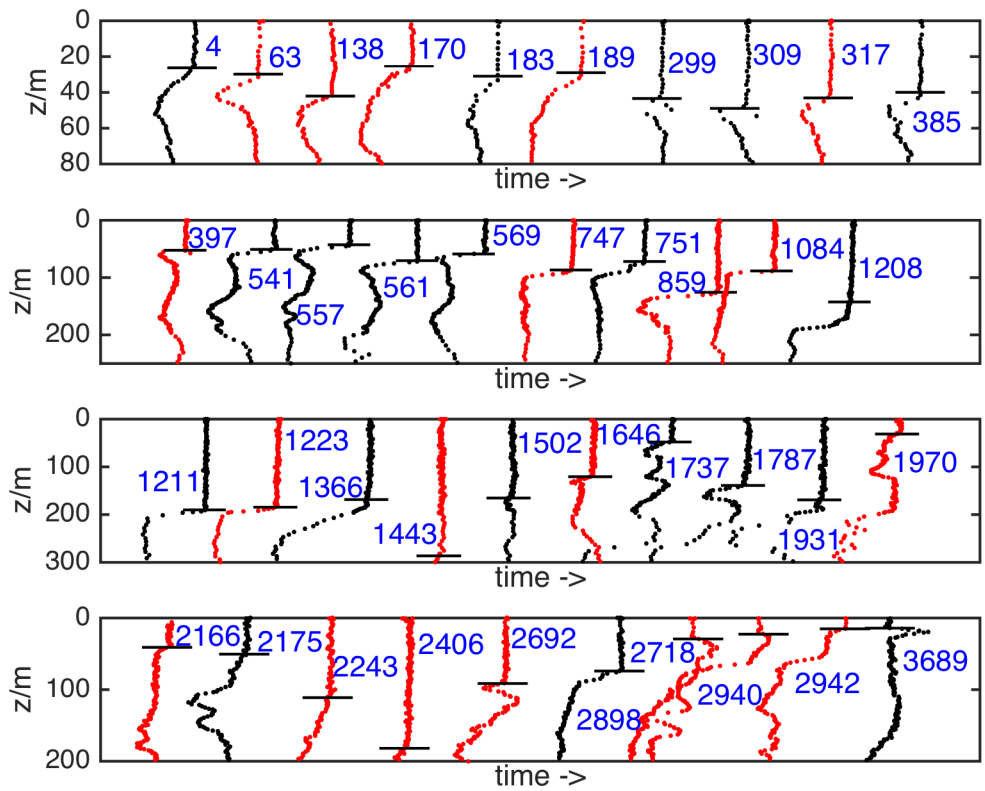


**Figure 4.2** Top 200 m of the 40 oxygen concentration profiles used for the calculation of the variability of values within the surface boundary layer. The depth of the layer (black horizontal lines) was visually identified as the maximum depth of the homogenous values. Black profiles are measured during the night and red profiles during the day.

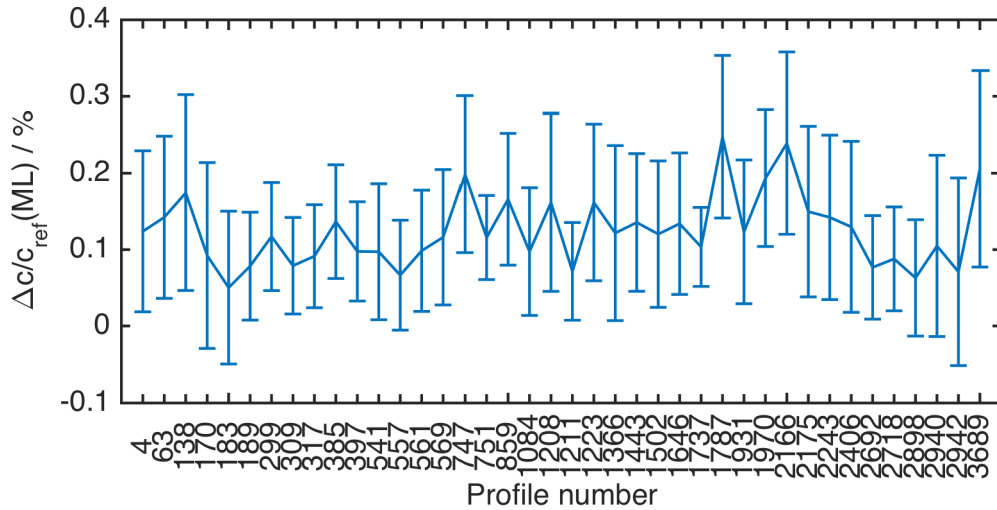


**Figure 4.3 Mean difference between oxygen concentrations and oxygen concentration reference within the ocean surface boundary layer of the 40 selected profiles. Error bars show  $\pm$  standard deviation.**

#### 4.2.2 Simulation of lower frequency

In order to evaluate how the frequency of sampling affects the estimates of the thickness of OSBL over time,  $z_{\text{mix}}$  time series was sub-sampled considering one profile measured at midnight every  $n$  days (with  $n = 1, 3, 5, 7$  and  $10$  d). Starting on midnight of day 1 ( $t_1$ ), the closest  $z_{\text{mix}}$  estimates to  $t_1+n, t_1+2n, \dots, t_1+kn$  were considered during the subsampling. The sub-dataset for each  $n$  were then plotted on top of the original time series to analyse their grade of agreement. The coefficient of correlation and the root mean square difference between the subsample and the original time series was also measured.

### 4.3 Results and discussion

#### 4.3.1 Smoothing process and oxygen reference concentration

The value of  $c_{\text{ref}}(\text{O}_2)$  per each profile after the smoothing process was obtained through interpolation and corresponds to the  $c(\text{O}_2)$  at the shallowest depth possible between 5 m and 10 m. The depth used for the calculation of  $c_{\text{ref}}(\text{O}_2)$  was 5 m for the vast majority of profiles (94 % of the total). For 76 profiles (1.8% of the total)  $c_{\text{ref}}(\text{O}_2)$  was not calculated because the shallowest oxygen data-point was deeper than 10 m.

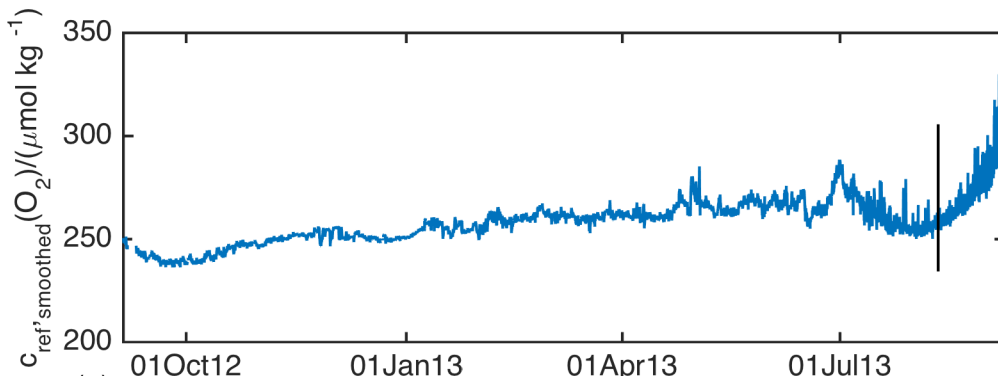


**Figure 4.4 Oxygen reference concentration used as proxy for the oxygen concentration in the homogeneous ocean surface boundary layer.**

### 4.3.2 Mixed layer calculation

$z_{\text{mix}}(\text{O}_2, 0.5\%)$  was measured per each profile as the depth where  $\Delta c/c_{\text{ref}}$  exceeded the value of 0.5% in the smoothed profile.  $z_{\text{mix}}(\text{O}_2, 0.5\%)$  values were visually analysed with respect to the shape of random profiles throughout the year to check the performance of this method in estimating the actual depth reached by the homogeneity. During the autumn,  $z_{\text{mix}}(\text{O}_2, 0.5\%)$  in most of the profiles corresponds to the seasonal oxycline (an example in figure 4.5a). As shown by Damerell et al. (2016), at this time of the year there is a destabilization of the column due to the heat loss at the sea surface. This leads to turbulence that mixes fully the water above the oxycline. Here XL equals ML and their depth is well described by  $z_{\text{mix}}(\text{O}_2, 0.5\%)$ . There are also autumn profiles in which  $z_{\text{mix}}(\text{O}_2, 0.5\%)$  is shallower than the seasonal oxycline (figure 4.5b). The homogeneity is maintained in the top metres by the turbulence, while  $c(\text{O}_2)$  gradually changes below. In these profiles the seasonal oxycline is the remnant of past stronger turbulence mixing and can therefore be assumed to be the ML. In these cases  $z_{\text{mix}}(\text{O}_2, 0.5\%)$  represents only XL. This distinction between XL and ML is more obvious and more frequent during the winter and early spring, when the seasonal oxycline is deeper and less sharp. In this period  $z_{\text{mix}}(\text{O}_2, 0.5\%)$  often picks up the signal of shallower and smaller oxyclines above the seasonal one (figure 4.5d). Sometimes this is due to the intrusion of water with a different  $c(\text{O}_2)$  that does not mix up because of the low turbulence. Nevertheless, there are profiles in which  $z_{\text{mix}}(\text{O}_2, 0.5\%)$  reaches the seasonal oxycline when turbulence is strong (figure 4.5c). Also in autumn,  $z_{\text{mix}}(\text{O}_2, 0.5\%)$  seems to track the depth reached by the active mixing (XL) while the seasonal oxycline is considered to be the trace of the recent-past deepest mixing events (ML). During the late spring and the summer, when a subsurface oxygen maximum is developed,  $z_{\text{mix}}(\text{O}_2, 0.5\%)$  describes the thickness of the thin and homogeneous layer interposed between the surface and the underlying oxygen maximum (figure 4.5e).  $z_{\text{mix}}(\text{O}_2, 0.5\%)$  is then considered a proxy of both XL and ML. There are however profiles with shallower oxyclines in this period as well (figure 4.5f) in which

there seems to be a difference between XL and ML. Taking in account these observations,  $z_{\text{mix}}(\text{O}_2, 0.5\%)$  can be considered to be a good proxy of XL depth throughout the year.

In some profiles  $z_{\text{mix}}(\text{O}_2, 0.5\%)$  did not correspond to any cline. In these profiles the water above the main (seasonal) oxycline was stratified with gradients that reached the surface (figure 4.5g-h). In this case the water was never homogeneous and therefore a XL was absent.  $z_{\text{mix}}(\text{O}_2, 0.5\%)$  was then a mere artefact and did not define any actual feature in the column. This situation is particularly frequent when the seasonal oxycline is deep (below  $\sim 100$  m, figure 4.5g), but gradients above the seasonal oxycline can be found throughout the year also when the seasonal oxycline is closer to the surface (figure 4.5h). In this case  $z_{\text{mix}}(\text{O}_2, 0.5\%)$  should be set to the depth of  $c_{\text{ref}}(\text{O}_2)$ , which is the minimum value allowed by assumptions. Despite this might seem a bias to the calculation, in section 4.3.5 is discussed the evidence that  $z_{\text{mix}}(\text{O}_2, 0.5\%)$  is a significant parameter even in these fully stratified profiles.

After the calculation of  $z_{\text{mix}}(\text{O}_2)$ , profiles starting below 10 m were re-analysed. For 25 of these, the depth of the shallowest  $c(\text{O}_2)$  measured ( $z_1$ ) was found to be shallower than  $z_{\text{mix}}(\text{O}_2)$  of the previous and following profiles. This allowed the calculation of their  $z_{\text{mix}}(\text{O}_2)$  using  $c(\text{O}_2, z_1)$  as  $c_{\text{ref}}(\text{O}_2)$ .

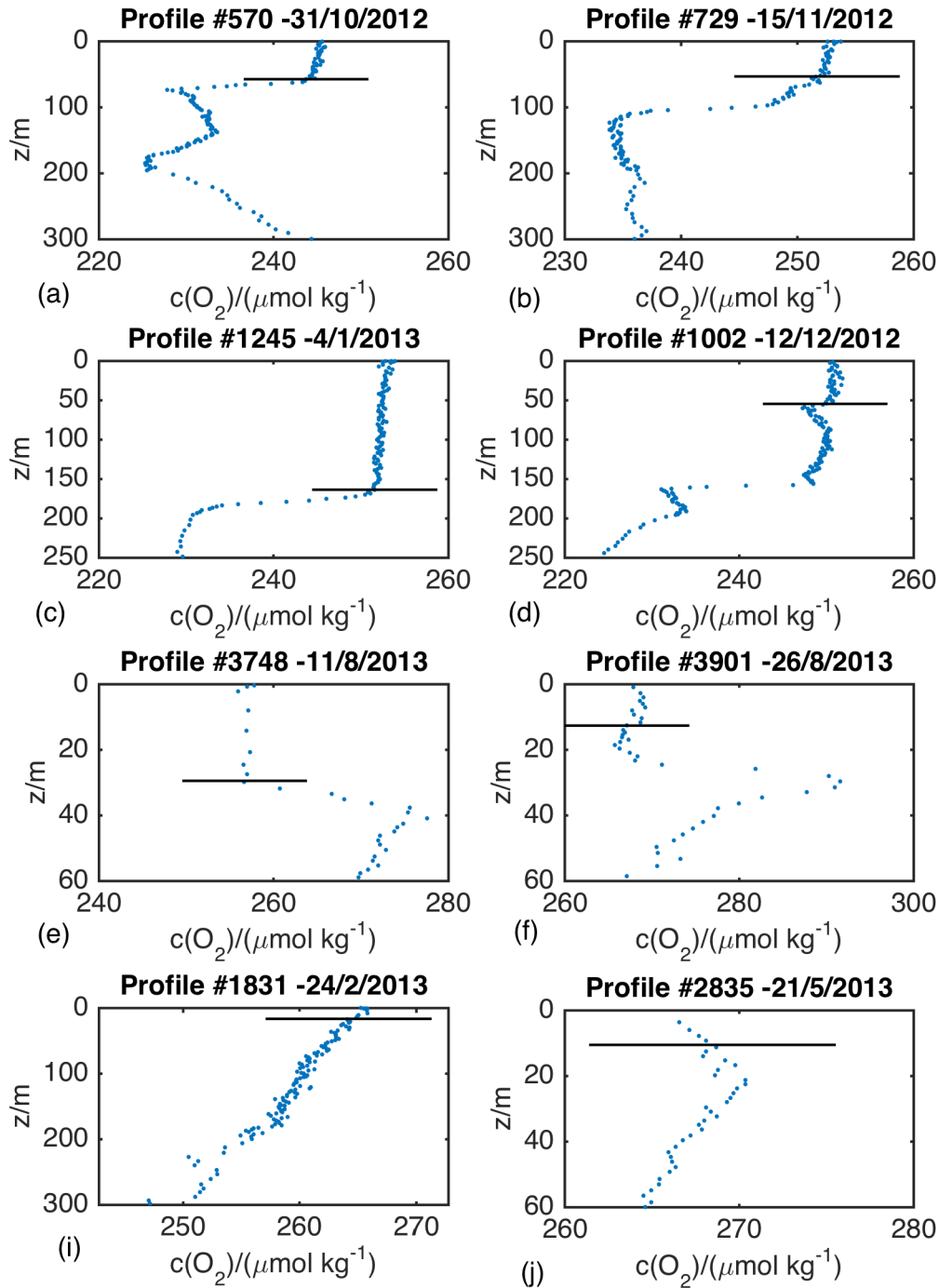


**Figure 4.5** Examples of profiles with their OSBL depth defined by oxygen concentration with the threshold of 0.5% (black horizontal lines). (a-f) shows profiles in which the homogeneous OSBL is obvious during the autumn (a-b), winter and early spring (c-d), late spring and summer (e-f). Panels (i-j) show examples of profiles with stratification spanning all the way to the surface. Please note different x and y axes for each panel.

### 4.3.3 Comparison between 0.5% and higher thresholds

As a test to check the sensitivity of the 0.5 % threshold,  $z_{\text{mix}}(\text{O}_2)$  was recalculated increasing the significant difference to 0.75 %, 1 %, 1.5 % and 2 % and using the original profiles. The results were then compared among each other and with  $z_{\text{mix}}(\text{O}_2, 0.5 \%)$ . The analysis of individual profiles showed that the thresholds of 1 % did not have a real meaning because in the majority of cases  $z_{\text{mix}}(\text{O}_2, 0.75 \%)$  and  $z_{\text{mix}}(\text{O}_2, 1 \%)$  (red and light blue horizontal lines in figure 4.6 respectively) did not appear to highlight any meaningful feature in the majority of the profiles, apart from when they agreed with other thresholds.  $z_{\text{mix}}(\text{O}_2, 2 \%)$  was instead almost always associated with the seasonal oxycline. This feature is a permanent oxycline present in the area throughout the season and that changes over long time-scale (weeks to months). The seasonal oxycline was sometimes deeper than the depth at which homogeneity stopped (green horizontal lines in figure 4.6).  $z_{\text{mix}}(\text{O}_2, 2 \%)$  was therefore considered not sensitive enough.  $z_{\text{mix}}(\text{O}_2, 1.5 \%)$  was instead useful to mark real features in many profiles (dark blue horizontal line in figure 4.6). In particular,  $z_{\text{mix}}(\text{O}_2, 1.5 \%)$  often lay at the depth of the seasonal oxycline even when  $z_{\text{mix}}(\text{O}_2, 0.5 \%)$  was shallower, but was more sensitive than 2 % to pick up where the actual homogeneity ended. A couple of profiles whose different thresholds gave significantly different  $z_{\text{mix}}(\text{O}_2)$  and that were used to decide which threshold had to be considered more meaningful than others are shown in figure 4.6a-b.

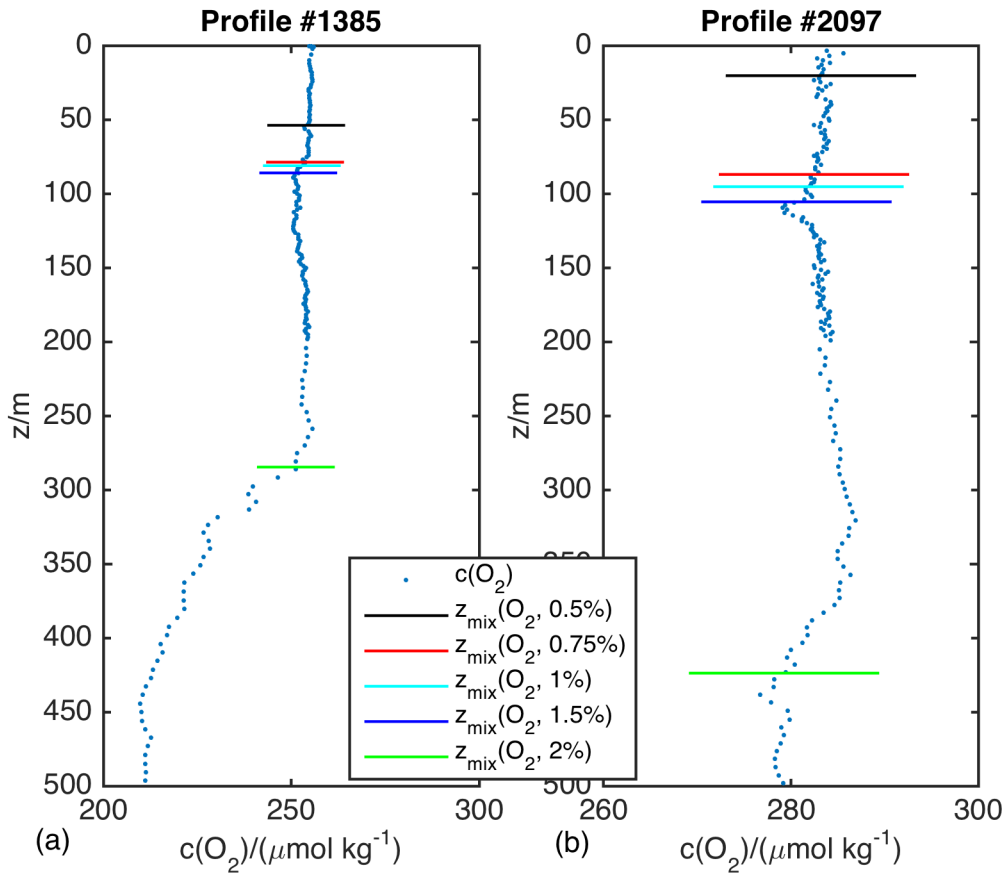


**Figure 4.6** Examples of profiles (1385 in a, 2097 in b) used for the validation of the thresholds used for the calculation of the OSBL depth.

$z_{\text{mix}}(\text{O}_2, 0.5\%)$  and  $z_{\text{mix}}(\text{O}_2, 1.5\%)$  were then compared over the year (figure 4.7a). Their difference seems to be related to their magnitude: they agree at the beginning and at the end of the time series, when they are shallower. During the winter and the beginning of the spring, instead, their values are more distant from each other. The match between  $z_{\text{mix}}(\text{O}_2, 0.5\%)$  and  $z_{\text{mix}}(\text{O}_2, 1.5\%)$  seems therefore to reflect the expected relation between XL and ML: these two layers match in the autumn and in the summer because of the strong turbulence and the strong stratification due to heating respectively. In these regimes ML and XL cannot really be distinguished. Instead, when ML is deeper, a XL can be identified in the column due to a reduction in the depth reached by the turbulence.  $z_{\text{mix}}(\text{O}_2, 1.5\%)$  is therefore taken as a proxy for ML depth, defined as the remnant trace of the deepest recent turbulence. The difference between  $z_{\text{mix}}(\text{O}_2, 0.5\%)$  and  $z_{\text{mix}}(\text{O}_2, 1.5\%)$  is then interpreted as the difference between XL and ML (figure 4.7b).

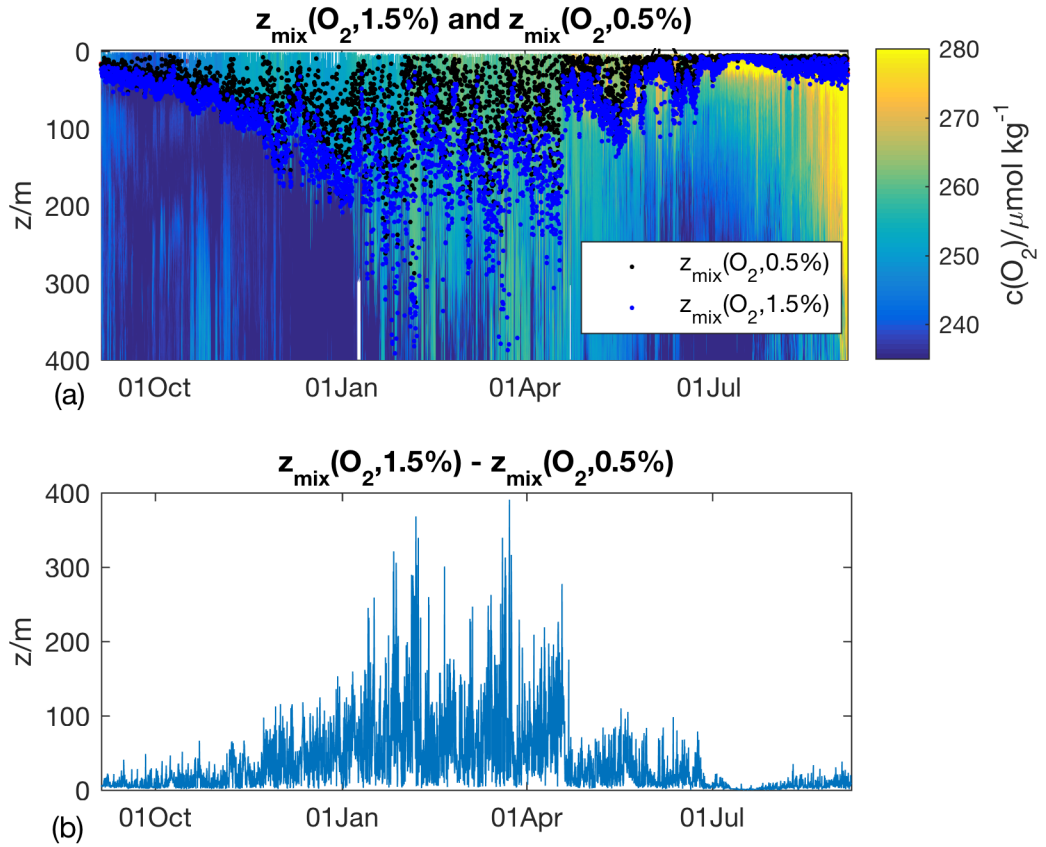


**Figure 4.7 (a) Time series of OSBL depth defined by oxygen with the threshold of 0.5% (black) and 1.5% (blue) over the timeseries of oxygen concentration; (b) difference between the two estimates measured per each profile.**

Both  $z_{\text{mix}}(\text{O}_2, 0.5\%)$  and  $z_{\text{mix}}(\text{O}_2, 1.5\%)$  become more variable when they are deep. This happens when gradients are weaker, spanning over a wider depth. In these weak gradients small changes in  $c(\text{O}_2)$  correspond to big changes in depth. This makes the computation very sensitive to the thresholds used and to the accuracy with which  $c_{\text{ref}}(\text{O}_2)$  actually estimates the  $c(\text{O}_2, \text{ML})$ . Part of the high variability during the winter and early spring should be then considered an artefact.

#### 4.3.4 Comparison among mixed layer estimates

$z_{\text{mix}}(\text{O}_2, 0.5\%)$  and  $z_{\text{mix}}(\text{O}_2, 1.5\%)$  were compared with  $z_{\text{mix}}$  defined by other parameters:  $z_{\text{mix}}(\sigma)$  based on physical parameters (density and temperature) and  $z_{\text{mix}}(\text{chl})$  based on chlorophyll *a* fluorescence.  $z_{\text{mix}}(\sigma)$  was calculated by Damerell et al. (2016) using a difference-based criterion as done for oxygen. Temperature and density reference values were calculated at 10 m and 20 m and  $z_{\text{mix}}(\sigma)$  was computed as the depth where the potential density diverged more than  $0.03 \text{ kg m}^{-3}$  or the temperature diverged more than  $0.2 \text{ }^\circ\text{C}$  from the reference value, whichever was shallower. These thresholds were chosen following the work of de Boyer

Montégut et al. (2004) in order to be compared with the previous  $z_{\text{mix}}$  estimates for the same area and for the world ocean. For each profile there were four possible values of  $z_{\text{mix}}(\sigma)$  (permutations of two thresholds and two reference depths) and the shallowest of them was used as  $z_{\text{mix}}(\sigma)$ .  $z_{\text{mix}}(\text{chl})$  was instead computed by Anna Rumyantseva at NOC Southampton with a gradient-based criterion as the depth at which the biggest gradient (the sharpest curvature in the profile) starts. Chlorophyll profiles were binned in 2-metre non overlapping vertical bins.

$z_{\text{mix}}(\text{O}_2, 0.5\%)$  is shallower than  $z_{\text{mix}}(\sigma)$  (figure 4.8) and  $z_{\text{mix}}(\text{chl})$  (figure 4.8b), with a mean difference of  $(-34 \pm 52)$  m and  $(-37 \pm 49)$  m and a fit with r-values of 0.71 and 0.66. The monthly-based RMS difference between these two timeseries (figure 4.9) shows an increased mismatch during the winter and spring. The mismatch can be explained considering that  $z_{\text{mix}}(\text{O}_2, 0.5\%)$  represents XL depth, while  $z_{\text{mix}}(\sigma)$  and  $z_{\text{mix}}(\text{chl})$  define the ML depth, as was argued for  $z_{\text{mix}}(\text{O}_2, 1.5\%)$ .

As expected, when the timeseries are superimposed,  $z_{\text{mix}}(\text{O}_2, 1.5\%)$  matches  $z_{\text{mix}}(\sigma)$  (figure 4.10a) and  $z_{\text{mix}}(\text{chl})$  (figure 4.10b) better than  $z_{\text{mix}}(\text{O}_2, 0.5\%)$ , with a respective mean difference of  $1 \pm 43$  m and  $4 \pm 43$  m. The fit between  $z_{\text{mix}}(\text{O}_2, 1.5\%)$  and  $z_{\text{mix}}(\sigma)$  is higher (r-value=0.82) than between  $z_{\text{mix}}(\text{O}_2, 0.5\%)$  and  $z_{\text{mix}}(\sigma)$ . The monthly-based RMS difference (red line in figure 4.9) follows the same pattern as the monthly-based RMS difference between  $z_{\text{mix}}(\sigma)$  and  $z_{\text{mix}}(\text{O}_2, 0.5\%)$  (blue line), showing a better agreement (lower RMS difference) in winter and spring. Part of the increase of RMS difference in winter and spring is due to the high sensitivity of the measurements in the presence of deep and weak gradients as already discussed in 4.3.3.

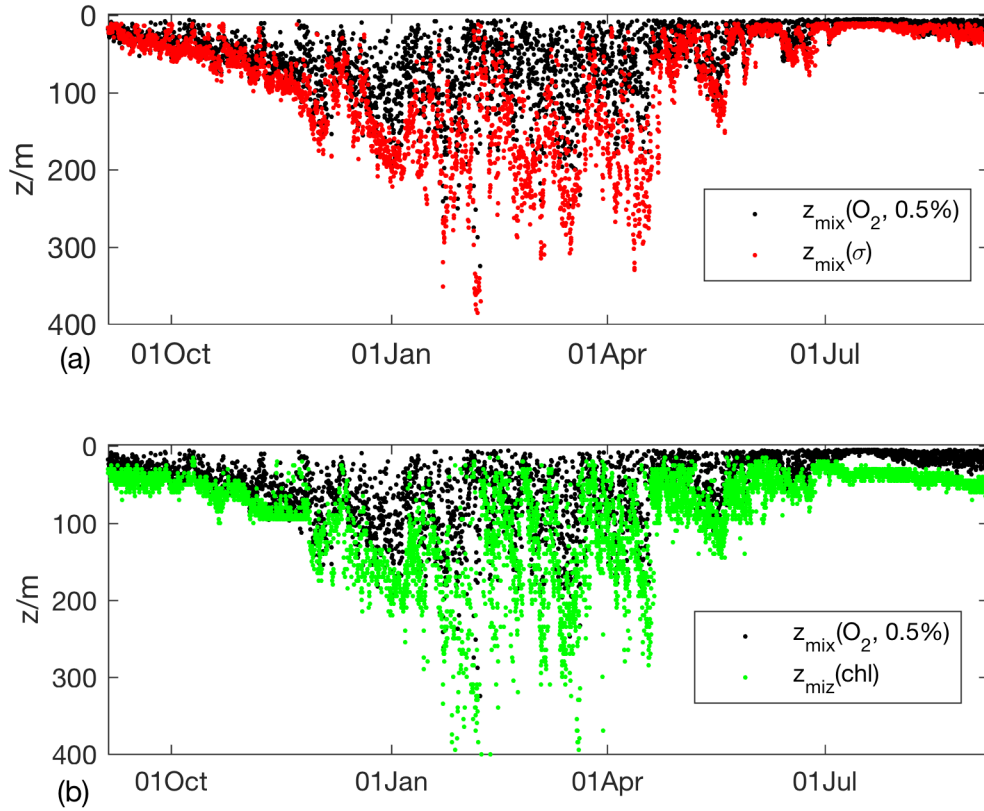


**Figure 4.8** Timeseries of  $z_{\text{mix}}$  defined by oxygen concentration with the threshold of 0.5% (black) compared with (a)  $z_{\text{mix}}$  defined by density and temperature (red) from Damerell et al. (2016) and (b) chlorophyll *a* concentration (green).

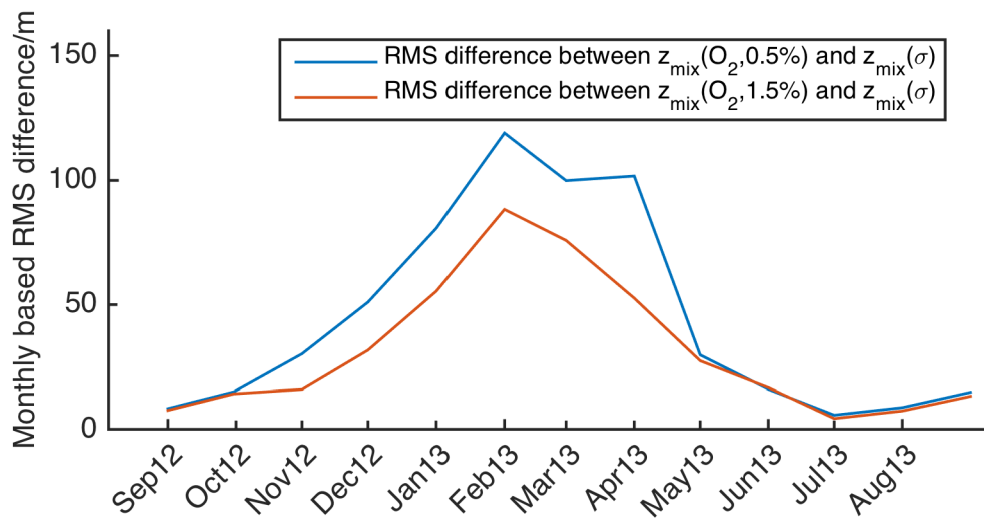


**Figure 4.9** Root mean square difference calculated for each month between September 2012 and September 2013 between  $z_{\text{mix}}$  defined by density/temperature and  $z_{\text{mix}}$  defined by oxygen concentration with a threshold of 0.5% (blue line) and 1.5% (red line).

The comparison between  $z_{\text{mix}}(\text{O}_2, 1.5\%)$  and  $z_{\text{mix}}(\text{chl})$  (figure 4.10 b) gave similar results to the one obtained comparing  $z_{\text{mix}}(\text{O}_2, 1.5\%)$  and  $z_{\text{mix}}(\sigma)$ . The main difference is the discrepancy that is visible from the beginning of July 2013, when there is a deep chlorophyll maximum (DCM) below the ML. In this period  $z_{\text{mix}}(\text{O}_2, 1.5\%)$ ,  $z_{\text{mix}}(\text{O}_2, 0.5\%)$  and  $z_{\text{mix}}(\sigma)$  are able to detect the actual ML (and XL) depth, while  $z_{\text{mix}}(\text{chl})$  lies at the bottom of the DCM. This is due to the different criteria used for the calculation of  $z_{\text{mix}}(\text{chl})$ , which is therefore not considered an adequate measurement of MLD in this regime.

There are similarities in the pattern of variation of these four  $z_{\text{mix}}(\sigma)$  estimates. It is possible to identify for all of them:

1. an initial deepening event lasting from September until the beginning of January apart from a pause for period 2;
2. a shallow period in the first half of December;
3. a deep period between the end of January and the beginning of February;
4. a highly variable period between March and April with deepening events;
5. a shallowing trend from mid-April onwards, with particularly shallow events in mid May and two other minor ones in June;
6. a shallow and stable period from the end of July until the end of the time series corresponding to the strong summer stratification with the formation of a deep chlorophyll maximum.

Part of the discrepancies among  $z_{\text{mix}}$  estimates are artefacts (i.e., due to thresholds,  $c_{\text{ref}}(\text{O}_2)$  or to criteria used for the calculation), but the majority of these differences are caused by actual processes acting in the water column. In particular, in section 4.3.6 it is analysed that the mismatch between XL and ML defined by different parameters is useful to understand biologically relevant events.

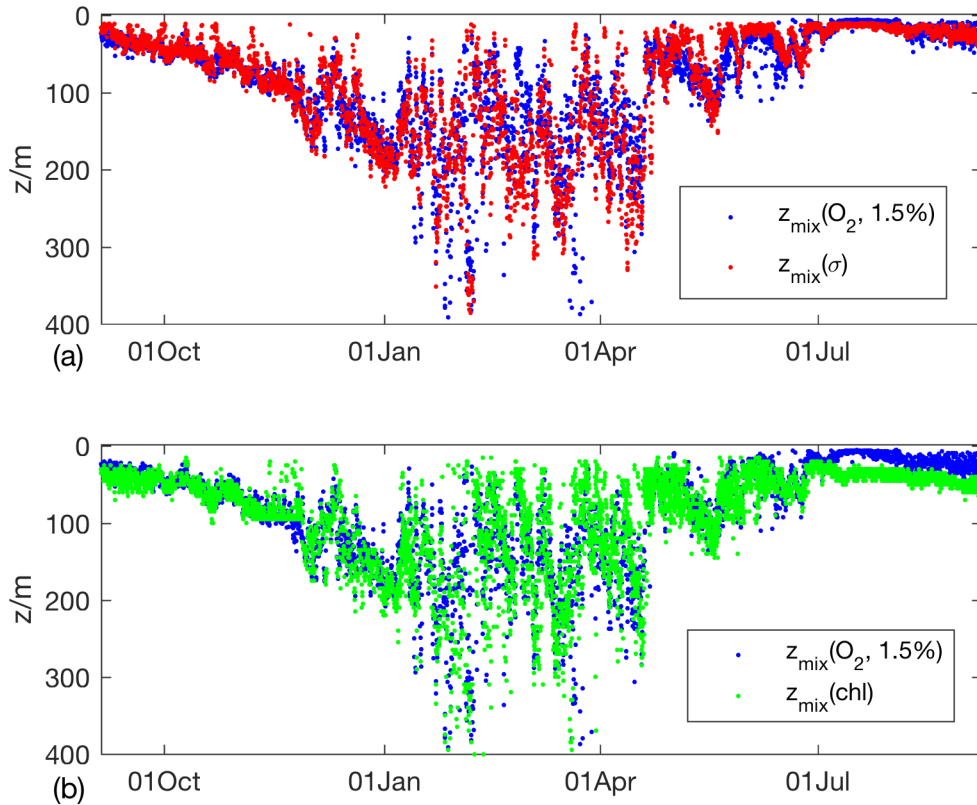


**Figure 4.10** Timeseries of  $z_{\text{mix}}$  defined by oxygen concentration with the threshold of 1.5% (blue) compared with (a)  $z_{\text{mix}}$  defined by density and temperature (red) from Damerell et al. (2016) and (b) chlorophyll *a* concentration (green).

#### 4.3.5 Profiles without mixed and mixing layer

As previously discussed (section 4.3.1), the shape of some  $c(\text{O}_2)$  profiles showed the presence of a gradient reaching the surface instead of the expected homogeneity (e.g. profile 1832 in figure 4.11a). This suggests that there was not any XL in the column above the seasonal oxycline. The values of  $z_{\text{mix}}(\text{O}_2, 0.5\%)$  and  $z_{\text{mix}}(\text{O}_2, 1.5\%)$  seem therefore not to represent any real feature.

However, the analysis of the density of a few of these stratified profiles revealed the actual presence of a XL at the top of the water column (e.g. profile 1861 in figure 4.11b). Interestingly,  $z_{\text{mix}}(\text{O}_2, 0.5\%)$  was a better proxy than  $z_{\text{mix}}(\sigma)$  for the depth of this layer, aligning close to the depth where density deviated from homogeneity. This gives support to  $z_{\text{mix}}(\text{O}_2, 0.5\%)$  as a measure of the XL depth even when  $c(\text{O}_2)$  does not show any homogeneous top layer. Using  $z_{\text{mix}}(\text{O}_2, 0.5\%)$  to trace the XL and its difference from the ML allows us to explain some dynamics of the biogeochemistry of the water column as, for example, what happens at

the end of February 2013 in the hereafter called End-February Event (EFE). This will be discussed in the next section.

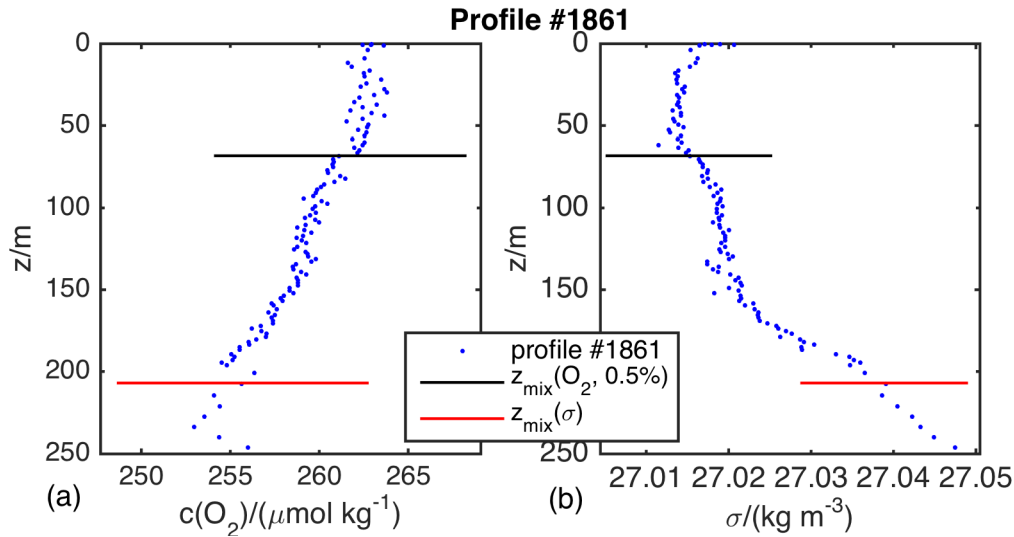


**Figure 4.11 Profile 1861 as an example of (a) an oxygen concentration profile with a gradient spanning all the way to the surface with its mixing layer depth defined by oxygen concentration (black line) and (b) its potential density profile with visible mixing layer whose depth aligns with the mixing layer defined by oxygen concentration. Red line is the mixed layer depth defined by density from Damerell et al. (2016).**

#### 4.3.6 End-February Event (EFE)

The End-February Event (EFE) is a short chlorophyll bloom happening at the top of the water column between 24th and 28th February 2013 (figure 4.12). During EFE  $z_{\text{mix}}(O_2, 0.5\%)$  is very shallow and steady around 20-25 m (black line in figure 4.12b-d) and it is well above a very deep  $z_{\text{mix}}(\sigma)$  that lies at about 200 m (red line in 4.12b and d).  $z_{\text{mix}}(\text{chl})$  (green line in figure 4.12c) and  $z_{\text{mix}}(O_2, 1.5\%)$  (blue line in figure 4.12b) are also shallow and are close to  $z_{\text{mix}}(O_2, 0.5\%)$ .  $c(\text{chl})$  and  $c(O_2)$  increase above  $z_{\text{mix}}(O_2, 0.5\%)$  as visible in figures 4.12b and 4.12c when the wind speed goes below  $5 \text{ m s}^{-1}$  and stay high until the wind speed is below  $7 \text{ m s}^{-1}$  (figure 4.12a). These speeds are lower than just before and just after EFE, suggesting a low-turbulence regime.

During EFE the mismatch between the ML and XL is clearly visible, whose depths are respectively estimated by  $z_{\text{mix}}(O_2, 0.5\%)$  and  $z_{\text{mix}}(\sigma)$ . This is confirmed by analysing the density distribution (figure 4.12d), that has lower values above  $z_{\text{mix}}(O_2, 0.5\%)$  during EFE. The presence of a shallow XL is therefore visible in both biogeochemical and physical parameters and can be considered a triggering factor of the EFE. This process would not have been revealed with the use of  $z_{\text{mix}}(\sigma)$  since its values during EFE are much deeper than  $z_{\text{eup}}$ .

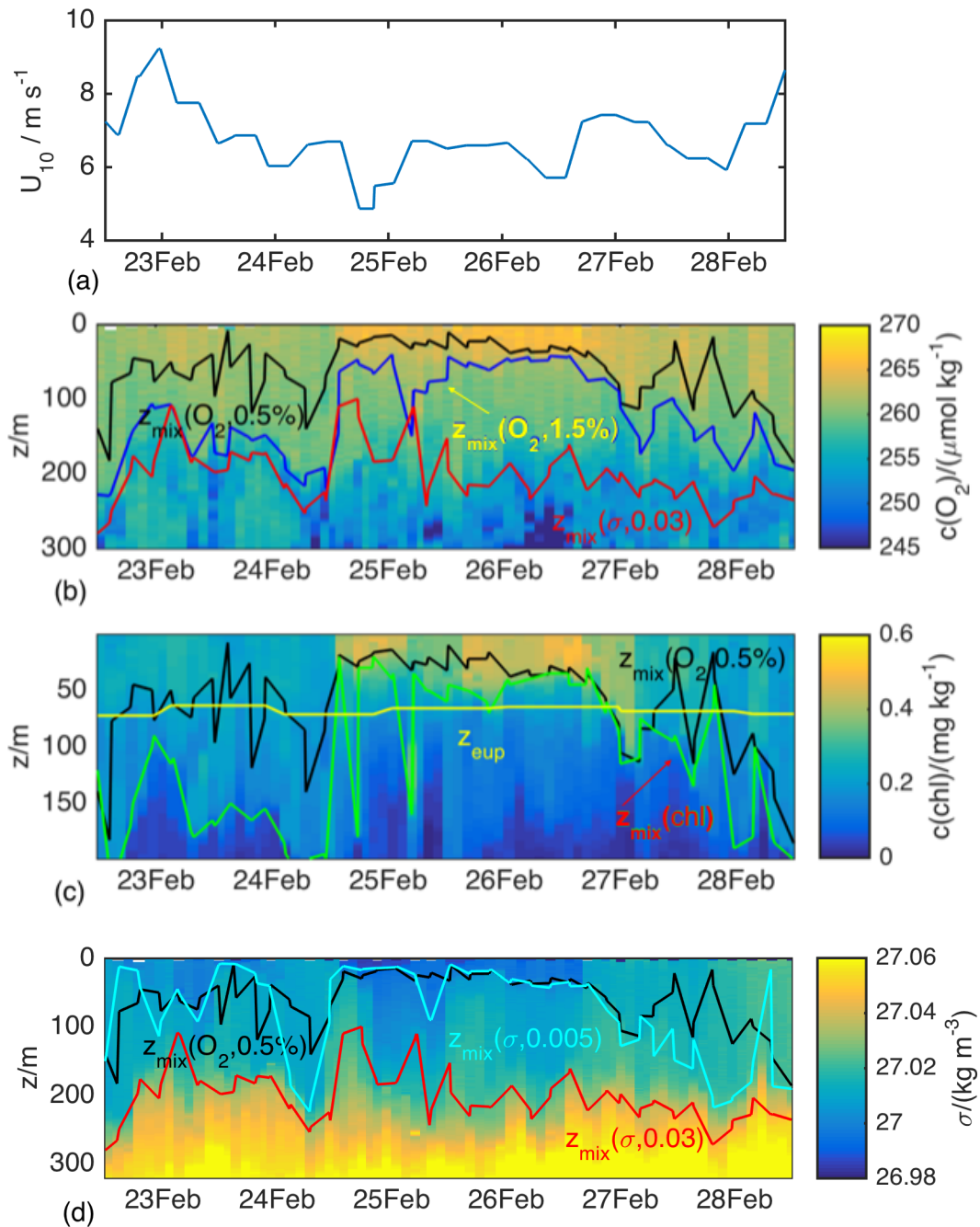


**Figure 4.12 End February Event.** (a) Wind speed at 10 m from the sea surface from ERA-Interim reanalysis; (b) oxygen concentration, (c) chlorophyll concentration and (d) potential density versus depth. The black line is the mixing layer depth defined by oxygen concentration with 0.5% threshold, the red line is the mixed layer depth defined by density/temperature according to Damerell et al. (2016), the blue line is the mixed layer depth defined by oxygen concentration with 1.5% threshold, the green line is the mixed layer depth defined by chlorophyll concentration and in bright blue is the mixing layer depth defined by density with  $0.005 \text{ kg m}^{-3}$  threshold. Euphotic depth is in yellow in panel c.

When the wind decreased below  $5 \text{ m s}^{-1}$  (figure 4.12a) the  $c(\text{O}_2)$  profiles had a continuous gradient going from the surface down to the seasonal pycno-oxycline (e.g. profile 1832 in figure 4.13 a). However, comparing  $c(\text{O}_2)$  with physical quantities (e.g. profile 1832 in figure 4.13 b-d) and chlorophyll  $a$  concentration (figure 4.13e), it is possible to see that  $z_{\text{mix}}(\text{O}_2, 0.5\%)$  in some profiles actually corresponds to small pycnoclines, revealing the recent presence of a XL. This is a validation for the use of  $z_{\text{mix}}(\text{O}_2, 0.5\%)$  as a proxy for XL depth and is the rationale for a further analysis of  $c(\text{O}_2)$  profiles that look completely stratified throughout the year. When the wind increased above  $6 \text{ m s}^{-1}$ , a surface XL was visible also in  $c(\text{O}_2)$  profiles (as in profile 1858 in figure 4.13f). In these profiles,  $z_{\text{mix}}(\text{O}_2, 0.5\%)$  aligns with small clines in every parameter analysed in the study (figure 4.13g-j).

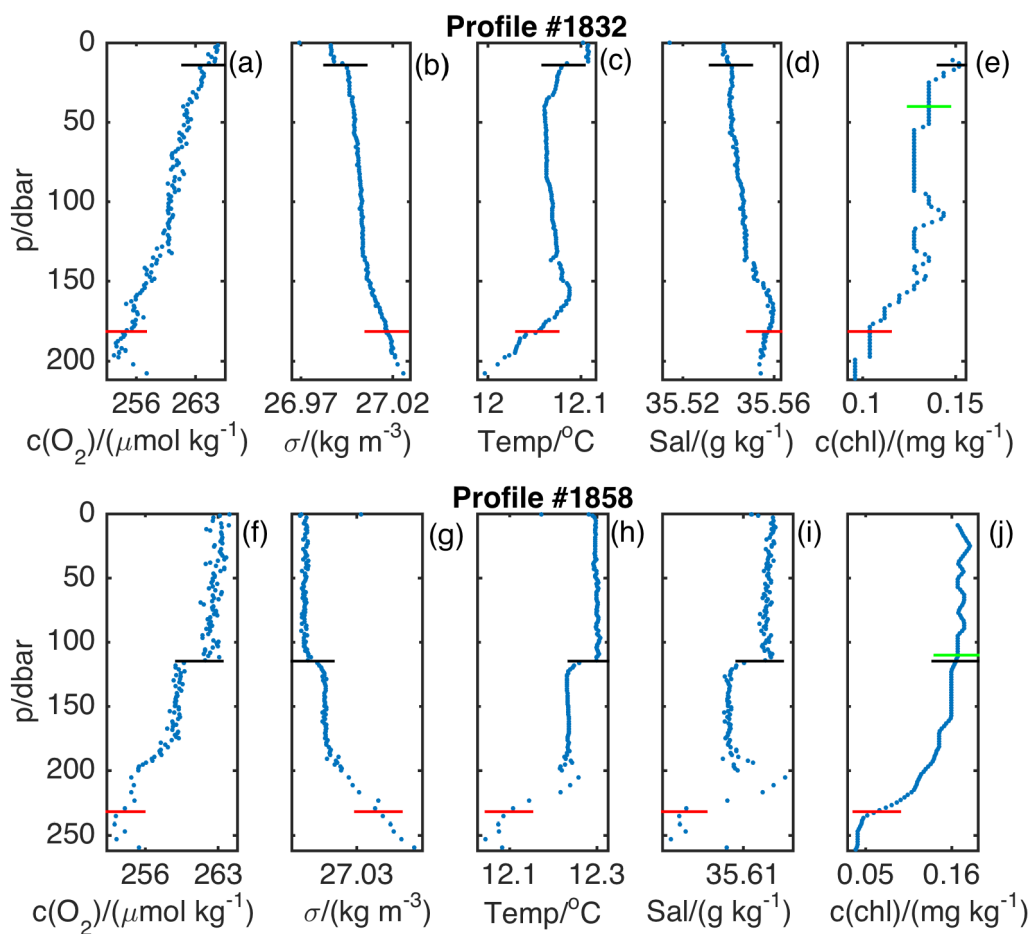


**Figure 4.13** Examples of (a-e) oxygen concentration profiles completely stratified with signs of a mixing layer defined by potential density and (f-j) oxygen concentration profiles with a mixing layer whose depth aligns to gradients in the physical parameters.

The difference between the density at the depth  $z_{\text{mix}}(\text{O}_2, 0.5\%)$ , as obtained by interpolation, and the density at 5 m, used as reference for  $z_{\text{mix}}(\text{O}_2, 0.5\%)$ , was measured for each profile during EFE. The mean value obtained was  $(0.005 \pm 0.004) \text{ kg m}^{-3}$ , almost 1/6 of the

threshold of  $0.03 \text{ kg m}^{-3}$  used by Damerell et al. (2016). As expected, increasing the sensitivity of the threshold used for density could be a way to obtain sensible estimates of the XL depth.

EFE shows the analysis of biological turbulence phenomena should be based on the mixing rather than mixed layer depth.  $z_{\text{mix}}(\text{O}_2, 0.5\%)$  is therefore more biologically relevant than  $z_{\text{mix}}(\sigma)$  measured by Damerell et al. (2016). The possibility of using the lower threshold of  $0.005 \text{ kg m}^{-3}$  to identify the mixing layer was then further investigated as described in section 4.3.7.

#### 4.3.7 Estimation of mixing layer depth based on density

$z_{\text{mix}}(\sigma)$  was calculated throughout the year using the new threshold of  $0.005 \text{ kg m}^{-3}$  of difference from the density measured at the same reference depth as  $c_{\text{ref}}(\text{O}_2)$ . The resultant  $z_{\text{mix}}(\sigma, 0.005)$  time series is plotted in bright blue in figure 4.14.  $z_{\text{mix}}(\sigma, 0.005)$  matches quite well with  $z_{\text{mix}}(\text{O}_2, 0.5\%)$  (black line in figure 4.14), being on average  $(5 \pm 43)\text{m}$  deeper and with a RMS difference of 10 m between the two timeseries.

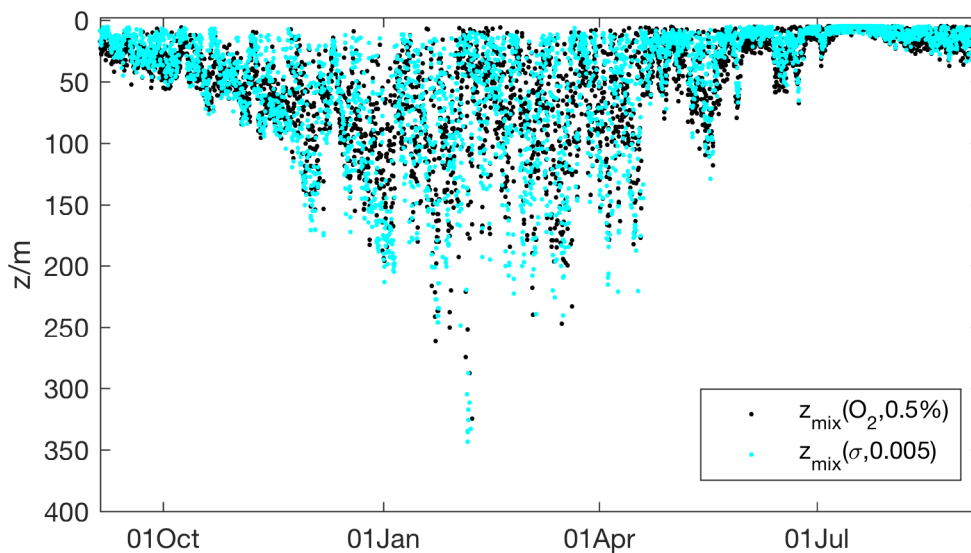


**Figure 4.14 Time series of mixing layer depth defined by potential density with the threshold of  $0.005 \text{ kg m}^{-3}$  (bright blue) superimposed at the time series of mixing layer depth defined by oxygen concentration with the threshold of 0.5% (black).**

Throughout the year it is possible to find profiles whose  $z_{\text{mix}}(\text{O}_2, 0.5\%)$  matches with  $z_{\text{mix}}(\sigma, 0.005)$  (e.g. profile 1280 in figure 4.15a-b). In these profiles these two highly sensitive thresholds seem therefore to be validated as a proxy for the XL depth, which is instead not picked up in the calculation with the density threshold of  $0.03 \text{ kg m}^{-3}$  (red line in figure 4.15a-b). However, in many profiles the two estimates do not agree. Understanding the reasons for this mismatch is difficult without direct measurements of the turbulence and considering the variability in values that derive from the high sensitivity of the thresholds. However, a few

speculations can be done. Particularly interesting is the case of a few profiles whose  $z_{\text{mix}}(\text{O}_2, 0.5\%)$  do not match with  $z_{\text{mix}}(\sigma, 0.005)$ , but agrees quite well with the euphotic depth  $z_{\text{eup}}$ . As discussed in section 4.1, this seems to be a typical example of two estimates that are influenced by different factors acting at different time scale. The agreement between  $z_{\text{mix}}(\text{O}_2, 0.5\%)$  and  $z_{\text{eup}}$  seems in fact to suggest that biology drives  $z_{\text{mix}}(\text{O}_2, 0.5\%)$  in these calculations. A regime of high production and low turbulence (or buoyant phytoplankton) would couple  $z_{\text{mix}}(\text{O}_2, 0.5\%)$  with the  $\text{O}_2$  production rates linked to the light rather than with the turbulence. This would allow for example the production of  $\text{O}_2$  below shallow  $z_{\text{mix}}(\sigma, 0.005)$  as can be seen in figures 4.15 c-d for profile 1825, but might also be linked to the production of  $\text{O}_2$  only in the top metres of the ML as hypothesised by Huisman et al. (1999) in his Critical Turbulence Hypothesis. In this case the mixing layer would shoal along with the production of more  $\text{O}_2$  in the top part of the water column and would deepen again only when the increase in turbulence would have a significant impact on plankton. This highlight is also in line with the prediction of Enriquez and Taylor (2015), who predicted a tight coupling between mixing layer variations and biological metabolic activity of the plankton.  $z_{\text{mix}}(\text{O}_2, 0.5\%)$  and  $z_{\text{mix}}(\sigma, 0.005)$  have therefore to be considered not as equivalent estimates of the same quantity, but rather as two separate entities whose comparison can give important hints about the dynamics in the water column. Due to the argued ability of  $z_{\text{mix}}(\text{O}_2, 0.5\%)$  of picking up the magnitude of the turbulence that actually influences the biology, it has to be considered the optimal proxy for the mixing layer depth used in biological analyses carried out in chapters 5 and 6.

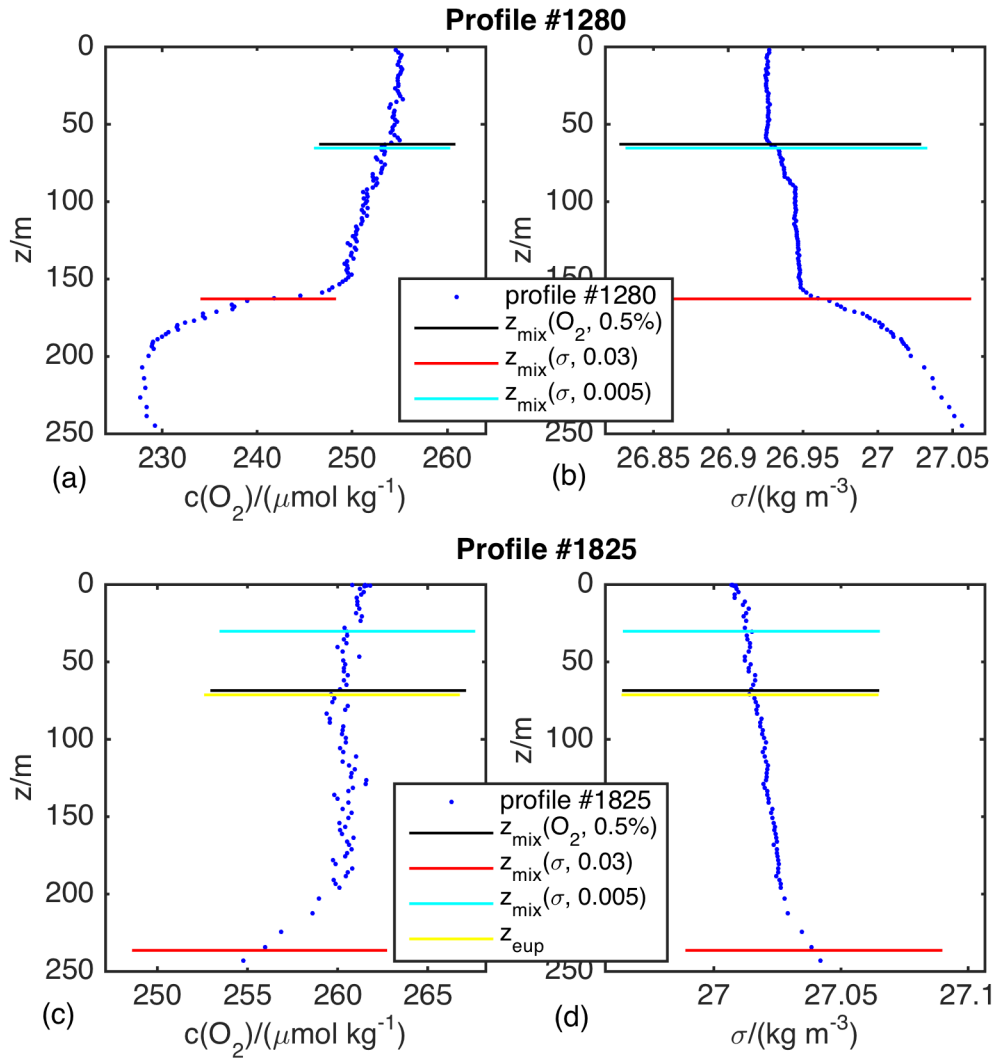


**Figure 4.15** Example of (a-b) profile in which the mixing layer defined by oxygen (black line) and density (bright blue line) match and (c-d) profile in which they do not match and the mixing layer defined by oxygen match with euphotic depth (yellow line). Red line is the mixed layer defined by density/temperature by Damerell et al. (2016).

#### 4.3.8 Simulation of lower frequency

Each subsample of the  $z_{\text{mix}}$  time series that simulates a low-frequency survey (one profile every 1, 3, 5, 7 and 10 days) was plotted on top of the original series to visually check their agreement (figure 4.16).

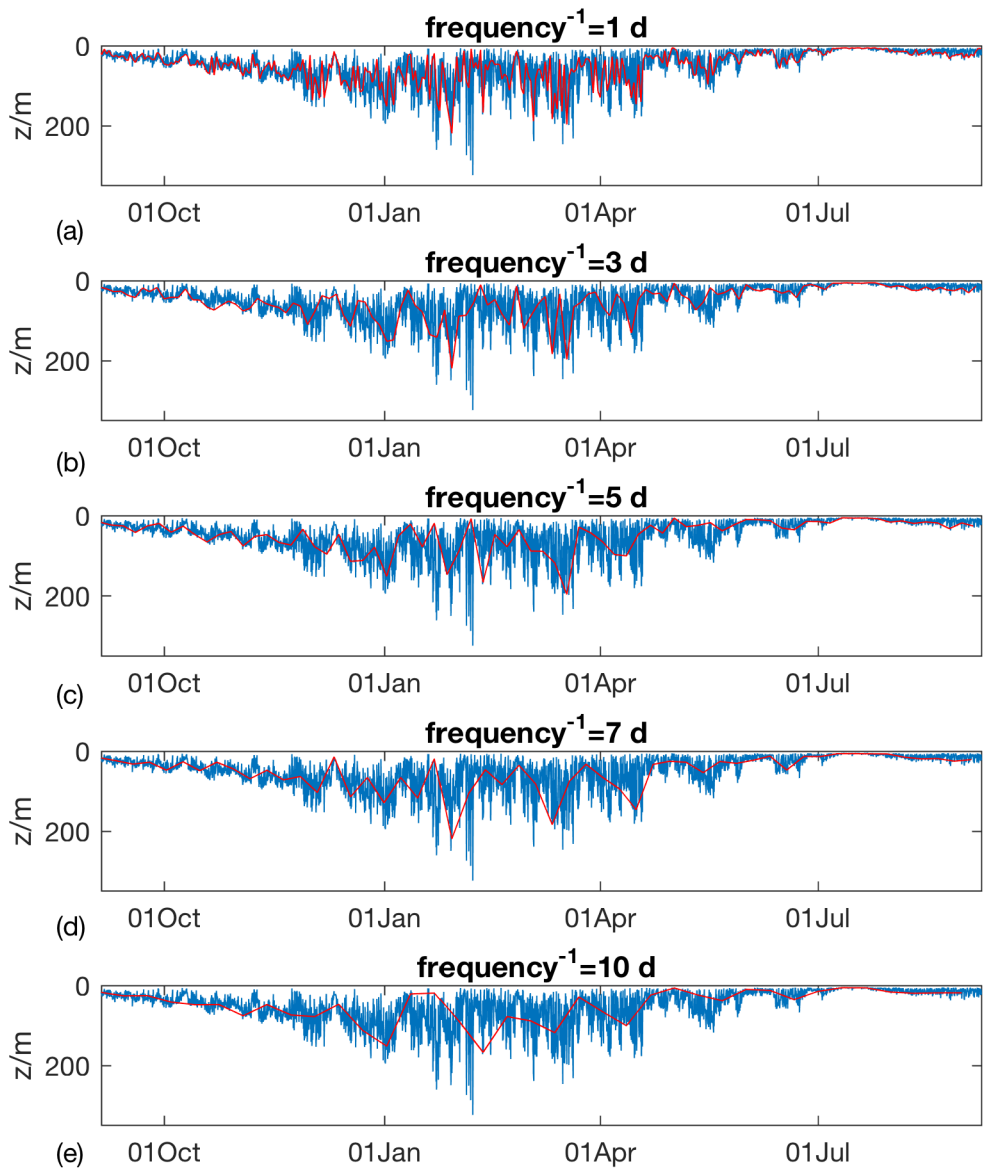


**Figure 4.16 (a-e) Complete time series of mixing layer at PAP station in blue and subsample considering one profile sampled at midnight every (a) 1, (b) 3, (c) 5, (d) 7 and (e) 10 days in red over one year cycle.**

Two statistical analysis were carried out in order to analyse the effect of an increasingly lower frequency in the sampling. The coefficient of correlation between the original and the subsample decreases at lower frequencies, passing from 0.72 to 0.54 (figure 4.17a). The root mean square (RMS) difference also increased at low frequencies, increasing from 30 m to 39 m (figure 4.17b).. This shows that higher frequencies are able to pick up events missed otherwise and that there might be very high bias in the estimation of the OSBL depth at low frequencies.

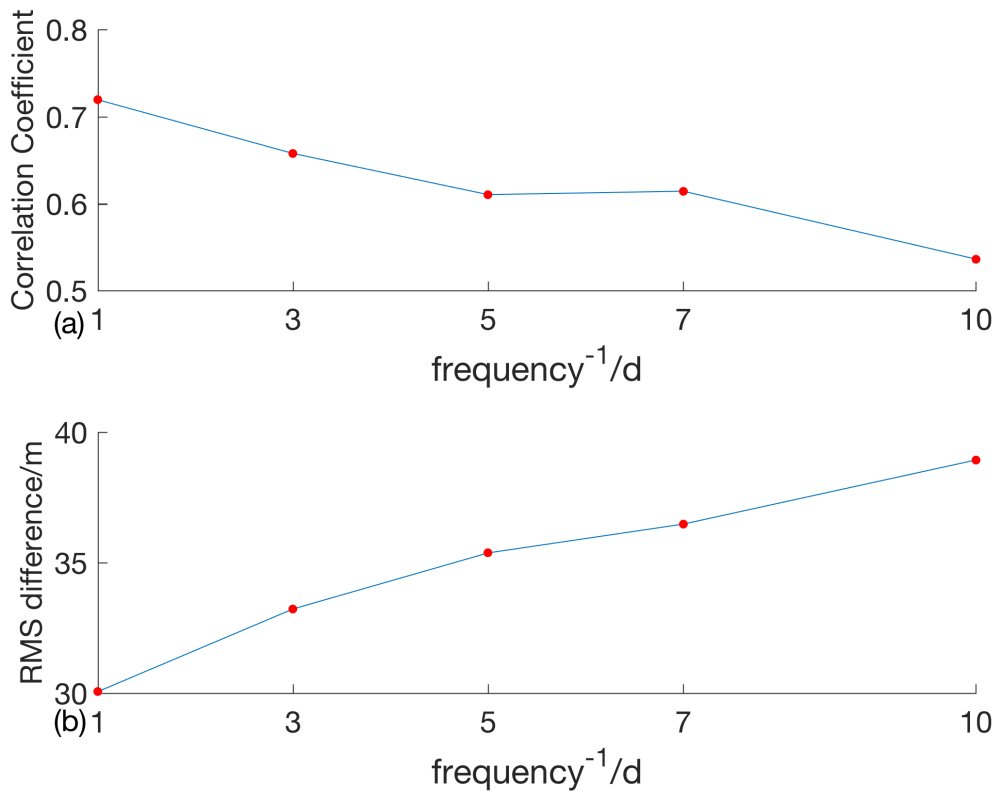


**Figure 4.17 (a) Correlation coefficient between the original mixing layer time series and each of the subsamples considering profiles measured at midnight every 1, 3, 5, 7 and 10 days; (b) root mean square difference between the original mixing layer time series and each of the subsamples considering profiles measured at midnight every 1, 3, 5, 7 and 10 days.**

#### 4.4 Differences between ascents and descents

The visual analysis of the time series revealed the presence of values of  $z_{\text{mix}}(\text{O}_2, 0.5\%)$  oscillating up and down between consecutive profiles, as can be seen for example looking at the black line in figure 4.12. This seemed to be connected to the phase of the dive in which the profiles had been measured. The hypothesis of a systematic difference between  $z_{\text{mix}}(\text{O}_2, 0.5\%)$  calculated in the ascents and in the descents of the glider dives was therefore tested. In order to do so,  $z_{\text{mix}}(\text{O}_2, 0.5\%)$  from each ascent was paired with the one of its following descent. These are paired data because, as explained in chapter 2, due to the short stay at the surface, the top part of these two profiles are assumed to be quasi-replicates of each other.

The mean difference between paired  $z_{\text{mix}}(\text{O}_2, 0.5\%)$  was  $(5 \pm 34)$  m, with the maximum value of 228 m.  $z_{\text{mix}}(\text{O}_2, 0.5\%)$  calculated during the descents was deeper. A t-test for paired samples was used to test the similarity of these two distributions. The test rejected the null hypothesis that the two time series are similar ( $p=2.11 \cdot 10^{-14}$ ), confirming statistically the significant difference between ascents and descents. The test gave the same result analysing the time series of  $z_{\text{mix}}(\text{O}_2, 0.75\%)$ ,  $z_{\text{mix}}(\text{O}_2, 1\%)$  ( $p=2.31 \cdot 10^{-24}$ ),  $z_{\text{mix}}(\text{O}_2, 1.5\%)$  ( $p=1.30 \cdot 10^{-11}$ ) and a  $z_{\text{mix}}(\text{O}_2, 2\%)$ . Also when  $c_{\text{ref}}(\text{O}_2)$  for  $z_{\text{mix}}(\text{O}_2, 0.5\%)$  was deepened from 5 m to 10 m ( $p=1.77 \cdot 10^{-11}$ ) or when original profiles before the smoothing step were used for the calculation. This difference seems therefore linked to the profiles themselves rather than to the choices (thresholds,  $c_{\text{ref}}$ ) done for  $z_{\text{mix}}(\text{O}_2)$  calculation.

The difference between ascents and descents are well known for oxygen optodes (Bittig et al., 2014). These are mainly due to errors in the corrections for the time response ( $\tau$ ), which varies from dive to dive according to the flow of the water near the foil. This problem affects in particular unpumped optodes as the ones used in this study (Bittig et al., 2014). When  $z_{\text{mix}}(\text{O}_2, 0.5\%)$  is used for the calculation of entrainment based on the XL depth variations, this phenomenon can significantly bias the results. It is therefore suggested as done in previous work (i.e., Nicholson et al., 2015) to use the descents and ascents profile as two parallel datasets.

## 4.5 General discussion

The OSBL is the layer in which the vertical turbulence induced by wind at the sea surface, waves and convective motion mixes heat, momentum and tracers (Noah and Lee, 2008). It has been classically identified with the depth  $z_{\text{mix}}$  over which the parameters are homogeneous, assuming a causal relation between the homogeneity and the turbulence. However, the presence of homogeneity in layers where turbulence has recently ended has prompted the necessity to distinguish between a mixed and a mixing layer (ML and XL), where at the moment of the measurements the turbulence is active only in the XL.

In the present chapter the first year-long time series of the OSBL depth as defined by  $c(\text{O}_2)$  was presented. A similar approach with similar thresholds was used to calculate  $z_{\text{mix}}$  in the Southern Ocean by Castro-Morales and Kaiser (2012). They suggested that this method could be applied in other areas of the ocean and in other times of the year. This study confirms that it is actually possible to obtain sensible results with this method and that it can describe the OSBL over the annual cycle. The visual analysis of  $c(\text{O}_2)$  profiles has confirmed that  $z_{\text{mix}}(\text{O}_2, 0.5\%)$  is able to identify the depth at which parameters diverge from the homogeneity that characterises the OSBL, lying at the level of the shallowest significant oxycline.

In the long-running discussion about the difference between XL and ML and about what  $z_{\text{mix}}$  measures when calculated with different criteria, parameters and thresholds (Brainerd and Gregg, 1995, Noh and Lee 2008; D'asaro, 2013; Sutherland et al., 2014), this study provides some evidence that  $z_{\text{mix}}(\text{O}_2, 0.5\%)$  is an estimate of XL depth while  $z_{\text{mix}}(\text{O}_2, 1.5\%)$  is an estimates of ML depth. It has also been shown that  $z_{\text{mix}}(\text{O}_2, 0.5\%)$  has a physical relevance as well, being able to describe indirectly the shallowest depth at which density diverges from the homogeneity.  $z_{\text{mix}}(\text{O}_2, 0.5\%)$  in fact picks up the signal of small pycnoclines that diverge as little as  $0.005 \text{ kg m}^{-3}$  from the reference values measured near the surface. This divergence is from 1/6 to 1/2 smaller than the thresholds usually used to calculate  $z_{\text{mix}}(\sigma)$  (Schneider and Müller, 1990; Brainerd and Gregg, 1995; Monterey and Levitus, 1997; Thomas and Fine, 2003; de Boyer-Montegut, 2004; Suga et al., 2004; Lozovatsky et al., 2006; Cisewski et al., 2008; Damerell et al., 2016). This sensitivity makes  $z_{\text{mix}}(\text{O}_2, 0.5\%)$  a method with great potential for the computation of the XL.

The importance that  $z_{\text{mix}}(\text{O}_2, 0.5\%)$  has for analysis of the biogeochemical phenomena happening in the water column has been shown analysing the bloom that happens at the surface at the end of February 2013 in the so-called EFE. Variations over time of  $z_{\text{mix}}(\text{O}_2, 0.5\%)$  have in fact been the key to explain the triggering factors of this little bloom with a mechanism which adheres to the classical CDH (Sverdrup, 1953). This has proved the efficacy with which  $z_{\text{mix}}(\text{O}_2, 0.5\%)$  can be used to describe turbulence variations that have a significant impact on the biological activity. This validates what was postulated by Franks (2014), which highlighted the need to test the CDH using XL and not ML. It is in fact XL, rather than ML, that matches the characteristics of the “mixed layer” described by Sverdrup (1953). Franks (2014) suggested that, since the majority of the studies use ML and not XL for their analysis, CDH had not been actually tested in the field as yet. This study starts to fill this gap presenting a field study that evidences how the CDH works when XL is taken into account.

The calculation of  $z_{\text{mix}}(\text{O}_2, 0.5\%)$  that was done in this chapter had the main goal to estimate the layer of the water column in which the biological activity takes place, classically identified as the OSBL. This was done in order to define the lower limit of the layers in which  $c(\text{O}_2)$  inventories have to be computed in the productivity calculations carried out in the following chapters.  $z_{\text{mix}}(\text{O}_2, 0.5\%)$  was also meant to estimate the variations in  $c(\text{O}_2)$  that are due to the entrainment of water when turbulence increases deepening the OSBL and to provide a biologically relevant quantity to be compared with other factors such as  $z_{\text{eup}}$  to explain the causes of biogeochemical phenomena such as phytoplankton blooms. The burst of biological activity in the EFE and the match between  $z_{\text{mix}}(\text{O}_2, 0.5\%)$  and  $z_{\text{eup}}$  in profiles throughout the year revealed the intimate link between  $z_{\text{mix}}(\text{O}_2, 0.5\%)$  with productivity and with turbulence, validating its use in the following steps of this study described in chapters 5 and 6.

Simulations of surveys performed with platform collecting data at a lower frequency for the same dataset were carried out subsampling the time series at midnight every  $n$  days since the beginning of the mission. This experiment has shown how, due to the high variability of the mixing layer depth, a high frequency is needed to detect the major variations that happen in the area. Profiling once a day gives still a very good approximation of the situation and could be considered comparable due to the high grade of correlation, despite missing some of the deeper events in the winter. It is worth noticing that sampling every 5 or 7 days does not change significantly the situation and in this case sampling at lower frequency would prolong the duration of the survey without affecting the results. As a general rule, lower frequencies could be used during the deepening phase of the mixing layer and during the spring/summer period. During winter, however, it is suggested the use of a frequency as high as possible.

Future research should be focused on the comparison between  $z_{\text{mix}}(\text{O}_2, 0.5\%)$  values and direct measurements of vertical turbulence in the water column to check the actual match of this proxy with the XL defined by the dissipation of energy. This analysis should be also carried out at different times of the year, possibly with a characterization of the plankton distribution in the water column to describe how much biological activity impacts  $z_{\text{mix}}(\text{O}_2, 0.5\%)$ . This would also identify the possible presence of periods when  $z_{\text{mix}}(\text{O}_2, 0.5\%)$  responds more to biological activity than to the turbulence, giving important information about the relative importance of these factors on the biogeochemical cycles of the ocean.

## 4.6 Conclusions

$z_{\text{mix}}(\text{O}_2, 0.5\%)$  is a reliable estimate of the XL throughout the year in the North Atlantic, while  $z_{\text{mix}}(\text{O}_2, 1.5\%)$  describes the ML due to the relaxation of the homogeneity assumption.  $z_{\text{mix}}(\text{O}_2, 0.5\%)$  values have both a biogeochemical and physical relevance, being able to identify the divergence from homogeneity not only in  $c(\text{O}_2)$  but also in the potential density.  $z_{\text{mix}}(\text{O}_2, 0.5\%)$  describes well the variations of turbulence and OSBL depth that affect the biological activity as seen during the EFE.  $z_{\text{mix}}(\text{O}_2, 0.5\%)$  is therefore the estimate of the XL depth that will be used in the productivity calculations carried out in the following chapters.  $z_{\text{mix}}(\text{O}_2, 0.5\%)$  analysis suggests the use of ascents and descents as separate datasets in order not to overestimate the entrainment including in the calculations apparent deepening events that do not correspond to reality.

# Chapter 5

## Net Community Production

Net community production in the euphotic layer (the portion of the water column above the depth where light intensity equals 1% of the incident radiation at surface) was measured between September 2012 and August 2013 at the Porcupine Abyssal Plain by analysing the variations of the oxygen inventory measured during three consecutive glider missions. Net community production was calculated as the variation in the inventory not due to physical processes. The comparison with wind speed, mixing layer depth (in relation to euphotic depth), net surface heat flux and other parameters helped to explain the pattern and triggering factors of the productivity increases and decreases visible in the time series.

### 5.1 Introduction

Marine net biological production ( $N$ ) is the balance between two metabolic activities, one fixing  $\text{CO}_2$  into organic compounds (production) and the other one using part of this organic carbon to produce energy (respiration).  $N$  is the parameter that quantifies the impact that the biota has on the biogeochemical cycles of elements such as carbon (C), nitrogen (N), oxygen ( $\text{O}_2$ ), phosphorus (P), silicon (Si) and others. N, C, P and Si are incorporated into organic compounds produced by the autotrophs and are re-mineralised during catabolic respiration reactions. In contrast,  $\text{O}_2$  is produced as a by-product during photosynthesis (carbon fixation) and is consumed during respiration.  $\text{O}_2$  is therefore produced when inorganic carbon is consumed and vice versa.  $N$  has therefore opposite effects on the budget of  $\text{O}_2$  and  $\text{CO}_2$  in the environment.

The magnitude of  $N$  is of great importance for Earth's climate on glacial/interglacial timescales (Falkowski, 1998; Alkire et al., 2014). The seas around the world harbour almost half of plant production (Field et al, 1998; Williams, 1998), moving carbon and oxygen within and across compartments and reservoirs. Supersaturating and/or undersaturating the water at the surface, the biota is able to trigger fluxes between the ocean and the atmosphere. This makes the ocean a carbon sink or a source depending on biological activity. This is very important in the determination of the global  $\text{CO}_2$  budget, which is relevant to study the climate change process because this is an important greenhouse gas.

In the open ocean, the plankton community can be considered responsible for the whole magnitude of  $N$ . Phytoplankton perform photosynthesis, quantified as Gross Primary Production ( $P$ ), whose calculation will be discussed in chapter 6. Part of  $P$  is consumed by the phytoplankton itself to produce energy and stay alive (autotrophic respiration,  $R_A$ ), while another part is respired by heterotrophs ( $R_H$ ). The difference between what is fixed by phytoplankton and what is consumed by the whole community is  $N$ .

$$N = P - (R_A + R_H) \quad (5.1)$$

The metabolic balance of some areas of the open ocean (i.e., the sign of  $N$ ) is the focus of a long-running debate (del Giorgio et al., 1997; Duarte and Agustí 1998; Williams 1998; Duarte et al., 1999; Williams and Bowers, 1999; del Giorgio and Duarte, 2002; Karl et al., 2003; Hansell et al., 2009; Ducklow and Doney, 2013; Williams et al., 2013; Duarte et al., 2013). The uncertainty derives from the use of different methods for the calculation of  $N$  and its components. Several biases are known to affect the *in vitro* measurements and the comparability of their results with the real ocean (Williams et al., 1998; Kaiser et al., 2005). It is not even clear what is actually measured by some of the methods that are used (Regaudie-de-Gioux et al., 2014). There are also challenges to separate the influence of biological and physical processes in the signals from *in situ* measurements (Hamme and Emerson, 2006; Emerson et al., 2008). This has also affected the length of the datasets because the influence of some physical factors can sometimes be neglected, but only for short period (e.g. Robertson et al., 1992). Long-term observations using consistent methods are therefore crucial to quantify correctly the intraseasonal variability and to estimate correctly the annual budget.

The debate about what factors influence production and trigger the accumulation of chlorophyll and supersaturation of the water at the surface ('bloom') is still open as well. Since the first hypothesis was proposed in 1953 by Sverdrup, many studies have been discussing the validity of its assumptions, have been adding new variables (for example turbulence) and have proposed alternative hypotheses (e.g. Huisman et al., 1999; Behrenfeld, 2010; Taylor and Ferrari, 2011; Enriquez and Taylor, 2015). A careful analysis of the pattern of variation among different parameters is therefore needed to understand the validity of all the different mechanisms proposed so far. Franks et al., 2014 highlighted also the interest for the use of the mixing layer depth, rather the mixed layer depth, in this kind of analysis.

The goal of the present study was to estimate the magnitude of  $N$  in the productive layer of the water column through the analysis of variations of the oxygen inventory,  $I(O_2)$ , over time, based on oxygen concentration,  $c(O_2)$ , measured *in situ*. The high frequency of glider measurements and the length of this time series let the present study try to overcome the limits that affect  $N$  calculated with other *in situ* measurements that are often due to the low spatial

resolution and/or scattered temporal distribution. The present study surveyed an area located in the North Atlantic, one of the basins historically most studied on the planet. The area is in the proximity of the frequently surveyed Porcupine Abyssal Plain (PAP) Sustained Observatory. This site is frequently visited by research cruises and this gave the possibility to compare  $N$  estimates with previous studies that focused on the same specific area (e.g., Körtzinger et al., 2008a; Frigstad et al., 2015), along with basin-wide estimates. Furthermore, the availability of a suite of different parameters, including the mixing layer depth as defined in chapter 4, was useful to give new insights in the mechanisms that trigger increases in production.

## 5.2 Ancillary data and methodology

### 5.2.1 Separation of descents and ascents

The profiles in the dataset were divided into two sub-datasets. One included only the descents of each glider dive and the second one included only the ascents. These two sub-datasets were considered equally valid, but were just analysed separately. This was done to ensure that the time intervals for the calculation of  $c(\text{O}_2)$  changes would be more even in duration at each depth. It took also in account the difference between profiles in ascent and descent phase as discussed in section 4.4. The methodology that will be explained from now on was therefore applied to the two sub-datasets separately. In chapter 3 it was shown that ascents were more affected by biofouling than descents, revealing interactions between sunlight and the foil. Data from descents were considered more reliable near the surface and therefore they will be used in the section 5.3 and 5.4 to analyse and discuss the data. Separate  $N$  estimates from the use of descents and ascents will be compared in section 5.3.6.

### 5.2.2 Inventory calculation

The estimation of  $N$  in this chapter was focused on the productive layer at the top of the water column and was based on the analysis of changes in the oxygen inventory (per unit area) above a depth  $z_{\text{lim}}$ ,  $I(z_{\text{lim}})$ . Considering that productivity is limited by light for photosynthesis, the mean euphotic depth ( $z_{\text{eup}}$ ) was used to approximate the depth of the productive layer of the water column, where most of  $N$  is carried out.  $z_{\text{eup}}$  is defined as the depth equivalent to the 1% PAR level and its mean value between the start of the dataset and the start of biofouling was  $(60 \pm 15)$  m,  $z_{\text{lim}}$  was therefore set at 60 m. PAR was measured by the gliders. The  $z_{\text{eup}}$  time series, shown in figure 5.1, was provided by Anna Rumyantseva from the National Oceanography Centre, Southampton.

$I(z_{lim})$  was computed per each profile integrating the oxygen concentration over depth as in equation 5.2, where  $c_i = c_i(O_2)$  is the oxygen concentration at any depth  $z_i$  above  $z_{lim}$ .

$$I(z_{lim}) = c_1 \frac{z_2 + z_1}{2} + \sum_{i=2}^{n-1} c_i \left( \frac{z_{i+1} - z_{i-1}}{2} \right) + c_n \left( z_{lim} - \frac{z_n + z_{n-1}}{2} \right) \quad (5.2)$$

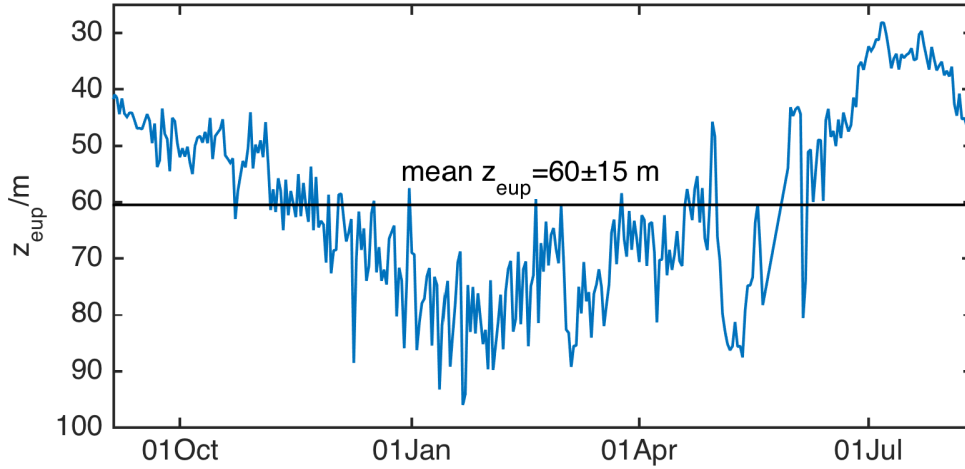


**Figure 5.1 Euphotic depth measured before the start of the biofouling event with horizontal bar showing its mean value.**

Time series of  $I(z_{lim})$  is in figure 5.2b. At the beginning and at the end of the mission (from September to mid-November 2012 and from the end of June to August 2013) the water column was stratified above  $z_{lim}$ , with features like the deep oxygen maximum visible at the end of the time series. During the rest of the year, the mixing layer depth  $z_{mix}$  (0.5% of  $c(O_2)$ , 5 m, see chapter 4) was usually deeper than 60 m, i.e. the column was homogenized above  $z_{lim}$  (figure 5.2a).

The surfacing times of each profile were used to compute the time gap  $\Delta t = t_2 - t_1$  that divided consecutive profiles. The rate of change in oxygen inventory between  $t_1$  and  $t_2$  was therefore  $\Delta I / \Delta t$  (equation 5.3). The time series of  $\Delta I / \Delta t$  is shown in figure 5.2c. Values were very variable with a mean of  $(3 \pm 724) \text{ mmol m}^{-2} \text{ d}^{-1}$  and values ranging between  $-6476 \text{ mmol m}^{-2} \text{ d}^{-1}$  to and  $5757 \text{ mmol m}^{-2} \text{ d}^{-1}$ .

$$\frac{\Delta I}{\Delta t} = \frac{I(z_{lim}, t_2) - I(z_{lim}, t_1)}{t_2 - t_1} \quad (5.3)$$

The  $O_2$  mass balance could be written as a flux of dissolved gas between  $t_1$  and  $t_2$  measured in  $\text{mmol m}^{-2} \text{ d}^{-1}$ . It is considered as the sum of three different components  $F_{as}$ ,  $E$  and  $N$

$$\frac{\Delta I}{\Delta t} = -F_{as} + E + N \quad (5.4)$$

where  $F_{as}$  is the air-sea  $O_2$  flux (positive for  $O_2$  outgassing),  $E$  is the entrainment and  $N$  is net community production.

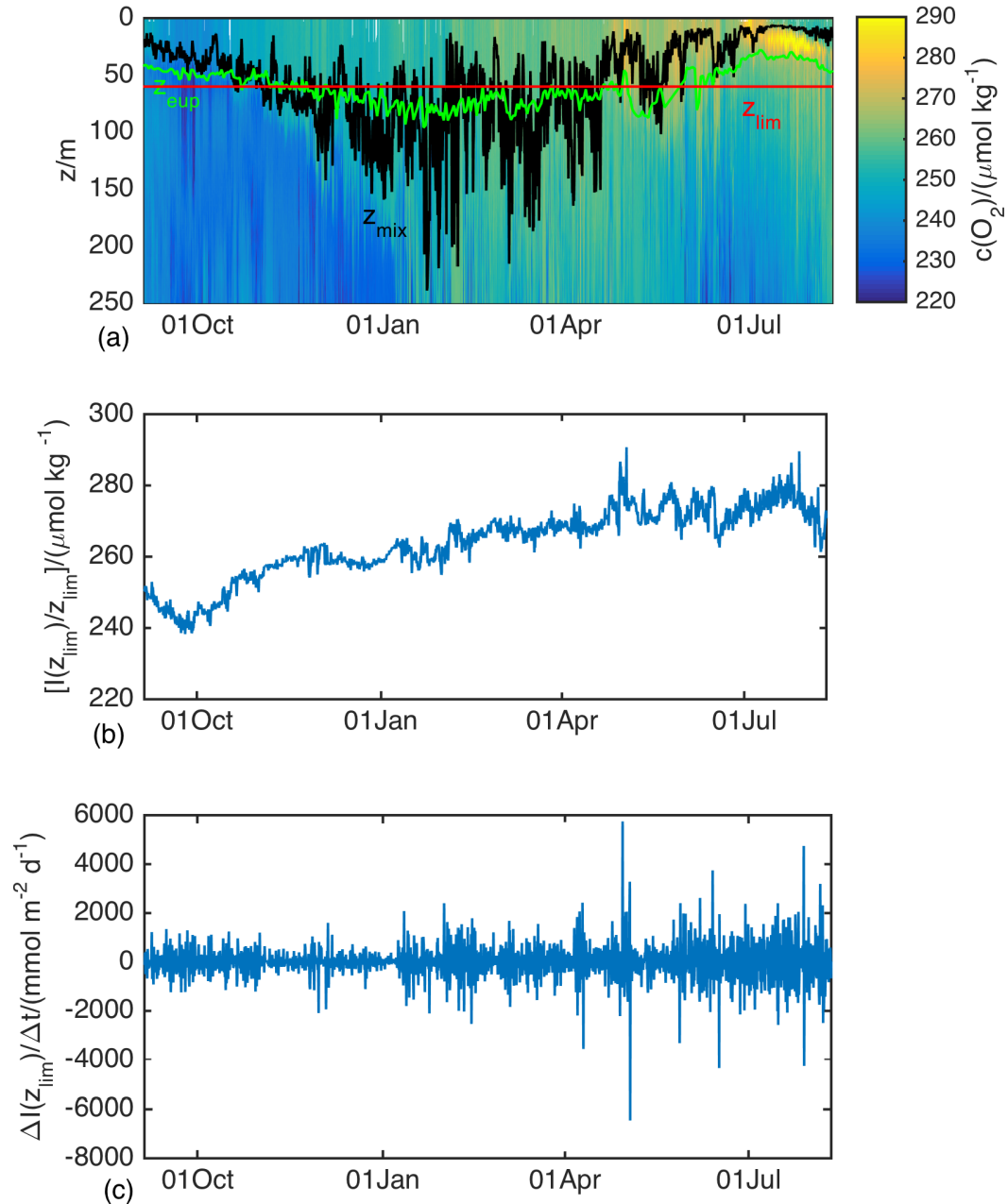


**Figure 5.2** (a) oxygen concentration in  $\mu\text{mol kg}^{-1}$  versus depth with mixing layer depth ( $z_{\text{mix}}$ , black line), euphotic depth ( $z_{\text{eup}}$ , green line) and  $z_{\text{lim}}$  (red, 60 m); (b) mean concentration of oxygen above  $z_{\text{lim}}$  calculated dividing the oxygen inventory by  $z_{\text{lim}}$ ; (c) rate of change in oxygen inventory between consecutive profiles.

### 5.2.3 Air-sea O<sub>2</sub> flux calculation

$F_{\text{as}}$  describes the exchange of O<sub>2</sub> between the ocean and the atmosphere that acts to equilibrate the gas concentration in the two compartments. It was calculated using the bulk gas transfer parameterisation

$$F_{\text{as}} = k(\text{O}_2)[c(\text{O}_2) - c_{\text{sat}}(\text{O}_2)] \quad (5.5)$$

where  $c(\text{O}_2)$  is the mean dissolved oxygen concentration and  $c_{\text{sat}}(\text{O}_2)$  is the oxygen saturation concentration (i.e., O<sub>2</sub> solubility).  $c_{\text{sat}}(\text{O}_2)$  was calculated according to Benson and Krause (1984) fit in Garcia and Gordon (1992) for each  $c(\text{O}_2)$  data point considering the corresponding potential temperature and absolute salinity as well as atmospheric pressure at sea level. Atmospheric pressure varied between 978 hPa and 1033 hPa (figure 5.2c) and was derived from ERA-Interim reanalysis (<http://www.ecmwf.int/en/research/climate-reanalysis/era-interim>) with a resolution of 6 hours and 0.125° in latitude and longitude. Atmospheric pressure values for each profile were obtained by interpolating to the nearest point in time and space in the ERA-Interim grid. No clear seasonality was visible in the time series, but there were high values from May until August. Values before March showed a continuous alternation of high and low pressure.  $c(\text{O}_2)$  and  $c_{\text{sat}}(\text{O}_2)$  used to calculate  $F_{\text{as}}$  were measured for each profile as the mean value in the top 10 m or as the mean above  $z_{\text{mix}}$  when  $z_{\text{mix}} < 10$  m.  $c_{\text{sat}}(\text{O}_2)$ , shown in figure 5.2d, varied between 224  $\mu\text{mol kg}^{-1}$  and 273  $\mu\text{mol kg}^{-1}$  and was strongly anti-correlated with water potential temperature ( $r^2 = 0.93$  from linear regression, data not shown) because of the solubility dependence on temperature. The pattern of variation in potential temperature at the surface shown in figure 5.2a follows in fact the pattern of variation in  $c_{\text{sat}}(\text{O}_2)$ .  $c_{\text{sat}}(\text{O}_2)$  reached minimum values in summer when the stratified water became warmer (Damerell et al., 2016).  $c(\text{O}_2)$  and  $c_{\text{sat}}(\text{O}_2)$  measured in this way were then used to calculate daily averages,  $\overline{c(\text{O}_2)}$  and  $\overline{c_{\text{sat}}(\text{O}_2)}$ , that were then used in the calculation of  $F_{\text{as}}$ .

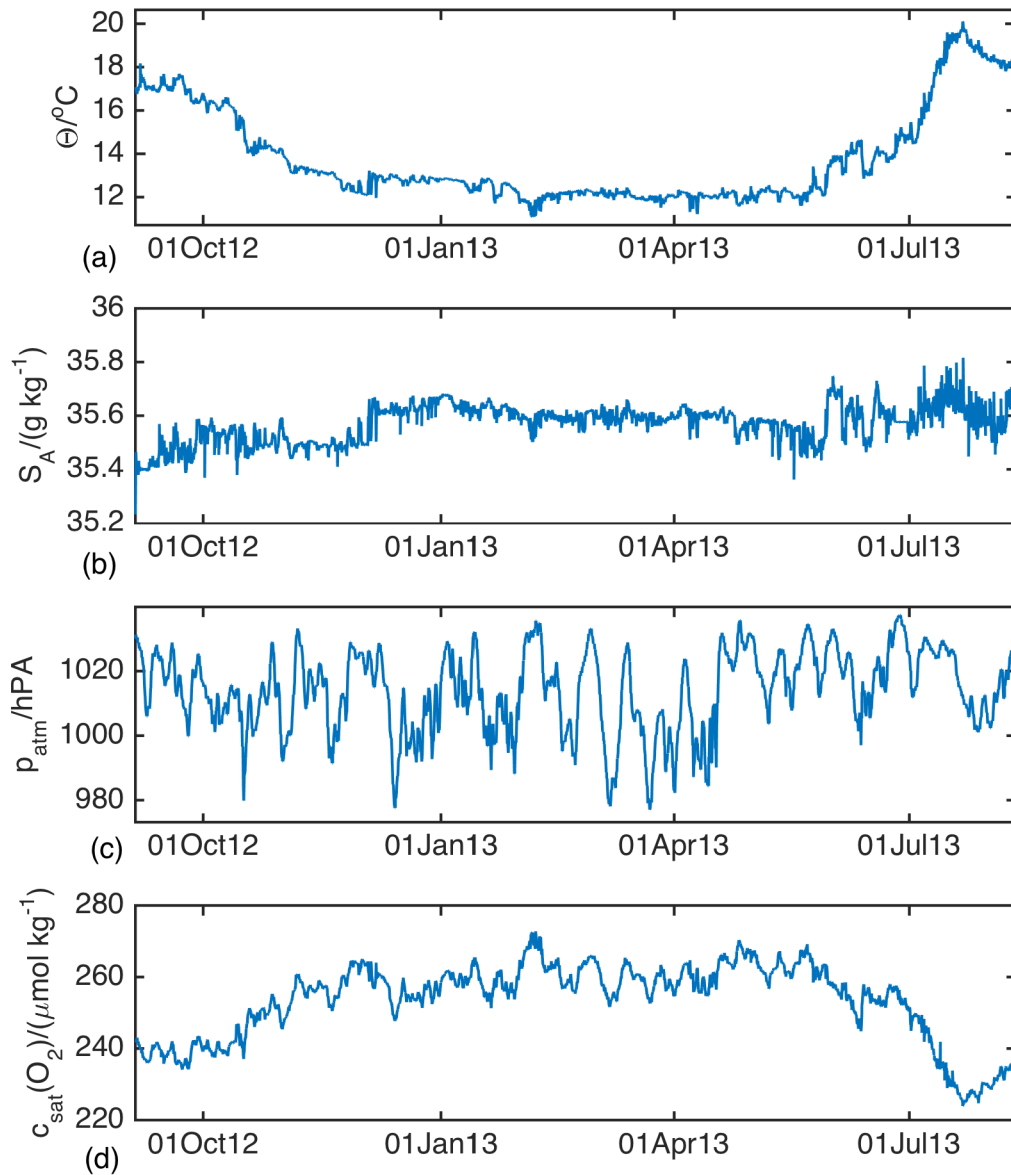


**Figure 5.3** (a) Mean potential temperature in the top 10 m of the water column for each profile in  $^\circ\text{C}$ ; (b) mean absolute salinity in the top 10 m of the water column for each profile in  $\text{g kg}^{-1}$ ; (c) atmospheric pressure from ERA-Interim reanalysis during each surface event; (d) mean oxygen saturation concentration in the top 10 m for each profile calculated according to García and Gordon (1992). When  $z_{\text{mix}} < 10$  m, values are the mean above  $z_{\text{mix}}$ .

The gas transfer velocity at a Schmidt number  $Sc = 600$  was parameterised following Nightingale et al. (2000) as in equation 5.6:

$$\frac{k_{600}}{\text{cm h}^{-1}} = 0.222 \left( \frac{\overline{U}_{10}}{\text{m s}^{-1}} \right)^2 + 0.333 \frac{\overline{U}_{10}}{\text{m s}^{-1}} \quad (5.6)$$

where  $\overline{U}_{10}$  is the daily averaged wind speed at 10 m. Wind speeds were derived from ERA-Interim reanalysis with the same resolution as the atmospheric pressure.  $U_{10}$  values for each profile were obtained interpolating the surfacing time and location to the nearest point in time and space in the ERA-Interim grid.  $U_{10}$  varied between  $0.4 \text{ m s}^{-1}$  and  $21.1 \text{ m s}^{-1}$  (figure 5.4a), while  $\overline{U}_{10}$  between  $1.5 \text{ m s}^{-1}$  and  $18.0 \text{ m s}^{-1}$  with a mean value of  $(8.7 \pm 3.3) \text{ m s}^{-1}$ .  $k_{600}$  ranged therefore from  $0.2 \text{ cm h}^{-1}$  to  $78 \text{ cm h}^{-1}$  (figure 5.4b).

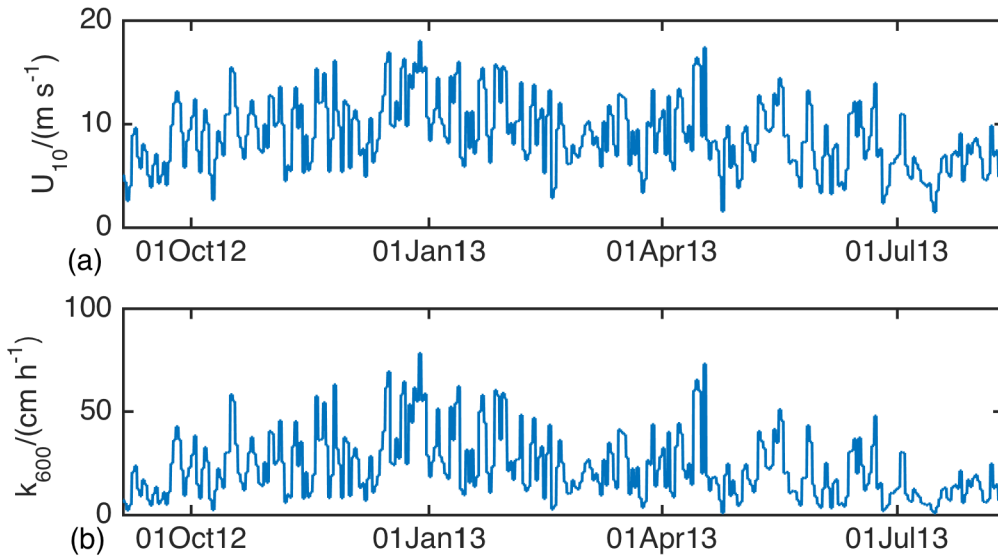


**Figure 5.4 (a) Daily averages of wind speed at 10 m above sea-surface from ERA-Interim reanalysis; (b)  $k_{600}$  as calculated based on wind speed plotted in (a).**

Values of  $k(\text{O}_2)$  for oxygen were obtained by scaling  $k_{600}$  using the Schmidt number ( $Sc$ ) dependence for rough surfaces (Raymond et al., 2012) as in equation 5.7.  $Sc(\text{O}_2)$  values depending on temperature were computed according to Wanninkhof (1992) as in equation 5.8. The water temperature,  $\theta$ , used to calculate  $Sc$  was the daily average of the mean potential temperature measured in the top 10 m of each profile (or above  $z_{\text{mix}}$  when  $z_{\text{mix}} < 10 \text{ m}$ ).

$$k(\text{O}_2) = k_{600} \left( \frac{Sc(\text{O}_2)}{600} \right)^{-0.5} \quad (5.7)$$

$$Sc = 1053.4 - \left[128\frac{\theta}{\text{°C}}\right] + \left[3.9918\left(\frac{\theta}{\text{°C}}\right)^2\right] + \left[0.050091\left(\frac{\theta}{\text{°C}}\right)^3\right] \quad (5.8)$$

$\theta$  varied between 11.3 °C and 19.8 °C (figure 5.5a) and resulted in  $Sc$  ranging from 594 to 946 (figure 5.5b).  $k_{O_2}$  ranged between 0.05 m d<sup>-1</sup> and 15.6 m d<sup>-1</sup> (figure 5.6).

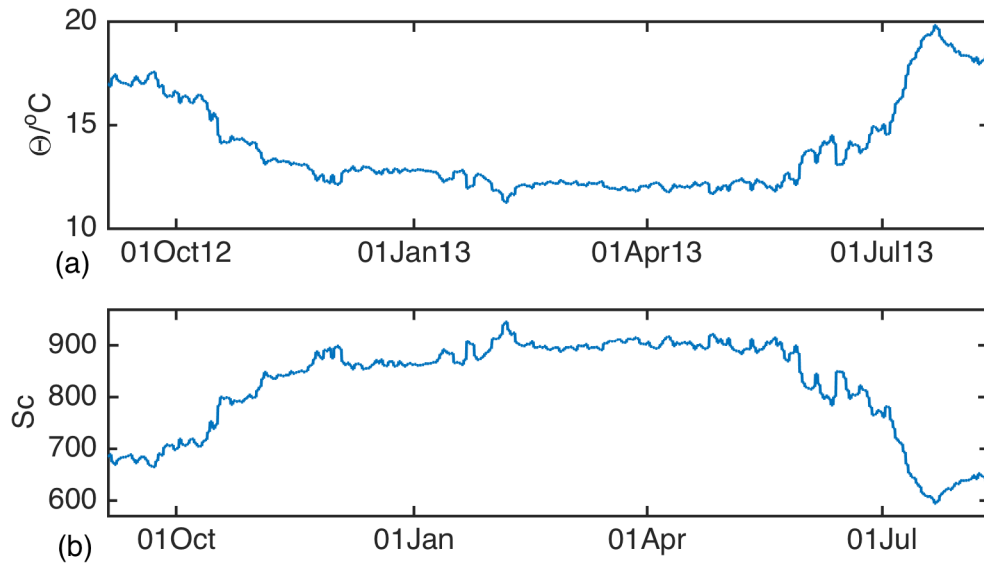


**Figure 5.5 Daily averages of (a) potential temperature used for Schmidt number calculation and (b) resultant Schmidt number time series.**

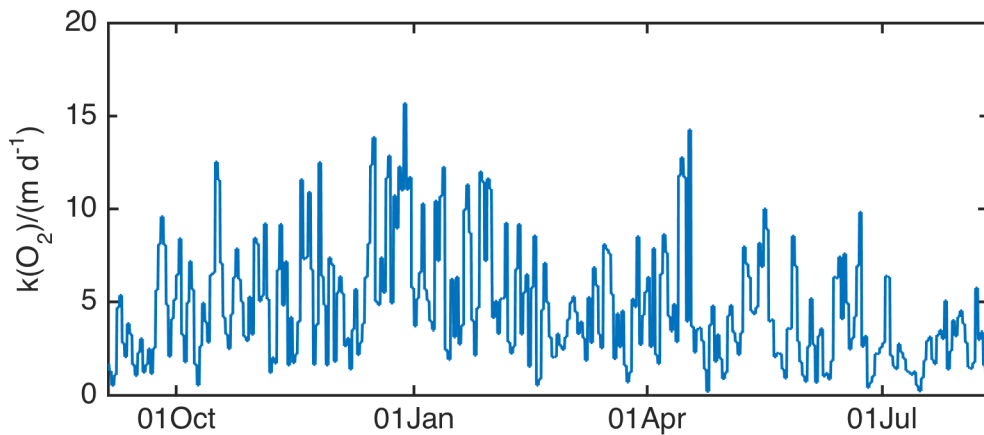


**Figure 5.6 Gas transfer velocities scaled for oxygen.**

In order to correct  $F_{as}$  for bubble injection, the formulation of Woolf and Thorpe (1991) was used as in equation 5.9.

$$F_{\text{as}} = k(\text{O}_2)[\overline{c(\text{O}_2)} - (1 + \Delta)\overline{c_{\text{sat}}(\text{O}_2)}] \quad (5.9)$$

where  $\Delta$  accounts for the increased  $c(\text{O}_2)$  and supersaturation due to the air bubble dissolution. Following Woolf and Thorpe (1991),  $\Delta$  is parameterized as a function of mean daily  $\overline{U_{10}}$  as in equation 5.10 and results are visible in figure 5.7b.

$$\Delta = 0.01 \times \left(\frac{\overline{U_{10}}}{9 \text{ m s}^{-1}}\right)^2 \quad (5.10)$$

The difference between  $\overline{c(\text{O}_2)}$  and  $\overline{c_{\text{sat}}(\text{O}_2)}$  (figure 5.7a) showed periods of supersaturation ( $\overline{c(\text{O}_2)} > \overline{c_{\text{sat}}(\text{O}_2)}$ ) at the beginning of the timeseries and after May. There was a long period of undersaturation ( $\overline{c(\text{O}_2)} < \overline{c_{\text{sat}}(\text{O}_2)}$ ) lasting from November until March as already discussed (see chapter 3) and then a period of quasi equilibrium from March to May.  $F_{\text{as}}$  varied between  $-193 \text{ mmol m}^{-2} \text{ d}^{-1}$  and  $155 \text{ mmol m}^{-2} \text{ d}^{-1}$ , with mean value of  $(-13 \pm 53) \text{ mmol m}^{-2} \text{ d}^{-1}$ . Negative values defined influx of  $\text{O}_2$  into the ocean and positive values defined outgassing into the atmosphere. As it is visible in figure 5.7c, the bubble influx was sometimes able to invert the sign of the flux, leading to ingassing in the water rather than outgassing. Overall, this region of the North Atlantic resulted to be a sink of oxygen rather than a source, with  $4.8 \text{ mol m}^{-2}$  of  $\text{O}_2$  absorbed by the ocean during the surveyed period. This is driven by pulses of strong influx due to high  $U_{10}$  (and correspondent high  $\Delta$ , figure 5.7b), but also by the late-occurring supersaturation. Furthermore, the data from 11<sup>th</sup> August 2013 were disregarded because of biofouling. This month was probably a productive period and therefore would have likely increased the magnitude of the annual outgassing if taken into account.

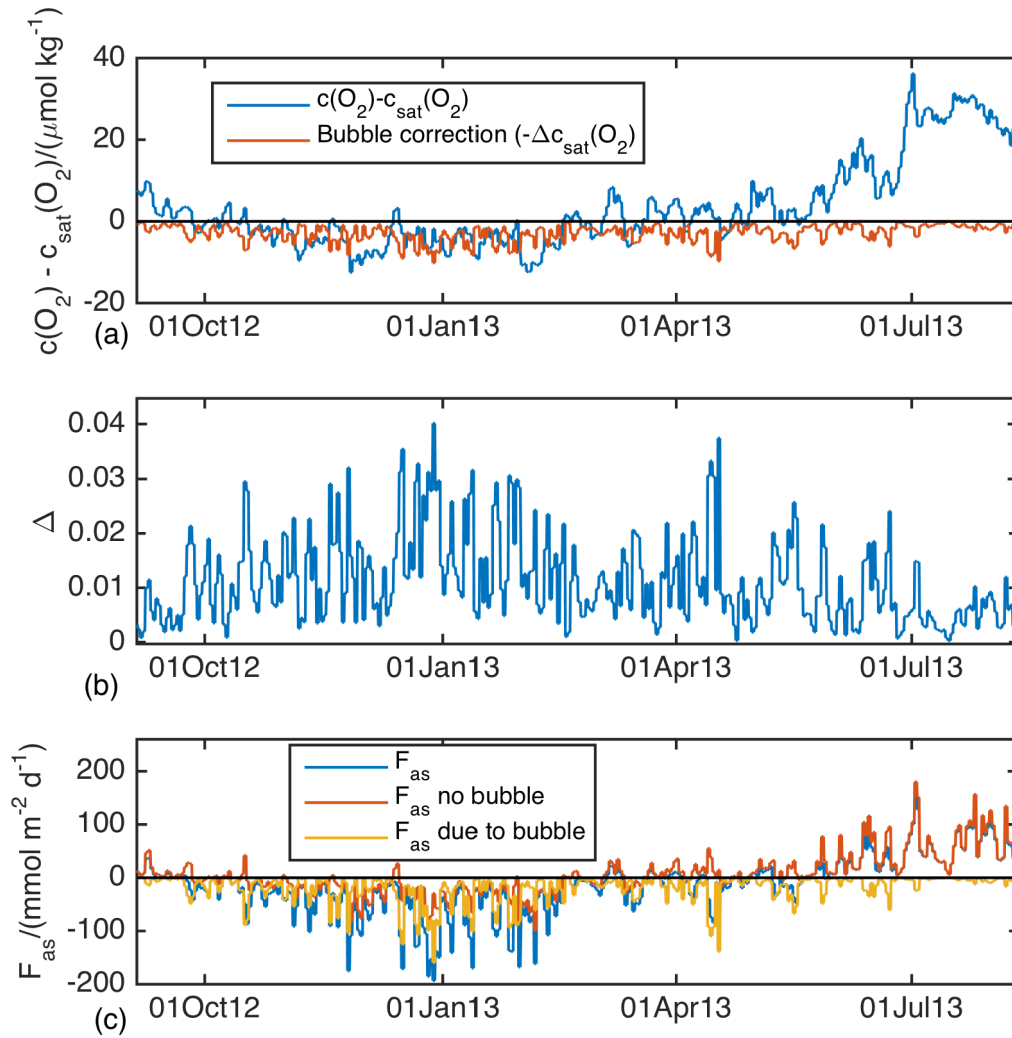


**Figure 5.7** (a) Difference between daily mean oxygen concentration and daily mean oxygen saturation concentration in the top 10 m used in the air-sea oxygen flux calculation (in blue) and magnitude of the bubble correction (in red). Positive values indicate supersaturation and negative values indicate undersaturation; (b) bubble supersaturation parameterisation ( $\Delta$ ) according to Woolf and Thorpe (1991); (c) air-sea oxygen flux (in blue), air-sea oxygen flux without considering bubble correction (in red) and air-sea oxygen flux due to bubbles (in yellow). Positive values indicate outgassing of oxygen in the atmosphere and negative values indicate influx of oxygen into the water column.

#### 5.2.4 Entrainment

Entrainment ( $E$ ) was defined as the change in  $I(\text{O}_2)$  that happens when the mixing layer,  $z_{\text{mix}}$ , deepens over time so that deeper water masses with different  $c(\text{O}_2)$  mix with the water

above. It corresponds to a flux of oxygen through  $z_{\text{lim}}$  when  $z_{\text{mix}}$  deepens from  $z_{\text{mix},1}$  at  $t_1$  to  $z_{\text{mix},2}$  at  $t_2$  and when  $z_{\text{mix},2}$  is below  $z_{\text{lim}}$ .

For each pair of consecutive profiles that matched these two conditions, the inventory of oxygen in  $z_{\text{mix},1}$ ,  $I_1(z_{\text{mix},1})$ , and the inventory of oxygen in  $\Delta z_{\text{mix}} = z_{\text{mix},2} - z_{\text{mix},1}$  at  $t_1$ ,  $I_1(\Delta z_{\text{mix}})$ , were computed as in equation 5.2.  $I_1(z_{\text{mix},1})$  and  $I_1(\Delta z_{\text{mix}})$  were assumed to fully mix. If no other processes were acting on the system, the expected  $I_{\text{exp2}}(z_{\text{mix},2})$  would be equal to the sum of  $I_1(z_{\text{mix},1})$  and  $I_1(\Delta z_{\text{mix}})$ , i.e.  $I_1(z_{\text{mix},2})$ , as

$$I_{\text{exp2}}(z_{\text{mix},2}) = I_1(z_{\text{mix},2}) = I_1(z_{\text{mix},1}) + I_1(\Delta z_{\text{mix}}) \quad (5.11)$$

Because  $E$  was measured when  $z_{\text{mix},2} > z_{\text{lim}}$  and water was fully mixed above  $z_{\text{mix}}$ ,  $I_{\text{exp2}}(z_{\text{lim}})$  was scaled as

$$I_{\text{exp2}}(z_{\text{lim}}) = I_1(z_{\text{mix},2}) \frac{z_{\text{lim}}}{z_{\text{mix},2}} \quad (5.12)$$

The entrainment was then calculated as the rate at which the difference between  $I_1(z_{\text{lim}})$  and  $I_{\text{exp2}}(z_{\text{lim}})$  was created:

$$E = \frac{I_1(z_{\text{mix},2}) \frac{z_{\text{lim}}}{z_{\text{mix},2}} - I_1(z_{\text{lim}})}{t_2 - t_1} \quad (5.13)$$

The entrainment flux could be positive or negative, corresponding to an increase or a decrease of the oxygen inventory due to mixing. In all the cases that did not match the condition of  $z_{\text{mix},1} < z_{\text{mix},2}$  and  $z_{\text{mix},2} > z_{\text{lim}}$ ,  $E$  was considered to be zero (figure 5.8b). When  $z_{\text{mix}}$  deepened, but remained above  $z_{\text{lim}}$ , a redistribution of the  $I(z_{\text{lim}})$  was assumed without any  $\text{O}_2$  flux occurring through  $z_{\text{lim}}$ . Also, when  $z_{\text{mix}}$  shoaled, the change in  $I(z_{\text{lim}})$  was assumed not to be related to any mixing with deeper water masses below  $z_{\text{lim}}$  and, therefore, no  $E$  was assumed to occur.

Fluctuation in  $z_{\text{mix}}$  linked to geographical variability and to the sensitivity of the threshold used for  $z_{\text{mix}}$  computation (see chapter 4) would affect  $E$  because it is not a symmetrical calculation and the contribution of  $z_{\text{mix}}$  deepening events is not compensated by a contribution of opposite sign during  $z_{\text{mix}}$  shoaling events, which contribute with a null value. In order to mitigate the effect of  $z_{\text{mix}}$  variability on  $E$  (and  $N$ ) calculation,  $z_{\text{mix}}$  values were smoothed with the ‘smooth’ function built in Matlab R2014b using the default option ‘moving’ with 5 points span (black line in figure 5.8a).

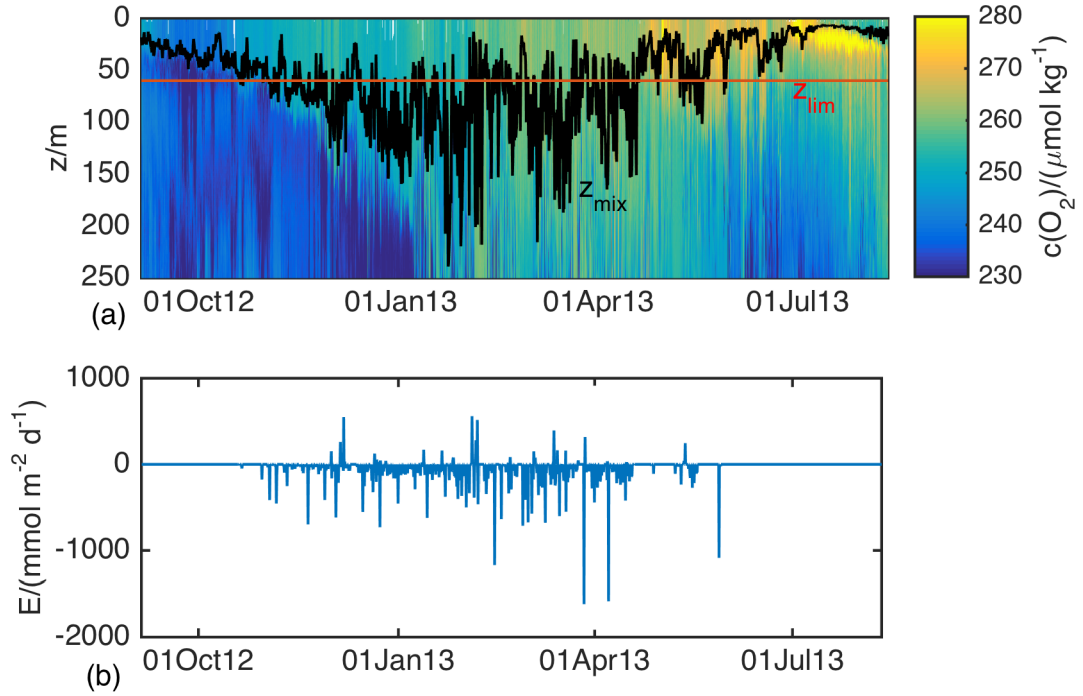


**Figure 5.8 (a) oxygen concentration versus depth with smoothed mixing layer depth (black line) and  $z_{\text{lim}} = 60$  m (red line); (b) entrainment flux, i.e. rate of change of oxygen inventory due to entrainment.**

### 5.2.5 Net community production calculation

Net community production was computed by rearranging equation 5.4 as in equation 5.14.  $N$  calculated between  $t_1$  and  $t_2$  was nominally associated with  $t_{1.5}$ ,  $N(t_{1.5})$ .  $t_{1.5}$  was measured as in equation 5.15.

$$N = \frac{\Delta I}{\Delta t} + F_{\text{as}} - E \quad (5.14)$$

$$t_{1.5} = \frac{t_1 + t_2}{2} \quad (5.15)$$

$F_{\text{as}}$  used to calculate  $N(t_{1.5})$  was the mean of the  $F_{\text{as}}$  measured at  $t_1$  and  $t_2$  (equation 5.17). Considering that the input of  $\text{O}_2$  into the ocean from the air-sea  $\text{O}_2$  flux would be mixed fully above  $z_{\text{mix}}$ ,  $F_{\text{as}}$  was scaled when  $z_{\text{mix}}(t_2) > z_{\text{lim}}$ :

$$F_{\text{as}} = \frac{z_{\text{lim}}}{z_{\text{mix}}(t_2)} \quad \text{for } z_{\text{mix}}(t_2) > z_{\text{lim}} \quad (5.16)$$

$$F_{as}(t_{1.5}) = \frac{F_{as}(t_1) + F_{as}(t_2)}{2} \quad (5.17)$$

This was an Eulerian rather than a Lagrangian study and therefore part of  $\Delta I$  between adjacent profiles was the signal of geographical heterogeneity (patchiness) and horizontal advection. The contribution of these processes to  $\Delta I$  and  $N$  was not estimated in the present study. Advection has been considered negligible in previous studies (Emerson et al., 2008; Nicholson et al., 2008; Nicholson et al., 2015) due to the rapid effect of air-sea  $O_2$  flux in equilibrating the concentration at the surface. However, this process has been recognised to have a significant impact on  $N$  estimates over time scales of days/months and for spatial scales less than 50 km (Alkire et al., 2014; Hull et al., 2016). These processes were considered to contribute randomly in the present study, increasing the noise in the values of  $\Delta I$  and  $N$  measured between consecutive profiles. This is visible in figure 5.2c where large positive values in  $\Delta I/\Delta t$  are followed by large negative values. These variations are due to the gliders entering and exiting mesoscale features, patches or parcels of water advected into the area and they cannot therefore be considered signals of biological activity. However, averaging individual  $N$  values over time windows longer than the time scale of these processes was assumed to cancel out their negative and positive contributions. In the present study running averages of  $N$  for overlapping 7 day-long bins were used as an estimate of biological activity. This bin length was chosen for two reasons. First, this was approximately the time it took for gliders to complete their butterfly- or hourglass-shaped transects, giving estimates of  $N$  for the entire surveyed area, disregarding geographical heterogeneity within it. Secondly, 7 days was also considered a time scale long enough for the gliders to enter and exit water parcels advected to the area since Alkire et al. (2014) in a similar glider experiment showed that the time scale of advection processes was around 4 days. Although Alkire's study was carried out in a more northerly area (59° N compared to 49° N), 4 days was considered to be indicative of the order of magnitude of the time scale of advection also in this study. The eventual residual influence of advection and geographical variability on 7 day-averaged  $N$  was then considered negligible. The arithmetic mean of all  $N$  values measured between midnight at the beginning of day 1 and midnight at the end of day 7 was nominally associated with the mid-point of the bin (noon of day 4). The effect of changing the averaging process to a bin length other than 7 days is analysed in section 5.3.6.

### 5.2.6 Average light in mixing layer

The amount of light experienced by the phytoplankton in the mixing layer was calculated based on the data from the NASA Moderate resolution Imaging Spectroradiometer

(MODIS, <https://modis.gsfc.nasa.gov/data/>), available for the whole year apart the period between 28<sup>th</sup> November 2012 and 14<sup>th</sup> January 2013.

The incident light at the surface was measured in einstein (E, moles of photons) per day and unit surface averaged over the study area. The incident light at the surface ( $L_0$ ) undergoes an exponential attenuation along depth governed by the attenuation coefficient  $k$ . The incident light that reaches depth  $z$  is therefore

$$L_z = L_0 e^{-kz}$$

Assuming a very efficient mixing in the mixing layer (above depth  $z_{mix}$ , see chapter 4), the light at which phytoplankton had been exposed was assumed to be the mean light in the mixed layer, measured as

$$\bar{L} = \frac{\int_0^{z_{mix}} L_0 e^{-kz} dz}{z_{mix}}$$

In the period when a deep chlorophyll maximum is present, the average amount of light at which phytoplankton is exposed was calculated not in the mixing layer, but above the euphotic depth since it aligns with the bottom limit of the deep chlorophyll maximum.

$$\bar{L} = \frac{\int_0^{z_{eup}} L_0 e^{-kz} dz}{z_{eup}}$$

The value  $L$  used from now on is the weekly averaged value of  $\bar{L}$  (figure 5.9b).

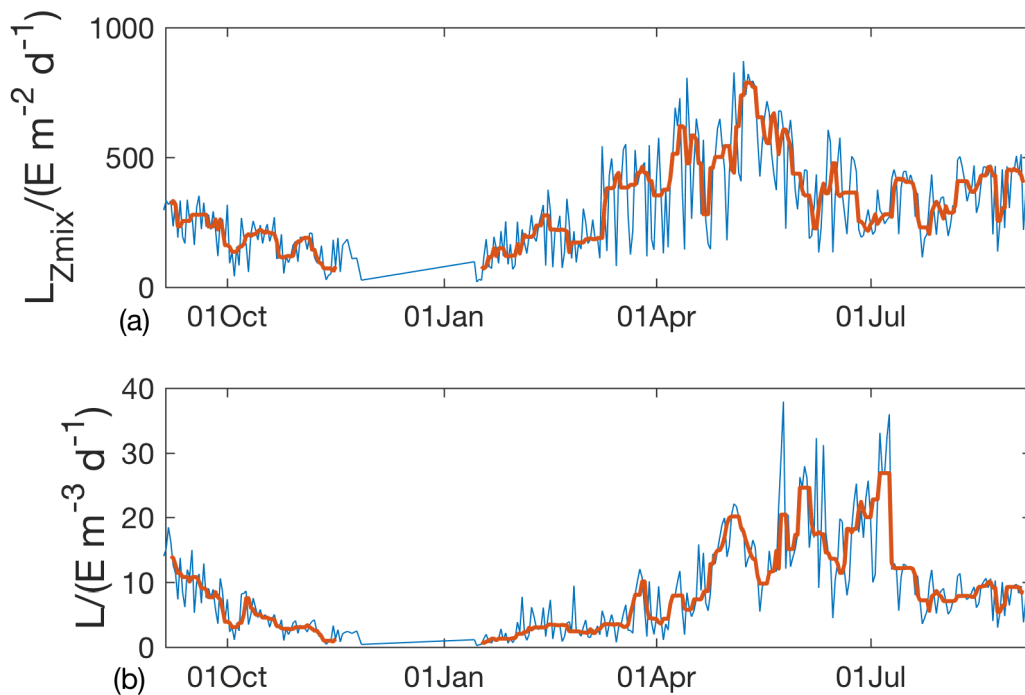


**Figure 5.9 (a) Time series of total amount of light intensity in einstein per unit surface and per day); (b) mean light in mixed layer. Daily values (blue) and weekly values (red).**

$L_o$  from MODIS ranged between 1 E m<sup>-2</sup> d<sup>-1</sup> to 60 E m<sup>-2</sup> d<sup>-1</sup>, with lowest values in January and highest ones in June-July. The pattern was sinusoidal as expected, but values seems to be high in the summer if compared to previous studies such as Boss and Beherefeld (2010) and Westberry et al. (2015), where maximum values stopped at ~40 E m<sup>-2</sup> d<sup>-1</sup>.

### 5.3 Results

As a guide for this section and for section 5.4, the values following the “±” symbol after mean values express standard deviations. Also,  $N$  is expressed in mmol m<sup>-2</sup> d<sup>-1</sup> as O<sub>2</sub> equivalents unless when stated for  $N$  as C equivalents.

#### 5.3.1 Year-long dataserries of net community production

The time series of  $N$  averaged in overlapping bins of 7 d is plotted in figure 5.10 along with the averaged values of  $\Delta I(z_{lim})/\Delta t$ ,  $F_{as}$  and  $E$ . The cumulative  $N$  between September 2012 and August 2013 is 6.4 mol m<sup>-2</sup> and the mean  $N$  was 19 mmol m<sup>-2</sup> d<sup>-1</sup>. These values showed net autotrophy in the area over a year cycle. The uncertainty associated to these values will be discussed in 5.3.6.

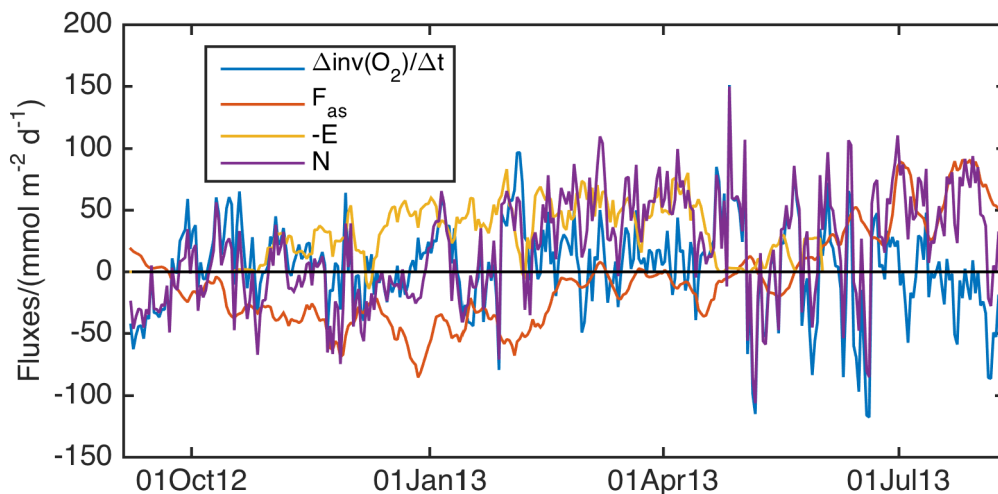


**Figure 5.10** Time series of (a)  $\Delta I(z_{lim})/\Delta t$  in blue, air-sea oxygen flux in red, entrainment in yellow and net community production in purple. All values are 7-day averages. Note that the sign of the entrainment is here inverted in order to represent its contribution to  $N$ .

The cumulative  $N$  was computed without the last month of the year, which was disregarded due to the biofouling. The shape of the biofouled profiles suggested however the presence of a deep chlorophyll maximum (DCM) above 60 m. This was considered evidence of production (data not shown). Biofouling and its progressive growth are another hint of a

productive phytoplankton community. The cumulative  $N$  of  $6.4 \text{ mol m}^{-2}$  was therefore an underestimation of the real production in the area.

Four periods were recognized within the cycle of  $N$  (figure 5.11). The first period had a series of positive peaks of  $N$  that were defined as the autumn bloom. The second period had mostly  $N < 0$  and was therefore defined as heterotrophic. The last two periods were productive (spring and summer). The difference between the two was at the passage from a month of oscillations between  $N > 0$  and  $N < 0$  to a regime of constant  $N > 0$ . In the last period also a DCM developed in the area. These periods are marked in figure 5.11 and will be discussed one by one in following sections.

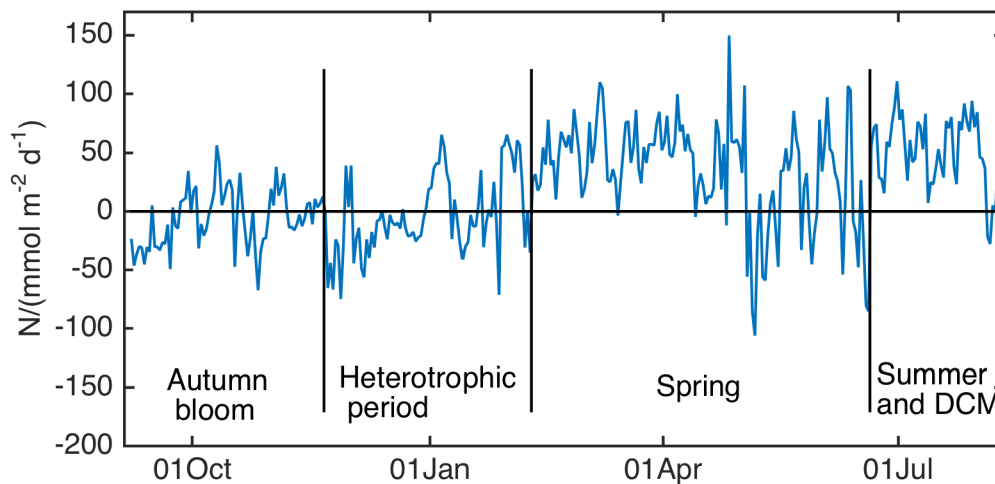


**Figure 5.11 Time series of net community production divided in the four periods analysed separately.**

### 5.3.2 Autumn bloom

The presence of productivity during autumn in this study area has been already shown by Rumyantseva et al. (2015) who analysed the variations of in situ chlorophyll  $a$  concentration,  $c(\text{Chl } a)$ , measured simultaneously with  $c(\text{O}_2)$  used in the present study. Their paper showed an increase in  $c(\text{Chl } a)$  after the passage of a storm in the area between September 24<sup>th</sup> and September 27<sup>th</sup> 2012. The start of this event coincided with an increase in  $N$  measured in the present study (first black vertical line in figure 5.12a). The community switched in fact from net respiration to net production. The independent analysis of  $I(\text{O}_2)$  and  $c(\text{Chl } a)$  therefore agreed in showing that this storm had a boosting effect on the phytoplankton. The present study was also able to quantify the magnitude of the bloom ( $16 \pm 12 \text{ mmol m}^{-2} \text{ d}^{-1}$ ) and could show the duration of this productive period, which lasted until 2<sup>nd</sup> October.

This increase in  $N$ , however, was not restricted to this first peak. The pattern was repeated after October 8<sup>th</sup> and 18<sup>th</sup> (figure 5.12a, vertical black lines), when  $U_{10}$  slowed down after sharp peaks (storms, figure 5.12c). On these two dates,  $N$  and  $c(\text{Chl } a)$  increased sharply (figures 5.12a-d).

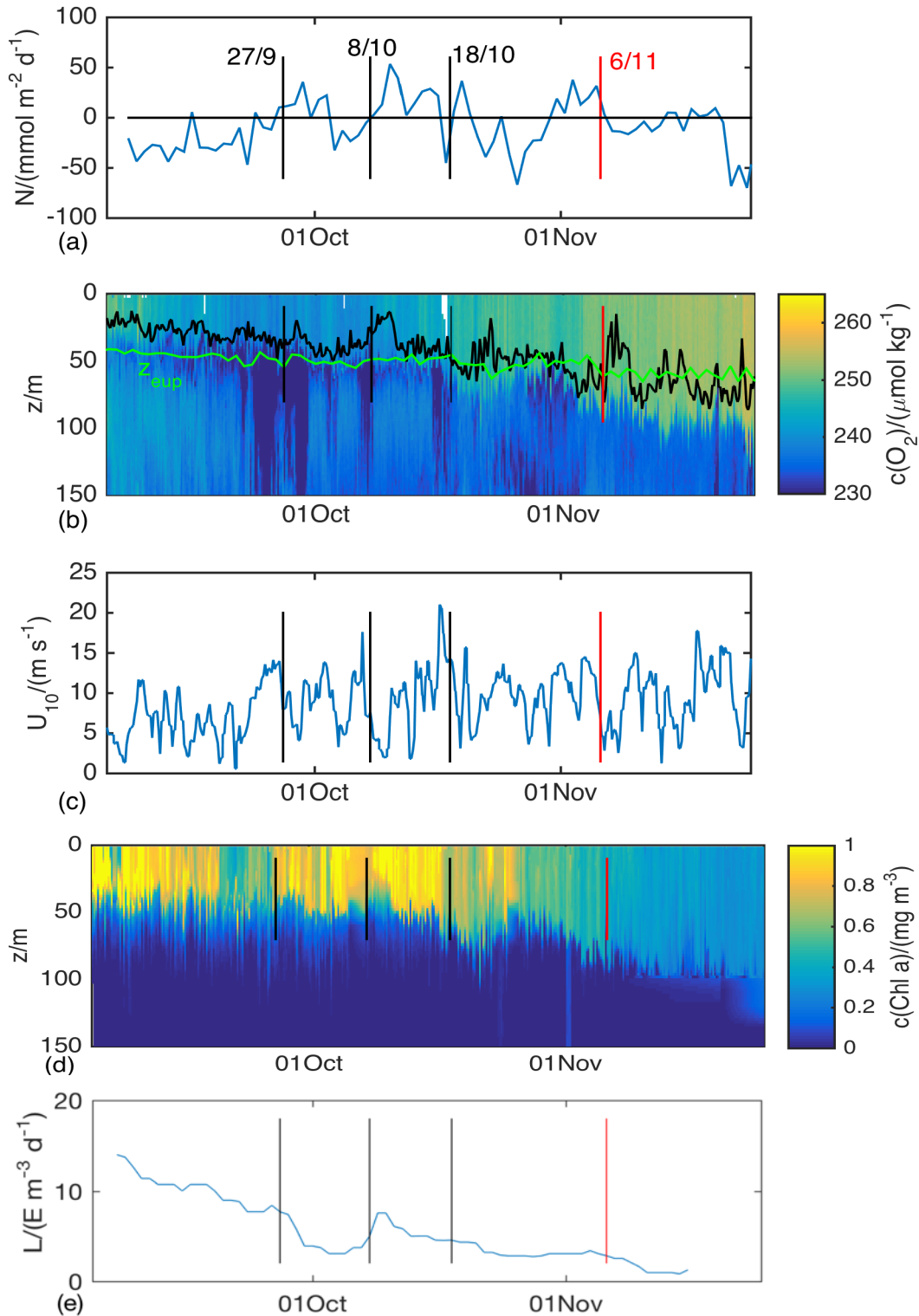


**Figure 5.12** (a) Net community production, (b) mixing layer and euphotic depths over oxygen concentration versus depth, (c) wind speed, (d) chlorophyll  $a$  concentration versus depth and (e) weekly mean light in the mixing layer during the autumn bloom. Black

**vertical lines indicate the end of wind speed increases (storms) after which there was an increase in biological productivity. The red vertical line marks a decrease in wind speed linked to the switch between net autotrophy and net heterotrophy during mixing layer depth shoaling.**

$N$  peaked again between 30<sup>th</sup> October and 6<sup>th</sup> November (vertical red line, figure 5.12a) and was linked to  $z_{\text{mix}}$  gradually deepening (figure 5.12b). However,  $N$  decreased to negative values when  $U_{10}$  decreased and  $z_{\text{mix}}$  shoaled, presumably reflecting a cut-off of nutrient supply from the deep. This also corresponded to a decrease in  $c(\text{Chl } a)$  as visible in figure 5.12d.

Considering only when  $N > 0$  in the autumn bloom, the mean  $N$  was  $(16.6 \pm 13.8)$  mmol  $\text{m}^{-2} \text{d}^{-1}$ , with the production of 432 mmol  $\text{m}^{-2}$ . This value is lower than the spring-summer bloom (see 5.3.4 and 5.3.5). These productive peaks were alternated with periods of net heterotrophy ( $N < 0$ ) and the mean  $N$  between 26<sup>th</sup> September and 22<sup>nd</sup> November was as low as  $(0.88 \pm 23)$  mmol  $\text{m}^{-2} \text{d}^{-1}$ .

During this period the mean amount of light in the mixed layer (figure 5.12e) decreases over time, reaching values below  $3 \text{ E m}^{-3} \text{ d}^{-1}$  after 6<sup>th</sup> November.

### **5.3.3 Heterotrophic period**

The period between 21<sup>st</sup> November 2012 and 9<sup>th</sup> February 2013 was dominated by  $N < 0$  (62 % of the time, figure 5.13a). The mean  $N$  for this period was  $(-3 \pm 34)$  mmol  $\text{m}^{-2} \text{d}^{-1}$ , showing net heterotrophy in the area. The consumption of  $-0.3 \text{ mol m}^{-2}$  was estimated.

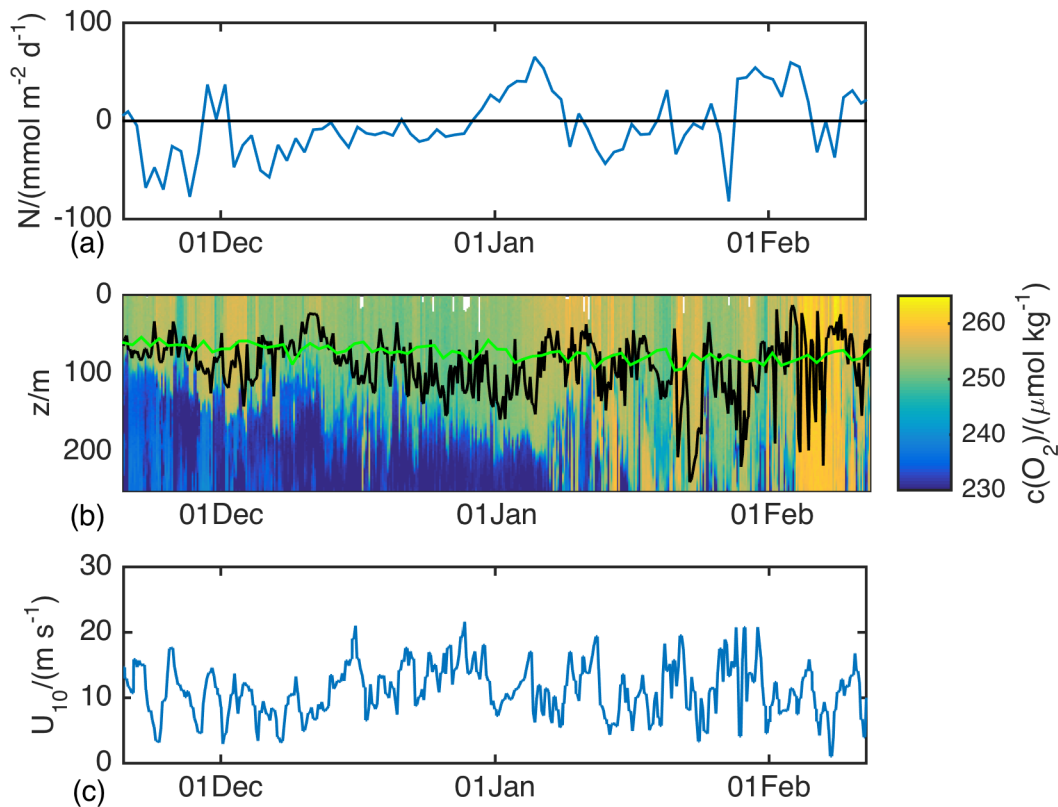


**Figure 5.13 (a) Net community production during the heterotrophic period; (b) oxygen concentration versus depth with mixing layer depth (black line) and euphotic depth (green line); (c) wind speed at 10 m from sea surface from ERA-Interim reanalysis.**

There were three productive peaks in this period. The first peak was between 29<sup>th</sup> November and 1<sup>st</sup> December 1<sup>st</sup> (figure 5.14a). It was linked to sharp changes in  $c(\text{O}_2)$  (figure 5.14b) occurring at the same time as a sharp changes in potential density (figure 5.14c). This suggested that there was heterogeneity in the area, with the glider entering and exiting a mesoscale feature.

A second peak developed between 30<sup>th</sup> December 2012 and 9<sup>th</sup> January 2013 (figure 5.13a) and was linked to  $z_{\text{mix}}$  gradually shoaling from below to above  $z_{\text{eup}}$  (figure 5.13b). This peak reached  $N > 65 \text{ mmol m}^{-2} \text{d}^{-1}$ . The third peak (28<sup>th</sup> January to 6<sup>th</sup> February) started when  $z_{\text{mix}}$  was very deep ( $z_{\text{mix}} > 220 \text{ m}$ , figure 5.13b). However,  $z_{\text{mix}}$  shoaled to the level of  $z_{\text{eup}}$  following a decrease in  $U_{10}$  (figure 5.13c).

Unfortunately, there are no data from MODIS about incident light at the surface in this period.

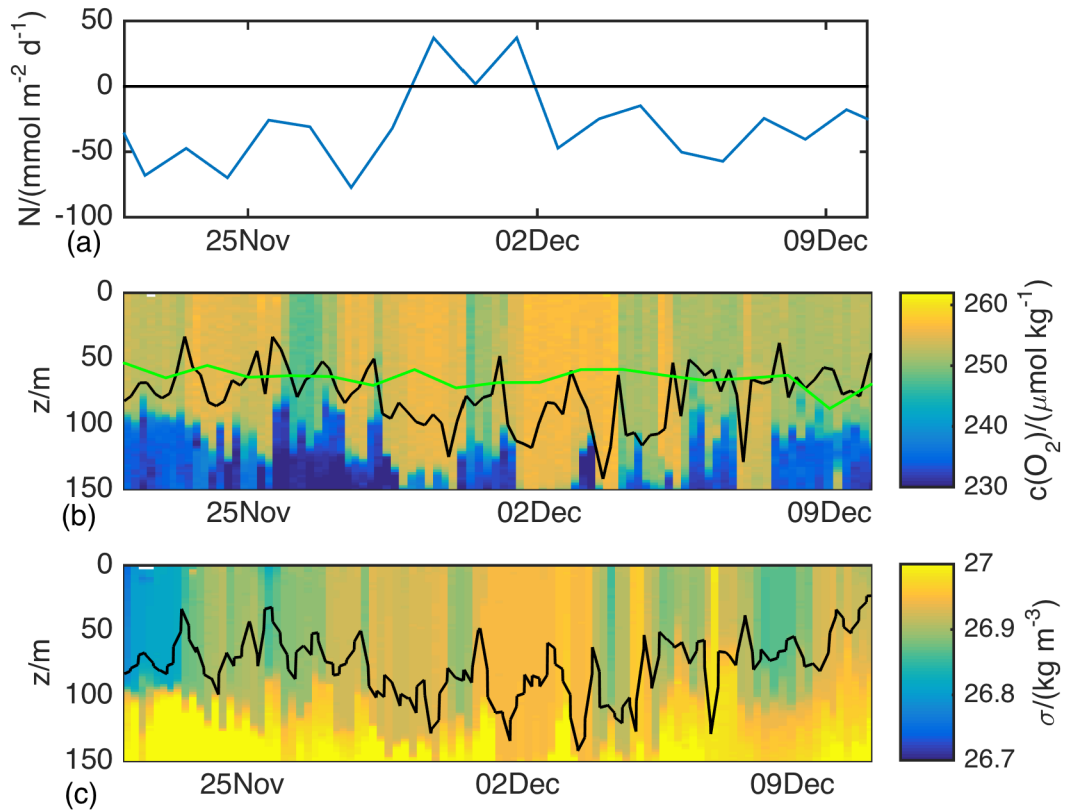


**Figure 5.14 (a) Net community production, (b) oxygen concentration and (c) potential density measured during the spike in net community production at the end of the autumn bloom. The exact correlation between variations in  $c(\text{O}_2)$  and  $\sigma$  suggests the presence of geographical features in the area.**

### 5.3.4 Spring

After February 9<sup>th</sup>,  $N$  stayed positive for a long period. This date was therefore chosen as the starting point for the analysis of the productive regime, which lasts until the end of the dataset in August. This productive period will be split in two parts. The first part, the spring, is discussed in this section and lasted until June 19<sup>th</sup>. The second part, starting from June 20<sup>th</sup>, is discussed in 5.3.5. Between these two parts, there is a period in which  $N$  oscillates between negative and positive values.

This spring season includes the last two thirds of the month of February. The area was autotrophic during these 130 days, with  $\text{O}_2$  production of  $4.5 \text{ mol m}^{-2}$  and a mean  $N$  of  $34 \text{ mmol m}^{-2} \text{ d}^{-1}$ . In this period, however, there was high variability ( $N$  standard deviation =  $44 \text{ mmol m}^{-2} \text{ d}^{-1}$ ) because production alternated with net respiration from the beginning of May.

The first peaks occurred when  $z_{\text{mix}}$  was at the level of  $z_{\text{cup}}$  (figure 5.15a). When  $U_{10}$  decreased between February 19<sup>th</sup> – 27<sup>th</sup> (figure 5.15c),  $z_{\text{mix}}$  shoaled (figure 5.15b). This peak of  $N$  includes the End-February Event (EFE) events described in chapter 4 that corresponds to the moment in which  $z_{\text{mix}}$  was the shallowest, allowing accumulation of Chl  $a$  and  $O_2$ . During the EFE event,  $N$  had its maximum values of the peak (figure 5.15a). This peak was also associated with the net heat flux ( $H$ ) becoming temporarily positive (figure 5.15e) and with an increase of  $c(\text{Chl } a)$  (figure 5.15d). Net heat flux was derived from ERA-Interim reanalysis summing up surface sensible heat flux, surface latent heat flux, surface net solar radiation and surface net thermal radiation. There is not any particular signal in the pattern of  $L$  (figure 5.15f)

A second peak occurred between 4<sup>th</sup> (red vertical line in figure 5.15) and 10<sup>th</sup> March. It was associated with a very moderate decrease in  $U_{10}$ , (figures 5.15c),  $H$  becoming temporarily positive again (figures 5.15d) and, then,  $z_{\text{mix}}$  shoaling (figure 5.15b) and a small increase in  $L$  (figure 5.15f). Another peak was visible starting on 16<sup>th</sup> March (light blue vertical line in figure 5.15) and started at the same time when  $z_{\text{mix}}$  started to shoal again (figure 5.15b).  $H$  was still negative (figure 5.15d), but from now on it started its gradual increase towards a period of more stable positive values. This suggests that this was a regime of gradual turbulence decrease. During this peak  $z_{\text{mix}}$  varied significantly and  $N$  showed small decreases in its magnitude every time  $z_{\text{mix}}$  deepened and peaks every time  $z_{\text{mix}}$  shoaled near the surface. Considering the duration and the increase in chlorophyll  $a$  (figure 5.15e), the peak between 16<sup>th</sup> March and 11<sup>th</sup> April might be considered a bloom, even if with a reduced magnitude.

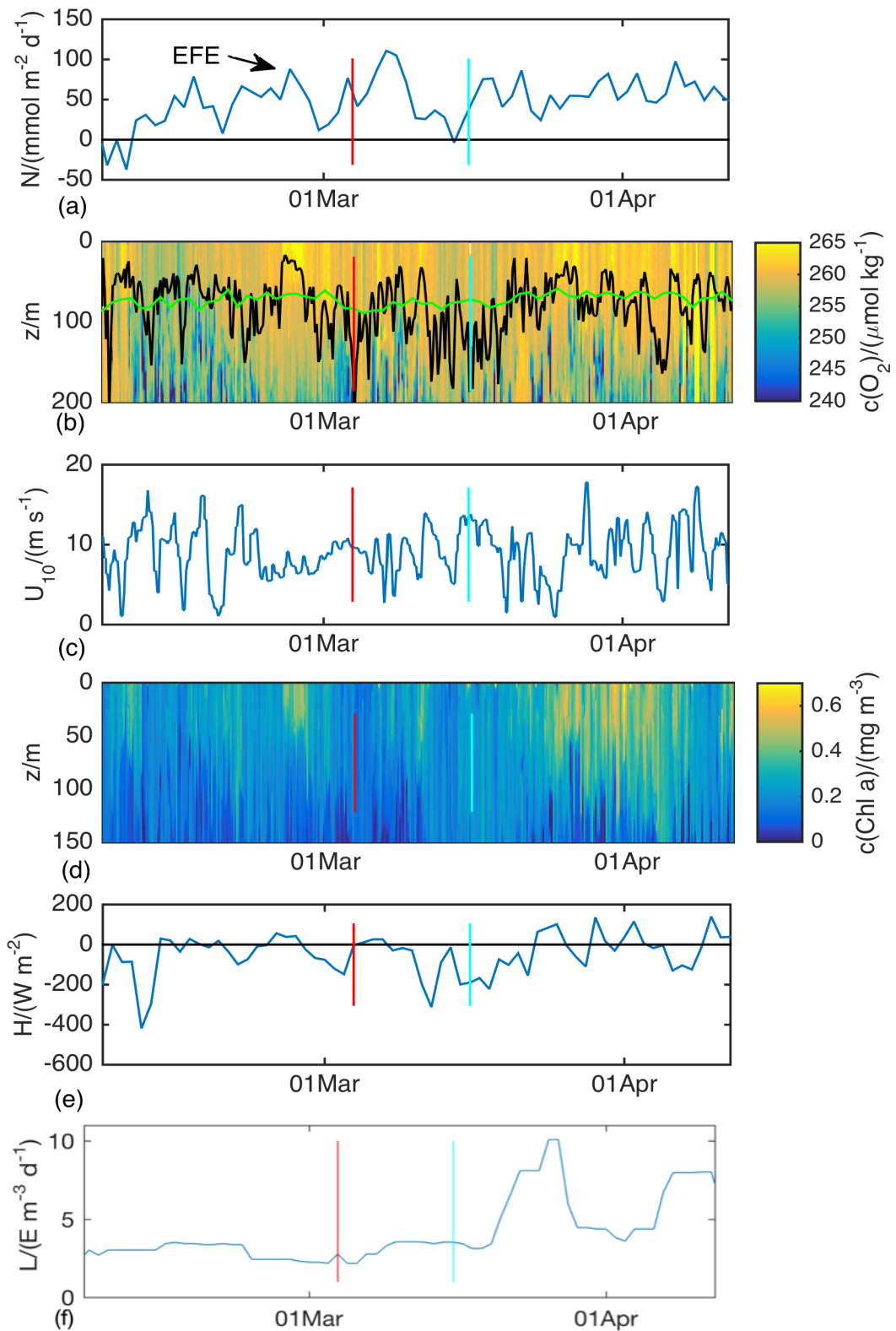


**Figure 5.15** (a) Net community production, (b) mixing layer and euphotic depths over oxygen concentration versus depth, (c) wind speed, (d) chlorophyll a concentration versus depth, (e) net heat flux and (f) weekly averaged light in the mixed layer between 9<sup>th</sup> February and 12<sup>th</sup> April. Red vertical line indicates the start of the peak on 4<sup>th</sup> March and light blue line the start of the peak on 16<sup>th</sup> March. In panel (a) is also shown the peak associated to End-February Event (see chapter 4).

Between 19<sup>th</sup> April (red vertical line on figure 5.16) and 27<sup>th</sup> May (green vertical line on figure 5.16),  $z_{\text{mix}}$  shoaled and stayed mostly stable above  $z_{\text{eup}}$  (figure 5.16e). This happened 10 days later than the switch of the heat flux from being mostly negative (water cooling down) to mostly positive (water warming up) (figure 5.16h). However, in these 10 days the  $U_{10}$  was high (figure 5.16c), delaying the decrease of turbulence needed to increase  $N$ , which started as soon as  $U_{10}$  decreased on 19<sup>th</sup> April (figure 5.16a). This was the main bloom of the spring period, with a big increase in  $c(\text{Chl } a)$  (figure 5.16b). The water retained at the surface started to increase its temperature (figure 5.16f) and decrease density (figure 5.16d) and then to accumulate phytoplankton biomass (figure 5.16b). However, after 15 days (on 3<sup>rd</sup> May, black vertical line in figure 5.16), there was a sudden decrease in  $N$  (figure 5.16a), followed by a decrease in  $c(\text{Chl } a)$  (figure 5.16b).  $z_{\text{mix}}$  was still very shallow and above  $z_{\text{eup}}$  (figure 5.16e). After five days (pink vertical line in figure 5.16),  $U_{10}$  increased again (figure 5.16c) and  $z_{\text{mix}}$  deepened (figure 5.16e). This was a gradual process, associated with little increases of  $N > 0$  (figure 5.16a) when  $U_{10}$  briefly decreased and  $z_{\text{mix}}$  briefly shoaled. The water below  $z_{\text{eup}}$ , in the absence of strong mixing, was likely richer in nutrients than above  $z_{\text{eup}}$ , where biological activity had probably led to nutrient depletion. Evidence of this is the peak starting on 16<sup>th</sup> May (light blue vertical line in figure 5.16). During this peak,  $U_{10}$  decreased (figure 5.16c) and  $z_{\text{mix}}$  shoaled in this low turbulence regime (figure 5.16e). This enhanced  $N$  again, producing a peak (figure 5.16a) and increasing  $c(\text{Chl } a)$  (figure 5.16b). This peak is linked to an increase in  $c(\text{O}_2)$  below  $z_{\text{mix}}$  rather than above, which is likely evidence of low nutrient concentrations at the surface (figure 5.16c). A slight increase of potential density (figure 5.16d) and slight decrease of temperature (figure 5.16f) are evidence of the mixing triggering this  $N$  peak when the wind deepens  $z_{\text{mix}}$ .

The peaks between 31<sup>st</sup> May and 19<sup>th</sup> June occurred during a very shallow  $z_{\text{mix}}$  (figure 5.17b) and  $N$  decreased below 0 when  $z_{\text{mix}}$  deepened down to  $z_{\text{eup}}$  and  $U_{10}$  increased (figure 5.17c). The main production oscillated between above and below  $z_{\text{mix}}$  showing heterogeneity in the area as also proved by variation of density at the surface (figure 5.17d). When  $N < 0$  on 10<sup>th</sup> June, there is the passage from production above  $z_{\text{mix}}$  to a DCM, with production in the latter weaker than heterotrophy at the surface.

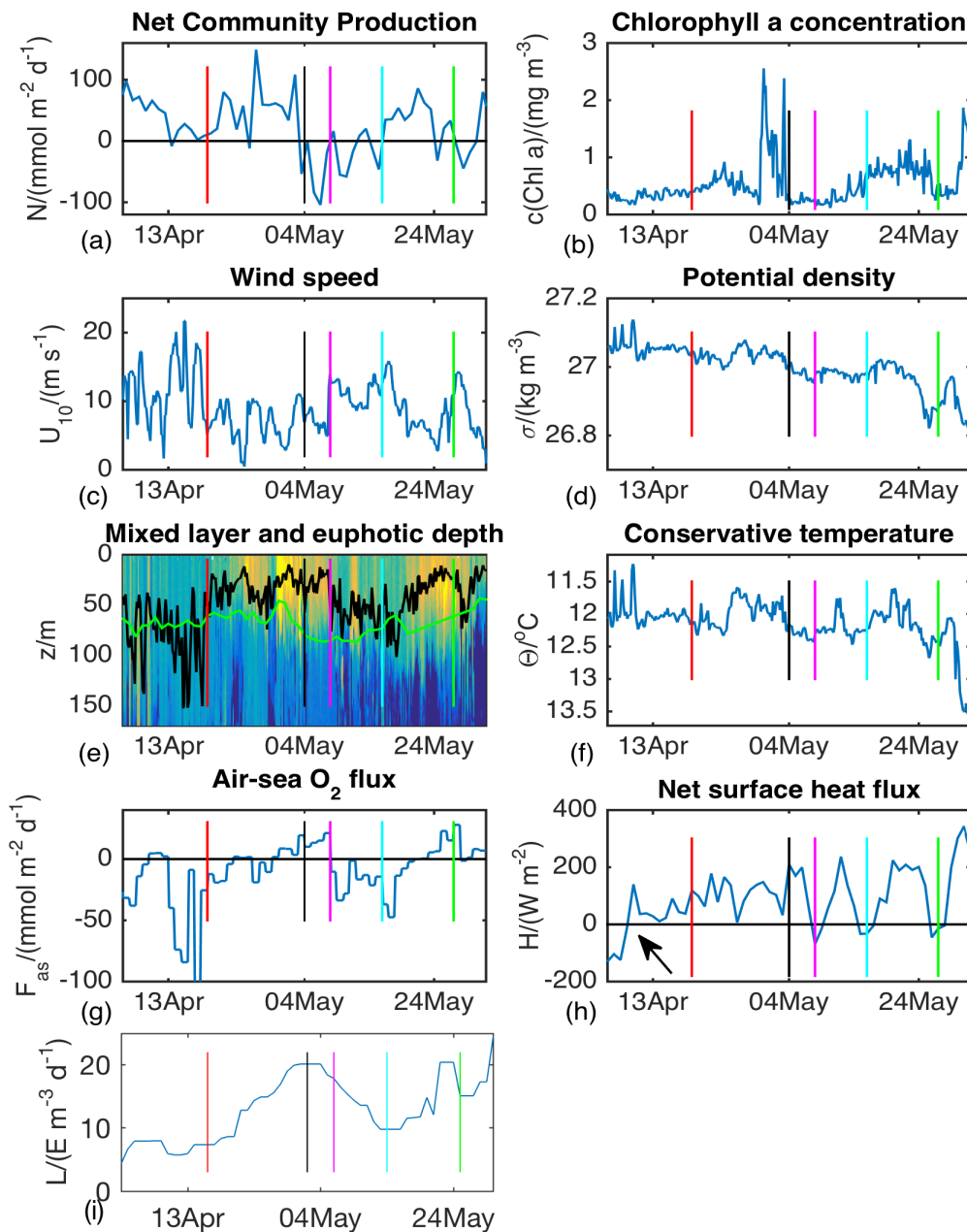


**Figure 5.16** Parameters between April 19<sup>th</sup> and May 27<sup>th</sup>. (a) Net community production above 60 m; (b) mean chlorophyll *a* concentration above 60 m (courtesy of Anna Rumyantseva, NOC); (c) wind speed (Era-Interim reanalysis); (d) mean potential density above 10 m; (e) mixing layer depth (in black), euphotic depth (in green) and oxygen concentration versus depth between 250  $\mu\text{mol kg}^{-1}$  and 275  $\mu\text{mol kg}^{-1}$ ; (f) mean temperature in the top 10 m; (g) air-sea flux including bubbles, (h) net surface heat flux (Era-Interim reanalysis) and (i) weekly mean light intensity in the mixed layer. Red line is the beginning of the peak (April 19<sup>th</sup>), black line is the beginning of the heterotrophic period (May 4<sup>th</sup>), pink line is the end of it (May 8<sup>th</sup>), light blue line is the deepening event replenishing the nutrients above  $z_{\text{mix}}$  (May 16<sup>th</sup>) and green line is the end of the productive peak (May 27<sup>th</sup>). The arrow in panel (h) marks the switch between a period of mean negative net surface heat flux and a period of mean positive net surface heat flux.

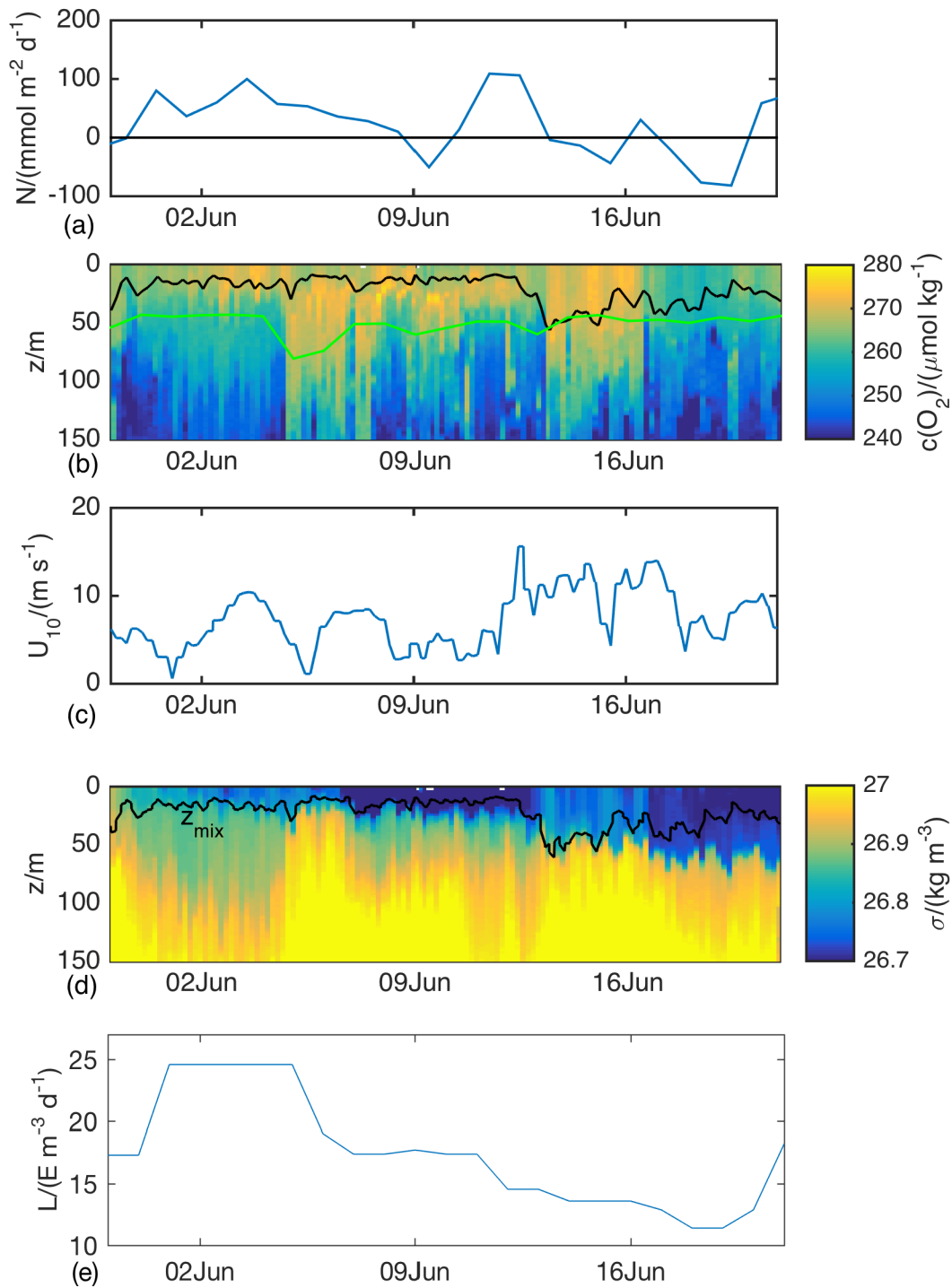


**Figure 5.17** (a) Net community production, (b) mixing layer depth and euphotic depth over oxygen concentration versus depth, (c) wind speed, (d) potential density versus depth with mixing layer depth and (e) weekly mean light intensity in the mixing layer between 31<sup>st</sup> May and 21<sup>st</sup> June.

Between the productive peaks discussed above (March 10<sup>th</sup>-15<sup>th</sup>, April 13<sup>th</sup> – 19<sup>th</sup>) and after the end of the latter one (May 28<sup>th</sup> -31<sup>st</sup>), increases in  $U_{10}$  caused  $z_{\text{mix}}$  to deepen below  $z_{\text{cup}}$  which coincided with decreases of  $N$  to negative values. These deepening events probably provided more nutrients to the surface.

This spring period was very productive with a mean  $N$  of  $(34 \pm 44)$  mmol m<sup>-2</sup> d<sup>-1</sup>. The total production for this period was estimated at 4.5 mol m<sup>-2</sup>. Six 7-day bins of  $N$  estimates were above 100 mmol m<sup>-2</sup> d<sup>-1</sup> with a maximum of 149 mmol m<sup>-2</sup> d<sup>-1</sup>.

### 5.3.5 Summer bloom and deep chlorophyll maximum

From 20<sup>th</sup> June until 27<sup>th</sup> July,  $N$  was relatively high and above zero (figure 5.18a). This corresponded to a period in which  $z_{\text{mix}}$  was always above  $z_{\text{cup}}$  (figure 5.18b). Until 23<sup>rd</sup> June,  $z_{\text{mix}}$  was close to  $z_{\text{cup}}$ , but afterwards  $U_{10}$  decreased (figure 5.18c) and  $z_{\text{mix}}$  became ~20 m shallower than  $z_{\text{cup}}$ . This enabled the development of a very productive bloom between 26<sup>th</sup> June and 4<sup>th</sup> July, both in terms of  $N$  and  $c(\text{Chl } a)$  (figures 5.18d and 3.3h).  $N$  decreased when  $U_{10}$  increased again and  $z_{\text{mix}}$  deepened. When  $U_{10}$  decreased, the column transitioned to a regime of low turbulence and strong stratification. At this point, after a first small increase, the production increased significantly from 8<sup>th</sup> July and led to the formation of a deep chlorophyll maximum (DCM, see review by Cullen, 2015). The limit of 60 m was able to include the subsurface oxygen- and chlorophyll-rich feature. During the time in which there was a DCM, the system remained productive until 4<sup>th</sup> August, when the productivity decreased along with the increase in  $U_{10}$  (figure 5.18c) and the arguably increase of turbulence in the water.  $z_{\text{mix}}$  deepened within the DCM, eroding it and mixing it with surface waters. The decrease of  $N$  at the end of DCM occurred at the same time as a decrease in the  $c(\text{Chl } a)$  visible in figure 5.18d.

The bloom at the end of June (figure 5.18b) had a mean  $N$  of  $(71 \pm 24)$  mmol m<sup>-2</sup> d<sup>-1</sup>, reaching 110 mmol m<sup>-2</sup> d<sup>-1</sup>. However, since it lasted only 8 days, it produced only 0.6 mol m<sup>-2</sup>. The DCM period instead lasted for 30 days (8<sup>th</sup> July to 8<sup>th</sup> August) producing 1.5 mol m<sup>-2</sup> with a mean  $N$  of  $(48 \pm 32)$  mmol m<sup>-2</sup> d<sup>-1</sup>. This summer period as a whole had a mean  $N$  of  $(47 \pm 36)$  mmol m<sup>-2</sup> d<sup>-1</sup> and produced 2.5 mol m<sup>-2</sup>.

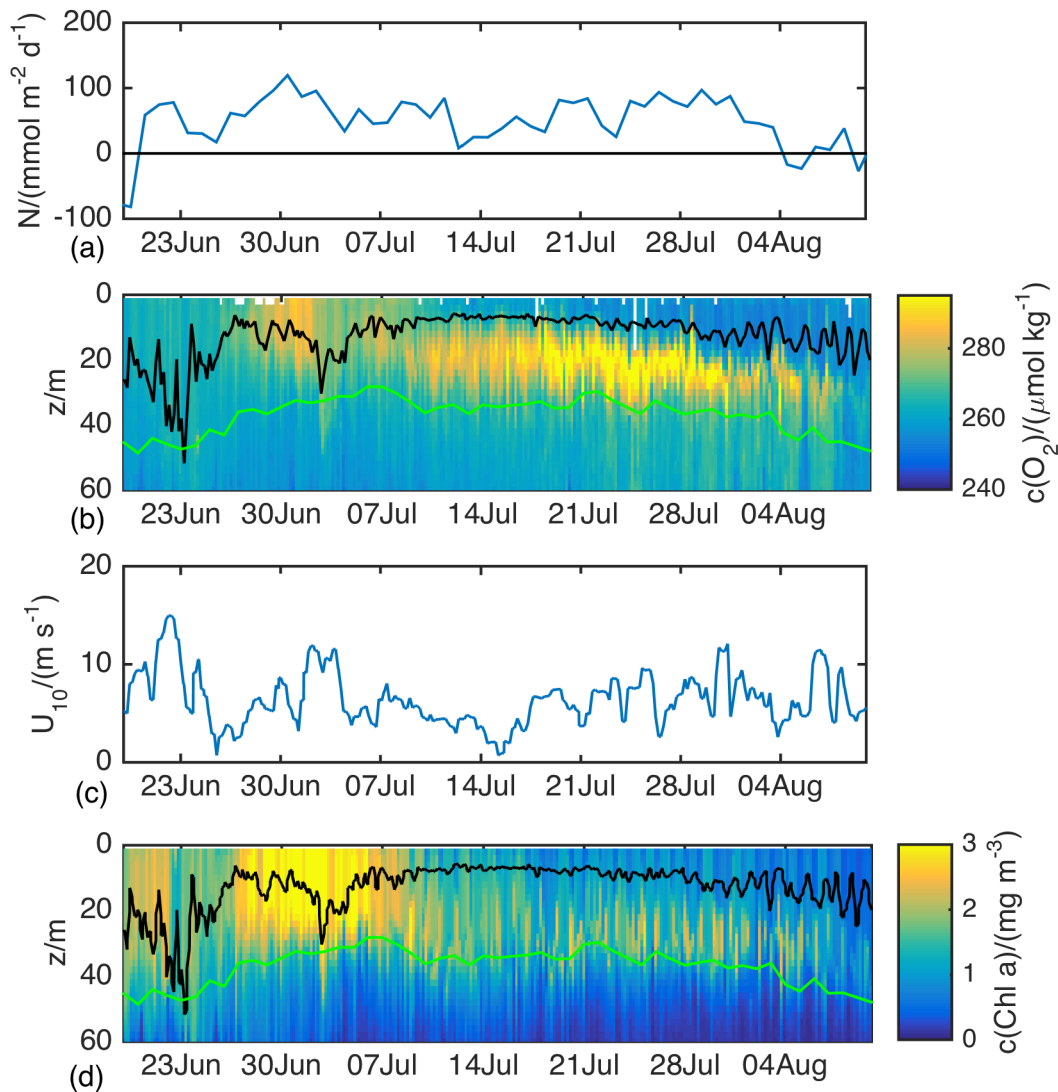


**Figure 5.18** (a) Net community production during the summer bloom and the deep chlorophyll maximum; (b) oxygen concentration over depth and time above  $z_{\text{lim}}$  with  $z_{\text{mix}}$  (black line) and  $z_{\text{eup}}$  (green line); (c) wind speed at 10 m above sea-surface from ERA-Interim reanalysis and (d) chlorophyll *a* concentration versus depth.

### 5.3.6 Method sensitivity

In order to test the sensitivity of the method and the uncertainties associated with the  $N$  estimates discussed above, a recalculation of the values was done changing some parameters and comparing the results with the time series discussed above.  $N$  was recalculated using the ascents instead of the descents and changing  $z_{\text{lim}}$ . Since the mean and standard deviation of  $z_{\text{eup}}$  were  $(60 \pm 15)$  m,  $N$  was recalculated using 45 m and 75 m as  $z_{\text{lim}}$  (figure 5.19).

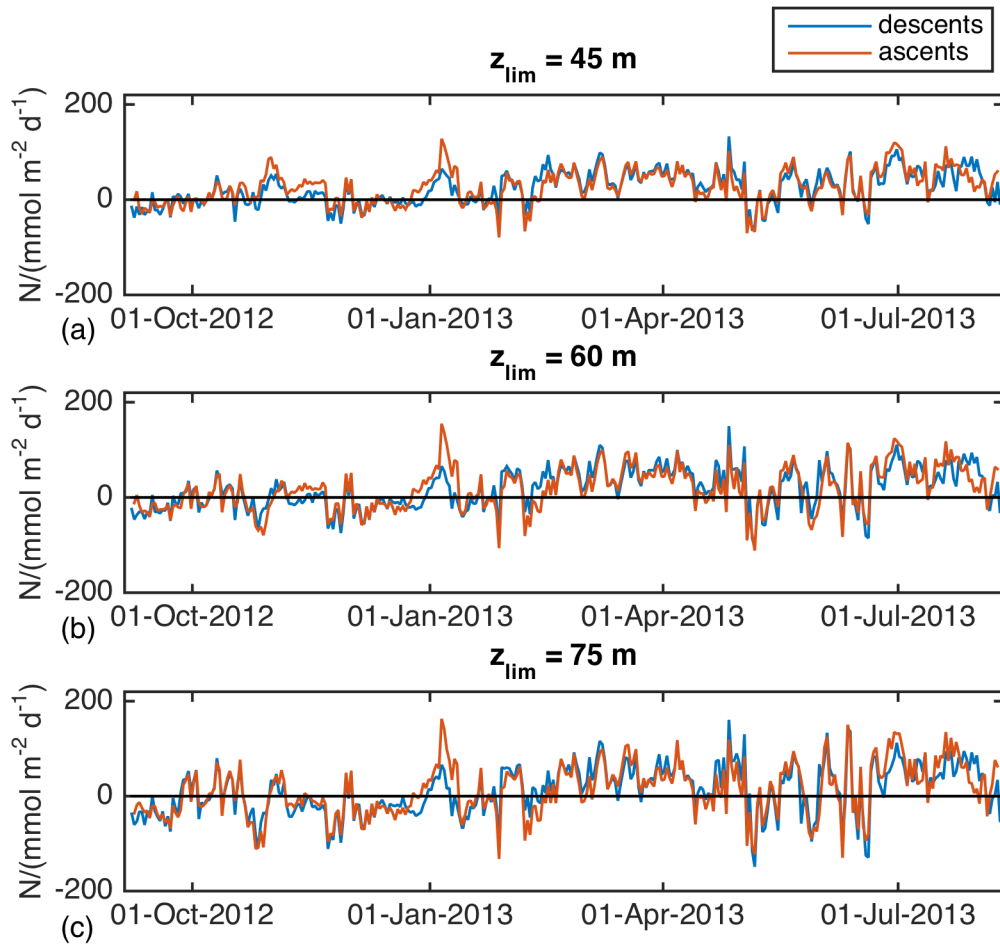


**Figure 5.19** Net community production time series measured above (a) 45 m, (b) 60 m and (c) 75 m using descents (blue lines) and ascents (red lines) from each glider dive

The pattern of  $N$  over time was conserved quite well in the time series based on both ascents and descents for each of the considered  $z_{lim}$ . The difference in the mean  $N$  between ascents and descents was 8 % for  $z_{lim} = 45$  m, 2 % for  $z_{lim} = 60$  m and 8 % for  $z_{lim} = 75$  m.

The differences at the end of the dataset series might be due to discrepancies between ascents and descents related to the very early stage of the biofouling. Despite this influence is small and not significant for the previous analysis, it would be more visible on  $N$  estimates since these are based on small differences in  $I(z_{lim})$  over time. In this case, considering that the biofouling affects less the descents than the ascents near the surface,  $N$  calculated on descents should be considered more reliable.

Mean and total cumulative  $N$  values obtained changing  $z_{lim}$  are listed in table 5.1.  $N$  measured using  $z_{lim} = 45$  m and  $z_{lim} = 75$  m were considered respectively an underestimation and overestimation of  $N$  in the euphotic depth. Their mean difference from  $N$  measured using  $z_{lim} = 60$  m was then used as a measure of the uncertainty associated to  $N_{eup}$  ( $\pm 6.3$  mmol m<sup>-2</sup> d<sup>-1</sup>,  $\pm 2.1$  mol m<sup>-2</sup>,  $\pm 30\%$ ).

**Table 5.1 Net community production mean, standard deviation and total sum calculated above 45 m, 60 m and 75 m.**

$z_{\text{lim}} / \text{m}$	Mean $N /$ $\text{mmol m}^{-2} \text{d}^{-1}$	Standard deviation $N /$ $\text{mmol m}^{-2} \text{d}^{-1}$	Total $N /$ $\text{mol m}^{-2}$
75 m	24.7	35.1	8.4
60 m	19.0	43.0	6.5
45 m	12.1	52.7	4.1

Another test was performed to assess the sensitivity of the method to the length of the averaging bins, which had been set to 7 d.  $N$  was recalculated binning individual  $N$  values between consecutive profiles over bins 1 d, 3 d, 5 d, 7 d, 9 d, 11 d, 13 d and 15 d long in order to cover a large range of possible choices. The maximum change with respect to the values averaged over from 7-day bins was obtained using 15-day bins, which increased mean  $N$  by 6.5 %. This value was one order of magnitude smaller than the uncertainty related to changes in  $z_{\text{lim}}$ . Therefore, the uncertainty of  $\pm 30$  % calculated before was still considered the valid one and the results from different bin-length were considered not significantly different.

**Table 5.2 Mean values of the net community production time series that were obtained averaging individual estimates between consecutive profiles over different bin lengths.**

Mean $N$ for time series obtained averaging over...							
1 day	3 days	5 days	7 days	9 days	11 days	13 days	15 days
19.0	18.9	18.9	19.0	19.2	19.6	20.0	20.3

The last test was done to assess the sensitivity of  $N$  estimates to its components (air-sea flux  $F_{\text{as}}$  and entrainment  $E$ ). The recalculation of  $N$  without considering  $F_{\text{as}}$  (figure 5.20a) increased  $N$  from  $19 \text{ mmol m}^{-2} \text{d}^{-1}$  to  $26 \text{ mmol m}^{-2} \text{d}^{-1}$  with a change of 37 %. The recalculation without  $E$  (figure 5.20b) decreased instead  $N$  to  $-10 \text{ mmol m}^{-2} \text{d}^{-1}$ , with a change of 155 %. This means that this method is more sensitive to  $E$  than  $F_{\text{as}}$ .

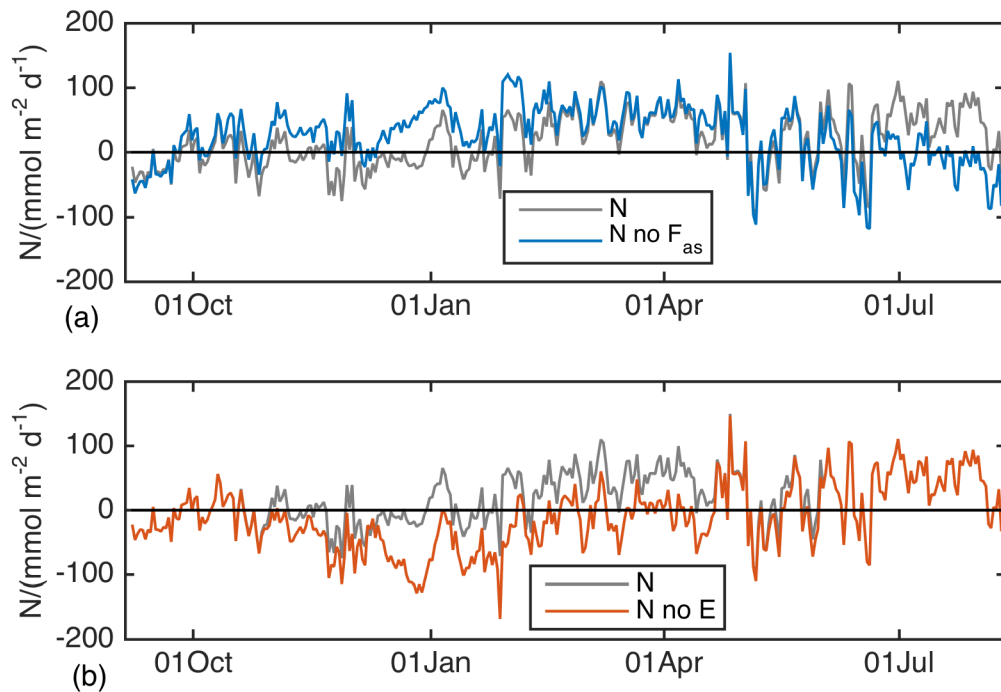


**Figure 5.20** Net community production measured above 60 m and averaged over 7 days-bins with values recalculated (a) not considering air-sea  $\text{O}_2$  flux (blue line) and (b) not considering entrainment flux (red line).

## 5.4 Discussion

### 5.4.1 Autumn

The presence of increased productivity during the autumn was already known for this part of the ocean and is usually referred as the “autumn bloom” (Colebrook, 1982; Longhurst, 1995; Dandonneau et al., 2004; Lévy et al., 2005; Neuer et al., 2007; Martinez et al., 2011).

In the present study, this bloom is actually characterised as a series of autotrophic peaks that were connected to the end of storms. Production enhancement after storms has already been seen in previous studies (Babin et al., 2004; Son et al., 2006; Wu et al., 2008, Rumyantseva et al., 2015). This is further evidence to the notion that nutrient pulses through the pycnocline sustain autumn blooms. These pulses are due to shear spiking (Rippeth et al., 2005, Rippeth et al., 2009; Williams et al., 2013, Rumyantseva et al., 2015) that is generated by the alignment of long lasting inertial oscillations produced by rapid change in wind stress (Pollard, 1980) with the direction of the wind stress. This suggests the presence of a nutrient depleted regime over shallow  $z_{\text{mix}}$ . It therefore makes sense that pulses of nutrients from the deep would stimulate

biological production. The present study showed that this dynamic was not limited to a single event, but that continuous pulses in this part of the year fuelled a series of productive peaks.

The fourth peak of this period is still related to the nutrient-deprived regime, but with another dynamic: the gradual deepening of  $z_{\text{mix}}$  in this case would have mixed nutrients from below enhancing the biological production until the 6<sup>th</sup> November when the decrease of  $c(\text{Chl } a)$  marks the passage to a less productive regime, with  $N$  not spiking even when  $z_{\text{mix}}$  shoaled. This peak seemed therefore to follow the classic dynamics according to which the nutrients input fuelling the autumn blooms are caused by the gradual deepening of  $z_{\text{mix}}$  (Marra et al., 1990; Findlay et al., 2006).

In the last peak, the increase of  $U_{10}$  was linked to the deepening of  $z_{\text{mix}}$  and, then, to an enhancement of production. However, in the previous post-storms bloom,  $U_{10}$  had to decrease before  $N$  could peak, while during the last peak the production increases before wind slows down. This relationship between  $U_{10}$  and  $N$  is not surprising. Dutkiewicz et al. (2001) has shown that increasing  $U_{10}$  can enhance  $N$  bringing nutrients towards the surface as well as decrease  $N$  moving phytoplankton cells deeper, where they consume more than they produce.

$N$  during the autumn was lower than in spring and summer. This is in line with the conclusions of Martinez et al. (2011) who showed an asymmetry in the magnitude of the blooms in different seasons. According to them, there was a shift from the 1980s, when autumn blooms had a magnitude comparable with the spring blooms, to the present days, when autumn blooms are smaller, as shown here. Martinez et al. (2011) linked this change to the delayed deepening of  $z_{\text{mix}}$  at the end of the summer that now happens later in the year than in the past. Lateral advection, presence of mesoscale events, change in zooplankton community or even the interaction with the wind and storms are other possible causes for the smaller magnitude of autumn blooms proposed by the same author. The present study brings further evidence to the conclusions of Martinez et al. (2011) of non-symmetric blooms between seasons, using *in situ* measurements to support their hypothesis, which was based on satellite data.

This autumn bloom happens in a period when the mean light at which the phytoplankton is exposed in the mixing layer decreases over time. At the beginning of this period, light is the high, but there is not production, which is an evidence for a nutrient deplete regime at the top of the water column. The pulses of nutrients due to the passage of storms increases  $N$  show that light is not a limiting factor for the production. However, after 6<sup>th</sup> November, light decreases below  $3 \text{ E m}^{-3} \text{ d}^{-1}$ , which seems to hamper the production even if the mixing layer shoals for a short period.

### 5.4.2 Heterotrophic period

The presence of regimes of negative  $N$  in the North Atlantic is known, but their magnitude and their impact on the annual metabolic balance of the basin are debated (Duarte et al., 2011, Duarte et al., 2013). Also, inter-annual variability in the metabolic state of the ocean at this time of the year is likely high. This is shown for example by the results of Ostle et al. (2015) who measured  $N$  based on basin-scale observations of  $c(\text{O}_2)$  at the surface between December 2011 and February 2013. The findings of their study are relevant for the present study because their ‘zone 2’ overlapped temporally and spatially with the glider survey at the PAP site analysed here. They found monthly average  $N > 0$  throughout 2012, confirming constant autotrophy in the basin as found also by Neuer et al. (2007). However, the following year they measured low  $N$  (not statistically different from zero) during December-January and net heterotrophy in February, showing that datasets longer than one year are able to pick up this interannual variability in the sign of  $N$ .

The first peak of  $N > 0$  in this period (figure 15.13a) was linked to the glider crossing a mesoscale feature. The averaging process was probably not able to fully eliminate the signal of this geographical heterogeneity in  $N$  because the feature stayed in the area longer than one week. The feature crossed by the glider had higher  $c(\text{O}_2)$  and part of this might be due to production. However, the density of the water was lower and an increase in  $c(\text{O}_2)$  was explainable by solubility effect (higher  $c_{\text{sat}}(\text{O}_2)$ ). This peak was therefore probably overestimating  $N$ .

The second peak started when  $z_{\text{mix}}$  stopped deepening and shoaled again above  $z_{\text{eup}}$ . This showed that the phytoplankton community was reacting to the decrease in turbulence and the fact that this peak was interrupted when the wind speed increased again is an evidence of this. This is also the case for the third peak of this period, with  $N$  increasing when  $z_{\text{mix}}$  stopped its deepening process and shoaled again.

The consumption estimated in the heterotrophic period ( $0.3 \text{ mol m}^{-2}$ ) was one order of magnitude lower than the production estimates in the rest of the year. The present study therefore shows that the presence of potentially protracted periods of net heterotrophy in this region of the ocean has only a moderate impact on the production on annual scale.

### 5.4.3 Spring

Spring is the time of the year in which the phytoplankton community in the area is supposed to bloom. The PAP site is located in the North Atlantic Drift (NADR) province where, according to Longhurst (1998), blooms are expected in May. The timing of this bloom and its intensity have high interannual and geographical variability (Ueyama and Monger, 2005; Henson et al., 2006; Henson et al., 2009; Kahru et al., 2011; Zhai et al., 2013; Cole et al., 2015)

and this explains why, despite being one of the most studied systems in the history of oceanography, the dynamics of the North Atlantic spring bloom has not been fully understood as yet.

Using a series of parameters ( $U_{10}$ ,  $z_{\text{mix}}$  in relation to  $z_{\text{eup}}$ , temperature, density, net heat flux, light) with  $N$ , it was possible to explain the variations of production over time. This period seems to be divided into two regimes. Before 3<sup>rd</sup> May,  $N$  increased when  $z_{\text{mix}}$  shoaled above  $z_{\text{eup}}$ , which corresponded to periods of positive net surface heat flux. This led to long periods of positive  $N$ , such as after 16<sup>th</sup> March and after 19<sup>th</sup> April. In particular, between 19<sup>th</sup> April and 3<sup>rd</sup> May the mean  $L$  in the mixing layer increased constantly. On 3<sup>rd</sup> May, despite shallow  $z_{\text{mix}}$  and high  $L$ , there was a sharp decrease in  $N$  to negative values and  $c(\text{Chl } a)$  decreased as well (figure 5.16). Considering the high light intensity experienced by the phytoplankton in this period, nutrient limitation is the most likely cause of this decrease in  $N$  and  $c(\text{Chl } a)$ . Another evidence of this nutrient limitation is the fact that after 3<sup>rd</sup> May  $N$  increased only after mixing events with deeper waters and when small DCMs were present below  $z_{\text{mix}}$ . Between 16<sup>th</sup> and 27<sup>th</sup> May,  $z_{\text{mix}}$  shoals after a deep period and  $L$  increases again. This system, full of nutrients again and plenty of light, is productive in terms of  $N$  and  $c(\text{Chl } a)$ . Lately in the season appears instead DCMs that have been associated to nutrient limitation at the surface in previous studies (Klausmeier and Litchman, 2001; Klausmeier et al., 2007, Denaro et al., 2013). The water at the surface during the first regime was then considered replete, while it was considered nutrient limited during the second regime. This would therefore be the cause of the oscillations between  $N > 0$  and  $N < 0$  in the second part of the spring, with phytoplankton becoming more productive when it gets access to nutrients. At the end of this period (from 1<sup>st</sup> to 20<sup>th</sup> June) there were rapid transitions between accumulation of oxygen at the surface and below  $z_{\text{mix}}$ . These were probably related to geographical patchiness and show the heterogeneity of the biological production at this time of the year.

In section 5.4.5,  $N$  estimates during the spring are compared with previous studies. In section 5.4.6 the information gathered about the start of the small and large bloom in this season are used to discuss how the present study fits in the frame of the existent theories about bloom start.

#### **5.4.4 Summer and deep chlorophyll maximum**

Just as for the second regime in spring, changes in nutrient concentrations can be assumed to be related to the variations of  $N$  seen during the summer.  $z_{\text{mix}}$  deepened between 20<sup>th</sup> and 23<sup>rd</sup> June, which probably mixed nutrient-rich waters to the surface. Until 19<sup>th</sup> June there was also net heterotrophy and the respiration process might have mobilised nutrients. These processes would explain what fuelled the bloom between 26<sup>th</sup> June and 4<sup>th</sup> July. The mean  $N$

reached  $70 \text{ mmol m}^{-2} \text{ d}^{-1}$  during this bloom, but then decreased when  $U_{10}$  increased, suggesting a role for turbulence and the  $z_{\text{mix}}$  deepening in the  $N$  decrease. The new decrease of nutrient concentration due to this bloom arguably led to new nutrient limitation at the surface, which explained the DCM.

The DCM developed and lasted for over 30 days in the area when there was a well stratified column with a very shallow  $z_{\text{mix}}$ . The presence of this feature has been related in past studies to nutrient limitation at surface (see chapter 1, section 1.4.1) and this is therefore evidence for the actual presence of this regime in this period.  $N$  measured during the period when DCM was present was high, accounting for 38 % of the cumulative  $N$  estimated above  $z_{\text{lim}}$  between September 2012 and August 2013. The formation of the DCM is usually related to increases in biomass (Beckmann and Hense, 2007) and/or to adaptation in the chlorophyll content of the cells (Fennel and Boss, 2003). As discussed in section 1.4.1, this feature is a challenge for  $N$  calculations based on remote measurements or on the sampling of the plankton community for *in vitro* incubation. The analysis of the colour of the ocean as measured by satellite-borne sensors can be biased if the DCM is shallower than 45 m depth such as the one showed in the present study (Stramska and Stramski, 2014), *de facto* decoupling fluorescence readings from the real value at surface.  $N$  estimates obtained with the method used in the present study should therefore be of higher accuracy and reliability than the ones based on remotely sensed ocean colour.

The demise of the DCM is also probably related to nutrient limitation.  $z_{\text{mix}}$  started to deepen, but was still above  $z_{\text{cup}}$  and so this decrease in  $N$  was not related to the limitation of light. Instead,  $U_{10}$  increased and the vertical turbulence exposed the plankton to the nutrient-limited water coming from above, lowering the production. Evidence of this is the decrease of  $c(\text{Chl } a)$  happening at the same time.

From the end of June,  $F_{\text{as}}$  is coupled to  $N$  values. The entrainment in this period is null or negligible, thanks to the strong stratification that allows the formation of the DCM. This  $F_{\text{as}}$  can be then considered biologically induced, as found by Kaiser et al. (2005) for systems with negligible vertical and horizontal mixing. The analysis of  $L$  in the mixing layer for this period is more complicated because the attenuation is affected by the presence of the DCM. However, the presence itself of the DCM shows that light is not a limiting factor because there is production at tens of meters below the surface.

As for the spring, a detailed comparison of  $N$  measured in this period with previous studies is carried out in section 5.4.5.

#### 5.4.5 Production estimates

The classically defined productive period (spring and summer together) spanned from 9<sup>th</sup> February to the start of the biofouling on 11<sup>th</sup> August and had a production of  $(7.1 \pm 2.1)$  mol m<sup>-2</sup> with a mean  $N$  of  $(39 \pm 41)$  mmol m<sup>-2</sup> d<sup>-1</sup>. The seasonal production was converted to C equivalents using the photosynthetic quotient (PQ) of 1.5 as in Alkire et al., (2014) and resultant  $N_C$  values are listed in Table 5.3.

During the productive period this area produced  $N_C = (4.8 \pm 1.4)$  mol m<sup>-2</sup> (uncertainty based on  $\pm 30\%$  as calculated in 5.3.6). This value is lower than the value of  $(6.4 \pm 1.1)$  mol m<sup>-2</sup> estimated by Körtzinger et al (2008a), but fits well with the value of  $(4.6 \pm 0.9)$  mol m<sup>-2</sup> estimated by Frigstad et al. (2015) for the PAP area in a similar time span.  $N_C$  is instead higher than the 3.0 mol m<sup>-2</sup> estimated by Ostle et al. (2015) on a basin scale and the value of 2.1 mol m<sup>-2</sup> estimated by Alkire et al. (2014) in a more northerly area (59 °N instead of 49 °N). The results therefore suggest that the region of the PAP site is particularly productive. In these comparisons it must be considered that previous studies considered shorter productive periods.

Considering the whole time series, the PAP site was autotrophic between September 2012 and August 2013, with net O<sub>2</sub> production of  $(6.4 \pm 1.9)$  mol m<sup>-2</sup> a<sup>-1</sup> ( $4.3 \pm 1.3$  mol m<sup>-2</sup> in C equivalents). This value is probably an underestimation of the real value due to the exclusion from the calculation of the last month, which very likely had a productive DCM. However, these values are higher than previous annual  $N_C$  estimates of Quay et al. (2012) who calculated 2.8 mol m<sup>-2</sup> or by Neuer et al. (2007) who calculated 3.3 mol m<sup>-2</sup> as a mean between 1996 and 2000 in a more southerly area. The annual production estimated in the present study is, however, similar to the 5.5 mol m<sup>-2</sup> estimated by Ostle et al. (2015) for 2012 in region 2 (where PAP site is located). This area was found in their study to be the most productive sector in the basin. This similarity, however, hides a big temporal difference since Ostle et al. (2015) seems to underestimate production during the productive period and overestimate it during the winter.

**Table 5.3 Net community production in carbon equivalent,  $N_C$  (adapted and expanded from Alkire et al. 2014). In bold are the results from studies analysing  $N_C$  directly, while in normal characters are the estimates in oxygen unit converted to  $N_C$  using the photosynthetic quotient, PQ. In these cases the PQ value used for the conversion is indicated.**

Study	Year	Period	$N_C$ mmol m <sup>-2</sup> d <sup>-1</sup>	PQ used	Notes
This study	2013	Autumn Bloom	11	1.5	PAP station, top 60 m (whole year does not include the period with biofouling)
		Spring	22		
		19 Apr – 3 May	54		
		Summer	31		
		26 Jun – 4 Jul	46		
		DCM	32		
		Spring+Summer	26		
		Whole year	13		
<b>Bender et al., 1992</b>	<b>1989</b>	<b>13 days between Apr and May</b>	<b>52</b>		<b>JGOFS-NABE</b>
<b>Robertson et al., 1992</b>	<b>1989</b>	<b>29 May – 5 Jun</b>	<b>42-34</b>		<b>JGOFS-NABE</b>
<b>Körtzinger et al., 2008a</b>	<b>2004</b>	<b>May –Aug</b>	<b>25</b>		<b>PAP station</b>
<b>Körtzinger et al., 2008b</b>	<b>2005</b>	<b>mid May -Jul</b>	<b>50-70</b>		<b>Labrador Sea</b>
Alkire et al. 2012	2008	Apr May (average)	66 115 (90)	1.5	Early Bloom Main Bloom
Alkire et al. 2014	2008	Apr-Jun 3-26 Jun	25 43	1.5	Considerind Alkire et al. 2012 +postbloom
Ostle et al., 2015	2012	Apr - Sep	16	0.8	Basin-wide, region 2 (see Ostle et al., 2015)
<b>Frigstad et al., 2015</b>	<b>2003- 2012</b>	<b>Feb - July</b>	<b>25 (72-6)</b>		<b>PAP site, MLD</b>

The differences among studies are probably due to a series of factors as annual variability in the area, but also by the differences in the method used for the calculations. It has also to be considered that  $N$  estimated in the present study was an estimate of the production in the euphotic layer and, therefore, studies analysing variation at greater depths than  $z_{\text{eup}}$  are expected to be lower because of the respiration happening deeper. For example, some of the studies compared here (e.g., Frigstad et al., 2015; Ostle et al., 2015) analyse the changes above  $z_{\text{mix}}$  rather than above  $z_{\text{eup}}$ , while others (i.e. Körtzinger et al., 2008a) use deeper  $z_{\text{lim}}$  (230 m) for the calculation of  $I(\text{O}_2)$ . The temporal patchiness of productivity also increases the variability among  $N$  estimates, especially when values are averaged over subsamples in the same productive period (Alkire et al., 2012).

#### **5.4.6 Revisiting the Sverdrup hypothesis**

The analysis of physical and biogeochemical parameters in relation to  $N$  showed that several mechanisms were able to explain the passage of  $N$  from negative to positive values, phenomenon here used as definition of bloom. Classically, pigment fluorescence has been considered a proxy for the production of the area and high production has been linked to chlorophyll accumulation in the water column. Using direct values of  $N$ , as in the present study, instead of defining plankton blooms in terms of chlorophyll fluorescence shows that in the area there is an alternation of heterotrophy and autotrophy throughout the whole year. It is therefore interesting to investigate what causes all these fluctuations in  $N$ , rather than focusing only on the classically defined fluorescence blooms.

Comparing the temporal variations of  $N$  with the patterns of different processes shows that several mechanisms trigger autotrophic periods according to the time of the year in which they develop. In a regime of nutrient limitation, as showed by low  $N$  despite high  $L$ , phytoplankton seems to increase its production following two mechanisms. During the autumn, a series of peaks in  $N$  were related to pulses of nutrients created by the interaction between wind and surface currents (see Palter, 2015; Rumyantseva et al., 2015). However, a later peak matches a more classical theory according to which autumn blooms are fuelled by the gradual deepening of the mixed layer into nutrient-richer waters (Marra et al., 1990; Findlay et al., 2006). This dynamic seems also to explain peaks of  $N$  at the end of the spring when a regime of low nutrient concentration can be assumed as well. The importance of nutrients in these parts of the year is shown by the fact that at the beginning of the time series and in some periods of the spring,  $L$  is higher but there is no production. This clearly shows that light is not the limiting factor.

The discussion about what triggers autotrophy when nutrients are not limited is more complicated. The classical Sverdrup Hypothesis (Critical Depth Hypothesis or CDH, Sverdrup, 1953) sees light as driving factor: the plankton community is productive when the mixed layer is shallower than the critical depth, which is a depth defined by light above which total production exceeds total respiration. Since 1953, a long discussion has flourished to confirm or confute the Sverdrup CDH and new hypotheses have been proposed based on its weak points such as the assumption that phytoplankton is rapidly mixed by strong turbulence. In particular, new hypotheses focus on the influence that turbulence has on the ability of the phytoplankton to access the light. According to the Critical Turbulence Hypothesis (CTH, Huismann, 1999), high turbulence displaces the plankton at a faster rate than its growth rate, moving it in portion of the water column where it consumes more than produces. When turbulence decreases below a critical value, plankton produces faster than it is displaced and this leads to blooms (i.e., accumulation of oxygen and chlorophyll at the surface). Taylor and Ferrari (2011) linked the turbulence to the net heat flux, suggesting that the inversion from negative heat flux (water cooling) to positive heat flux (water warming) and the consequent shut down of convective mixing is a reliable parameter to predict the start of the bloom on interannual analysis (Heat Flux Hypothesis or HFH). Enriquez and Taylor (2015) proposed another model linking the variations in turbulence induced by the wind stress and by the water cooling (negative net heat flux leading to convective mixing) to the depth of the mixing layer. They predicted that when the mixing layer shoals, the phytoplankton would respond with an increased growth rate (and then increased production).

The present study compared the variations of  $N$  with temporal patterns of  $z_{\text{mix}}$ ,  $U_{10}$ ,  $L$ ,  $H$ , temperature and density. It suggests a mechanism that merges Sverdrup's CDH, Huismann's CTH and the model proposed by Enriquez and Taylor (2015). When nutrients are not limiting, decreasing wind speed and positive net heat flux decreases the turbulence in the water. In February, during the EFE event (section 4.3.6), there is higher productivity at the very top of the water column despite  $z_{\text{mix}}$  calculated on density is much deeper. This dynamic reflects the one proposed by Huismann, where production is faster than turbulence and oxygen and chlorophyll accumulates in the best lit part of the water column. This leads to a shoaling mixing layer measured by oxygen not followed by the one measured by density that remains deep. Other times mixing and mixed layers (measured respectively by oxygen and density) shoal together. In some cases, this is linked with a rapid increase of  $N$  without any substantial variation of  $L$  as, for example, on 4<sup>th</sup> March (red line in figure 5-14). Positive  $N$  in absence of an increase in  $L$  confirms Enriquez and Taylor (2015), where the leading factor is the mixing layer depth, which follows switches to positive  $H$ . However, later in the season when  $H$  is constantly positive, the accumulation of chlorophyll  $a$  and the positive  $N$  happen when  $z_{\text{mix}}$  shoals above  $z_{\text{cup}}$  and  $L$  increases, a mechanism that recall Sverdrup CDH. This suggests that the plankton community

needs low turbulence conditions in order to bloom, but that light still plays a role once the net heat flux is positive and there is tendency for stratification. The magnitude of the blooms also is also related to the amount of light in the mixing layer. The main blooms develop when low turbulence shoaled  $z_{\text{mix}}$  near or just above  $z_{\text{cup}}$ , increasing  $L$ . The increase of production when mixing layer shoaled not always corresponded to significant increases of chlorophyll  $a$  concentration at the surface when light is low (e.g., the peak starting on 3<sup>rd</sup> March, figure 3.14). This shows how much the definition of the bloom (chlorophyll- or oxygen-based) can influence the analysis of the dynamics in the water column.

Most of the peaks of  $N$  are related to positive heat flux. In particular, the start of the main bloom during the spring has actually been related to the switch between the period of mean negative net heat flux and a period of mean positive net heat flux at the beginning of April as predicted by HFH. This is evidence to confirm that the time of this switch could be used as a proxy to analyse the beginning of the most productive time of the year in interannual comparisons. However,  $N$  increased after a delay due to the presence of a storm, showing the need to take into consideration the turbulence induced by the wind stress to have more accurate estimates as hypothesised by Chiswell (2011) and Brody et al. (2013).<sup>1</sup>

Behrenfeld et al. (2010) suggested the Recoupling-Dilution Hypothesis, according to which phytoplankton is more productive when the mixed layer is deepening because of lower predation pressure. As said in chapter 1, in order to confirm this theory  $N$  should have increased during the deepening phase of  $z_{\text{mix}}$ . In the present study,  $N$  increased when the mixed layer stopped deepening and started to shoal while there was net heterotrophy during the winter, when mixed layer was actively deepening. When  $z_{\text{mix}}$  deepens again at the end of January,  $N$  does not become positive. These evidences seem therefore to confute the Recoupling-dilution hypothesis.

This study also highlights that in order to analyse correctly the triggering factors that increase production, peaks not related to the chlorophyll fluorescence-defined blooms have to be considered. It is also important to use high temporal resolution *in situ* data instead of climatologies to better appreciate the high variability of the system. The use of the mixing layer depth instead of the mixed layer depth is also important to analyse variations in turbulence that actually affect the plankton and its metabolic activity.

## 5.5 Future work

Many aspects of this analysis were based on speculations about the availability of nutrients near the surface of the ocean and their distribution in the water column. These were based on proxies as the presence of subsurface  $c(\text{O}_2)$  increases (DCM). Future studies should include a systematic analysis of nutrients in the water with a resolution as close as possible to

the other parameters already measured. The development of sensors to detect nutrient concentrations to fit on gliders is therefore a priority for the correct analysis of production. The comparison with direct turbulence analysis is also needed to confirm the speculation that was carried out assuming that  $z_{\text{mix}}$  was a valid proxy to estimate turbulence and changes in the OSBL. A more accurate estimate of the advection in the area with the use of the second glider deployed in the area is also needed to quantify the magnitude of this process and confirm that the averaging process was sufficient to lower its influence to negligible values. A depth-resolved estimate of  $N$  would also accurately describe the vertical heterogeneity in production occurring in periods when there are obvious features as the DCM.

## 5.6 Conclusions

Net community production ( $N$ ) above the mean euphotic depth near the PAP site from September 2012 to August 2013 has been calculated analysing the variations in  $I(\text{O}_2)$  over time. Air-sea flux and entrainment have been calculated in order to account for the changes due to physics and calculate the residual biological signal. A 7 d averaging step has been used in order to reduce the variability due to geographical patchiness and advection. Calculation of under- and overestimates of  $N$  has constrained the uncertainty of these estimates to  $\pm 30\%$ .

The area is autotrophic, with a mean  $N$  value of  $19 \text{ mmol m}^{-2} \text{ d}^{-1}$  and an estimated annual  $\text{O}_2$  production of  $7 \text{ mol m}^{-2}$  ( $4.7 \text{ mol m}^{-2} \text{ C}$  equivalents). The values calculated fit the range of estimates done in the past for net community production in the basin and in the same area. The variations within this range are attributed in part to the differences among the methods used for the calculations and, also, to the interannual variability that has been shown in the ocean.

The analysis of the annual cycle of net community production has shown the presence of four periods with different regimes: an autumn bloom, a heterotrophic period and two productive periods (spring and summer) that are separated by the depletion of nutrients after the spring bloom. During the summer a deep chlorophyll maximum developed and this period was responsible for a significant portion of the annual production.

Variations in production have been successfully associated with factors such as wind speed, net heat flux and mixing layer depth. The model proposed by Enriquez and Taylor (2015) is suggested to be the mechanism that can explain how the system passes from net heterotrophy to net autotrophy every time that favourable conditions are matched. This model unifies the CDH with the CTH and the HFH suggesting that the net surface heat flux and the wind modify the mixing layer depth that, when shoals above a certain depth, can trigger the bloom. In this study the euphotic depth was proposed as the value above which the mixing layer

depth has to shoal to trigger an increase in production. The validity of the Recoupling-Dilution Hypothesis of Behrenfeld (2010) could not be confirmed instead.

# Chapter 6

## Gross primary production

A new method was applied for the calculation of the gross primary production based on diel variations of oxygen concentration. Four periods between October 2012 and May 2013 are chosen to calculate gross primary production, which is then compared with estimates from previous studies. The limitations and possible further developments of the new method are also discussed.

### 6.1 Introduction

The calculation of gross primary production ( $P$ ) related to phytoplankton activity in the ocean is fundamental to understanding the role of marine biota in the carbon cycle. The importance of this parameter is proven by the several million estimates in the literature (del Giorgio and Williams, 2005). However, different *in vitro* and *in situ* methods often give different results for the same location (Robinson et al., 2009; Regaudie-de-Gioux et al., 2014).

Oxygen concentration ( $c(\text{O}_2)$ ) was used in one of the first estimates of gross primary production (Gaarder and Gran, 1927). When a system is driven by biology,  $c(\text{O}_2)$  varies following a diel cycle with increases due to net production ( $P$ ) during the day and net respiration ( $R$ ) in dark hours.  $P$  and  $R$  can therefore be calculated observing the diel cycle and measuring the magnitude of its oscillation. This was a challenging task until the 1960's because the Winkler titration method was not precise enough to detect variations due to low values of  $P$ . Even after the development of protocols for high-precision titrations (Carpenter, 1965; Carrit and Carpenter, 1966),  $c(\text{O}_2)$  analysis still faced many challenges. For example, *in vitro* measurements (bottle incubations) proved to be biased by significant differences in nutrient concentrations, light, temperature and community composition with respect to the real world (Maske and Garcia-Mendoza, 1994; Karl et al., 1998; Robinson and Williamson, 2005; Duarte et al., 2013; Williams et al., 2013, Regaudie-de-Gioux et al., 2014). Furthermore, technical issues in experimental design due to wavelength and intensity of light and the materials used for the incubation vessels also influenced the results (Kirk, 1994; Godoy et al., 2012; Agustí et al., 2014).

*In situ* studies face other challenges, such as the influence of air-sea  $\text{O}_2$  fluxes, entrainment and natural geographical heterogeneity in the measurements. The presence of many

factors hampers the isolation of the signal due to the individual processes. In order to isolate the biological from the physical signal, a large number of data-points is needed. The first study of this kind (Tijssen (1979)) used direct high-precision Winkler titrations, a time consuming process applicable only to short periods that only permits the analysis of a small number of samples. Robertson et al. (1992) analysed diel variations of oxygen over 4 days measured with a pulsed sensor with up to 30 points measured per hour. They sampled water from 2-3 m depth with the ship's non-toxic seawater supply and observed an increase in  $c(\text{O}_2)$  during the day and its decrease during the night. However, they used these data to analyse N over the sampled period rather calculating P. The availability of high-resolution data obtained with optodes mounted on autonomous underwater vehicles has allowed more recently a new and more fruitful use of the  $\text{O}_2$  bulk approach to calculate P. The small spatial and temporal scale that these new technologies are able to resolve (Rudnick, 2016) can be used to analyse variations not accessible in the past. Thanks to the advent of gliders, datasets at high resolution were used to compute  $R$  and  $P$  in the Pacific Ocean using diel variations (Johnson et al., 2010; Wilson et al., 2014, Nicholson et al., 2015).

The method used in this chapter measures P through the analysis of diel variations of  $c(\text{O}_2)$  within the OSMOSIS dataset.  $c(\text{O}_2)$  values were calibrated as in chapter 2 and the last part of the dataset (after 11<sup>th</sup> August 2013) was disregarded due to biofouling of the sensor on the last glider mission (see chapter 2).

## 6.2 Method description

The method was used in the top 20 m of the water column. This depth was chosen because it is shallower than  $z_{\text{mix}}(\text{O}_2)$  for most of the year and therefore its variations can be considered a proxy for variations within the whole mixed layer. Glider descents and ascents were analysed separately following what has been done in similar studies (Nicholson et al., 2008, Nicholson et al., 2015). Data-points were used individually without any averaging or binning process.

The dataset was split into days and nights. In this particular context, a “day” refers to the time between a sunrise and the consecutive sunset and a “night” to the time between a sunset and the following sunrise. Local sunrise and sunset times were determined using the function ‘suncycle’ on Matlab 2014b.

For each day, a regression line was calculated to fit the distribution of  $c(\text{O}_2)$  over time between one hour before sunrise and one hour after sunset. The operation was repeated for each night considering the data measured between one hour before sunset and one hour after sunrise. The slopes of these regression lines were the rates of change of  $c(\text{O}_2)$ . These rates are the result of the effects of the different factors that influence  $c(\text{O}_2)$  as described in equations 6.1 and 6.2

$$\Delta c(\text{O}_2)/\Delta t \text{ (day)} = P + R + F_{\text{as}} + E + A \quad (6.1)$$

$$\Delta c(\text{O}_2)/\Delta t \text{ (night)} = R + F_{\text{as}} + E + A \quad (6.2)$$

where  $F_{\text{as}}$  is the air-sea  $\text{O}_2$  flux,  $E$  is the entrainment,  $A$  is the lateral advection,  $P$  is gross primary production and  $R$  is community respiration. If  $F_{\text{as}}$ ,  $E$ ,  $R$  and  $A$  are considered constant between day and night, the difference between  $\Delta c(\text{O}_2)/\Delta t \text{ (day)}$  and  $\Delta c(\text{O}_2)/\Delta t \text{ (night)}$  equals  $P$ .

The timeseries of fitting lines was checked visually to identify periods of 7 or more consecutive days in which a persistent diel cycle of diurnal  $c(\text{O}_2)$  increase and nocturnal decrease was visible. This was done assuming that a clear diel cycle was a proxy for periods in which the biological activity was the strongest determining factor of  $c(\text{O}_2)$ .  $P$  estimates were calculated for these periods that had a relatively strong biological signal.

Mean  $F_{\text{as}}$  values (see chapter 5) were determined for each day and compared with mean  $F_{\text{as}}$  during the following night using a paired-samples t-test to check the validity of the assumption of equal  $F_{\text{as}}$  between day and night. The same test was carried out comparing  $z_{\text{mix}}(\text{O}_2)$  values (see chapter 4) to check whether  $E$  was the same during day and night.  $R$  was considered to have a constant magnitude within the 24 hours following the approach of previous similar studies (e.g., Nicholson et al., 2015).  $A$  is supposed to be a random process without any prevalence during the day or night and the averaging process obtained over 7 or more days was supposed to get rid of its influence as discussed in chapter 5.

For each period exhibiting an obvious diel cycle, the mean diurnal increase rate and mean nocturnal decrease rate (and their standard deviations) were calculated.  $P$  during the period was assumed to be the difference of the two means, while the standard deviations were combined to quantify the error associated with  $P$ .

### 6.3 Results

Four periods in the time series showed a clear diel cycle over several days: from 4<sup>th</sup> to 13<sup>th</sup> October 2012 (figure 6.1b), from 19<sup>th</sup> to 27<sup>th</sup> March 2013 (figure 6.2b), from 14<sup>th</sup> to 21<sup>st</sup> April 2013 (figure 6.3b) and from 14<sup>th</sup> to 22<sup>nd</sup> May 2013 (figure 6.4b). Figures 6.1b-6.4b show this cycle with the alternation of  $c(\text{O}_2)$  increases (red line fits) and decreases (black line fits). During these periods  $F_{\text{as}}$  was constant and generally low, usually between  $\pm 20 \text{ mmol m}^{-2} \text{ d}^{-1}$  (figures 6.1c-4c). Considering the median  $F_{\text{as}}$  value and the mean  $z_{\text{mix}}(\text{O}_2)$  in each period,  $F_{\text{as}}$  per unit volume was equal to  $0.02 \text{ mmol m}^{-3} \text{ d}^{-1}$  (October 2012),  $0.03 \text{ mmol m}^{-3} \text{ d}^{-1}$  (March 2013),  $0.28 \text{ mmol m}^{-3} \text{ d}^{-1}$  (April 2013) and  $0.28 \text{ mmol m}^{-3} \text{ d}^{-1}$  (May 2013).  $z_{\text{mix}}(\text{O}_2)$  was either stable and shallow or in a shoaling trend (figures 6.1a-6.4a). This suggested that  $E$  had a negligible influence on  $c(\text{O}_2)$ .

The assumption that  $F_{as}$  and  $z_{mix}(O_2)$  were similar during days and nights was also validated. Within each period, the mean  $F_{as}$  values from each day were paired with the mean  $F_{as}$  of the following nights and their similarity was tested with a paired-samples t-test.  $F_{as}$  was found to be not statistically different between days and nights for the period of October 2012 ( $t(20)=-0.9861$ ,  $p=0.3358$ ), March 2013 ( $t(16)=0.0862$ ,  $p=0.9324$ ), April 2013 ( $t(18)=0.0500$ ,  $p=0.9606$ ), and May 2013 ( $t(18)=-0.3745$ ,  $p=0.7124$ ). The same test was repeated for the  $z_{mix}(O_2)$  means, which were found not statistically different between days and nights for October 2012 ( $t(20)=1.0921$ ,  $p=0.2878$ ), March 2013 ( $t(16)=0.4748$ ,  $p=0.6414$ ), April 2013 ( $t(18)=0.7943$ ,  $p=0.4373$ ), and May 2013 ( $t(18)=0.1397$ ,  $p=0.8905$ ). Since the assumptions were valid, the  $P$  estimates were calculated and results based on the glider descent profiles are shown in table 6.1. Calculations of  $P$  were repeated using the ascents and the results were not statistically different, as can be seen in figure 6.5.

**Table 6.1 Rates of mean diurnal increase and mean nocturnal decrease in oxygen concentration for unit volume calculated for each of the four periods where a diel cycle is visible. Gross primary production per unit volume is measured as the difference between the mean increase and decrease.**

Period	Mean $\Delta c(O_2)/\Delta t$ (day) $\pm$ s.d. / $\text{mmol d}^{-1} \text{m}^{-3}$	Mean $\Delta c(O_2)/\Delta t$ (night) $\pm$ s.d. / $\text{mmol d}^{-1} \text{m}^{-3}$	$P \pm$ s.d. / $\text{mmol d}^{-1} \text{m}^{-3}$	Mean $z_{mix}(O_2)$ $\pm$ s.d. / m
4–13/10/2012	4.2 $\pm$ 2.2	-2.2 $\pm$ 1.7	6.4 $\pm$ 2.8	36.0 $\pm$ 12.4
19–27/3/2013	6.4 $\pm$ 3.7	-6.3 $\pm$ 4.8	12.7 $\pm$ 6.0	74.2 $\pm$ 39.6
14–21/4/ 2013	4.3 $\pm$ 2.7	-4.6 $\pm$ 2.3	8.9 $\pm$ 3.6	81.3 $\pm$ 54.2
14-22/5/2013	4.3 $\pm$ 3.2	-4.1 $\pm$ 2.6	8.4 $\pm$ 4.1	64.3 $\pm$ 23.6

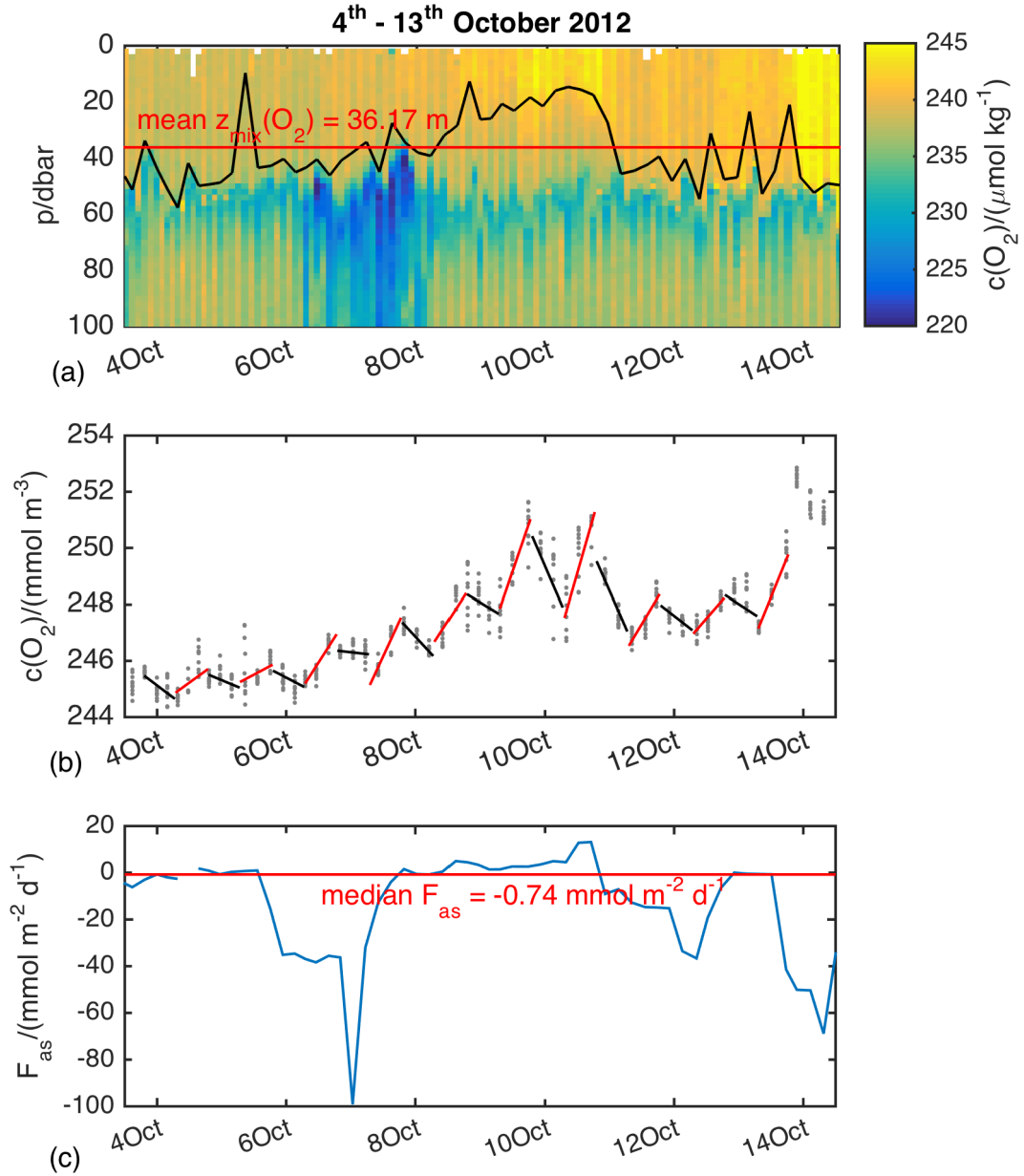


**Figure 6.1** (a) Oxygen concentration timeseries between 4<sup>th</sup> and 13<sup>th</sup> October 2012 versus pressure and time. The mean mixed layer depth is also shown; (b) Oxygen concentration in the top 20 m (grey) with line fits calculated per each day (red) and night (black). The diel cycle is visible through the alternation of oxygen increase during the day and decrease during the night; (c) air-sea oxygen flux where positive values mean outgassing and negative ones mean ingassing. The median value for the period is also plotted.

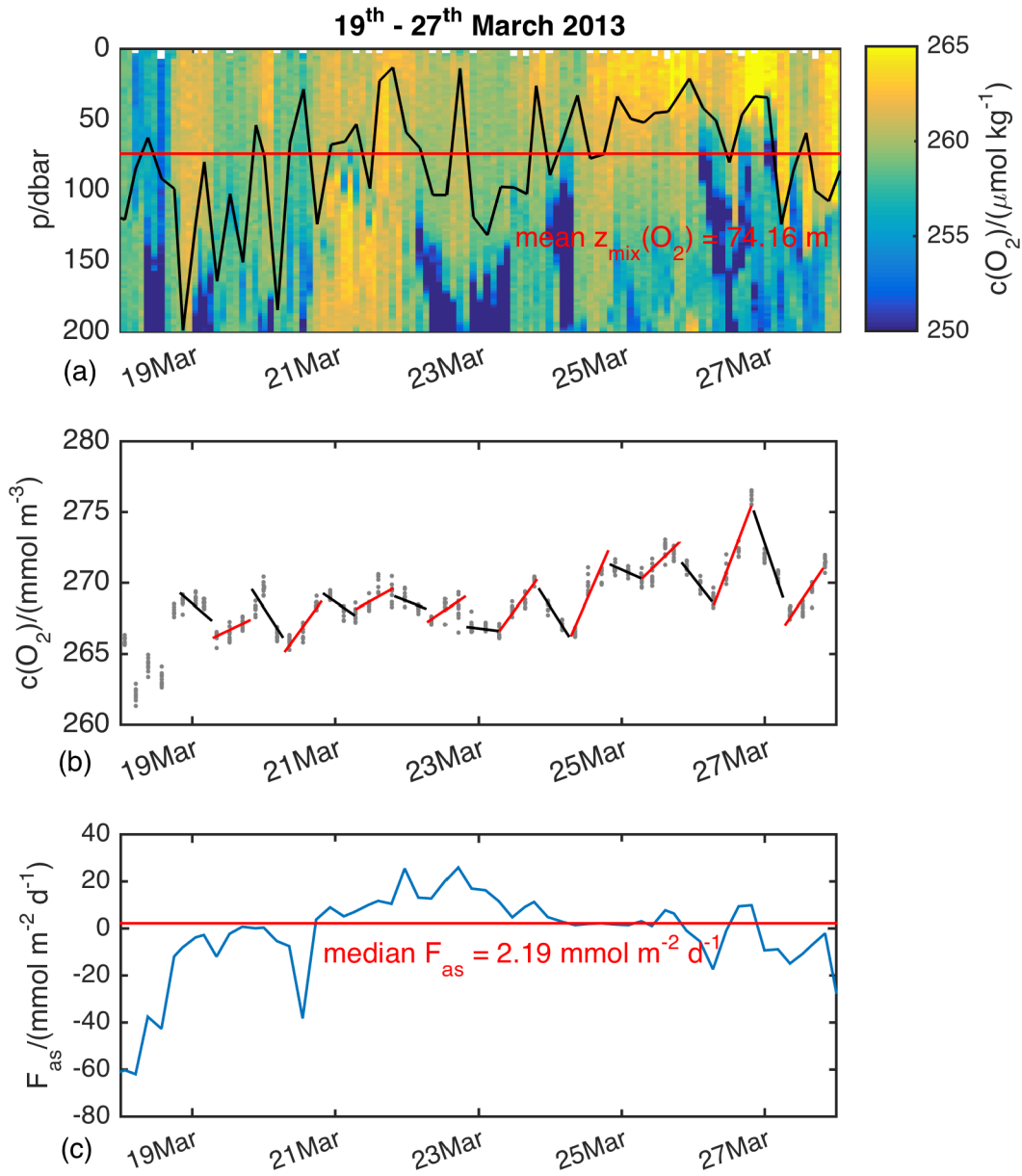
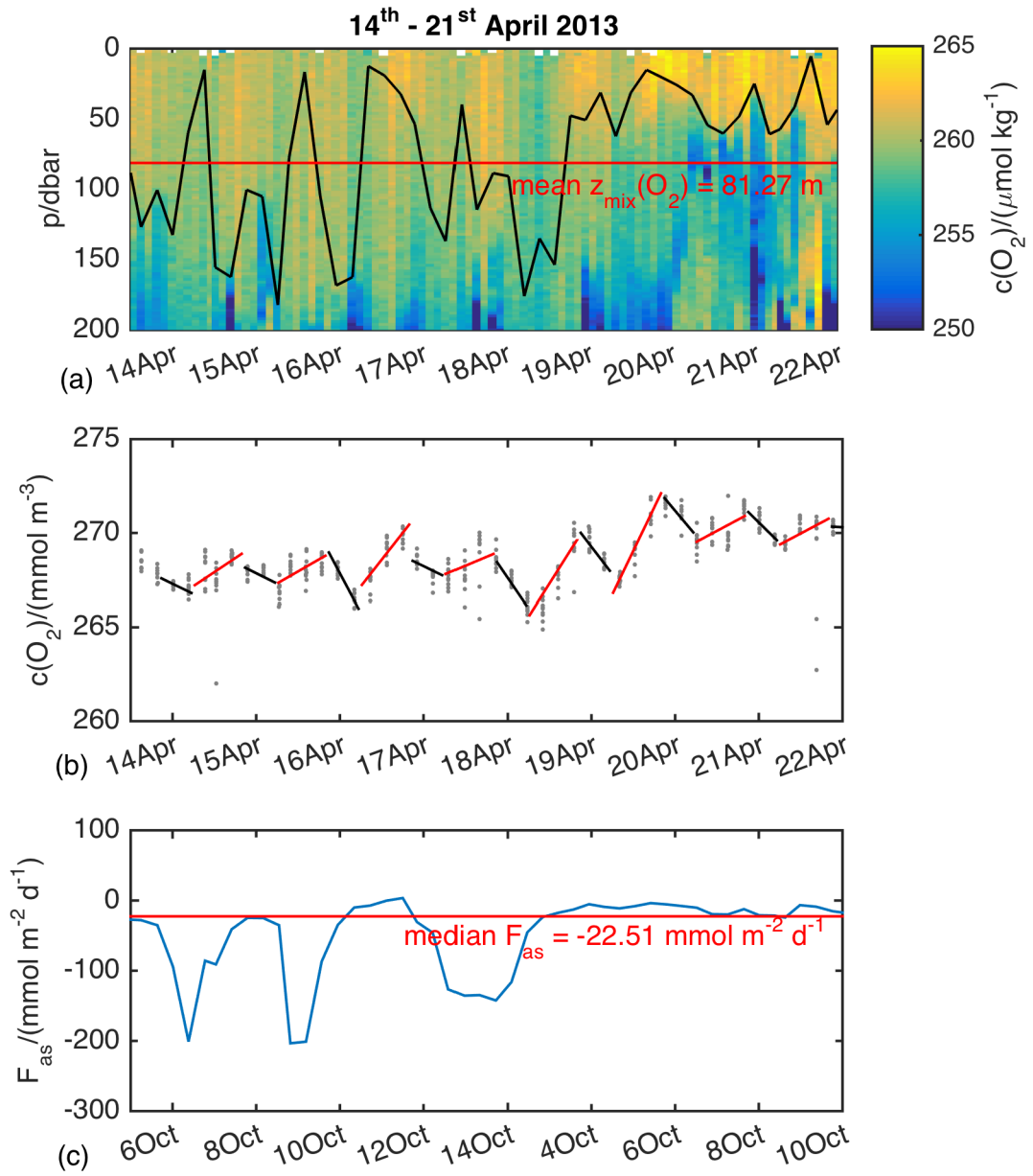
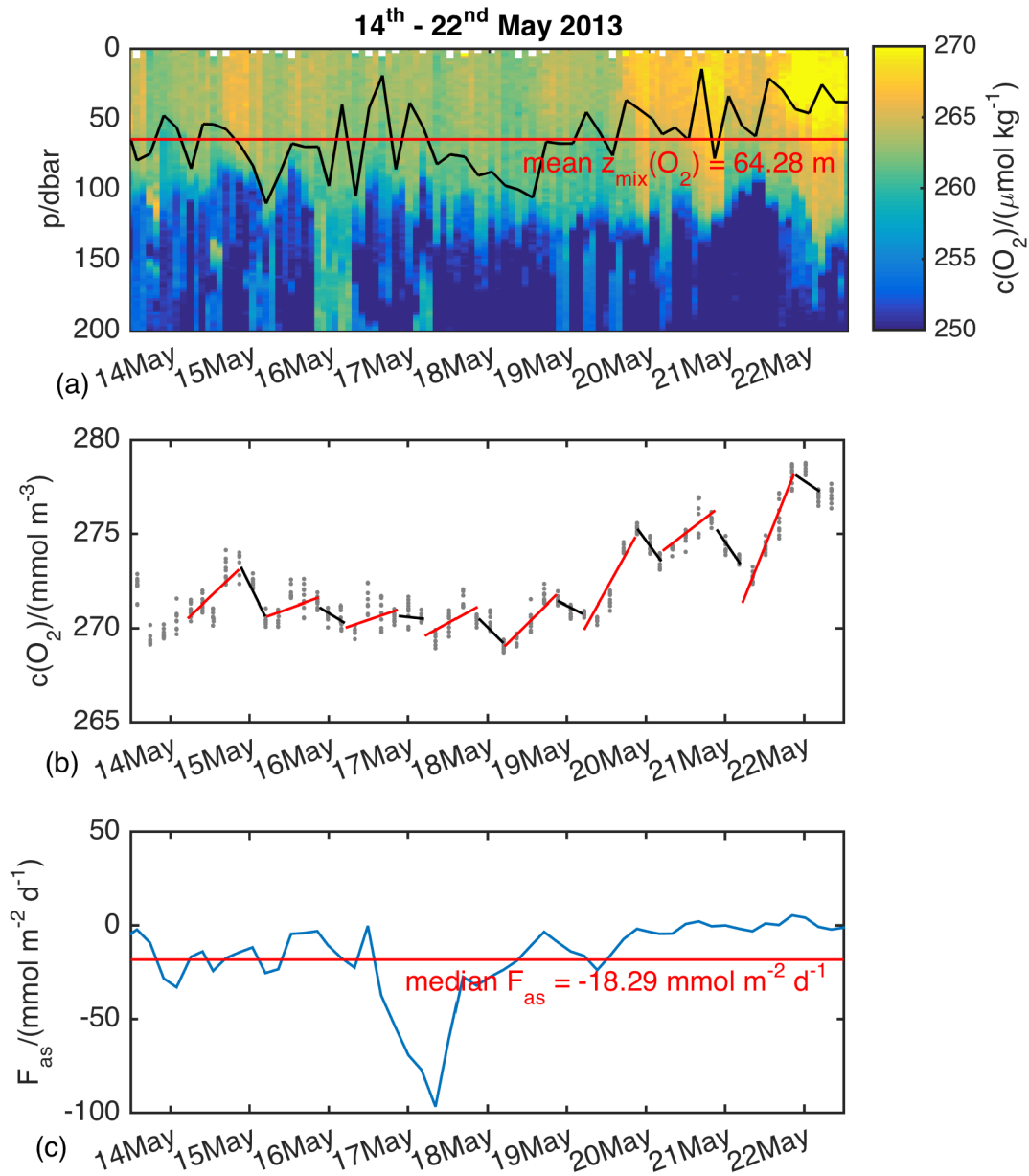


Figure 6.2 As figure 6.1 but for period between 19<sup>th</sup> and 27<sup>th</sup> March 2013.



**Figure 6.3** As figure 6.1 but for period between 14<sup>th</sup> and 21<sup>st</sup> April 2013.



**Figure 6.4** As figure 6.1 but for period between 14th and 22nd May 2013.

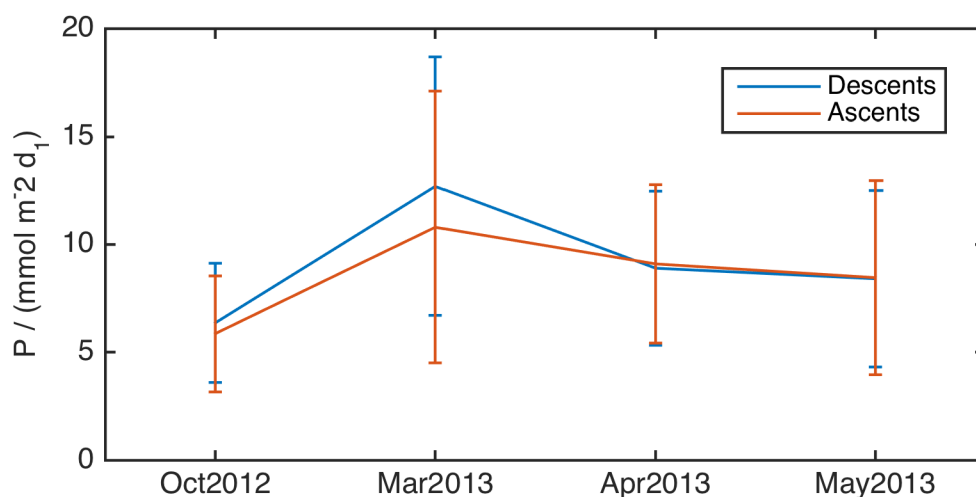


**Figure 6.5** Gross primary production estimated for the four periods using ascents and descents. The error bars are based on the standard deviations of the mean increase and decrease rates of oxygen concentration within each period.

$z_{\text{mix}}(\text{O}_2)$  decreased in every period, with two to three days in which it lay at around 50 m or less (figures 6.1a-6.4a). When  $z_{\text{mix}}(\text{O}_2)$  shoaled there was higher  $c(\text{O}_2)$ . In these days,  $P$  values are higher than in the rest of the same period as shown in table 6.2 and in figures 6.1b-4b. These events might be due to the passage of features at surface that re-stratify the column. These shoaling events show the importance of the averaging process over 7 day periods to have trustable estimates of  $P$  rates in the period. They also show the influence that variations in mixing layer depth have on the biological activity.

**Table 6.2** Gross primary production per unit volume measured in each period according to the depth of the mixed layer. The days in which the mixed layer shoals are also listed. Mixed layer depth is indicated and used for the conversion between gross primary production per unit volume and unit surface.

Period	Deep ML		Shallow ML	
	$P \pm \text{s.d.}$ / $\text{mmol d}^{-1} \text{m}^{-3}$	$z_{\text{mix}}(\text{O}_2) / \text{m}$	$P \pm \text{s.d.}$ / $\text{mmol d}^{-1} \text{m}^{-3}$	$z_{\text{mix}}(\text{O}_2) / \text{m}$ (days / d)
4–13/10/2012	$4.8 \pm 1.8$	$41.8 \pm 9.7$	$10.1 \pm 3.2$	$23.6 \pm 8.0$ (8-10/10/2012)
19–27/3/2013	$8.8 \pm 3.6$	$85.8 \pm 43.7$	$17.8 \pm 7.8$	$48.0 \pm 17.7$ (24-26/3/2013)
14–21/4/ 2013	$9.0 \pm 3.5$	$96.6 \pm 54.8$	$9.5 \pm 4.0$	$39.1 \pm 18.2$ (19-22/4/2013)
14-22/5/2013	$6.2 \pm 3.3$	$73.1 \pm 22.4$	$12.0 \pm 4.1$	$49.6 \pm 18.0$ (19-21/5/2013)

## 6.4 Discussion and Conclusions

In this chapter a new method has been proposed for the calculation of gross primary production ( $P$ ) using the difference between the rate of diurnal  $c(\text{O}_2)$  increase and nocturnal  $c(\text{O}_2)$  decrease. The method assumes that physical processes influencing  $c(\text{O}_2)$  such as  $F_{\text{as}}$  and  $E$  are constant between day and night and that the presence of a diel cycle is a proxy for periods in which biological activity is stronger than the other processes. The equality of physical processes between day and night was confirmed where a diel cycle was particularly obvious, validating the assumptions. In the four periods analysed here,  $F_{\text{as}}$  was usually low. Furthermore,  $z_{\text{mix}}(\text{O}_2)$  was constant or shoaling, in accordance to Robertson et al. (1992) that found a shoaling mixed layer to be a regime particularly favourable to the identification of diel cycles in  $c(\text{O}_2)$  *in situ*. This is an indirect validation that the biological activity was probably the main factor acting on  $c(\text{O}_2)$ . It is not surprising that these four periods are found during the autumn bloom and during the spring, when the phytoplankton community is often particularly productive (see chapter 5). The influence of lateral advection in disrupting the diel cycle is likely to be the reason why this method not always works.

$P$  was higher during the spring (March, April and May), while in October values were lower. However, more analysis would be needed to narrow the error associated to these measurements and prove statistically this difference. The presence of a shallow  $z_{\text{mix}}(\text{O}_2)$  is linked to two kinds of responses. During October, March and May,  $P$  increases rapidly. This would explain the rapid increase of  $c(\text{O}_2)$  and the small blooms visible throughout the spring. This effect could be a triggering mechanism for increased net community production in shallow mixing layer as explained in the model of Enriquez and Taylor (2015): when the plankton is retained above a certain depth, its net community production increases because its average  $P$  increases, generating the bloom. In April the situation seems to be different, with a virtually absent increase of  $P$  when  $z_{\text{mix}}(\text{O}_2)$  shoals. This difference needs further analysis in order to be explained fully.

$P$  determined with this new method was compared with previous  $P$  estimates obtained for the same area.  $P$  values per unit volume matched the order of magnitude of the estimates calculated by Serret et al. (2001) north of  $48^\circ\text{N}$ . During the AMT-6 cruise in 1998 (Aiken et al., 2000) they used an *in vitro* approach and found  $P$  above  $10 \text{ mmol O}_2 \text{ m}^{-3} \text{ d}^{-1}$  and up to more than  $22 \text{ mmol O}_2 \text{ m}^{-3} \text{ d}^{-1}$  near the surface, in the same portion of the water column where the present study is focused. Robinson et al. (2009) carried out incubation experiments at the same latitudes but closer to the continental shelf. Their  $P$  estimates also match the order of magnitude of those found in the present study, ranging from  $2 \text{ mmol O}_2 \text{ m}^{-3} \text{ d}^{-1}$  up to almost  $40 \text{ mmol O}_2 \text{ m}^{-3} \text{ d}^{-1}$ . Interestingly, they also found big variations in  $P$  from day to day. This is in accordance with the rapid change of  $P$  in response to the shoaling mixing layer that has been shown in the present study. This is the first time that this metabolic response is shown so clearly and quantified. If

this  $P$  enhancement was confirmed, it could be an important parameterization to explain the processes through which small blooms happen in regimes of low turbulence.

The new method used in this chapter relies on assumptions that cannot be considered valid for most of the year. During the winter, the diel cycle is not visible and, for example,  $c(\text{O}_2)$  increases during the night. The assumption that biological processes have to be more important than physical factors is therefore crucial.

The method is not able to work for the whole year and therefore cannot provide estimate of the annual  $P:R$  ratio. Nevertheless, future work should assess whether the method can yield reliable calculation of  $R$  rates in the area and, then, if it could contribute to estimate this ratio for productive periods, which could be helpful in limiting which value discerns heterotrophic and autotrophic systems, since the estimates of this threshold currently span over one order of magnitude (Serret et al., 2001). A further analysis of the influence that  $F_{\text{as}}$  and  $E$  have on the diel cycle could also be useful to apply the method to the rest of the year, highlighting diel variations that are now hidden by stronger physical forcing.



# Chapter 7

## Conclusions

Rudnick (2016) affirmed that ‘the enthusiasm for gliders led to some early missions that focused on possibilities rather than fundamental research, so more critical members of the community were understandably skeptical’. Along with evidence of the possibility to perform long-lasting and multi-platform studies using gliders, the present study shows how glider applications have matured and can now provide genuine new insights to understand fundamental biological processes occurring in the water column. A discussion of the results and some suggestions for future work in the light of these findings are presented in this chapter.

### 7.1 Findings and estimates

#### 7.1.1 Biofouling

The calibration process revealed that different oxygen concentrations at the top of the water column between consecutive ascents and descents can be an easy diagnostic to identify from remote the growth of biofilm on the sensor. There is a systematic increase of the oxygen concentration during the ascents when biofilm develops and this is visible even in profiles prior to calibration or drift correction. This is important for gliders since biofouling can affect navigation performance because of drag, as well as affecting the data quality.

#### 7.1.2 Dataset

The calibration process enabled the successful merging of three individual missions into a unique and coherent time series using ship-CTD casts for the inter-calibration between consecutive glider missions. This approach is new and different from previous missions of glider fleets that focused on the inter-calibration of gliders working at the same time rather than in series. The approach used in this study would permit an expansion of the time-span of glider surveys, creating long-term datasets from consecutive missions.

The final dataset consisted of 4035 profiles describing the distribution of oxygen concentration from near the surface to 1000 m of depth over one year. This was the longest continuous dataset for biogeochemical purposes obtained by the means of Seagliders so far.

Analysing the spectra of frequencies of variation in temperature, salinity and oxygen concentration, three layers were identified in the water column. The layer from the surface to 150 m was directly influenced by exchange of oxygen with the atmosphere and by plankton metabolic activity. There was strong seasonality in this layer, following the annual cycle of temperature (and its relation with oxygen solubility) and plankton activity, which led to supersaturation in spring and summer. The second layer, from 150 m to 700 m, did not show the anti-correlation between oxygen and temperature that is expected in solubility-driven systems. Respiration rates and the age of the water were therefore the most important processes in determining oxygen concentrations. At the bottom of the water column lay the oxygen minimum layer. It showed the least variability in oxygen concentration, apart from intrusions of filaments of Mediterranean Outflow Water, which lowered oxygen concentration even more.

The area was in general influenced by very high spatial and temporal variability. The spatial variability was due to the passage of mesoscale features, which influenced the two layers at the top of the column, triggering the injection below the ocean surface boundary layer of parcels of surface water. The biological processes had also high temporal variability. Before the start of the main bloom in April and when the nutrient became arguably limiting, there were increases in *N* lasting just a few days and rapid oscillations between net autotrophy and net heterotrophy. This variability confirms the conclusions of Damerell et al. (2016), who saw high intraseasonal variability also in salinity and temperature.

### **7.1.3 Mixed and mixing layer depth**

The top layer of the water column included the ocean surface boundary layer (OSBL). This layer, classically described as the mixed layer, has been used in previous studies to define the vertical extent of the biological activity in the water column considering that turbulent mixing homogenises the plankton within it. Enhanced biological activity, along with the air-sea gas exchange flux, altered the oxygen concentration in this layer creating a significant difference with respect to the water just below. Therefore, the possibility to use oxygen concentrations as a proxy to define the vertical extent of the OSBL was investigated. This approach had already been proven to work in the Southern Ocean (Castro-Morales and Kaiser, 2012) and the calculations done in the present work aimed to show the validity of this methodology in another area of the Earth with a different regime and during a whole year cycle. The results showed that the depth at which oxygen concentration deviates 0.5 % from its value at the surface (here taken as the concentration at 5 m) was a meaningful criterion to define the OSBL. In particular, this method was able to mark the depth reached by the homogeneous layer visible in the profiles for a multitude of parameters, which was taken as a proxy for active vertical turbulent mixing. The OSBL defined by oxygen was sometimes very different from the mixed layer depth as calculated for the same dataset by Damerell et al. (2016), that was based

on density and temperature with a difference criterion using the widely used thresholds of de Boyer Montégut et al. (2004). When the two estimates were different, the ones based on oxygen proved to be more sensitive because they were able to pick the signal of small pycnoclines near the surface that were instead missed using density or temperature. These pycnoclines were the shallowest deviation from the homogeneity and therefore the results obtained with this oxygen-based method were considered a proxy for the mixing layer depth.

Since oxygen concentrations are responding to physical and biological processes, this mixing layer was related to the magnitude of biological activity at different depths in the water. This means that in case of very low turbulence, the mixing layer depth defined by oxygen was able to describe the actual vertical extent of the productive layer, an important parameter for the analysis of biogeochemical data. This allows the detection of variations in turbulence that actually have an impact on biological activity. Oxygen concentration should therefore be used in future biogeochemical studies in order to define the mixing layer depth and the extent of the biological activity, at least when ship-, Argo- or glider-based profiles with similar vertical resolution are used. Oxygen concentration was also shown to be a better proxy than chlorophyll *a* concentration, especially in important periods such as during the presence of the deep chlorophyll maximum.

#### **7.1.4 Net community production**

The estimation of biological production had two main foci: the calculation of its magnitude and the definition of its pattern over time. The magnitude of net community production was used to determine whether the area is autotrophic or heterotrophic and to quantify the impact of the plankton on the carbon cycle in this area. The pattern, through comparison with other parameters, gave hints about the mechanisms that increase production in the ocean, leading to blooms.

The analysis was carried out in the productive layer of the water column, described by the euphotic depth, where light sustains photosynthesis. Analysing the changes in oxygen inventory above the mean euphotic depth, the biological signal was split from the physical signal with an oxygen mass balance approach. This study gave evidence of net autotrophy over a one-year cycle. The annual production was higher than the majority of the estimates found in previous studies. This was probably due to the fact that the other studies used deeper limits for the calculation of the oxygen inventory, which would include the respiration happening below the euphotic depth and so bias their estimates low. The productive season started in February and was therefore longer than what considered in previous studies.

During the first part of the campaign, from September to February,  $(0.8 \pm 0.2)$  mol m<sup>-2</sup> in O<sub>2</sub> equivalents were consumed, while from February to August (i.e., the productive period, spring plus summer)  $(7.2 \pm 2.2)$  mol m<sup>-2</sup> were produced, resulting on a total production of  $(6.4 \pm$

1.9) mol m<sup>-2</sup>. The estimate of the production in the spring-summer is also an underestimation because the last month of the year-cycle was disregarded due to biofouling, but had signs of a deep chlorophyll maximum. There was one order of magnitude of difference between the estimates in the two halves of the year, showing that protracted periods of heterotrophy have a very limited impact on the production in this part of the ocean. This is partly due to the numerous peaks of autotrophy outside the main bloom, in particular during the autumn. The estimate for the spring-summer period agreed well with that obtained by Frigstad et al. (2015) who analysed the downward movement of dissolved inorganic carbon from sediment traps at PAP from February to July between 2003 and 2012. The area was shown to be very productive, with autotrophy peaks happening during the whole year.

An important estimate was the net community production during the presence of the deep chlorophyll maximum, whose calculation represents a challenge for other methods (ocean colour from satellites or *in vitro* incubations). During the presence of the deep chlorophyll maximum, the system produced 1.5 mol m<sup>-2</sup>, above 20 % of the total annual production. The limit of 60 m used here was deep enough to include the chlorophyll and oxygen maxima and, therefore, the calculation were considered an adequate estimate of the production of the whole community in this period. This period was proven to be very important in the area and miscalculations of the production in this period can affect the computations of the total annual production rates.

The pattern of net community production over time was compared with other parameters (such as wind speed, mixing layer, net surface heat flux, mean light in the mixing layer) in order to provide possible triggers for the increases and decreases of production. Apart mixing layer, the other parameters were obtained from re-analysis (ERA-Interim and MODIS) and were useful tools to test the hypothesis linked with the different mechanisms that have been suggested to explain the start of plankton blooms. A bloom was defined as the switch from negative to positive net community production. In, Sverdrup's Critical Depth Hypothesis would be confirmed if blooms occurred when the mean light in the mixing layer increased. The Recoupling-Dilution Hypothesis suggested by Behrenfeld et al. (2010) would be confirmed if there was production while mixing layer was deepening and production decreased when the deepening phase stopped. The model proposed by Taylor and Ferrari (2011) would be confirmed if the bloom was triggered by the switch between negative and positive net surface heat flux, while the model from Enriquez and Taylor (2015) would be confirmed if blooms occurred when mixing layer shoaled because of the positive net surface heat flux. All these mechanisms consider water column not nutrient-depleted.

In the time series, two regimes were identified, linked to the argued nutrient limitation in some parts of the year. Periods of nutrient limitation were identified looking at the patterns of light and plankton production. When the water column was well lit but the planktonic community showed heterotrophy (negative net community production), the system was

assumed to be nutrient limited. In these periods, production was enhanced when water from below was mixed into the surface layer. This happened either by pulses due to storms, identified by peaks in wind speed, or by gradual deepening of the mixing layer. In the summer, when stratification was strong and vertical mixing did not occur, deep chlorophyll and oxygen maxima developed.

In periods when nutrients were assumed not to be limited, turbulence and light played a fundamental role in production. Small blooms happened before the shift from a period with fluctuating net surface heat flux to a period of constantly positive net surface heat flux. These peaks in production occurred when wind decreased or when convective turbulence was decreased due to a positive net surface heat flux (water warming). In these cases mixing layer shoaled, showing a mechanism similar to the one suggested by Enriquez and Taylor (2015). This sometimes happened without any significant increase in the mean light or in chlorophyll *a* concentration. After the switch, when the net surface heat flux is constantly positive, the main blooms (identified by accumulation of chlorophyll at the surface) appeared. However, Taylor and Ferrari (2011) suggested that this switch should have been linked directly to the bloom. The present study has shown instead the presence of a delay between the switch and the accumulation of chlorophyll *a* and a further increase of production. The bloom starts only when mixing layer shoaled, as suggested by Enriquez and Taylor (2015). Furthermore, later in the season, another bloom occurred without any significant change in the sign of the net surface heat flux. In this case, light in the mixing layer increased due to the shoaling of the mixing layer, but the shoaling does not appear to be driven by the heat flux. This dynamic confirms the Sverdrup's hypothesis.

It is also interesting to notice that during the End-February-Event (section 4.3.6) there is a small bloom during which there is no variation in the depth of mixed layer based on density, but there is accumulation of oxygen and chlorophyll at the top of the water column. This happens in a period of positive heat flux and slow wind, which can be related to low turbulence. This event seems therefore explainable with Huismann's Critical Turbulence Hypothesis: the production was faster than the mixing, leading to the accumulation of production in the well lit part of the water column.

The mechanism proposed in this study to explain the start of blooms when nutrients are not limited is therefore a mix between the model proposed by Enriquez and Taylor (2015), the Sverdrup's Critical Depth Hypothesis and Huismann's Critical Turbulence Hypothesis. The decrease of turbulence due to the positive net surface heat flux plays a role in triggering blooms shoaling the mixing layer depth. This also leads to chlorophyll accumulation (figure 7.1). When the heat flux stays positive, though, other factors such as wind stress can deepen the mixing layer. Blooms in this case happen when the mixing layer shoals again even without any significant switch in the sign of the heat flux. These blooms are mostly driven by the increase in the mean light intensity in the mixing layer with a dynamic that resembles Sverdrup's Critical

Depth Hypothesis. The present study shows also that the relative depth of the mixing layer with respect to the euphotic depth has an important impact on biology, working with the same mechanism of a “critical depth” as defined by Sverdrup (1953). As suggested Taylor and Ferrari (2011), the date in which the net surface heat flux changes sign can still be used to analyse the start of the productive period in multiannual analysis because all the main blooms happen after it.

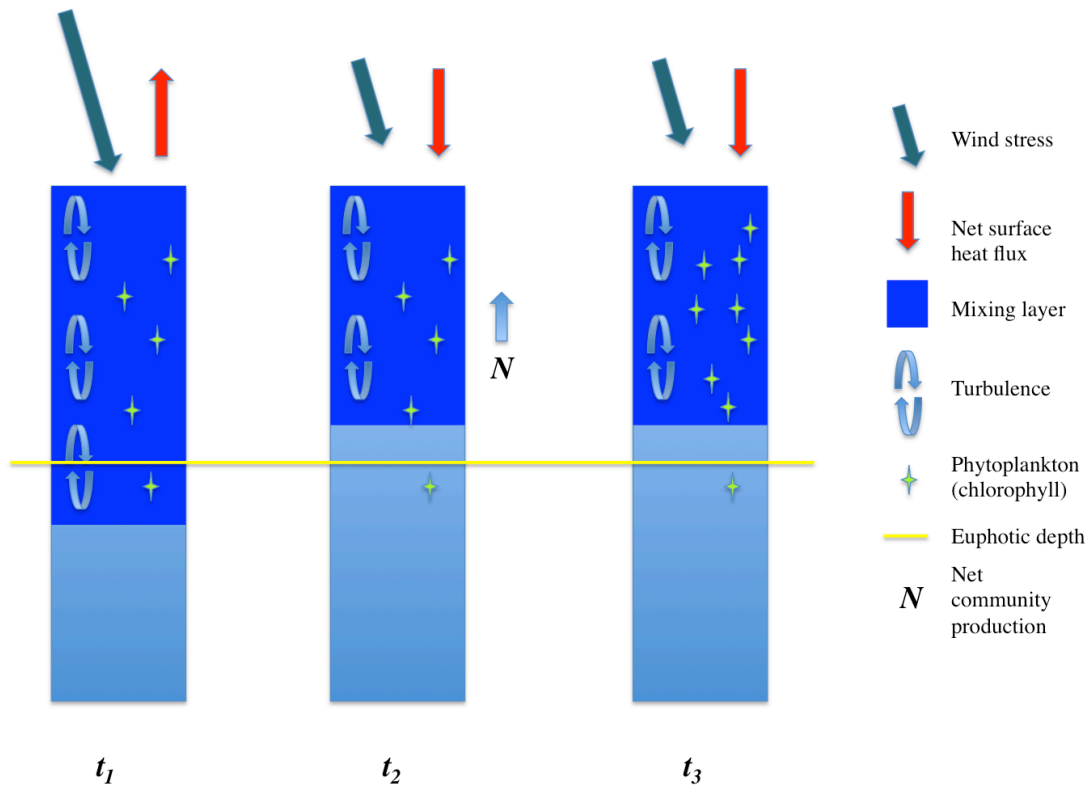


**Figure 7.1 Model of the mechanism proposed to explain the start of the spring bloom. The mixing layer (dark blue layer) shoals above the euphotic depth (yellow line) (from  $t_1$  to  $t_2$ ). This occurs when the turbulent mixing (circular arrows) decreases because the wind speed decreases (dark green arrow) and the net surface heat flux (red arrow) switches from cooling to warming of surface water. As a consequence, the net community production increases and this leads to the accumulation of biomass and, then, chlorophyll ( $t_3$ ).**

### 7.1.5 Gross primary production

The autotrophic biological production of the phytoplankton was measured in terms of gross primary production. A new method for its calculation was developed based on the daily increase and night-time decrease in oxygen concentration in the top 20 m of the water column.

This method was based on the methodology used by *in vitro* measurements and relies on the assumption that physical processes happened with the same magnitude during day and night. The presence of a protracted clear diel cycle in oxygen concentration was used as a proxy to identify periods in which changes in oxygen concentrations were dominated primarily by biological activity.

Only four periods over the year showed a diel cycle for at least 7 days in row. During the rest of the year other factors such as air-sea oxygen flux, entrainment, advection and geographical patchiness disrupted the diel cycle and the data were therefore not suitable for this calculation. The gross primary production estimates that were obtained fit within the range of previous estimates per unit volume in the North Atlantic (Alkire et al., 2000; Robinson et al., 2009). Values seem to be higher in the March, April and May than in October, even though the uncertainty is high (up to 50 % of the values).

A prominent biological signal in the oxygen variations was visible in a regime of low turbulence, which led to the shoaling of the mixing layer in all the periods analysed. This was linked to an increase of gross primary production. Although the method is based on many assumptions and more analyses are needed to confirm its validity, the results linked the increase of net community production when the mixing layer shoals not only to a reduction of the respiration rate (as assumed by Sverdrup, 1953), but also to an increase of the primary production that could be a causing factor of blooms.

## 7.2 Considerations and suggestions

A considerable portion of this work has been spent on calibrating the dissolved oxygen data from the gliders. The biofouling was a major problem, invalidating data in a probably productive period of the year (August-September). However, the biofouling might have invalidated an even greater portion of the dataset because it affected the optode during the calibration at the end of the third mission, which should have been used to correct for the drift in the data. However, the presence of CTD casts from cruise JC087 (June 2013) permitted a reliable correction and, thus, the calibration of the glider-data until the start of the biofouling. Five months out of six (from April 2013 to the beginning of August 2013) could then be used. If JC087 data had not been available, the whole third mission would have been disregarded. This shows that in case of long missions, in particular during productive periods such as spring and summer, two calibrations (one at the beginning and one at the end of the mission) might not be sufficient to ensure valid data for the analysis, especially when linear corrections of the drift are applied. It is therefore suggested for future glider campaigns to plan more cruises for the collection of Winkler and CTD data during this kind of mission.

The presence of the drift in the data is not optimal and the sensor stability should be improved to reduce this problem. There were also residual differences between ascents and

descents that even after the temporal shift of the data applied to correct for the response-time of the optode. A reduction of the response time would decrease this variability between profiles according to the vertical direction of the glider.

The automatic flagging of the spikes in oxygen concentration was attempted here, but gave a high number of false positives and, eventually, a time consuming visual check was needed. This is obviously not ideal, especially when dealing with datasets as big as the one used in this study. It is thus particularly important for future studies to make a bigger effort to improve the flagging algorithm.

The calculation of net community production proved to be sensitive to the entrainment, which is in turn sensitive to the mixing layer depth. The geographical heterogeneity and the influence of biological activity on the mixing layer defined by oxygen concentration might lead to biases due to the asymmetrical contribution of deepening and shoaling events to entrainment and production calculation. In this study, time averaging (smoothing) of the mixing layer was used to attenuate this problem, but this should be explored more carefully. The importance of the entrainment suggests caution in the use of climatologies to describe the OSBL in net community production calculations.

## **7.3 Future work**

### **7.3.1 Development of this dataset**

The first development of this work should be the comparison with the second glider of each pair that was deployed during each mission of OSMOSIS. These second gliders should be calibrated and used to explore temporal and spatial variability in more detail. Having two gliders in the water at any time was useful because it allowed choosing the glider mission with better quality data. In previous works the use of two gliders working simultaneously was useful to quantify processes such as advection and geographical patchiness (e.g., Alkire et al., 2012; Alkire et al., 2014). Delays in processing the fundamental data (CTD casts, calibrated and despiked salinity) forced the study to focus only on one glider at time in order to have a complete annual cycle. The natural progression of this work is therefore to use both parallel datasets for both comparison and integration, testing the results, increasing the accuracy and lowering the uncertainties of the different calculations. However, during the biofouling period, the optode working on the second glider had a fault and did not record any data. The use of the second dataset is therefore not going to be useful to complete the annual cycle.

Further analysis of net community production should include a depth-resolved analysis of the process. This would be useful to better understand phenomena such as the deep chlorophyll maximum, which has been linked to nutrient limitation in the top part of the water column. The analysis of net community production below the productive layer would also be

useful to estimate the respiration process and, then, have an idea of the net metabolic activity at depth. The analysis of gross primary production should be also continued in order to find more periods over the year to apply the new method. This could imply the creation of a 1D model that simulates the changes in oxygen due to physical processes. The differences between the values obtained with this model and the *in situ* observations would help describe the diel signal due to biological processes.

Future observations should be aimed at comparing direct measurements of the vertical attenuation of the turbulent mixing with estimates of the surface mixing layer depth as defined by oxygen concentration to validate the method. A comparison between mixed layer depth as defined by density and mixing layer depth as defined by oxygen should be conducted on a global scale in order to quantify the difference between these two parameters at different times and locations. The commercialization of microstructure-gliders makes this comparison very likely to be carried out in the next years.

### **7.3.2 Development of glider-based surveys**

The use of gliders and fleet of autonomous vehicles for observational studies is becoming very common in oceanography and the nature of data collected is very diverse (physical parameters, biogeochemical parameters, turbulence measurements). The huge amount of data that are collected with gliders is of great importance for the scientific community considering the peculiar characteristics of these datasets when compared with the ones collected by the mean of other platforms. Glider outperforms cruises in the costs-per-data and allows a much higher temporal and geographical resolution. They can also observe the vertical structure of the water column, which is an advantage with respect to remote sensing satellites data. When compared to mooring stations, gliders have a greater vertical resolution and can move, allowing both Lagrangian and Eulerian studies. Argo and BioArgo technology have comparable resolution to gliders, but cannot be directed to specific target and cannot be recovered to establish the status of the sensors (e.g. biofouling). However, glider have to be used as part of multi-platforms studies since, at the moment, ship-CTD are required for an accurate calibration. Furthermore, during the data-analysis step, data with a larger geographical scale (satellite data) and longer temporal span (moorings) are required to contextualise the values on a broader scale. The use of different platforms will be more and more important in the future because the spatial resolution of the models is rapidly increasing, letting scientists reproduce *in silico* many features that could not be modelled until a recent past. It will be therefore important to have data of different quality and resolution to test and validate the models and their feature at every geographical and temporal scale.

The glider data today are still not perfect and some ameliorations are needed in order for these data to be complete and fill some of the gaps in the observations that are required by the

scientific community to answer some unresolved questions. OSMOSIS project, for example, was meant at the analysis of the very top meters of the water column, but the quality control carried out in the present study showed that gliders and their sensors need to be improved to collect reliable data in the very first top meters under the ocean surface. Solving this problem would improve the already high performances that gliders have in the analysis of the ocean surface boundary layer. This would be really useful to physicists to restrain the mixing dynamics at the top of the water column, but also to biogeochemists and ecologists to understand to describe, model and predict the highly variable productivity of phytoplankton in the euphotic layer.

The miniaturization of the sensors is a trend in this moment with several companies and universities developing new probes for the measurements of new parameters through gliders (pH, nutrients, alkalinity). In particular, the present study highlights the need to develop high-resolution nutrient sensors to fit on gliders. In facts, the systematic measurement of nutrient concentrations during long-term observations such as the ones carried during the OSMOSIS project would help the interpretation of the triggering and limiting factors of blooms and small production increases.

## **7.4 Summary**

The study was successful in its aim to quantify net community production at the PAP site over a one year cycle, apart from the last month (August-September 2013), which was disregarded because of biofouling. The study also succeeded in providing a suite of high-resolution data (mixing layer, net surface heat flux, wind speed) for a detailed analysis of net community production variation over time. The comparison of these data led to the confirmation of the model proposed by Enriquez and Taylor (2015) to explain the initiation of the spring bloom. This result was possible thanks to the use of oxygen concentration to define a mixing layer depth to be used instead of the mixed layer depth. The increase of net community production when the mixing layer shoals was linked to an increase in gross primary production.





# Abbreviations

AAIW	Antarctic Intermediate Water
EFE	End-February Event
IW	Intermediate water
MOW	Mediterranean Outflow Water
ML	Mixed layer
OSBL	Ocean surface boundary layer
OSI	Oxygen sub-surface increase
PAP	Porcupine Abyssal Plain
SAIW	Subarctic Intermediate Water
WOCE	World Ocean Circulation Experiment
XL	Mixing layer



# Mathematical annotations

AOU	$\mu\text{mol kg}^{-1}$	Apparent oxygen utilization
$c(\text{Chl } a)$	$\text{mg m}^{-3}$	Chlorophyll <i>a</i> concentration
$c(\text{O}_2)$	$\mu\text{mol kg}^{-1}$	Oxygen concentration
	or	
	$\mu\text{mol l}^{-1}$	
	(i.e., $\text{mmol m}^{-3}$ )	
$c_{\text{ref}}$	$\mu\text{mol l}^{-1}$	Oxygen reference (concentration at 5 m)
	(i.e., $\text{mmol m}^{-3}$ )	
$c_{\text{sat}}(\text{O}_2)$	$\mu\text{mol kg}^{-1}$	Oxygen saturation concentration
$E$	$\text{mmol m}^{-2} \text{d}^{-1}$	Entrainment
$F_{\text{as}}$	$\text{mmol m}^{-2} \text{d}^{-1}$	Air-sea oxygen flux
$H$	$\text{W m}^{-2}$	Net surface heat flux
$I(\text{O}_2)$	$\text{mmol m}^{-2}$	Oxygen inventory
$k_{600}$		Gas transfer velocity for $Sc=600$
$k(\text{O}_2)$		Gas transfer velocity for oxygen
$N$	$\text{mmol m}^{-2} \text{d}^{-1}$	Net community production (oxygen equivalents)
$N_C$	$\text{mmol m}^{-2} \text{d}^{-1}$	Net community production (carbon equivalents)
$P$	$\text{mmol m}^{-3} \text{d}^{-1}$	Gross primary production
$p$	dbar	Pressure
$p(\text{vap})$	dbar	Water vapour pressure
$R$	$\text{mmol m}^{-2} \text{d}^{-1}$	Respiration
$R_A$	$\text{mmol m}^{-2} \text{d}^{-1}$	Autotrophic respiration
$R_H$	$\text{mmol m}^{-2} \text{d}^{-1}$	Heterotrophic respiration
$s(\text{air})$		Air saturation
$s(\text{O}_2)$		Oxygen saturation
$S_A$	$\text{g kg}^{-1}$	Absolute salinity
$Sc$		Schmidt number
$t$	d	Time
$U_{10}$	$\text{m s}^{-1}$	Wind speed at 10 m over the sea surface
$z$	m	Depth
$z_{\text{eup}}$	m	Euphotic depth
$z_{\text{lim}}$	m	Limit depth for the calculation of the oxygen inventory
$z_{\text{mix}}$	m	Ocean surface boundary layer depth (mixing layer)
$z_{\text{mix}}(\text{O}_2)$	m	$z_{\text{mix}}$ defined by oxygen concentration
$z_{\text{mix}}(\sigma)$	m	$z_{\text{mix}}$ defined by density/temperature

$z_{\text{mix}}(\text{chl})$	m	$z_{\text{mix}}$ defined by chlorophyll <sub>a</sub> concentration
$\Delta$		Equilibrium fractional supersaturation
$\Theta$	°C	Potential temperature
$\mu$	s	Mean
$\rho$	kg m <sup>-3</sup>	Potential density
$\sigma$	kg m <sup>-3</sup>	Potential density - 1000
$\tau$	s	Optode response time (lag)
$\phi_{\text{cal}}$		Optode TCPhase
$\phi_{\text{TC}}$		Optode CalPhase

## References

- AGUSTÍ, S., REGAUDIE-DE-GIOUX, A., ARRIETA, J. M. & DUARTE, C. M. 2014. Consequences of UV-enhanced community respiration for plankton metabolic balance. *Limnology & Oceanography*, 59, 223-232.
- AIKEN, J., REES, N., HOOKER, S., HOLLIGAN, P., BALE, A., ROBINS, D., MOORE, G., HARRIS, R. & PILGRIM, D. 2000. The Atlantic Meridional Transect: overview and synthesis of data. *Progress in Oceanography*, 45, 257-312.
- ALKIRE, M. B., D'ASARO, E., LEE, C., JANE PERRY, M., GRAY, A., CETINIĆ, I., BRIGGS, N., REHM, E., KALLIN, E., KAISER, J. & GONZÁLEZ-POSADA, A. 2012. Estimates of net community production and export using high-resolution, Lagrangian measurements of O<sub>2</sub>, NO<sub>3</sub><sup>-</sup>, and POC through the evolution of a spring diatom bloom in the North Atlantic. *Deep Sea Research Part I: Oceanographic Research Papers*, 64, 157-174.
- ALKIRE, M. B., LEE, C., D'ASARO, E., PERRY, M. J., BRIGGS, N., CETINIĆ, I. & GRAY, A. 2014. Net community production and export from Seaglider measurements in the North Atlantic after the spring bloom. *Journal of Geophysical Research: Oceans*, 119, 6121-6139.
- ALLEN, J. T. & SMEED, D. A. 1996. Potential Vorticity and Vertical Velocity at the Iceland-Færøes Front. *Journal of Physical Oceanography*, 26, 2611-2634.
- ANDERSON, L. A. & SARMIENTO, J. L. 1994. Redfield ratios of remineralization determined by nutrient data analysis. *Global Biogeochem. Cy.*, 8, 65-80.
- ARÍSTEGUI, J., DUARTE, C., AGUSTÍ, S., DOVAL, M., ÁLVAREZ-SALGADO, X. A. & HANSELL, D. A. 2002. Dissolved organic carbon support of respiration in the dark ocean. *Science*, 298.
- BABIN, S. M., CARTON, J. A., DICKEY, T. D. & WIGGERT, J. D. 2004. Satellite evidence of hurricane-induced phytoplankton blooms in an oceanic desert. *Journal of Geophysical Research: Oceans*, 109. DOI: 10.1029/2003JC001938
- BARTON, A.D., FINKEL, Z.V., WARD, B.A., JOHNS, D.G., FOLLOWS, M.J., 2013. On the roles of cell size and trophic strategy in North Atlantic diatom and dinoflagellate communities, *Limnology and Oceanography*, 58, DOI: 10.4319/lo.2013.58.1.0254.
- BECKMANN, A. & HENSE, I. 2007. Beneath the surface: Characteristics of oceanic ecosystems under weak mixing conditions – A theoretical investigation. *Progress in Oceanography*, 75, 771-796.
- BEHRENFELD, M. J. 2010. Abandoning Sverdrup's Critical Depth Hypothesis on phytoplankton blooms. *Ecology*, 91, 977-989.
- BEHRENFELD, M. J. & BOSS, E. S. 2014. Resurrecting the ecological underpinnings of ocean plankton blooms. *Annual Review of Marine Science*, 6, 167-194.
- BENDER, M., DUCKLOW, H. W., KIDDON, J., J., M. & MARTIN, J. 1992. The carbon balance during the 1989 spring bloom in the North Atlantic Ocean, 47N/20W. *Deep Sea Research*, 39, 1707-1725.

- BERSCH, M. 2002. North Atlantic Oscillation–induced changes of the upper layer circulation in the northern North Atlantic Ocean. *Journal of Geophysical Research: Oceans*, 107, 3156.
- BERSCH, M., YASHAYAEV, I. & KOLTERMANN, K. 2007. Recent changes of the thermohaline circulation in the subpolar North Atlantic. *Ocean Dynamics*, 57, 223-235.
- BETT, B. J., MALZONE, M. G., NARAYANASWAMY, B. E. & WIGHAM, B. D. 2001. Temporal variability in phytodetritus and megabenthic activity at the seabed in the deep Northeast Atlantic. *Progress in Oceanography*, 50, 349-368.
- BIJMA J. 1991. Lunar pulses of carbonate output by spinose planktonic Foraminifera. Protozoa and their role in marine processes, ed. PC Reid, CM Turley, PH Burkill, pp. 353-54. Plymouth: Elsevier
- BILLETT, D. S. M., BETT, B. J., REID, W. D. K., BOORMAN, B. & PRIEDE, I. G. 2010. Long-term change in the abyssal NE Atlantic: The ‘Amperima Event’ revisited. *Deep Sea Research Part II: Topical Studies in Oceanography*, 57, 1406-1417.
- BITTIG, H. C., FIEDLER, B., SCHOLZ, R., KRAHMANN, G. & KÖRTZINGER, A. 2014. Time response of oxygen optodes on profiling platforms and its dependence on flow speed and temperature. *Limnology and Oceanography: Methods*, 12, 617-636.
- BITTIG, H. C. & KÖRTZINGER, A. 2015. Tackling oxygen optode drift: Near-surface and in-air oxygen optode measurements on a float provide an accurate in situ reference. *Journal of Atmospheric and Oceanic Technology*, 32, 1536-1543.
- BOSS, E. & BEHRENFELD, M. 2010. In situ evaluation of the initiation of the North Atlantic phytoplankton bloom. *Geophysical Research Letters*, 37, DOI: 10.1029/2010GL044174.
- BOWER, A. S. & VON APPEN, W. J. 2008. Interannual variability in the pathways of the north atlantic current over the mid-atlantic ridge and the impact of topography. *Journal of Physical Oceanography*, 3, 104-120.
- BOYER, T. P., ANTONOV, J. I., BARANOVA, O. K., GARCIA, H. E., JOHNSON, D. R., LOCARNINI, R. A. & LEVITUS, S. 2009. World ocean database 2009. NOAA Atlas NESDIS, 66.
- BRAINERD, K. E. & GREGG, M. C. 1995. Surface mixed and mixing layer depths. *Deep Sea Research Part I: Oceanographic Research Papers*, 42, 1521-1543.
- BRIGGS, N., PERRY, M. J., CETINIĆ, I., LEE, C., D'ASARO, E., GRAY, A. M. & REHM, E. 2011. High-resolution observations of aggregate flux during a sub-polar North Atlantic spring bloom. *Deep Sea Research Part I: Oceanographic Research Papers*, 58, 1031-1039.
- BROECKER, W. S. & PENG, T.-H. 1992. Interhemispheric transport of carbon dioxide by ocean circulation. *Nature*, 356, 587-589.
- BROECKER, W. S. & TAKAHASHI, T. 1985. Reconstruction of past atmospheric CO<sub>2</sub> from the chemistry of the contemporary ocean: An evaluation. Tech. Rep., TR-020.
- BRUNET, C., CASOTTI, R. & VANTREPOTTE, V. 2008. Phytoplankton diel and vertical variability in photobiological responses at a coastal station in the Mediterranean Sea. *Journal of Plankton Research*, 30, 645-654.
- BURY, N. R., GROSELL, M., WOOD, C. M., HOGSTRAND, C., WILSON, R. W., RANKIN, J. C., BUSK, M., LECKLIN, T. & JENSEN, F. B. 2001. Intestinal iron uptake in the European flounder (*Platichthys flesus*). *Journal of Experimental Biology*, 204, 3779-3787.

- BUSHINSKY, S. M. & EMERSON, S. 2015. Marine biological production from in situ oxygen measurements on a profiling float in the subarctic Pacific Ocean. *Global Biogeochemical Cycles*, 29, 2050-2060.
- CABEÇADAS, G., JOSÉ BROGUEIRA, M., GELENA CAVACO, M. & GONÇALVES, C. 2010. Chemical signature of intermediate water masses along western Portuguese margin. *Journal of Oceanography*, 66, 201-210.
- CARLSON, C. A., HANSELL, D. A., NELSON, N. B., SIEGEL, D. A., SMETHIE, W. M., KHATIWALA, S., MEYERS, M. M. & HALEWOOD, E. 2010. Dissolved organic carbon export and subsequent remineralization in the mesopelagic and bathypelagic realms of the North Atlantic basin. *Deep Sea Research Part II: Topical Studies in Oceanography*, 57, 1433-1445.
- CARPENTER, J. H. 1965. THE ACCURACY OF THE WINKLER METHOD FOR DISSOLVED OXYGEN ANALYSIS<sup>1</sup>. *Limnology and Oceanography*, 10, 135-140.
- CARRIT, D. E. & CARPENTER, J. H. 1966. Comparison and evaluation of currently employed modifications of the Winkler method for determining dissolved oxygen in sea-water. . *J. Mar. Res.*, 24, 286-318.
- CASTRO, C. G., PÉREZ, F. F., HOLLEY, S. E. & RÍOS, A. F. 1998. Chemical characterisation and modelling of water masses in the Northeast Atlantic. *Progress in Oceanography*, 41, 249-279.
- CASTRO-MORALES, K. & KAISER, J. 2012. Using dissolved oxygen concentrations to determine mixed layer depths in the Bellingshausen Sea. *Ocean Science*, 8, 1-10.
- CETINIĆ, I., TORO-FARMER, G., RAGAN, M., CARL OBERG, C. & JONES, B. H. 2009. Calibration procedure for Slocum glider deployed optical instruments. *Opt. Express*, 17, 15420-15430.
- CHARRIA, G., DADOU, I., CIPOLLINI, P., DRÉVILLON, M. & GARÇON, V. 2008. Influence of Rossby waves on primary production from a coupled physical-biogeochemical model in the North Atlantic Ocean. *Ocean Science*, 4, 199-213.
- CHESTER, R. 2000. *Marine Geochemistry*, 2nd ed., Blackwell, Malden, Mass.
- CIPOLLINI, P., CROMWELL, D., CHALLENGOR, P. G. & RAFFAGLIO, S. 2001. Rossby waves detected in global ocean colour data. *Geophysical Research Letters*, 28, 323-326.
- CISEWSKI, B., STRASS, V. H., LOSCH, M. & PRANDKE, H. 2008. Mixed layer analysis of a mesoscale eddy in the Antarctic Polar Front Zone. *Journal of Geophysical Research: Oceans*, 113(C5). DOI: 10.1029/2007JC004372
- COLE, H.S., HENSON, S., MARTIN, A.P. AND YOOL, A., 2015. Basin-wide mechanisms for spring bloom initiation: how typical is the North Atlantic?. *ICES Journal of Marine Science: Journal du Conseil*, p.fsu239. DOI: 10.1093/icesjms/fsu239
- COLEBROOK, J. M. 1982. Continuous plankton records: seasonal variations in the distribution and abundance of plankton in the North Atlantic Ocean and the North Sea. *Journal of Plankton Research*, 4, 435-462.
- CULBERSON, C. H. 1991. Dissolved Oxygen. WHP Operations and Methods. Unpublished manuscript, 15pp.

- CULLEN, J. J. 2015. Subsurface Chlorophyll Maximum Layers: Enduring Enigma or Mystery Solved? *Annual Review of Marine Science*, 7, 207-239.
- D'ASARO, E. A. 2014. Turbulence in the upper-ocean mixed layer. *Annual review of marine science*, 6, 101-115.
- DAMERELL, G. M., HEYWOOD, K. J., THOMPSON, A. F., BINETTI, U. & KAISER, J. 2016. The Vertical Structure of Upper Ocean Variability at the Porcupine Abyssal Plain during 2012-2013. *J. Geophys. Res. - Oceans*, Submitted.
- DANDONNEAU, Y., DESCHAMPS, P.-Y., NICOLAS, J.-M., LOISEL, H., BLANCHOT, J., MONTEL, Y., THIEULEUX, F. & BÉCU, G. 2004. Seasonal and interannual variability of ocean color and composition of phytoplankton communities in the North Atlantic, equatorial Pacific and South Pacific. *Deep Sea Research Part II: Topical Studies in Oceanography*, 51, 303-318.
- DAVIES, J. M. & WILLIAMS, P. J. LEB. 1984. Verification of  $^{14}\text{C}$  and  $\text{O}_2$  derived primary organic production measurements using an enclosed ecosystem. *Journal of Plankton Research*, 6, 457-473.
- DE BOYER MONTEGUT, C., MADEC, G., FISCHER, A. S., LAZAR, A. & IUDICONE, D. 2004. Mixed layer depth over the global ocean: An examination of profile data and a profile-based climatology. *J. Geophys. Res.*, 109(C12). DOI: 10.1029/2004JC002378
- DEL GIORGIO, P. A., COLE, J. J. & CIMBLERIS, A. 1997. Respiration rates in bacteria exceed phytoplankton production in unproductive aquatic systems. *Nature*, 385, 148-151.
- DEL GIORGIO, P. A. & DUARTE, C. M. 2002. Respiration in the open ocean. *Nature*, 420, 379-384.
- DEL GIORGIO, P. A. & WILLIAMS, P. J. L. B. 2005. *Respiration in Aquatic Ecosystems*. Oxford: University Press.
- DELAUNEY, L., COMPERE, C. & LEHAITRE, M. 2010. Biofouling protection for marine environmental sensors. *Ocean Science*, 6, 503-511.
- DENARO, G., VALENTI, D., LA COGNATA, A., SPAGNOLO, B., BONANNO, A., BASILONE, G., MAZZOLA, S., ZGOZI, S. W., ARONICA, S. & BRUNET, C. 2013. Spatio-temporal behaviour of the deep chlorophyll maximum in Mediterranean Sea: Development of a stochastic model for picophytoplankton dynamics. *Ecological Complexity*, 13, 21-34.
- DICKSON, A. G. 1996. Determination of dissolved oxygen in seawater by Winkler titration. *WOCE Operations Manual. Volume 3: The Observational Programme. Volume 3. Section 3.1: WOCE Hydrographic Programme. Part 3.1.3: WHP Operations and Methods*, edited by World Ocean Circulation Experiment, Woods Hole, Massachusetts, USA.
- DIMIER, C., GIOVANNI, S., FERDINANDO, T. & BRUNET, C. 2009. Comparative Ecophysiology of the Xanthophyll Cycle in Six Marine Phytoplanktonic Species. *Protist*, 160, 397-411.
- DONEY, S.C., FABRY, V. J., FEELY, R. A., KLEYPAS, J. A. 2009. Ocean Acidification: The Other  $\text{CO}_2$  Problem. *Annual Review of Marine Science*, Vol. 1: 169 -192. DOI: 10.1146/annurev.marine.010908.163834
- DONG, S., SPRINTALL, J., GILLE, S. T. & TALLEY, L. 2008. Southern Ocean mixed-layer depth from Argo float profiles. *J. Geophys. Res.*, 113(C6). DOI: 10.1029/2006JC004051

- DOVAL, M. D. & HANSELL, D. A. 2000. Organic carbon and apparent oxygen utilization in the western South Pacific and the central Indian Oceans. *Marine Chemistry*, 68, 249-264.
- DUARTE, C. M. & AGUSTÍ, S. 1998. The CO<sub>2</sub> Balance of Unproductive Aquatic Ecosystems. *Science*, 281, 234-236.
- DUARTE, C. M., REGAUDIE-DE-GIOUX, A., ARRIETA, J. M., DELGADO-HUERTAS, A. & AGUSTÍ, S. 2013. The Oligotrophic Ocean Is Heterotrophic. *Annual Review of Marine Science*, 5, 551-569.
- DUCKLOW, H. W. & DONEY, S. C. 2013. What is the metabolic state of the oligotrophic ocean? A debate. *Annual review of marine science*, 5, 525-533.
- DUCKLOW, H. W. & HARRIS, R. P. 1993. Introduction to the JGOFS North Atlantic bloom experiment. *Deep Sea Research Part II: Topical Studies in Oceanography*, 40, 1-8.
- DUTEIL, O., KOEVE, W., OSCHLIES, A., BIANCHI, D., GALBRAITH, E., KRIEST, I. & MATEAR, R. 2013. A novel estimate of ocean oxygen utilisation points to a reduced rate of respiration in the ocean interior. *Biogeosciences*, 10, 7723-7738.
- DUTKIEWICZ, S., FOLLOWS, M., MARSHALL, J. & GREGG, W. W. 2001. Interannual variability of phytoplankton abundances in the North Atlantic. *Deep Sea Research Part II: Topical Studies in Oceanography*, 48, 2323-2344.
- EMERSON, S., QUAY, P. D., STUMP, C., WILBUR, D. & SCHUDLICH, R. 1995. Chemical tracers of productivity and respiration in the subtropical Pacific Ocean. *Journal of Geophysical Research: Oceans*, 100, 15873-15887.
- EMERSON, S., STUMP, C. & NICHOLSON, D. 2008. Net biological oxygen production in the ocean: Remote in situ measurements of O<sub>2</sub> and N<sub>2</sub> in surface waters. *Global Biogeochemical Cycles*, 22, GB3023.
- ENRIQUEZ, R. M. & TAYLOR, J. R. 2015. Numerical simulations of the competition between wind-driven mixing and surface heating in triggering spring phytoplankton blooms. *ICES Journal of Marine Science: Journal du Conseil*, 72, 1926-1941.
- ERIKSEN, C. C., OSSE, T. J., LIGHT, R. D., WEN, T., LEHMAN, T. W., SABIN, P. L., BALLARD, J. W. & CHIODI, A. M. 2001. Seaglider: a long-range autonomous underwater vehicle for oceanographic research. *Oceanic Engineering, IEEE Journal of*, 26, 424-436.
- EVANS, M. A., MACINTYRE, S. & KLING, G. W. 2008. Internal wave effects on photosynthesis: Experiments, theory, and modeling. *Limnology and Oceanography*, 53, 339-353.
- FAIRALL, C. W., HARE, J. E., EDSON, J. B. & MCGILLIS, W. R. 2000. Measurement and parameterization of air-sea gas transfer. *Boundary Layer Meteorol*, 96, 63-105.
- FALKOWSKI, P. G., BARBER, R. T. & SMETACEK, V. 1998. Biogeochemical Controls and Feedbacks on Ocean Primary Production. *Science*, 281, 200-206.
- FASHAM, M. J. R., PLATT, T., IRWIN, B. & JONES, K. 1985. Factors affecting the spatial pattern of the deep chlorophyll maximum in the region of the Azores front. *Progress in Oceanography*, 14, 129-165.
- FENNEL, K. & BOSS, E. 2003. Subsurface maxima of phytoplankton and chlorophyll: Steady-state solutions from a simple model. *Limnology and Oceanography*, 48, 1521-1534.

- FERNAND, L., WESTON, K., MORRIS, T., GREENWOOD, N., BROWN, J. & JICKELLS, T. 2013. The contribution of the deep chlorophyll maximum to primary production in a seasonally stratified shelf sea, the North Sea. *Biogeochemistry*, 113, 153-166.
- FERNÁNDEZ I, C., RAIMBAULT, P., CANIAUX, G., GARCIA, N. & RIMMELIN, P. 2005. Influence of mesoscale eddies on nitrate distribution during the POMME program in the northeast Atlantic Ocean. *Journal of Marine Systems*, 55, 155-175.
- FERNÁNDEZ I, C., RAIMBAULT, P., GARCIA, N., RIMMELIN, P. & CANIAUX, G. 2005. An estimation of annual new production and carbon fluxes in the northeast Atlantic Ocean during 2001. *Journal of Geophysical Research: Oceans*, 110, C07S13.
- FERRARI, R., MERRIFIELD, S. T. & TAYLOR, J. R. 2015. Shutdown of convection triggers increase of surface chlorophyll. *Journal of Marine Systems*, 147, 116-122.
- FIELD, C. B., BEHRENFELD, M. J., RANDERSON, J. T. & FALKOWSKI, P. 1998. Primary Production of the Biosphere: Integrating Terrestrial and Oceanic Components. *Science*, 281, 237-240.
- FINDLAY, H. S., YOOL, A., NODALE, M. & PITCHFORD, J. W. 2006. Modelling of autumn plankton bloom dynamics. *Journal of Plankton Research*, 28, 209-220.
- FRAJKA-WILLIAMS, E., CUNNINGHAM, S. A., BRYDEN, H. & KING, B. A. 2011. Variability of Antarctic Bottom Water at 24.5°N in the Atlantic. *Journal of Geophysical Research: Oceans*, 116, C11026.
- FRAJKA-WILLIAMS, E., RHINES, P. B. & ERIKSEN, C. C. 2009. Physical controls and mesoscale variability in the Labrador Sea spring phytoplankton bloom observed by Seaglider. *Deep Sea Research Part I: Oceanographic Research Papers*, 56, 2144-2161.
- Franks, P.J., 2015. Has Sverdrup's critical depth hypothesis been tested? Mixed layers vs. turbulent layers. *ICES Journal of Marine Science: Journal du Conseil*, 72(6), pp.1897-1907. DOI: 10.1093/icesjms/fsu175
- FRIGSTAD, H., HENSON, S. A., HARTMAN, S. E., OMAR, A. M., JEANSSON, E., COLE, H., PEBODY, C. & LAMPITT, R. S. 2015. Links between surface productivity and deep ocean particle flux at the Porcupine Abyssal Plain sustained observatory. *Biogeosciences*, 12, 5885-5897.
- GAARDER, T. & GRAN, H. H. 1927. Investigations of the production of plankton in the Oslo Fjord. *Rapp. P. v. Reun. Cons. Perm. Int. Explor. Mer.*, 42, 1-48.
- GARCIA, H. E. & GORDON, L. I. 1992. Oxygen solubility in seawater: better fitting equations. *Limnology & Oceanography*, 37, 1307-1312.
- GARÇON, V. C., OSCHLIES, A., DONEY, S. C., MCGILLICUDDY, D. & WANIEK, J. 2001. The role of mesoscale variability on plankton dynamics in the North Atlantic. *Deep Sea Research Part II: Topical Studies in Oceanography*, 48, 2199-2226.
- GAXIOLA-CASTRO, G., ÁLVAREZ-BORREGO, S., NÁJERA-MARTÍNEZ, S. & ZIRINO, A. R. 2002. Internal waves effect on the Gulf of California phytoplankton. *Ciencias Marinas*, 28, 297-309.
- GODDIJN-MURPHY, L., WOOLF, D. K., CHAPRON, B. & QUEFFEULOU, P. 2013. Improvements to estimating the air-sea gas transfer velocity by using dual-frequency, altimeter backscatter. *Remote Sensing of Environment*, 139, 1-5.

- GODOY, N., CANEPA, A., LASTERNAS, S., MAYOL, E., RÚIZ-HALPERN, S. & AGUSTÍ, S. 2012. Experimental assessment of the effect of UVB radiation on plankton community metabolism along the Southeastern Pacific off Chile. *Biogeosciences*, 9, 1267-1276.
- GOERICKE, R., MONTOYA, J.P., 1998. Estimating the contribution of microalgal taxa to chlorophyll a in the field-variations of pigment ratios under nutrient-and light-limited growth. *Mar Ecol Prog Ser* 169:97–112
- GOODAY, A. J., MALZONE, M. G., BETT, B. J. & LAMONT, P. A. 2010. Decadal-scale changes in shallow-infaunal foraminiferal assemblages at the Porcupine Abyssal Plain, NE Atlantic. *Deep Sea Research Part II: Topical Studies in Oceanography*, 57, 1362-1382.
- GRUBER, N. & SARMIENTO, J. L. 1997. Global patterns of marine nitrogen fixation and denitrification. *Global Biogeochemical Cycles*, 11, 235-266.
- GUTKNECHT, E., DADOU, I., CHARRIA, G., CIPOLLINI, P. & GARÇON, V. 2010. Spatial and temporal variability of the remotely sensed chlorophyll a signal associated with Rossby waves in the South Atlantic Ocean. *Journal of Geophysical Research: Oceans*, 115, C05004.
- HAMME, R. C. & EMERSON, S. 2006. Constraining bubble dynamics and mixing with dissolved gases: Implications for productivity measurements by oxygen mass balance. *Journal of Marine Research*, 64, 73-95.
- HANSELL, D. A., CARLSON, C. A., REPETA, D. J. & SCHLITZER, R. 2009. Dissolved organic matter in the ocean: A controversy stimulates new insights. *Oceanography*, 22, 202-211.
- HARTMAN, S. E., LARKIN, K. E., LAMPITT, R. S., LANKHORST, M. & HYDES, D. J. 2010. Seasonal and inter-annual biogeochemical variations in the Porcupine Abyssal Plain 2003–2005 associated with winter mixing and surface circulation. *Deep Sea Research Part II: Topical Studies in Oceanography*, 57, 1303-1312.
- HENSON, S. A., DUNNE, J. P. & SARMIENTO, J. L. 2009. Decadal variability in North Atlantic phytoplankton blooms. *Journal of Geophysical Research: Oceans* (1978–2012), 114(C4). DOI: 10.1029/2008JC005139
- HENSON, S. A., ROBINSON, I., ALLEN, J. T. & WANIEK, J. J. 2006. Effect of meteorological conditions on interannual variability in timing and magnitude of the spring bloom in the Irminger Basin, North Atlantic. *Deep Sea Research Part I: Oceanographic Research Papers*, 53, 1601-1615.
- HENRIKSEN, P., RIEMANN, B., KAAS, H., SØRENSEN, H.M., SØRENSEN, H.L., 2002. Effects of nutrient-limitation and irradiance on marine phytoplankton pigments. *J Plankton Res* 24:835–858
- HEUPEL, M. R., REISS, K. L., YEISER, B. G. & SIMPFENDORFER, C. A. 2008. Effects of biofouling on performance of moored data logging acoustic receivers. *Limnology and Oceanography: Methods*, 6, 327-335.
- HOUGHTON, R. A. 2007. Balancing the global carbon budget. *Annu. Rev. Earth Planet. Sci.* , 35, 313-347.
- HUISMAN, J., OOSTVEEN, P. V. & WEISSING, F. J. 1999. Critical Depth and Critical Turbulence: Two Different Mechanisms for the Development of Phytoplankton Blooms. *Limnology and Oceanography*, 44, 1781-1787.

- HUISMAN, J., SHARPLES, J., STROOM, J. M., VISSER, P. M., KARDINAAL, W. E. A., VERSPAGEN, J. M. H. & SOMMEIJER, B. 2004. Changes in turbulent mixing shift competition for light between phytoplankton species. *Ecology*, 85, 2960-2970.
- HULL, T., GREENWOOD, N., KAISER, J. & JOHNSON, M. 2016. Uncertainty and sensitivity in optode-based shelf-sea net community production estimates. *Biogeosciences*, 13, 934-959.
- ITO, T., FOLLOWS, M. J. & BOYLE, E. A. 2004. Is AOU a good measure of respiration in the oceans? *Geophysical Research Letters*, 31(17). DOI: 10.1029/2004GL020900
- JOHNSON, G. C. & GRUBER, N. 2007. Decadal water mass variations along 20°W in the Northeastern Atlantic Ocean. *Progress in Oceanography*, 73, 277-295.
- JOHNSON, K. S. 2010. Simultaneous measurements of nitrate, oxygen, and carbon dioxide on oceanographic moorings: Observing the Redfield ratio in real time. *Limnology & Oceanography*, 55, 615-627.
- JURADO, E., VAN DER WOERD, H. J. & DIJKSTRA, H. A. 2012. Microstructure measurements along a quasi-meridional transect in the northeastern Atlantic Ocean. *Journal of Geophysical Research: Oceans*, 117, C04016.
- KAHRU, M., BROTHAS, V., MANZANO-SARABIA, M. & MITCHELL, B. G. 2011. Are phytoplankton blooms occurring earlier in the Arctic? *Global Change Biology*, 17, 1733-1739.
- KAISER, J., REUER, M. K., BARNETT, B. & BENDER, M. L. 2005. Marine productivity estimates from continuous O<sub>2</sub>/Ar ratio measurements by membrane inlet mass spectrometry. *Geophysical research letters*, 32. DOI: 10.1029/2005GL023459
- KALOGEROPOULOU, V., BETT, B. J., GOODAY, A. J., LAMPADARIOU, N., MARTINEZ ARBIZU, P. & VANREUSEL, A. 2010. Temporal changes (1989–1999) in deep-sea metazoan meiofaunal assemblages on the Porcupine Abyssal Plain, NE Atlantic. *Deep Sea Research Part II: Topical Studies in Oceanography*, 57, 1383-1395.
- KAMYKOWSKI, D. 1979. The growth response of a model *Gymnodinium splendens* in stationary and wavy water columns. *Marine Biology*, 50, 289-303.
- KARA, A. B., ROCHFORD, P. A. & HURLBURT, H. E. 2000. Mixed layer depth variability and barrier layer formation over the North Pacific Ocean. *J. Geophys. Res.*, 105, 783-816.
- KARL, D. M., HEBEL, D. V., BJÖRKMAN, K. & LETELIER, R. M. 1998. The role of dissolved organic matter release in the productivity of the oligotrophic North Pacific Ocean. *Limnology & Oceanography*, 43, 1270-1286.
- KARL, D. M., LAWS, E. A., MORRIS, P., WILLIAMS, P. J. L. & EMERSON, S. 2003. Global carbon cycle (communication arising): Metabolic balance of the open sea. *Nature*, 426, 32-32.
- KEELING, R. F., KÖRTZINGER, A. & GRUBER, N. 2009. Ocean Deoxygenation in a Warming World. *Annual Review of Marine Science*, 2, 199-229.
- KINKADE, C. S., MARRA, J., DICKEY, T. D. & WELLER, R. 2001. An annual cycle of phytoplankton biomass in the Arabian Sea, 1994–1995, as determined by moored optical sensors. *Deep Sea Research Part II: Topical Studies in Oceanography*, 48, 1285-1301.
- KIRK, J. T. O. 1994. *Light and Photosynthesis in Aquatic Ecosystems*. 2nd Edn. Cambridge: Univ. Press. .

- KLAUSMEIER, C. A. & LITCHMAN, E. 2001. Algal games: The vertical distribution of phytoplankton in poorly mixed water columns. *Limnology & Oceanography*, 46, 1998-2007.
- KLAUSMEIER, C. A., LITCHMAN, E. & LEVIN, S. A. 2007. A model of flexible uptake of two essential resources. *Journal of Theoretical Biology*, 246, 278-289.
- KOEVE, W. 2004. Spring bloom carbon to nitrogen ratio of net community production in the temperate N. Atlantic. *Deep Sea Research Part I: Oceanographic Research Papers*, 51, 1579-1600.
- KÖRTZINGER, A., KOEVE, W., KÄHLER, P. & MINTROP, L. 2001. C:N ratios in the mixed layer during the productive season in the northeast Atlantic Ocean. *Deep Sea Research Part I: Oceanographic Research Papers*, 48, 661-688.
- KÖRTZINGER, A., SCHIMANSKI, J., SEND, U. & WALLACE, D. 2004. The Ocean Takes a Deep Breath. *Science*, 306, 1337-1337.
- KÖRTZINGER, A., SEND, U., LAMPITT, R. S., HARTMAN, S., WALLACE, D. W. R., KARSTENSEN, J., VILLAGARCIA, M. G., LLINÁS, O. & DEGRANDPRE, M. D. 2008a. The seasonal pCO<sub>2</sub> cycle at 49°N/16.5°W in the northeastern Atlantic Ocean and what it tells us about biological productivity. *Journal of Geophysical Research: Oceans*, 113, C04020.
- KÖRTZINGER, A., SEND, U., WALLACE, D. W. R., KARSTENSEN, J. & DEGRANDPRE, M. D. 2008b. Seasonal cycle of O<sub>2</sub> and pCO<sub>2</sub> in the central Labrador Sea: Atmospheric, biological, and physical implications. *Global Biogeochemical Cycles*, 22, GB1014.
- KRAHMANN, G., KANZOW, T., KARSTENSEN, J. & SCHLUNDT, M. 2011. Results from a Glider Swarm Experiment near Cape Verde. [http://eprints.uni-kiel.de/12248/1/EGO\\_2011\\_-\\_Gerd\\_Krahmann.pdf](http://eprints.uni-kiel.de/12248/1/EGO_2011_-_Gerd_Krahmann.pdf)
- LAMPITT, R. S., BETT, B. J., KIRIAKOULAKIS, K., POPOVA, E. E., RAGUENEAU, O., VANGRIESHEIM, A. & WOLFF, G. A. 2001. Material supply to the abyssal seafloor in the Northeast Atlantic. *Progress in Oceanography*, 50, 27-63.
- LAMPITT, R. S., BILLET, D. S. M. & MARTIN, A. P. 2010. The sustained observatory over the Porcupine Abyssal Plain (PAP): Insights from time series observations and process studies. *Deep Sea Research Part II: Topical Studies in Oceanography*, 57, 1267-1271.
- LAMPITT, R. S., SALTER, I., DE CUEVAS, B. A., HARTMAN, S., LARKIN, K. E. & PEBODY, C. A. 2010. Long-term variability of downward particle flux in the deep northeast Atlantic: Causes and trends. *Deep Sea Research Part II: Topical Studies in Oceanography*, 57, 1346-1361.
- LANGDON, C. 1984. Dissolved oxygen monitoring system using a pulsed electrode: design, performance and evaluation. *Deep-Sea Research*, 31, 1357-1367.
- LE QUÉRÉ, C., AUMONT, O., MONFRAY, P. & ORR, J. C. 2003. Propagation of climatic events on ocean stratification, marine biology, and CO<sub>2</sub>: case studies over the 1979–1999 period. *J. Geophys. Res.*, 108, 3375.
- LETELIER, R. M., KARL, D. M., ABBOTT, M. R. & BIDIGARE, R. R. 2004. Light driven seasonal patterns of chlorophyll and nitrate in the lower euphotic zone of the North Pacific Subtropical Gyre. *Limnology and Oceanography*, 49, 508-519.
- LETERME, S. C., M. EDWARDS, L. SEURONT, M. J. ATTRILL, P. C. REID, AND A. W. G. JOHN. 2005. Decadal basin-scale changes in diatom, dinoflagellates, and phytoplankton

color across the North Atlantic. *Limnol. Oceanogr.* 50: 1244–1253, DOI:10.4319/lo.2005.50.4.1244.

LÉVY, M., KLEIN, P. & TREGUIER, A.-M. 2001. Impact of sub-mesoscale physics on production and subduction of phytoplankton in an oligotrophic regime. *Journal of marine research*, 59, 535-565.

LÉVY, M., LEHAHN, Y., ANDRÉ, J.-M., MÉMERY, L., LOISEL, H. & HEIFETZ, E. 2005. Production regimes in the northeast Atlantic: A study based on Sea-viewing Wide Field-of-view Sensor (SeaWiFS) chlorophyll and ocean general circulation model mixed layer depth. *Journal of Geophysical Research: Oceans*, 110, .

LOBE, H., HALDEMAN, C. & GLENN, S. M. 2010. ClearSignal Coating Controls Biofouling On the Rutgers Glider Crossing. *Sea Technol*, 51, 91-96.

LOHMANN, R., JURADO, E., DIJKSTRA, H. A. & DACHS, J. 2013. Vertical eddy diffusion as a key mechanism for removing perfluorooctanoic acid (PFOA) from the global surface oceans. *Environmental Pollution*, 179, 88-94.

LONGHURST, A. 1998. *Ecological geography of the Sea*. Academic, San Diego.

LONGHURST, A., SATHYENDRANATH, S., PLATT, T. & CAVERHILL, C. M. 1995. An estimate of global primary production in the ocean from satellite radiometer data. *Journal of Plankton Research*, 17, 1245-1271.

LOZOVATSKY, I. D., ROGET, E., FERNANDO, H. J. S., FIGUEROA, M. & SHAPOVALOV, S. 2006. Sheared turbulence in a weakly stratified upper ocean. *Deep Sea Research Part I: Oceanographic Research Papers*, 53, 387-407.

LUKAS, R. & LINDSTROM, E. 1991. The mixed layer of the western equatorial Pacific Ocean. *J. Geophys. Res.*, 96, 3343-335. DOI: 10.1029/90JC01951

LUZ, B., BARKAN, E., BENDER, M.L., THIEMENS, M.H. & BOERING, K.A., 1999. Triple-isotope composition of atmospheric oxygen as a tracer of biosphere productivity. *Nature*, 400(6744), pp.547-550.

LUZ, B., & BARKAN, E. (2000). Assessment of oceanic productivity with the triple-isotope composition of dissolved oxygen. *Science* 288, 2028–2031. DOI: 10.1126/science.288.5473.2028

MACHU, E., FERRET, B. & GARÇON, V. 1999. Phytoplankton pigment distribution from SeaWiFS data in the subtropical convergence zone south of Africa: A wavelet analysis. *Geophysical Research Letters*, 26, 1469-1472.

MAHADEVAN, A. 2006. Modeling vertical motion at ocean fronts: Are nonhydrostatic effects relevant at submesoscales? *Ocean Modelling*, 14, 222-240.

MANN, K. H. & LAZIER, R. H. 1996. *Dynamics of Marine Ecosystems*. Blackwell Publishing, Malden, MA.

MANOV, D. V., CHANG, G. C. & DICKEY, T. D. 2004. Methods for reducing biofouling of moored optical sensors. *Journal of Atmospheric and Oceanic Technology*, 21, 958-968.

MARGALEF, R., 1978. Life-forms of phytoplankton as survival alternatives in an unstable environment. *Oceanol. Acta* 1: 493–509.

- MARRA, J. 2012. Comment on “Measuring primary production rates in the ocean: Enigmatic results between incubation and non-incubation methods at Station ALOHA” by Quay, P. D., et al. *Glob. Biogeochem. Cycles* 26(2). DOI: 10.1029/2011GB004087
- MARRA J., BIDIGARE, R. R. & D., D. T. 1990. Nutrients and mixing, chlorophyll and phytoplankton growth. *Deep Sea Research* 37, 127-143.
- MARTIN, J., KNAUER, G., KARL, D., BROENKOW, W.: VERTEX: carbon cycling in the Northeast Pacific, *Deep-Sea Res.*, 34, 267– 285, 1987.
- MARTIN, A. P., LUCAS, M. I., PAINTER, S. C., PIDCOCK, R., PRANDKE, H., PRANDKE, H. & STINCHCOMBE, M. C. 2010. The supply of nutrients due to vertical turbulent mixing: A study at the Porcupine Abyssal Plain study site in the northeast Atlantic. *Deep Sea Research Part II: Topical Studies in Oceanography*, 57, 1293-1302.
- MARTIN, P., LAMPITT, R. S., JANE PERRY, M., SANDERS, R., LEE, C. & D'ASARO, E. 2011. Export and mesopelagic particle flux during a North Atlantic spring diatom bloom. *Deep Sea Research Part I: Oceanographic Research Papers*, 58, 338-349.
- MARTINEZ, E., ANTOINE, D., D'ORTENZIO, F. & DE BOYER MONTÉGUT, C. 2011. Phytoplankton spring and fall blooms in the North Atlantic in the 1980s and 2000s. *Journal of Geophysical Research: Oceans*, 116..
- MASKE, H. & GARCIA-MENDOZA, E. 1994. Adsorption of dissolved organic matter to the inorganic filter substrate and its implications for <sup>14</sup>C uptake measurements. *Appl. Environ. Microb.* , 60, 3887–3889.
- MCCARTNEY, M. S. & TALLEY, L. D. 1982. The Subpolar Mode Water of the North Atlantic Ocean. *Journal of Physical Oceanography*, 12, 1169-1188.
- MCNEIL, C. L. & D'ASARO, E. A. 2014. A calibration equation for oxygen optodes based on physical properties of the sensing foil. *Limnol. Oceanogr.: Methods*, 12, 139-154.
- MCQUATTERS-GOLLOP, A., D. RAITOS, M. EDWARDS, AND M. J. ATTRILL. 2007. Spatial patterns of diatom and dinoflagellate seasonal cycles in the NE Atlantic Ocean. *Mar. Ecol. Prog. Ser.* 339: 301–306, DOI:10.3354/meps339301
- MOLINE, M. A. & WENDT, D. 2011. Evaluation of glider coatings against biofouling for improved flight performance. DTIC Document.
- MONTEREY, G. I., LEVITUS, S., UNITED STATES. NATIONAL ENVIRONMENTAL SATELLITE, D. & INFORMATION, S. 1997. Seasonal variability of mixed layer depth for the world ocean, US Department of Commerce, National Oceanic and Atmospheric Administration, National Environmental Satellite, Data, and Information Service.
- MUACHO, S., DA SILVA, J. C. B., BROTAS, V. & OLIVEIRA, P. B. 2013. Effect of internal waves on near-surface chlorophyll concentration and primary production in the Nazaré Canyon (west of the Iberian Peninsula). *Deep Sea Research Part I: Oceanographic Research Papers*, 81, 89-96.
- NEUER, S., CIANCA, A., HELMKE, P., FREUDENTHAL, T., DAVENPORT, R., MEGGERS, H., KNOLL, M., SANTANA-CASIANO, J. M., GONZÁLEZ-DAVILA, M., RUEDA, M.-J. & LLINÁS, O. 2007. Biogeochemistry and hydrography in the eastern subtropical North Atlantic gyre. Results from the European time-series station ESTOC. *Progress in Oceanography*, 72, 1-29.

- NICHOLSON, D., EMERSON, S. & ERIKSEN, C. C. 2008. Net community production in the deep euphotic zone of the subtropical North Pacific gyre from glider surveys. *Limnology and Oceanography*, 53, 2226-2236.
- NICHOLSON, D. P., WILSON, S. T., DONEY, S. C. & KARL, D. M. 2015. Quantifying subtropical North Pacific gyre mixed layer primary productivity from Seaglider observations of diel oxygen cycles. *Geophys. Res. Lett.*, 42, 4032-4039.
- NIGHTINGALE, P. D., MALIN, G., LAW, C. S., WATSON, A. J., LISS, P. S., LIDDICOAT, M. I., BOUTIN, J. & UPSTILL-GODDARD, R. C. 2000. In situ evaluation of air-sea gas exchange parameterizations using novel conservative and volatile tracers. *Global Biogeochemical Cycles*, 14, 373-387.
- NOH, Y. & LEE, W. S. 2008. Mixed and Mixing Layer Depths Simulated by an OGCM. *Journal of Oceanography*, 64, 217-225.
- OGURA, N. 1970. The relation between dissolved organic carbon and apparent oxygen utilisation in the Western North Pacific. *Deep Sea Research*, 17, 221-231.
- OOMAND, M.M., D'ASARO, E.A., LEE, C.M., PERRY, M.J., BRIGGS, N., CETINIĆ, I. AND MAHADEVAN, A., 2015. Eddy-driven subduction exports particulate organic carbon from the spring bloom. *Science*, 348(6231), pp.222-225. DOI: 10.1126/science.1260062
- MAND, M. M., D'ASARO, E. A., LEE, C. M., PERRY, M. J., BRIGGS, N., CETINIĆ, I. & MAHADEVAN, A. 2015. Eddy-driven subduction exports particulate organic carbon from the spring bloom. *Science*.
- OSTLE, C., JOHNSON, M., LANDSCHÜTZER, P., SCHUSTER, U., HARTMAN, S., HULL, T. & ROBINSON, C. 2015. Net community production in the North Atlantic Ocean derived from Volunteer Observing Ship data. *Global Biogeochemical Cycles*, 29, 80-95.
- PAINTER, S. C., LUCAS, M. I., STINCHCOMBE, M. C., BIBBY, T. S. & POULTON, A. J. 2010. Summertime trends in pelagic biogeochemistry at the Porcupine Abyssal Plain study site in the northeast Atlantic. *Deep Sea Research Part II: Topical Studies in Oceanography*, 57, 1313-1323.
- PAINTER, S. C., PIDCOCK, R. E. & ALLEN, J. T. 2010. A mesoscale eddy driving spatial and temporal heterogeneity in the productivity of the euphotic zone of the northeast Atlantic. *Deep Sea Research Part II: Topical Studies in Oceanography*, 57, 1281-1292.
- PALEVSKY, H. I., RIBALET, F., SWALWELL, J. E., COSCA, C. E., COKELET, E. D., FEELY, R. A., ARMBRUST, E. V. & QUAY, P. D. 2013. The influence of net community production and phytoplankton community structure on CO<sub>2</sub> uptake in the Gulf of Alaska. *Global Biogeochemical Cycles*, 27, 664-676.
- PAN, X., WONG, G. T. F., SHIAH, F. K. & HO, T. Y. 2012. Enhancement of biological productivity by internal waves: Observations in the summertime in the northern South China Sea. *Journal of Oceanography*, 68, 427-437.
- POLLARD, R. T. 1980. Properties of Near-Surface Inertial Oscillations. *Journal of Physical Oceanography*, 10, 385-398.
- POLLARD, R. T. & PU, S. 1985. Structure and circulation of the Upper Atlantic Ocean northeast of the Azores. *Progress in Oceanography*, 14, 443-462.

- QUAY, P., PEACOCK, C., BJÖRKMAN, K. & D., K. 2010. Measuring primary production rates in the ocean: Enigmatic results between incubation and non-incubation methods at Station ALOHA. *Global Biogeochem. Cycles*, 24. DOI: 10.1029/2009GB003665
- QUAY, P. D., STUTSMAN, J. & STEINHOFF, T. 2012. Primary production and carbon export rates across the subpolar N. Atlantic Ocean basin based on triple oxygen isotope and dissolved O<sub>2</sub> and Ar gas measurements. *Global Biogeochemical Cycles*, 26(2). DOI: 10.1029/2010GB004003
- REGAUDIE-DE-GIOUX, A., LASTERNAS, S., AGUSTÍ, S. & DUARTE, C. 2014. Comparing marine primary production estimates through different methods and development of conversion equations. *Frontiers in Marine Science*, 1-p 19. DOI: 10.3389/fmars.2014.00019
- RICE, A. L., BILLET, D. S. M., THURSTON, M. H. & LAMPITT, R. S. 1991. The Institute Of Oceanographic Sciences Biology Programme In The Porcupine Seabight: Background And General Introduction. *Journal of the Marine Biological Association of the United Kingdom*, 71, 281-310.
- RIESEBELL, U., ZONDERVAN, I., ROST, B., TORTELL, P. D., ZEEBE R. E., MOREL, F. M. M. 2000. Reduced calcification of marine plankton in response to increased atmospheric CO<sub>2</sub>. *Nature* 407:364–67
- RÍOS, A. F., PÉREZ, F. F. & FRAGA, F. 1992. Water masses in the upper and middle North Atlantic Ocean east of the Azores. *Deep Sea Research Part A. Oceanographic Research Papers*, 39, 645-658.
- RIPPETH, T. P., PALMER, M. R., SIMPSON, J. H., FISHER, N. R. & SHARPLES, J. 2005. Thermocline mixing in summer stratified continental shelf seas. *Geophysical Research Letters*, 32(5). DOI: 10.1029/2004GL022104
- RIPPETH, T. P., WILES, P., PALMER, M. R., SHARPLES, J. & TWEDDLE, J. 2009. The diapycnal nutrient flux and shear-induced diapycnal mixing in the seasonally stratified western Irish Sea. *Continental Shelf Research*, 29, 1580-1587.
- ROBERTSON, J.E., WATSON, A.J., LANGDON, C., Ling, R.D. & WOOD, J.W. 1992. Diurnal variation in surface pCO<sub>2</sub> and O<sub>2</sub> at 60°N, 20°W in the North Atlantic. *Deep-Sea Res II*, vol. 40, no.1/2, pp 409-422.
- ROBINSON, C., TILSTONE, G. H., REES, A. P., SMYTH, T. J., FISHWICK, J. R. & TARRAN, G. A. 2009. Comparison of in vitro and in situ plankton production determinations. *Aquat. Microb. Ecol.*, 54, 13-34.
- ROBINSON, C. & WILLIAMS, P. J. L. B. 2005. Respiration and its measurement in surface marine waters. *Respiration in aquatic ecosystems*, 147-180.
- ROEMMICH, D., JOHNSON, G. C., RISER, S., DAVIS, R. & GILSON, J. 2009. The Argo program observing the global ocean with profiling floats. *Oceanography* 22, 34-43.
- RUDNICK, D. L. 2016. Ocean Research Enabled by Underwater Gliders. *Annual review of marine science*, 8, 519-541.
- RUMYANTSEVA, A., LUCAS, N., RIPPETH, T., MARTIN, A., PAINTER, S. C., BOYD, T. J. & HENSON, S. 2015. Ocean nutrient pathways associated with the passage of a storm. *Global Biogeochemical Cycles*, 29, 1179-1189.

RUSSELL, J.L. AND DICKSON, A.G., 2003. Variability in oxygen and nutrients in South Pacific Antarctic intermediate water. *Global biogeochemical cycles*, 17(2). DOI: 10.1029/2000GB001317

SABINE, C. L., FEELY, R. A., GRUBER, N., KEY, R. M. & LEE, K. 2004. The oceanic sink for anthropogenic CO<sub>2</sub>. *Science*, 305, 367-371.

SABINE, C. L., KEY, R. M., JOHNSON, K. M., MILLERO, F. J., POISSON, A., SARMIENTO, J. L., WALLACE, D. W. R. & WINN, C. D. 1999. Anthropogenic CO<sub>2</sub> inventory of the Indian Ocean. *Global Biogeochemical Cycles*, 13, 179-198.

SAKSHAUG, E., BRICAUD, A., DANDONNEAU, Y., FALKOWSKI, P., KIEFER, D., LEGEDRE, L., MOREL, A., PARSLow, J., TAKAHASHI M., 1997. *J Plank- ton Res* 19:1637–1670

SANGRÁ, P., BASTERRETXEA, G., PELEGRÍ, J. L. & ARÍSTEGUI, J. 2001. Chlorophyll increase due to internal waves on the shelf break of Gran Canaria (Canary Islands). *Scientia Marina*, 65, 89-97.

SARAFANOV, A. 2009. On the effect of the north Atlantic oscillation on temperature and salinity of the subpolar north Atlantic intermediate and deep waters. *ICES Journal of Marine Science*, 66, 1448-1454.

SARAFANOV, A., FALINA, A., SOKOV, A. & DEMIDOV, A. 2008. Intense warming and salinification of intermediate waters of southern origin in the eastern subpolar North Atlantic in the 1990s to mid-2000s. *Journal of Geophysical Research: Oceans*, 113. DOI: 10.1029/2008JC004975

SATHYENDRANATH, S., LONGHURST, A., CAVERHILL, C. M. & PLATT, T. 1995. Regionally and seasonally differentiated primary production in the North Atlantic. *Deep Sea Research Part I: Oceanographic Research Papers*, 42, 1773-1802.

SATHYENDRANATH, S., PLATT, T., CAVERHILL, C. M., WARNOCK, R. E. & LEWIS, M. R. 1989. Remote sensing of oceanic primary production: computations using a spectral model. *Deep Sea Research Part A. Oceanographic Research Papers*, 36, 431-453.

SAVIDGE, G., TURNER, D. R., BURKILL, P. H., WATSON, A. J., ANGEL, M. V., PINGREE, R. D., LEACH, H. & RICHARDS, K. J. 1992. The BOFS 1990 spring bloom experiment: Temporal evolution and spatial variability of the hydrographic field. *Progress in Oceanography*, 29, 235-281.

SCHNEIDER, N. & MULLER, P. 1990. The meridional and seasonal structures of the mixed-layer depth and its diurnal amplitude observed during the Hawaii-to-Tahiti Shuttle Experiment. *Journal of Physical Oceanography*, 20, 1395-1404.

SCHOFIELD, O., KOHUT, J., ARAGON, D., CREED, L. & GRAVER, J. 2007. Slocum gliders: robust and ready. *J. Field Robot*, 24, 473-485.

SERRET, P., ROBINSON, C., FERNÁNDEZ, E., TEIRA, E. AND TILSTONE, G., 2001. Latitudinal variation of the balance between plankton photosynthesis and respiration in the eastern Atlantic Ocean. *Limnology and Oceanography*, 46(7), pp.1642-1652. DOI: 10.4319/lo.2001.46.7.1642

SHERMAN, J., DAVIS, R. E., OWENS, W. B. & VALDES, J. 2001. The autonomous underwater glider "Spray". *IEEE J. Ocean. Eng.*, 26, 437-446.

- SHILLER, A. M. (1981). Calculating the oceanic CO<sub>2</sub> increase: A need for caution, *J. Geophys. Res.*, 86(C11), 11083–11088, DOI:10.1029/JC086iC11p11083.
- SHOOSMITH, D.R., RICHARDSON, P.L., BOWER, A.S. AND ROSSBY, H.T., 2005. Discrete eddies in the northern North Atlantic as observed by looping RAFOS floats. *Deep Sea Research Part II: Topical Studies in Oceanography*, 52(3), pp.627-650.
- SIEGEL, D. A., DONEY, S. C. & YODER, J. A. 2002. The North Atlantic Spring Phytoplankton Bloom and Sverdrup's Critical Depth Hypothesis. *Science*, 296, 730-733.
- SOMMER, U., ADRIAN, R., DE SENERPONT DOMIS, L., ELSER, J. J., GAEDKE, U., IBELINGS, B., JEPPESEN, E., LÜRLING, M., MOLINERO, J. C., MOOIJ, W. M., VAN DONK, E. & WINDER, M. 2012. Beyond the Plankton Ecology Group (PEG) Model: Mechanisms Driving Plankton Succession. *Annual Review of Ecology, Evolution, and Systematics*, 43, 429-448.
- SON, S., PLATT, T., BOUMAN, H., LEE, D. AND SATHYENDRANATH, S., 2006. Satellite observation of chlorophyll and nutrients increase induced by Typhoon Megi in the Japan/East Sea. *Geophysical research letters*, 33(5). DOI: 10.1029/2005GL025065
- SOTO, E. H., PATERSON, G. L. J., BILLET, D. S. M., HAWKINS, L. E., GALÉRON, J. & SIBUET, M. 2010. Temporal variability in polychaete assemblages of the abyssal NE Atlantic Ocean. *Deep Sea Research Part II: Topical Studies in Oceanography*, 57, 1396-1405.
- STANLEY, R. H. R., DONEY, S. C., JERKINS, W. J. & LOTT, D. E. 2012. Apparent oxygen utilization rates calculated from tritium and helium-3 profiles at the Bermuda Atlantic Time-series Study site. *Biogeosciences*, 9, 1969-1983.
- STENDARDO, I. & GRUBER, N. 2012. Oxygen trends over five decades in the North Atlantic. *Journal of Geophysical Research: Oceans*, 117, C11004.
- STENDARDO, I., KIEKE, D., RHEIN, M., GRUBER, N. & STEINFELDT, R. 2015. Interannual to decadal oxygen variability in the mid-depth water masses of the eastern North Atlantic. *Deep Sea Research Part I: Oceanographic Research Papers*, 95, 85-98.
- STRASS, V. H. & WOODS, J. D. 1991. New production in the summer revealed by the meridional slope of the deep chlorophyll maximum. *Deep Sea Research Part A. Oceanographic Research Papers*, 38, 35-56.
- SUTHERLAND, G., REVERDIN, G., MARIÉ, L. AND WARD, B., 2014. Mixed and mixing layer depths in the ocean surface boundary layer under conditions of diurnal stratification. *Geophysical Research Letters*, 41(23), pp.8469-8476. DOI: 10.1002/2014GL061939
- SVERDRUP, H. U. 1953. On Conditions for the Vernal Blooming of Phytoplankton. *Journal du Conseil*, 18, 287-295.
- TAKAHASHI, T., SUTHERLAND, S. C., SWEENEY, C., POISSON, A., METZL, N., TILBROOK, B., BATES, N., WANNINKHOF, R., FEELY, R. A., SABINE, C., OLAFSSON, J. & NOJIRI, Y. 2002. Global sea–air CO<sub>2</sub> flux based on climatological surface ocean pCO<sub>2</sub>, and seasonal biological and temperature effects. *Deep Sea Research Part II: Topical Studies in Oceanography*, 49, 1601-1622.
- TAYLOR, J. R. & FERRARI, R. 2011. Shutdown of turbulent convection as a new criterion for the onset of spring phytoplankton blooms. *Limnology and Oceanography*, 56, 2293-2307.

- TENGBERG, A., HOVDENES, J., ANDERSSON, H., BROCANDEL, O., DIAZ, R., HEBERT, D., ARNERICH, T., HUBER, C., KÖRTZINGER, A., KHRIPOUNOFF, A., REY, F., RONNING, C., SCHIMANSKI, J., SOMMER, S. & STANGELMAYER, A. 2006. Evaluation of a lifetime-based optode to measure oxygen in aquatic systems. *Limnol. Oceanogr. Methods*, 4, 7-17.
- THOMSON, R. E. & FINE, I. V. 2003. Estimating mixed layer depth from oceanic profile data. *J. Atmos. Oceanic Technol.*, 20, 319 – 329.
- TIJJSSEN, S. B. 1979. Diurnal oxygen rhythm and primary production in the mixed layer of the Atlantic Ocean at 20°N. *Neth. J. Sea Res.*, 13, 79-84.
- TOGGWEILER, J. R. 1993. Carbon overconsumption. *Nature*, 363, 210-211.
- TOSTESON, T. R., ZAIDI, B. R., REVUELTA, R., IMAN, S. H., AXTMAYER, R. W., DEVORE, D., BALLANTINE, D. L., SASSCER, D. S., MORGAN, T. O. & RIVERA, C. 1982. OTEC biofouling, corrosion, and materials study from a moored platform at Punta Tuna, Puerto Rico. II. Microbiofouling. *Ocean science and engineering*.
- TOWNSEND, D. W., KELLER, M. D., SIERACKI, M. E. & ACKLESON, S. G. 1992. Spring phytoplankton blooms in the absence of vertical water column stratification. *Nature*, 360, 59-62.
- UEYAMA, R. & MONGER, B. C. 2005. Wind-induced modulation of seasonal phytoplankton blooms in the North Atlantic derived from satellite observations. *Limnology and Oceanography*, 50, 1820-1829.
- UZ, B. M., YODER, J. A. & OSYCHNY, V. 2001. Pumping of nutrients to ocean surface waters by the action of propagating planetary waves. *Nature*, 409, 597-600.
- VAN AKEN, H. M. 2000. The hydrography of the mid-latitude Northeast Atlantic Ocean: II: The intermediate water masses. *Deep Sea Research Part I: Oceanographic Research Papers*, 47, 789-824.
- VAN AKEN, H. M. & BECKER, G. 1996. Hydrography and through-flow in the north-eastern North Atlantic Ocean: the NANSEN project. *Progress in Oceanography*, 38, 297-346.
- VAN AKEN, H. M. & DE BOER, C. J. 1995. On the synoptic hydrography of intermediate and deep water masses in the Iceland Basin. *Deep Sea Research Part I: Oceanographic Research Papers*, 42, 165-189.
- VÁZQUEZ, A., FLECHA, S., BRUNO, M., MACÍAS, D. & NAVARRO, G. 2009. Internal waves and short-scale distribution patterns of chlorophyll in the Strait of Gibraltar and Alborán Sea. *Geophysical Research Letters*, 36, L23601.
- VELDHUIS, M. J. W. & KRAAY, G. W. 2004. Phytoplankton in the subtropical Atlantic Ocean: towards a better assessment of biomass and composition. *Deep Sea Research Part I: Oceanographic Research Papers*, 51, 507-530.
- VISBECK, M., CHASSIGNET, E. P., CURRY, R. G., DELWORTH, T. L., DICKSON, R. R. & KRAHMANN, G. 2003. The Ocean's Response to North Atlantic Oscillation Variability. *The North Atlantic Oscillation: Climatic Significance and Environmental Impact*. American Geophysical Union.
- VOLK, T. & HOFFERT, M. I. 1985. Ocean carbon pumps: Analysis of relative strengths and efficiencies in ocean driven atmospheric CO<sub>2</sub> changes, in *The Carbon Cycle and Atmospheric CO<sub>2</sub>: Natural Variations Archaean to Present*. Geophys. Monogr. Ser., AGU, Washington, D. C., 32, 99 – 110.

- WANG, Y.-H., DAI, C.-F. & CHEN, Y.-Y. 2007. Physical and ecological processes of internal waves on an isolated reef ecosystem in the South China Sea. *Geophysical Research Letters*, 34, L18609.
- WANNINKHOF, R. 1992. Relationship between wind speed and gas exchange over the ocean. *Journal of Geophysical Research: Oceans*, 97, 7373-7382.
- WEBB, D. C., SIMONETTI, P. J. & JONES, C. P. 2001. SLOCUM: an underwater glider propelled by environmental energy. *IEEE J. Ocean. Eng.*, 26, 447-452.
- WESTBERRY, T. K., M. J. BEHRENFELD, P. SCHULTZ, J. P. DUNNE, M. R. HISCOCK, S. MARITORENA, J. L. SARMIENTO, & D. A. SIEGEL (2016), Annual cycles of phytoplankton biomass in the subarctic Atlantic and Pacific Ocean, *Global Biogeochem. Cycles*, 30, 175–190, DOI:10.1002/2015GB005276.
- WESTON, K., FERNAND, L., MILLS, D. K., DELAHUNTY, R. & BROWN, J. 2005. Primary production in the deep chlorophyll maximum of the central North Sea. *Journal of Plankton Research*, 27.
- WHELAN, A. & REGAN, F. 2006. Antifouling strategies for marine and riverine sensors. *J. Environ. Monit.*, 8, 880-886.
- WIKNER, J., PANIGRAHI, S., NYDAHL, A., LUNDBERG, E., BAMSTEDT, U. & TENGBERG, A. Precise continuous measurements of pelagic respiration in coastal waters with Oxygen Optodes. *Limnol. Oceanogr. Methods*, 11, 1-15.
- WILLIAMS, P.J.le B. & JENKINSON, N.W., 1982. 'A transportable microprocessor-controlled precise Winkler titration, suitable for field station and shipboard use', *Limnol. Oceanogr.*, 27, 576-584.
- WILLIAMS, C., SHARPLES, J., MAHAFFEY, C. & RIPPETH, T. 2013. Wind-driven nutrient pulses to the subsurface chlorophyll maximum in seasonally stratified shelf seas. *Geophysical Research Letters*, 40, 5467-5472.
- WILLIAMS, P. J. L. B. 1998. The balance of plankton respiration and photosynthesis in the open oceans. *Nature*, 394, 55-57.
- WILLIAMS, P. J. L. B. & BOWERS, D. G. 1999. Regional Carbon Imbalances in the Oceans. *Science*, 284, 1735-1735.
- WILLIAMS, P. J. L. B., QUAY, P. D., WESTBERRY, T. K. & BEHRENFELD, M. J. 2013. The Oligotrophic Ocean Is Autotrophic. *Annual Review of Marine Science*, 5, 535-549.
- WILSON, J. M., SEVERSON, R. & BEMAN, J. M. 2014. Ocean-Scale Patterns in Community Respiration Rates along Continuous Transects across the Pacific Ocean. *PLoS ONE*, 9, e99821.
- WOLANSKI, E. & DELEERSNIJDER, E. 1998. Island-generated internal waves at Scott Reef, Western Australia. *Continental Shelf Research*, 18, 1649-1666.
- WOOLF, D. K. & THORPE, S. A. 1991. Bubbles and the air-sea exchange of gases in near-saturation conditions. *Journal of Marine Research*, 49, 435-466.
- WU, Y., PLATT, T., TANG, C. C. L., SATHYENDRANATH, S., DEVRED, E. & GU, S. 2008. A summer phytoplankton bloom triggered by high wind events in the Labrador Sea, July 2006. *Geophysical Research Letters*, 35. DOI: 10.1029/2008GL033561.

YOSHIKAWA, Y. 2015. Scaling surface mixing/mixed layer depth under stabilizing buoyancy flux. *Journal of Physical Oceanography*, 45, 247-258.

ZHAI, L., PLATT, T., TANG, C., SATHYENDRANATH, S. & WALNE, A. 2013. The response of phytoplankton to climate variability associated with the North Atlantic Oscillation. *Deep Sea Research Part II: Topical Studies in Oceanography*, 93, 159-168.

# Appendix I

## Alternative net community production calculation

An alternative method for the calculation of net community production was attempted in parallel to the one presented in chapter 5. The alternative method was based on the use of daily-averaged profile instead of individual profiles (figure I.1). All profiles measured in each day were binned in depth using 2 m wide non-overlapping bins. The daily mean oxygen concentration,  $c(\text{O}_2)$ , for each bin was calculated and used in the daily averaged profile. This profile was nominally associated at noon of the day, spacing evenly the profiles over time.

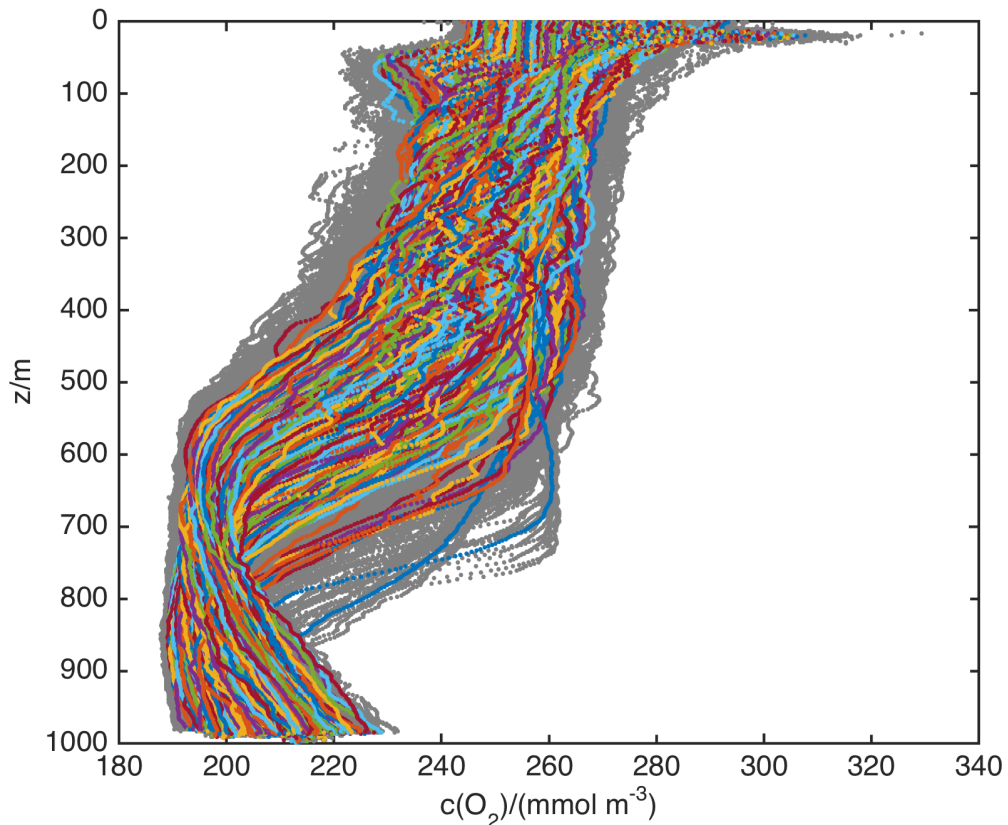


**Figure I.1 Daily averaged oxygen concentration profiles (coloured) over individual profiles used for the calculation of net community production in chapter 5 (grey)**

The mixing layer depth,  $z_{\text{mix}}$ , for each daily averaged profile was calculated using the threshold of 0.5% of difference with respect to  $c_{\text{ref}}(\text{O}_2, 5 \text{ m})$  as discussed in chapter 4 (red line in figure I.2d). Oxygen inventory,  $I(\text{O}_2)$ , was computed above  $z_{\text{lim}} = 60 \text{ m}$  (see chapter 5). This was also the value of the rate of variation,  $\Delta I(\text{O}_2)/\Delta t$ , since the temporal distance between consecutive profiles was 1 day (red line in figure I.2a). Air-sea oxygen flux,  $F_{\text{as}}$ , value per each day was measured following equation 5.9 (red line in figure I.2b). Entrainment,  $E$ , was measured between following daily averaged profiles using following what described in section 5.2.4 (red line in figure I.2c). In figure I.2,  $\Delta I(\text{O}_2)/\Delta t$ ,  $F_{\text{as}}$ ,  $E$  and  $z_{\text{mix}}$  are averaged over 7-day bins to be compared with values from chapter 5 (blue line in each subplot).

The differences between the two methods could be considered related almost exclusively to  $E$ . This process was found to influence significantly  $N$  calculations in chapter 5. The differences are due to the fact that each deepening event of  $z_{\text{mix}}$  is taken in account in the calculation of  $E$ , while  $z_{\text{mix}}$  shoaling events are not considered. This means that the calculation is not counterbalanced. The not-symmetrical effect of  $z_{\text{mix}}$  variations produces  $E$  estimates with lower absolute values when the  $z_{\text{mix}}$  varies less, as occurs using the daily averaged profiles. The result is that the total cumulative  $E$  used in the calculations of chapter 5 was  $-7.7 \text{ mol m}^{-2}$ , while the total cumulative  $E$  using daily averaged profiles was  $-2.9 \text{ mol m}^{-2}$ . There was a significant reduction in the absolute value of this process of 62 %.

$N$  was measured for each couple of consecutive daily averaged profiles using equation 5.14.  $N$  values were then averaged using running means over 7-day bins (red line in figure I.3). The influence of the differences in  $E$  between the two methods was clear in figure I.3: the time series agreed in their pattern apart when  $E$  was included in the calculation of  $N$ . From September 2012 to the beginning of December 2012 and between the beginning of May 2013 until the end of the mission (11<sup>th</sup> August 2013),  $z_{\text{mix}}$  was above  $z_{\text{lim}}$ ,  $E$  was not used in the calculation and the estimates from the two methods agreed.

The result is a significant difference between the two  $N$  time series. Using daily averaged profiles, the mean  $N$  is  $(4.8 \pm 40) \text{ mmol m}^{-2} \text{ d}^{-1}$  instead of  $(19 \pm 43.2) \text{ mmol m}^{-2} \text{ d}^{-1}$  calculated in chapter 5 for individual profiles (uncertainty based on  $\pm$  standard deviation in the time series). The total cumulative  $N$  is lowered from  $(6.4 \pm 1.9) \text{ mol m}^{-2}$  (chapter 5) to  $(1.6 \pm 0.5) \text{ mol m}^{-2}$  (uncertainty derived based on  $\pm 30 \%$  as calculated in section 5.3.6).

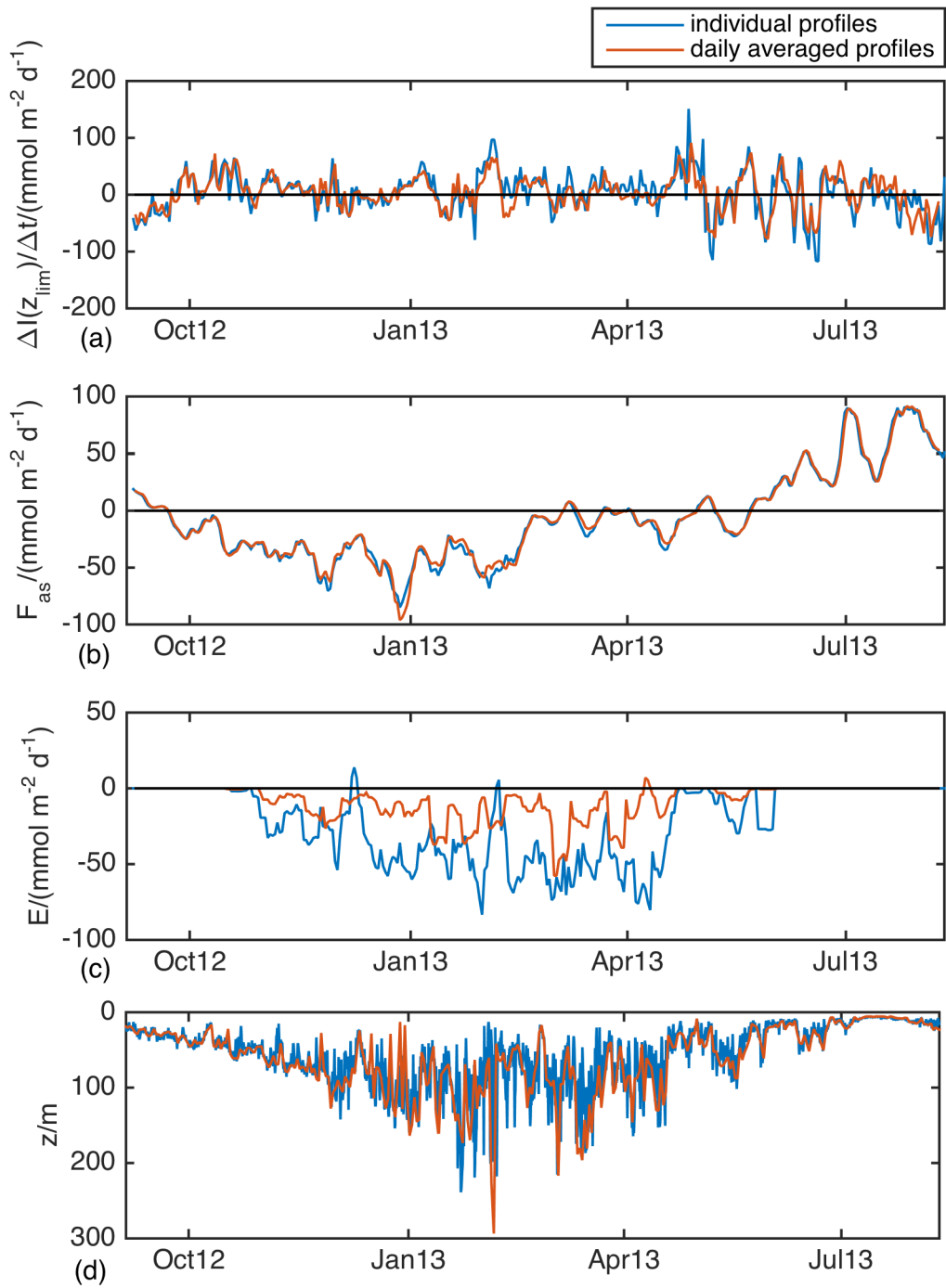


**Figure I.2 Comparison between (a) rate of variation in oxygen inventory, (b) air-sea flux, (c) entrainment and (d) mixing layer depth between the values used for calculations in chapter 5 and based on individual profiles (blue line) and values obtained using daily averaged profiles (red line). All values are mean over 7-day overlapping bins.**

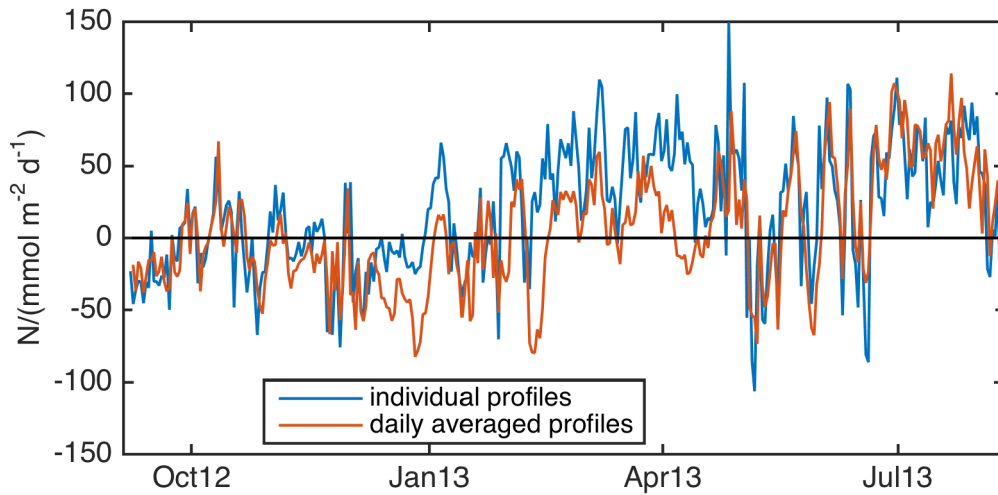


**Figure I.3 Net community production time series obtained considering individual profiles (blue) or daily averaged profiles (red). Values are averaged over 7-day overlapping bins.**

The method on daily averaged profiles gives stronger heterotrophy in winter and lower autotrophy in spring. However, the peaks during the spring, such as the one linked to the End-February Event, are preserved and correspond to the passage of the net surface heat flux to positive values. This confirms what said in chapter 5 about the validity of the model proposed by Enriquez and Taylor (2015).

Considering a  $z_{lim}$  value lower than the deepest  $z_{mix}$  would eliminate the differences between the two methods because entrainment would be considered null. However, this would include in the calculation substantial portions of the water column below the euphotic depth. The estimates would then reflect something else with respect to  $N$  in the productive layer, which was the goal of this study.

The decision about the method to use can be therefore reduced to the decision whether to consider the variations in  $z_{mix}$  between consecutive individual profiles as a real signal. In chapter 4 it has been proved that  $z_{mix}$  defined by oxygen corresponded also to density features, evidence that the variations of  $z_{mix}$  were considered actual variations in the depth of the ocean surface boundary layer. This explains the decision of considering the method based on the individual profiles more accurate.

The use of this alternative method showed the importance that  $E$  has on the calculation of  $N$ .  $z_{mix}$  calculated based on the daily averaged profiles can be considered more similar to the ‘climatologies’ that are often used for studies that estimate production. The present study therefore suggests caution in the use of derived  $z_{mix}$  values, showing potential significant bias in the calculations of  $N$  because of erroneous  $E$ .

# **Appendix II**

## **Damerell et al. (2016)**

### **[manuscript]**

In the next pages is presented the manuscript of the paper “The Vertical Structure of Upper Ocean Variability at the Porcupine Abyssal Plain during 2012-2013” which has been referred in the text as ‘Damerell et al. (2016)’. This paper includes a detailed hydrographic description of the time series of physical parameters measured by the gliders during the OSMOSIS project. The paper has been submitted to JGR-Oceans for publication. The paper also used the oxygen concentrations that have been analysed in this thesis.

# The Vertical Structure of Upper Ocean Variability at the Porcupine Abyssal Plain during 2012-2013

Gillian M. Damerell<sup>1</sup>, Karen J. Heywood<sup>1</sup>, Andrew F. Thompson<sup>2</sup>, Umberto Binetti<sup>1</sup>, Jan Kaiser<sup>1</sup>

<sup>1</sup>Centre for Ocean and Atmospheric Sciences, School of Environmental Sciences, University of East Anglia, Norwich, UK.

<sup>2</sup>California Institute of Technology, Pasadena, USA.

## Key Points:

- Intraseasonal variability in upper ocean temperature and salinity, not previously reported.
- Mode-1 baroclinic internal tide detected.
- Deep variability dominated by intermittent patches of Mediterranean Water, which show evidence of filamentation.

---

Corresponding author: Gillian M. Damerell, [g.damerell@uea.ac.uk](mailto:g.damerell@uea.ac.uk)

## Abstract

This study presents the characterization of variability in temperature, salinity and oxygen concentration, including the vertical structure of the variability, in the upper 1000m of the ocean over a full year in the northeast Atlantic. Continuously profiling ocean gliders with vertical resolution between 0.5-1m provide more information on temporal variability throughout the water column than time series from moorings with sensors at a limited number of fixed depths. The heat, salt and dissolved oxygen content are quantified at each depth. While the near surface heat content is consistent with the net surface heat flux, heat content of the deeper layers is driven by gyre-scale water mass changes. Below  $\sim 150\text{m}$ , heat and salt content display intraseasonal variability which has not been resolved by previous studies. A mode-1 baroclinic internal tide is detected as a peak in the power spectra of water mass properties. The depth of minimum variability is at  $\sim 415\text{m}$  for both temperature and salinity, but this is a depth of high variability for oxygen concentration. The deep variability is dominated by the intermittent appearance of Mediterranean Water, which shows evidence of filamentation. Susceptibility to salt fingering occurs throughout much of the water column for much of the year. Between about 700-900m, the water column is susceptible to diffusive layering, particularly when Mediterranean Water is present. This unique ability to resolve both high vertical and temporal resolution highlights the importance of intraseasonal variability in upper ocean heat and salt content, variations that may be aliased by traditional observing techniques.

## 1 Introduction

The ocean and the atmosphere exchange heat, salt, momentum and tracers through an ocean surface boundary layer, in which biological activity is also focused. However, long time series of upper ocean observations are challenging to obtain. Most previous studies of upper ocean variability have relied on ship CTD profiles (Conductivity, Temperature, Depth) with limited temporal coverage and resolution and an inevitable summer bias (examples in the northeast Atlantic include *Bray* [1982]; *Harvey* [1982]; *Rios et al.* [1992]; *Prieto et al.* [2013]) or on moorings with instruments at a limited number of depths [*Chidichimo et al.*, 2010; *Machin et al.*, 2010; *Hartman et al.*, 2012]. Even studies which combine ships, moorings, Argo floats and satellite observations [*Hartman et al.*, 2010; *Ullgren and White*, 2010, 2012], do not obtain coverage of a full year with sufficient temporal and vertical resolution to capture many ocean processes.

Here we document an ocean glider-based study of the temporal variability of the upper ocean. The Ocean Surface Mixing, Ocean Submesoscale Interaction Study (OSMOSIS) incorporated a year-long observational program centered 41 km to the southeast of the Porcupine Abyssal Plain sustained observatory (PAP-SO), with observations collected within a 15 km radius of  $48.7^\circ\text{ N}$ ,  $16.2^\circ\text{ W}$  (Fig. 1). The PAP-SO [*Lampitt et al.*, 2010] is situated in the Northeast Atlantic ( $49.0^\circ\text{ N}$   $16.5^\circ\text{ W}$ ) at a water depth of 4800 m. This location is considered remote from the topographic complexities of the continental slope and the Mid-Atlantic Ridge [*Hartman et al.*, 2012], and thus remote from places where strong internal tides might be generated. It is located in the inter-gyre region between the North Atlantic subpolar and subtropical gyres where the mean flow is relatively weak and eddy kinetic energy is moderate. The variability in physical properties is likely to be representative of large areas of the mid-latitude gyres.

As part of the OSMOSIS field campaign, pairs of Seagliders were deployed for periods varying between two and five months, between them covering an entire year from 4th September 2012 to 7th September 2013. Here we use the glider data set to show the seasonal evolution of the uppermost 1000 m of the water column and determine the characteristic timescales of variability in temperature, salinity and dissolved oxygen concentration. We discuss the likely causes of that variability and how it compares with surface forcing such as the heat and freshwater fluxes, and wind stress. This allows us to resolve fluctuations in processes

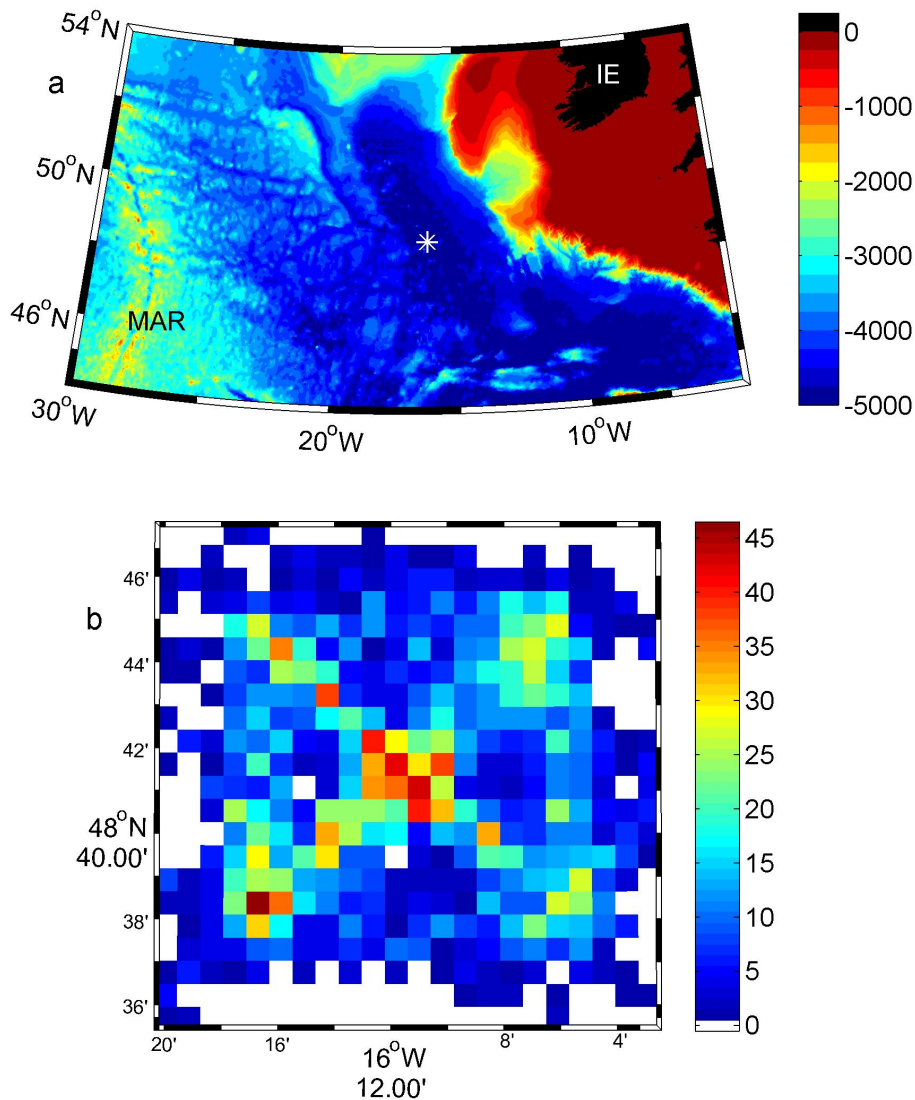


**Figure 1.** a) Bathymetry of the north-east Atlantic basin. The white asterisk marks the location of the OSMOSIS field campaign. MAR=mid-Atlantic Ridge. IE=Ireland. b) Number of profiles in each  $1 \times 1$  km grid cell collected during the OSMOSIS campaign and used in this paper (i.e., from only one Seaglider at a time, not both), centred around  $48.7^\circ\text{N}$ ,  $16.2^\circ\text{W}$ .

whose signature in vertical variability happens on relatively small scales, such as the internal tides, and compact mesoscale features.

## 2 Data and Methods

The Seaglider is a small, autonomous, buoyancy-driven vehicle which profiles to a maximum depth of 1000 m in a sawtooth pattern [Eriksen *et al.*, 2001]. All the Seagliders deployed during the OSMOSIS field campaign carried a Seabird SBE3 temperature sensor and SBE4 conductivity sensor (known collectively as the CT sail), and an Aanderaa 4330F oxygen optode. Following calibration (see below), temperature, salinity and oxygen concentrations are accurate to  $0.01^\circ\text{C}$ ,  $0.01 \text{ g kg}^{-1}$  and  $2 \mu\text{mol kg}^{-1}$ , respectively. Sensor precision is  $0.001^\circ\text{C}$

and  $0.0003 \text{ S m}^{-1}$  for temperature and conductivity respectively, combining to a salinity precision of approximately  $0.001 \text{ g kg}^{-1}$ . Sampling occurred approximately every 5 seconds ( $0.5 \text{ m}$  vertical resolution at typical vertical speeds of  $0.1 \text{ m s}^{-1}$ ) in the upper part of the water column, and every 10 seconds ( $1 \text{ m}$  vertical resolution) below that. The depth at which the vertical resolution changed varied between 200 and 400 m, depending on battery constraints.

The Seaglider hydrodynamic flight model is tuned following *Frajka-Williams et al.* [2011]. Dive-average currents are calculated from the difference between the glider's flight path found from GPS positions at the beginning and end of each dive, and the glider's flight path as calculated from the Seaglider hydrodynamic model. The thermal lag of the CT sensor is corrected following the methods of *Garau et al.* [2011]. Occasional poor quality data (e.g., from biofouling of the conductivity sensor, from poor flushing of the conductivity cell when the glider is moving slowly) are flagged and discarded; this accounts for 2.6% of the total data collected. CTD casts were collected from the ships *RRS Discovery* (September 2012), *RV Celtic Explorer* (January 2013), and *RRS James Cook* (April, June and September 2013). Salinity and dissolved oxygen concentrations from the Seagliders were calibrated against the ship CTD salinities and dissolved oxygen concentrations from each cruise, which in turn were calibrated against discrete water samples analysed with an Autosal salinometer and an automated Winkler titration system.

Figure 1b) shows the observational density of the glider profiles used in this paper. These are taken from one glider during each deployment period, selecting the glider which remained most closely within the OSMOSIS observational domain, and which had the least sensor issues (e.g., minimal biofouling of the conductivity cell). By concatenating three glider deployments we obtain a time series for the entire year totaling 4096 profiles (Fig. 2). (The OSMOSIS observational programme collected 8138 glider profiles in total, but the data from the second glider during each deployment is not used in the time series analysis conducted here.) 95% of the 4096 profiles used in this paper lie within 15 km of  $48.7^\circ \text{ N}$ ,  $16.2^\circ \text{ W}$ . 15 km is comparable to the spacing between CTD locations of a typical ship-based hydrographic survey, and for the purposes of this paper, we treat the data as if they had all been obtained at the same location. There is an implicit linkage between spatial and temporal variability in glider observations, and here we choose to treat it as purely temporal variability. Submesoscale motions and small-scale spatial variability observed in this dataset are discussed by *Thompson et al.* [2016]. Glider profiles collected outside the study region (i.e., more than 15 km from  $48.7^\circ \text{ N}$ ,  $16.2^\circ \text{ W}$ ) are not included, and after removal of these and the occasional poor quality data (as above), 3785 profiles remain.

To attribute variability to physical processes including mesoscale variability, wave motion and tides, we use the multi-taper method [*Thomson, 1982; Percival and Walden, 1993*], to generate frequency spectra of temperature, salinity, dissolved oxygen concentration and dive-average currents. The average dive duration was  $\sim 4$  hours, and we treat the dive and climb sections of each glider dive as separate vertical profiles. Although samples along a constant depth surface are obtained at roughly two hourly intervals mid-way down the profiles, at the surface and at dive-apogee two profiles are obtained within a few minutes of each other followed by a near 4-hour delay until the next two profiles are obtained (Fig. 3). We therefore average the data into 4-hour bins, giving a Nyquist frequency of 1 cycle per 8 hours, or 3 cycles  $\text{day}^{-1}$ , for the entire dataset. The glider takes typically 6 days to occupy the survey pattern, occupying each corner of the domain in turn in a bow-tie pattern, so any apparent 4-10 day signal may represent spatial variability, sampled by the glider as it moves through the survey box, that for the purposes of this analysis is interpreted solely in the time domain. There will also be some aliasing of internal waves. The buoyancy frequency, which represents the upper bound of the internal wave frequency band, varies in this dataset from  $0.001$  to  $0.05 \text{ s}^{-1}$ , corresponding to internal waves with periods of a few minutes (in the pycnocline) up to 2 hours (in the weak stratification of the layer below the pycnocline down to  $\sim 500 \text{ m}$ ). Variance at higher-than-resolved frequencies, including from internal waves (or, due to glider spatial sampling, at low frequencies but higher-than-resolved wavenumbers) will be aliased onto those

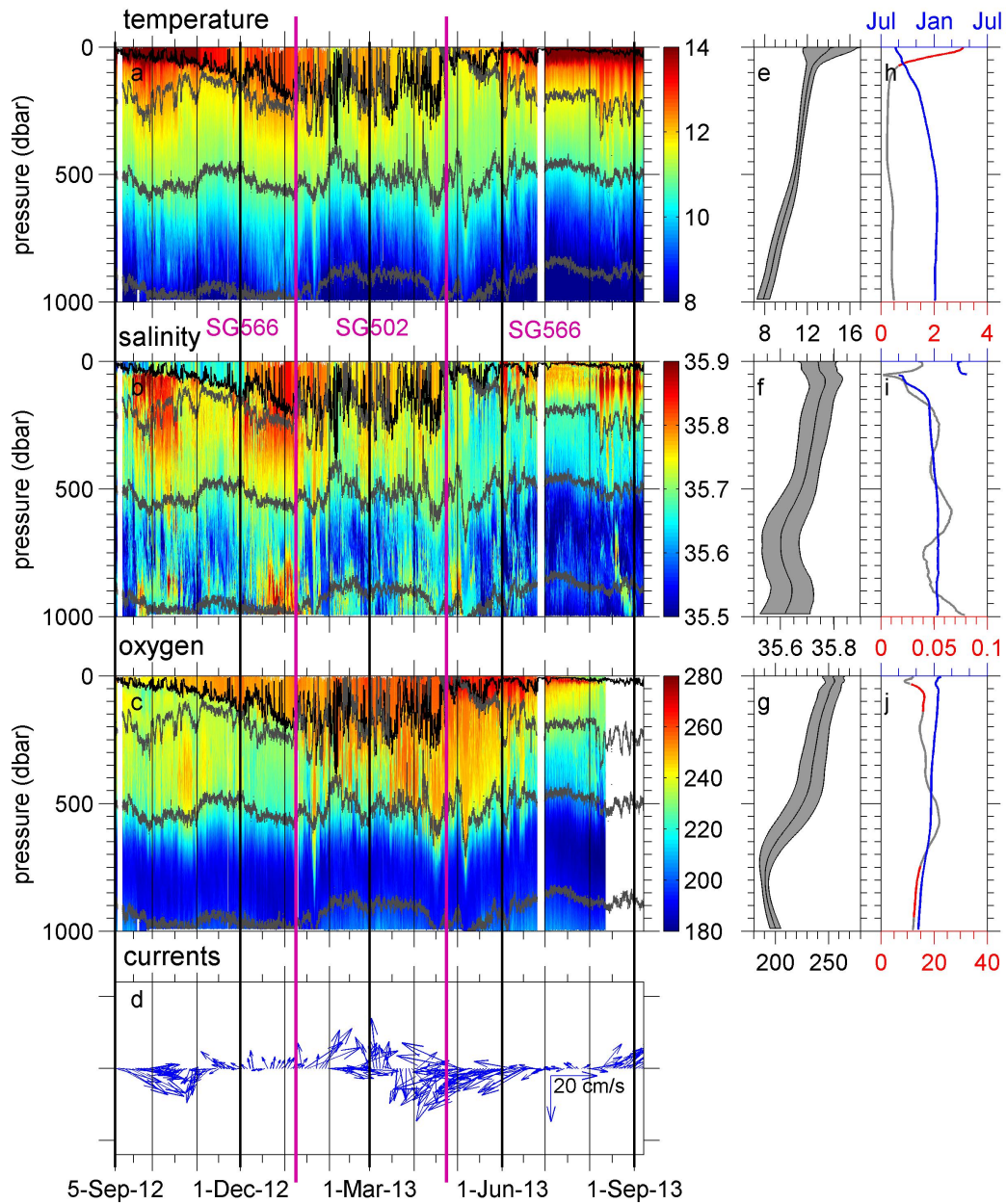


**Figure 2.** Time series of (a) conservative temperature ( $^{\circ}\text{C}$ ), (b) absolute salinity ( $\text{g kg}^{-1}$ ) (c) dissolved oxygen concentration ( $\mu\text{mol kg}^{-1}$ ) and (d) dive-average currents ( $\text{cm s}^{-1}$ , detided), as measured by gliders SG566 (September to January), SG502 (January to April) and SG566 (April to September). Different gliders are separated by pink vertical lines, and black vertical lines are gridlines every month, with thicker black lines every 3 months to show approximate seasons. In panels a, b and c the black contour shows the ML depth and the grey contours show  $\sigma_{\theta}$  surfaces 27.04, 27.2 and 27.6. The dive-average currents are shown as 2 day averages for clarity. Panel (e) shows the mean temperature (central line) plus and minus one standard deviation (grey area). Panels (f) and (g) are as panel (e) for salinity and dissolved oxygen concentration respectively. Panels (h) and (i) and (j) show the phase (blue) and amplitude of the annual harmonic at each depth for temperature, salinity and dissolved oxygen concentration respectively. The amplitude is shown in red when the annual harmonic is a good fit to the observations, grey otherwise (see main text). The phase is represented as the time of year of the peak of the annual harmonic.

resolved in this dataset, resulting in a distortion of the observed spectra relative to the true values, particularly at higher frequencies [Rudnick and Cole, 2011]. Spectra computed from moored instruments deployed as part of OSMOSIS below the surface layer, sampling every 10 minutes (Figure S1), are very similar to those from the gliders, indicating that this effect does not significantly influence the conclusions here.

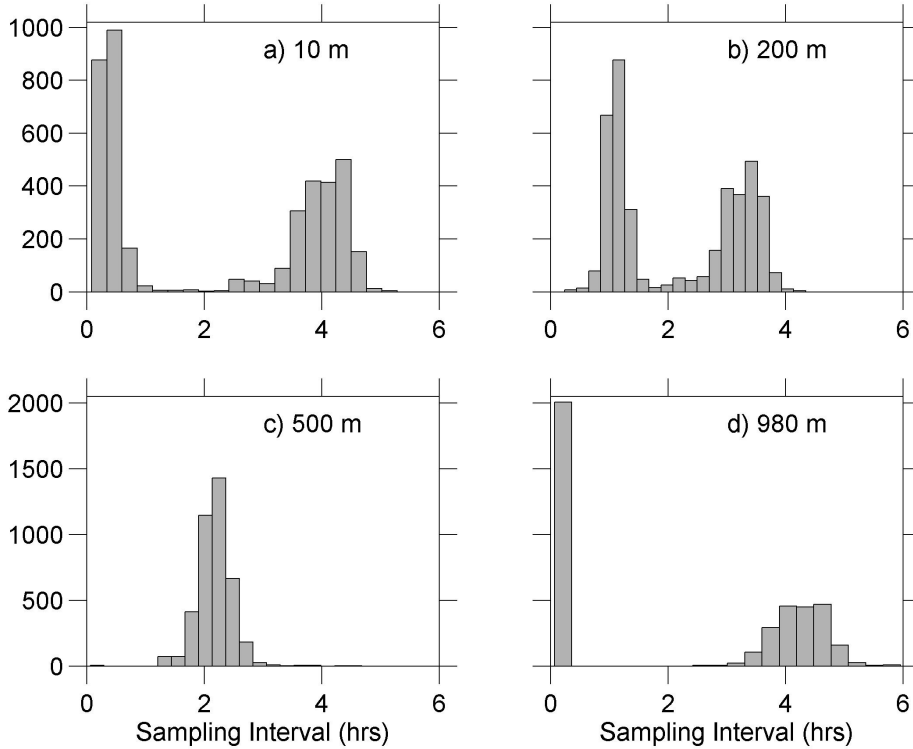


**Figure 3.** Histograms of the intervals between profiles at example depths: a) 10 m, b) 200 m, c) 500 m, d) 980 m.

The depth of the surface mixed layer (ML) is calculated using a threshold value of temperature or density from a near-surface value at 10 m depth ( $\Delta T = 0.2^\circ\text{C}$  or  $\Delta\sigma_\theta = 0.03$ ), whichever is the shallower [de Boyer Montegut *et al.*, 2004]. Thus, we aim to find the depth of the ML even in cases where temperature and salinity vary with depth in a density-compensating manner, as well as cases where density varies with depth due to changes in salinity rather than temperature. Annual harmonics of temperature, salinity and oxygen concentration are found by fitting (using a least squares approach) a sine wave with a period of 365 days to the temperature, salinity and oxygen concentration at each depth: the amplitude and phase of the fitted sine waves are shown in Figure 2h-j. To highlight whether the annual harmonic is a good fit to the observations at each depth, we divide the standard deviation of the residuals (observations minus fitted sine wave) by the standard deviation of the observations. When this ‘goodness-of-fit’ number ( $\gamma$ ) is small, the residuals are small and much of the variance in the observations is explained by an annual harmonic. For illustrative purposes, Figure 2h-j colors the amplitude red when  $\gamma$  is less than 0.6 (40% of variance explained by annual harmonic), but this is not intended to denote an abrupt cut-off from good fits to bad. Using  $\gamma = 0.5$  (0.7), for example, simply contracts (expands) the depths colored red by  $\sim 50$  m.

Vertical diffusive and gravitational stability are assessed from individual profiles by calculating the spiciness  $\pi$  and stability angle  $\phi$  following Flament [2002]. Spiciness is a state

variable used to characterize water masses, being largest for warm and salty waters.  $\phi$  is calculated over vertical intervals larger than the scale of the fine-structure, here found to be  $\sim 50$  m. In this calculation it is assumed that variability over these vertical scales is of sufficiently low vertical-to-horizontal aspect ratio that it is not appreciably distorted by the slantwise profiling of the Seaglider.  $|\phi| > 90^\circ$  indicates that the water column is gravitationally unstable,  $|\phi| < 45^\circ$  indicates that the water column is diffusively stable, diffusive layering occurs when  $45^\circ < \phi < 90^\circ$  and salt fingering when  $-90^\circ < \phi < -45^\circ$ .

Sea surface temperature (SST), surface wind speed and surface fluxes of heat (short-wave and longwave radiation, latent and sensible heat fluxes) and freshwater (precipitation and evaporation) were extracted from the European Centre for Medium Range Weather Forecasting (ECMWF) ERA-Interim re-analysis [Dee *et al.*, 2011] at the nearest gridpoint to the OSMOSIS site (24 km west of the center of the OSMOSIS site). (The PAP-SO meteorological buoy failed for approximately 6 months of the OSMOSIS observational period and it was considered better to use a consistent source for meteorological variables for the whole year.) A hypothetical ML temperature was derived by assuming the net surface heat flux is the only source of temperature change in the ML. It was calculated as follows:

$$\Delta T = \frac{F \Delta t}{c \rho h} \quad (1)$$

where  $\Delta T$  is the temperature change over a time period  $\Delta t$  (here 6 hours, the time step of the ERA-Interim reanalysis dataset),  $F$  is the surface heat flux,  $\rho$  the ML density, and  $h$  the ML depth at that time.  $c$  is the specific heat capacity of seawater appropriate when using conservative temperature [IOC *et al.*, 2010]. This gives a temperature change rather than an absolute temperature; for ease of display we set the hypothetical ML temperature equal to the observed ML temperature at the coldest point in the year. Similarly, a hypothetical ML salinity was calculated from the ERA-Interim net surface freshwater flux as follows:

$$S_n = S_0 \prod_{t=1}^n \left( \frac{h_t}{h_t + FW_t \cdot \Delta t} \right) \quad (2)$$

where  $S_n$  is the salinity at time  $t = n \cdot \Delta t$ ,  $S_0$  is an initial salinity at time  $t = 0$ ,  $h_t$  is the ML depth at time  $t$  and  $FW_t$  is the net freshwater flux at time  $t$ . The evolution of this hypothetical mixed layer salinity is not sensitive to the choice of initial value,  $S_0$ .

Note that throughout this paper we use conservative temperature and absolute salinity ( $S_A$ ) following IOC *et al.* [2010]. All densities are potential density anomalies ( $\sigma_\theta$ ) relative to the surface and will be given without units.

### 3 Results and Discussion

#### 3.1 Water masses and vertical stability

The frequency of occurrence of the main water masses observed throughout the year is illustrated in Figure 4. Surface waters ( $\sigma_\theta < 27$ ) are the warmest water masses (11-20°C) and highest in dissolved oxygen concentration (Fig. 2c). The  $\sigma_\theta = 27$  isopycnal reaches its maximum depth of approximately 200 m in July (Fig. 2). The subsurface fresher, colder and less oxygenated water masses are Eastern North Atlantic Central Water (ENACW) of subtropical (ENACWt) and subpolar (ENACWp) origin [Harvey, 1982]. ENACW is thought to be formed by deep winter mixing in a wide region from the Azores to the European boundary, bounded on the west and north by the North Atlantic Current and to the south by the Azores Current [Pollard and Pu, 1985; Pollard *et al.*, 1996]. ENACWt is found at  $\sigma_\theta$  in the range 27 to 27.2, and is warmer, saltier and more oxygenated than ENACWp. In this dataset, ENACWt extends down to approximately 500 m (as seen from the depth of the 27.2 isopycnal on Figure 2), below which we find ENACWp. The slight salinity minimum around  $\sigma_\theta = 27.3$  is charac-

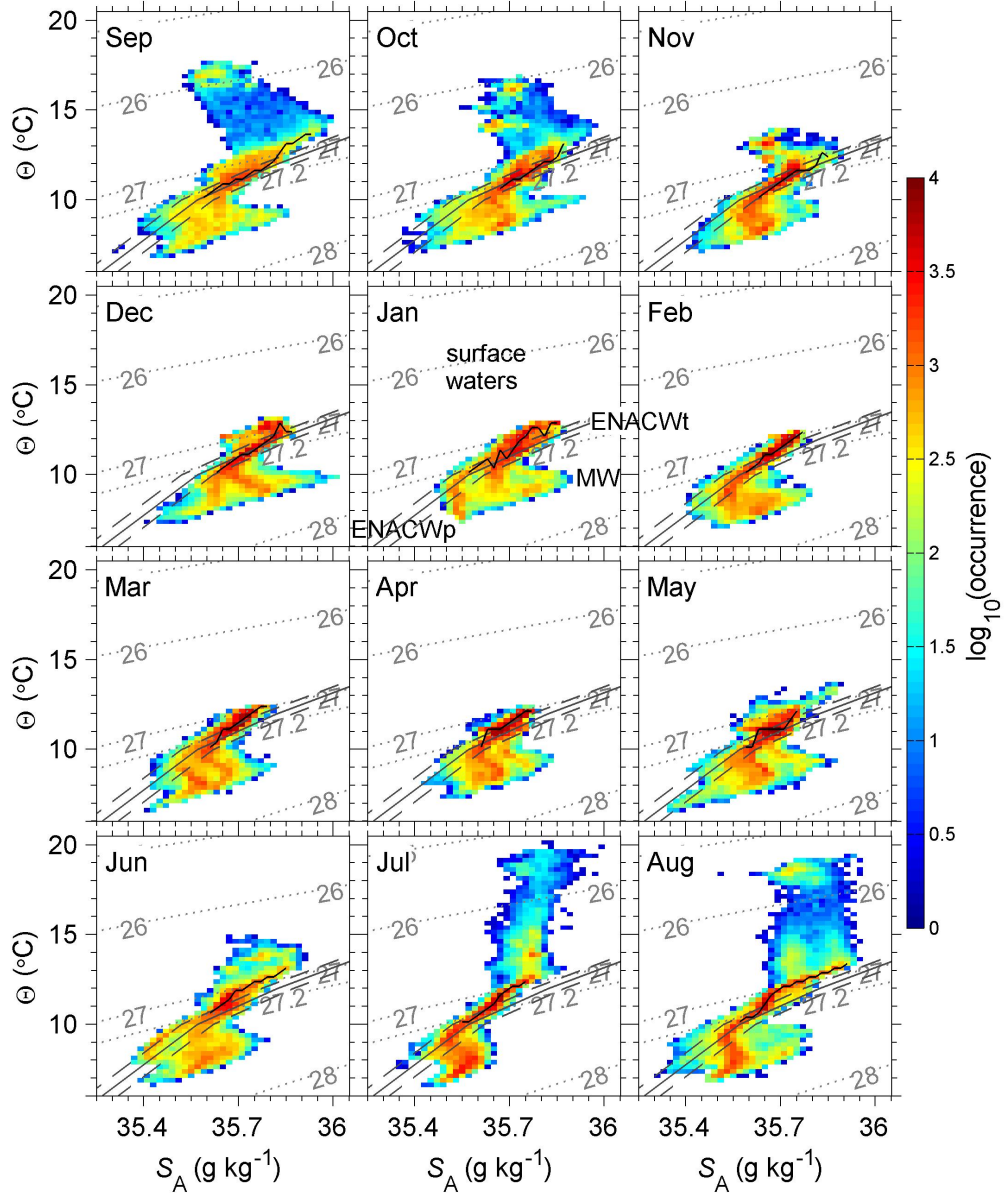


**Figure 4.**  $\Theta - S_A$  diagrams for each month. The colors show the  $\log_{10}$  of the number of data points in that  $\Theta - S_A$  grid cell (i.e., the occurrence). The dotted light grey lines are  $\sigma_\theta$  isopycnals. The  $\sigma_\theta = 27.2$  isopycnal is included to illustrate the boundary between ENACWt and ENACWp. The solid, darker grey line denotes ENACW as defined by *Harvey* [1982] and extended by *Rios et al.* [1992], with ENACWp at the cooler and fresher end, and ENACWt at the warmer and saltier end. Water mass labels are included on the January plot. Points between the grey dashed lines ( $S_{ENACW} \pm 0.05$ ) can be considered as ENACW. (We have converted the ENACW line to conservative temperature and absolute salinity.) The black line joins points of maximum occurrence for each isohaline, referred to in the main text as the 'core' of the water masses observed here. It is only shown for  $\Theta - S_A$  grid cells containing more than 500 data points, and for temperatures  $> 10^\circ\text{C}$ .

teristic of the influence of Sub-Arctic Intermediate Water [Arhan, 1990]. Previous studies in this region have shown that waters which are slightly fresher than ENACW at similar densities show some mixing with Western North Atlantic Water (WNAW). Specifically, water with a  $\Theta - S_A$  relationship parallel with the ENACW line but fresher by 0.1 at the same temperature can be considered WNAW [Rios *et al.*, 1992; Pollard *et al.*, 1996].

The 'core' of the water masses observed here (Fig. 4) is defined as a line joining the grid cell maximum occurrence for each isohaline. The water mass core is only shown for temperatures  $> 10^\circ\text{C}$  as below this the water mass properties are significantly influenced by the presence of Mediterranean Water (MW) so comparisons with ENACW are not relevant. The core lies, at times, along the line of ENACW, but is often shifted somewhat to the left of this line (especially in summer), i.e., the waters are warmer and/or fresher. If this shift were entirely due to a change in temperature, then on average the core observed here is  $0.40^\circ\text{C}$  warmer than the ENACW line at the same salinity. The shift might be due to a difference in salinity rather than temperature, but the maximum salinity difference along isotherms between the core observed here and the ENACW line reaches 0.16 in September, and is greater than 0.1 in 9 months out of 12 (Fig. 4). In other words, if the difference were purely due to a change in salinity then the waters observed here, well within the eastern North Atlantic, are even fresher than WNAW. Thus we posit that at least some of the difference between the water mass core observed here and the ENACW line must be due to an increase in temperature since the ENACW line was first defined by Harvey [1982], using data collected in the 1950s and 60s.

The oxygen minimum layer occurs at an average depth of 785 m. Below 700 m, there are intermittent patches of high salinity due to the influence of MW [Mauritzen *et al.*, 2001], characterized by a salinity maximum (up to  $36.01 \text{ g kg}^{-1}$ ) centered at  $\sigma_\theta = 27.6$  (Fig. 4). These MW characteristics are similar to those observed by Ullgren and White [2010, 2012] at the southern entrance to the Rockall Trough, 480 km north of the OSMOSIS site. ENACWp and MW are both found at  $\sigma_\theta > 27.2$  (Figs. 2 and 4). There is more MW in winter than in summer with an especially noticeable patch of very saline MW from mid-December to mid-January (Fig. 2b), consistent with the results of Prieto *et al.* [2013], who find that MW detaches from the Iberian slope and spreads into the outer ocean more in winter than in summer. Below the MW, there is perhaps some evidence of the colder and fresher Labrador Sea Water, but this dataset does not extend deep enough to explore that fully.

Depths between approximately 700-1000 m exhibit high variability at all timescales in salinity and temperature but much less so in dissolved oxygen concentration (Fig. 5). The high variability in salinity and temperature at these depths can be ascribed to the occurrence of MW being intermittent on multiple timescales. The patches of MW show variability on time scales as short as a day, and Thompson *et al.* [2016] discuss their spatial variability across the  $\sim 20$  km OSMOSIS domain. These features are suggestive of a filamentary structure (an example is shown in Fig. 6). However, the ENACWp and MW have similar dissolved oxygen concentrations ( $\sim 194$  and  $\sim 189 \mu\text{mol kg}^{-1}$  respectively), so the oxygen concentration does not exhibit as much variability as temperature and salinity (Fig. 5).

The MW/ENACWp layer between approximately 700 and 1000 m is often diffusively stable (Fig. 7), but with periods of susceptibility to diffusive layering largely corresponding to times when more saline MW is present (Fig. 2b). ENACWt is largely susceptible to salt fingering, but between December and April when ENACWt extends to the surface there are occasional periods when the ML is gravitationally unstable (Fig. 7c), which correspond to rapidly deepening ML depths due to convective overturning. The gravitational instabilities observed here are of comparable magnitude to those observed by Anis and Moum [1992], consisting of perturbations from a stable profile of order  $0.01\text{-}0.02^\circ\text{C}$  (considerably larger than the sensor precision). We are observing ENACW as it is being locally formed by deep winter mixing. Since the stability angle  $\phi$  is calculated over vertical intervals of 50 m, there appear to be no gravitational instabilities shallower than 25 m in Figure 7c. This leads to an inevitable bias towards detecting gravitational instabilities in the ML in winter, rather than in

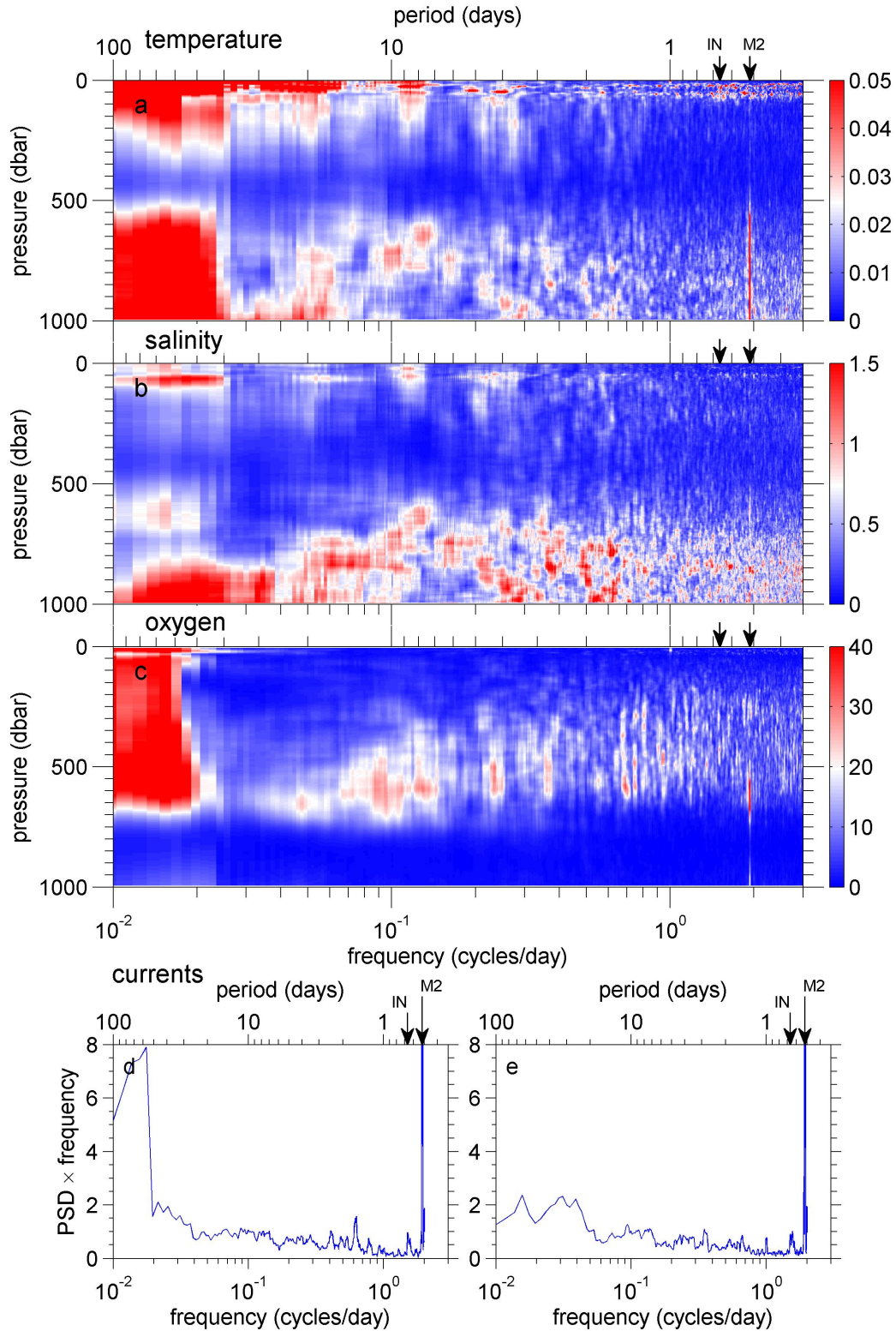


**Figure 5.** Variance preserving spectra for (a) temperature (b) salinity, (c) dissolved oxygen concentration, (d) zonal and (e) meridional component of the dive-average currents, all  $\times 10^{-3}$  except temperature and dissolved oxygen. In panels (a) to (c), the colors show the power spectral density  $\times$  frequency. The inertial frequency (IN) and M2 tidal frequency are marked as black arrows on the upper axis.

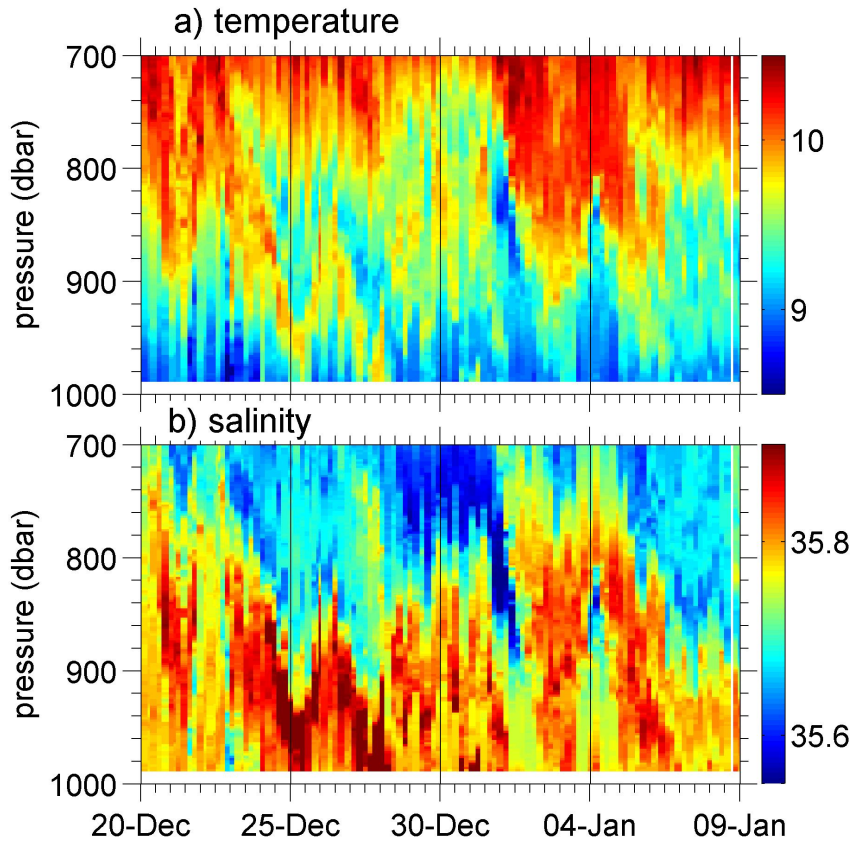


**Figure 6.** Expanded view of (a) conservative temperature ( $^{\circ}\text{C}$ ) and (b) absolute salinity ( $\text{g kg}^{-1}$ ) of a patch of Mediterranean Water showing the filamented nature of the patch, with high variability in time and depth.

summer when the ML is shallow. However, in Figure 4 one can also see the  $\Theta - S_A$  properties collapsing onto the ENACW line towards the end of winter (except at greater densities where some MW influence remains), whereas in summer the water mass properties at the surface diverge, which would not be the case if there was frequent convective overturning due to gravitational instabilities.

### 3.2 Mixed layer variability and air sea fluxes/exchange

The obvious seasonal cycle in the temperature of the uppermost 150 m is due to solar insolation (Figs. 2a and 8). Temperatures within the top 10 m, where the amplitude of the annual harmonic is greatest (Fig. 2h), range from approximately  $12^{\circ}\text{C}$  in winter to  $19^{\circ}\text{C}$  in July, comparable to that observed by *Hartman et al.* [2010] at the PAP-SO between 2003 and 2005. The temporal standard deviation of temperature (Fig. 2e) decreases rapidly from the surface to approximately 60 m and decreases slowly to  $\sim 200$  m. The minimum in standard deviation of temperature occurs at  $\sim 400$  m. Below 150 m an annual harmonic does not fit the observed variability well.

The ML temperature is strongly correlated ( $r = 0.98$ , Fig. 8b) with the ECMWF ERA-Interim SST. The ML temperature is also correlated with the cumulative ERA-Interim net surface heat flux into the ocean ( $r = 0.87$ ). (Here the ML temperature is averaged to the same

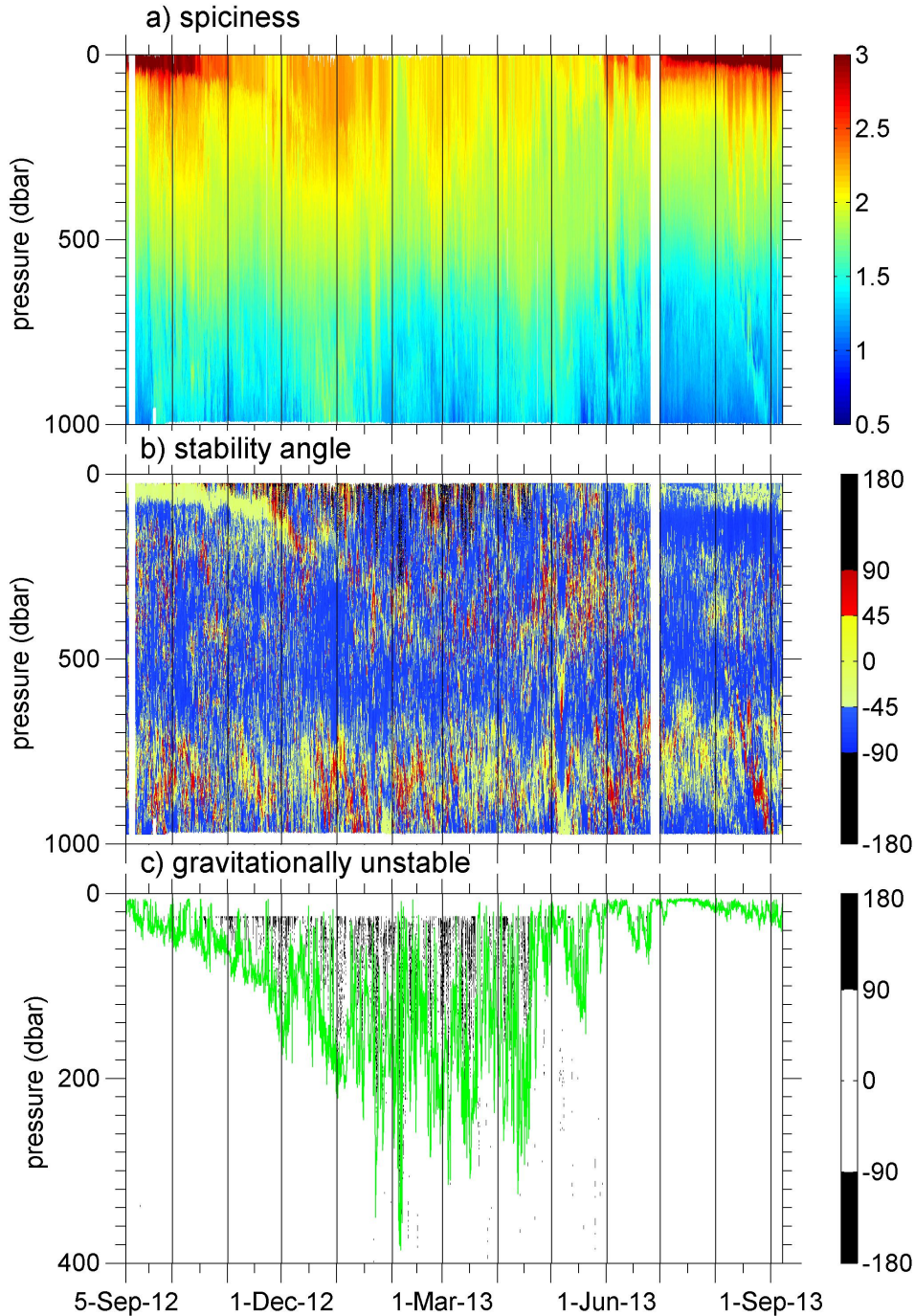


**Figure 7.** Time series of (a) spiciness ( $\pi$ ) and (b) stability angle ( $\phi$ ).  $|\phi| > 90^\circ$  indicates that the water column is gravitationally unstable (black),  $|\phi| < 45^\circ$  indicates that the water column is diffusively stable (yellow), diffusive layering occurs when  $45^\circ < \phi < 90^\circ$  (red) and salt fingering when  $-90^\circ < \phi < -45^\circ$  (blue). Note that because  $\phi$  is calculated over 50 m, there are no  $\phi$  values in the top and bottom 25 m. Panel (c) shows an expanded view of  $\phi$  above 400 m, showing only those occasions when it is gravitationally unstable. In panel (c) the green line is the ML depth.

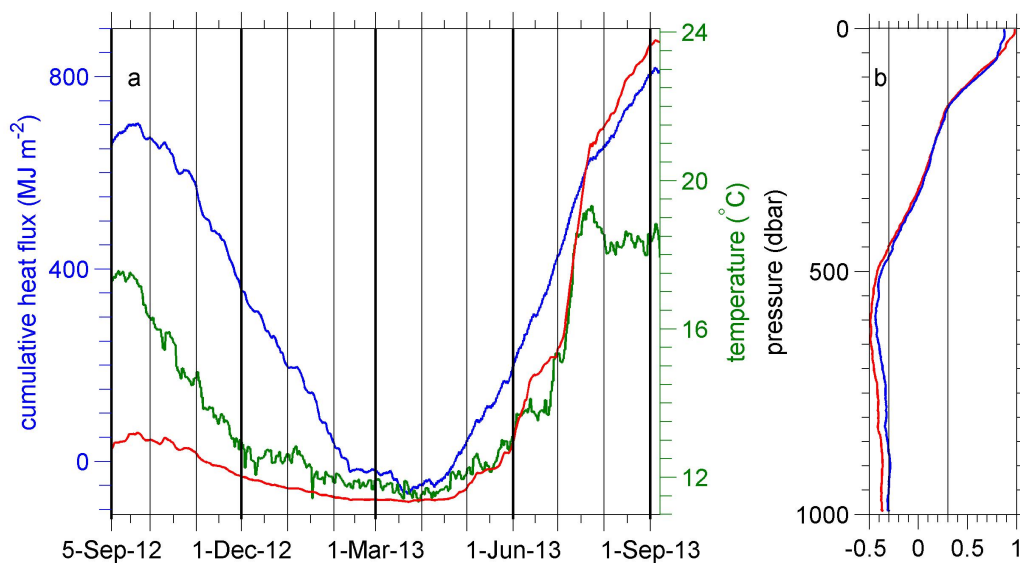


**Figure 8.** (a) Time series of cumulative net surface heat flux ( $\text{MJ m}^{-2}$ , positive downwards, blue), sea surface temperature (SST,  $^{\circ}\text{C}$ , green) from the ECMWF ERA-Interim reanalysis dataset at the nearest gridpoint to the OSMOSIS site, and a hypothetical ML temperature calculated by assuming the surface heat flux is the only source/sink of heat in the ML (red, see main text). Panel (b) shows the correlation with depth between the glider-measured temperature and the cumulative net surface heat flux (blue) and SST (red) at zero lag. Correlations with magnitude  $> 0.3$  are considered to be significant: the black vertical lines mark correlations of  $-0.3$  and  $+0.3$ .

times as the ERA-Interim data.) Temperatures below 150 m are not correlated with the cumulative net surface heat flux (Fig. 8b). Figure 8a also shows (red curve) the hypothetical ML temperature derived by assuming that the surface heat flux is the only source of temperature change in the ML. This hypothetical ML temperature will only be reasonable if there is no heat flux from/to the ocean interior (whether by entrainment or by the diffusive export of heat from the ML to the layer below such as discussed by *Cronin et al.* [2015] and *Lee et al.* [2015]), no advection of water with anomalous temperatures by the circulation, no horizontal or vertical mixing with waters at a different temperature, even when the depth of the ML increases, and if all the surface heat flux is absorbed in the ML. This hypothetical ML temperature covaries with the actual ML temperature reasonably well during the winter and during the warming in spring (within  $1^{\circ}\text{C}$  from the start of December to the end of May), but not in autumn when the ML deepens and cools, and also not during late summer. In late summer, the ML is often very shallow (see below and Fig. 2) and it is likely that some fraction of the solar absorption occurs below the ML due to penetrative radiation. Thus the hypothetical ML temperature should be considered as, at best, an upper bound on the possible ML temperature tendency at times when the ML is very shallow. Cooling occurs primarily at times when the ML is deepening and there is a temperature difference between the ML and waters below (Figs. 2a and 8a). This cooling of the ML may be initiated by cooling at the surface leading to convective overturning, but the subsequent change in temperature is also influenced by entrainment of cooler waters from the ocean interior, such as are seen just below the ML during the autumn (Fig. 2a).

The ML salinity does not have an obvious seasonal cycle, is not well described by an annual harmonic, and is variable on all time scales (Fig. 5). It is not correlated with the Aquarius satellite sea surface salinity (Level 3 Sea Surface Salinity Standard Mapped Image 7-Day Data V3, *Lee et al.* [2012]) at the nearest gridpoint to the OSMOSIS site. The hypothetical

ML salinity expected from the ERA-Interim surface freshwater flux (not shown) is not correlated with the measured salinity, and the range is an order of magnitude smaller than that of the measured salinity. Thus precipitation and evaporation are not the major drivers of changes in salinity in the ML. The changes in ML salinity must be primarily due to advection into the area of water masses of different salinity and/or vertical mixing with waters of different salinity from the ocean interior. The changes are too persistent to be solely due to eddies and are therefore likely to be associated with variations in the gyre-scale circulation.

The de-tided dive-average currents (Fig. 2d) are weak, reaching a maximum of  $0.38 \text{ m s}^{-1}$  in late January. In only 1/4 of the record is the speed above  $0.2 \text{ m s}^{-1}$ . *Painter et al.* [2010] found velocities of a comparable magnitude during a vessel-mounted Acoustic Doppler Current Profiler survey at the PAP-SO in 2006. Despite the low speeds, the dive-average currents are often persistent in direction for periods of a month or more. During September 2012 and January, February and August 2013, the currents are persistently eastward. From mid-April to late June, the currents are persistently westward. The dive-average currents are not correlated with local ECMWF ERA-Interim wind speeds, but they are weakly correlated with the salinity ( $r \approx 0.4$ ) observed by the gliders down to 300 m (not shown), suggesting that the advection of different water masses into the region is one source of the water mass variability. Mixed layer dissolved oxygen concentration is dominated by the temperature dependence of oxygen solubility [*Emerson*, 1987; *Najjar and Keeling*, 1997], biological processes and air-sea gas exchange and is not discussed further in this paper.

The ML depth observed here is comparable to that discussed by *Hartman et al.* [2010], which was obtained by taking monthly averages of the ML depth from Argo float data collected in a region centred around PAP-SO ( $45^\circ\text{N}$  to  $52^\circ\text{N}$ ,  $26.08^\circ\text{W}$  to  $8.92^\circ\text{W}$ , excluding the shelf area) between January 2003 and July 2005. *Hartman et al.* [2010] also found that the ML depth reaches a maximum of approximately 300-400 m (though generally in March whereas here the maximum depth occurred in early February), and that the ML depth has much greater variability in winter than in summer. We find shallower ML depths in the summer than they observed: in July and August 288 out of 654 profiles show stratification up to the minimum depth (3-5 m) reliably observed by the gliders, whereas the minimum ML depths observed by *Hartman et al.* [2010] were approximately 20-30 m. This difference is likely due to the higher vertical resolution of the Seagliders compared with Argo floats. The glider campaign provides greater temporal resolution, allowing us to observe, for example, that the spring shoaling of the ML is not a gradual and smooth process; instead there is a rapid onset of shoaling in April (daily average ML depths change from being around 200 m to around 50 m in 2 days) followed by several deepening and restratifying events in May and June (seen most clearly in Fig. 7c).

### 3.3 Intraseasonal variability below the mixed layer

In the OSMOSIS study area, the heat and salt content of the upper 1000 m are not dominated by the highly variable top 150 m. While the temperature varies over a much greater range in the uppermost 150 m than at depth (Fig. 2e), salinity does not. Moreover, below 150 m the low-pass filtered temperature and salinity show a dominant barotropic structure and also vary in phase with each other (Fig. 2). Due to this largely barotropic structure, the variability in the heat and salt content of the upper 1000 m are in fact dominated by the variability below 150 m (Fig. 9). The heat and salt content of the upper 1000 m are strongly correlated with each other ( $r = 0.73$ ); this is largely due to the strong correlation below 150 m ( $r = 0.86$ , Fig. 9).

*Prieto et al.* [2013] observed intermediate waters that were warmer and saltier in winter than summer between 2003-2010 along a section at  $43^\circ\text{N}$  extending 200 nm off Cape Finisterre. Similar seasonal cycles were observed in various locations in the Eastern North Atlantic by *Bray* [1982]; *Chidichimo et al.* [2010]; *Machin et al.* [2010] and are thought to be due to an increased admixture of cooler and fresher Western North Atlantic Water/Sub Arctic Intermediate Water during the summer. The results of *Bray* [1982] are based on CTD

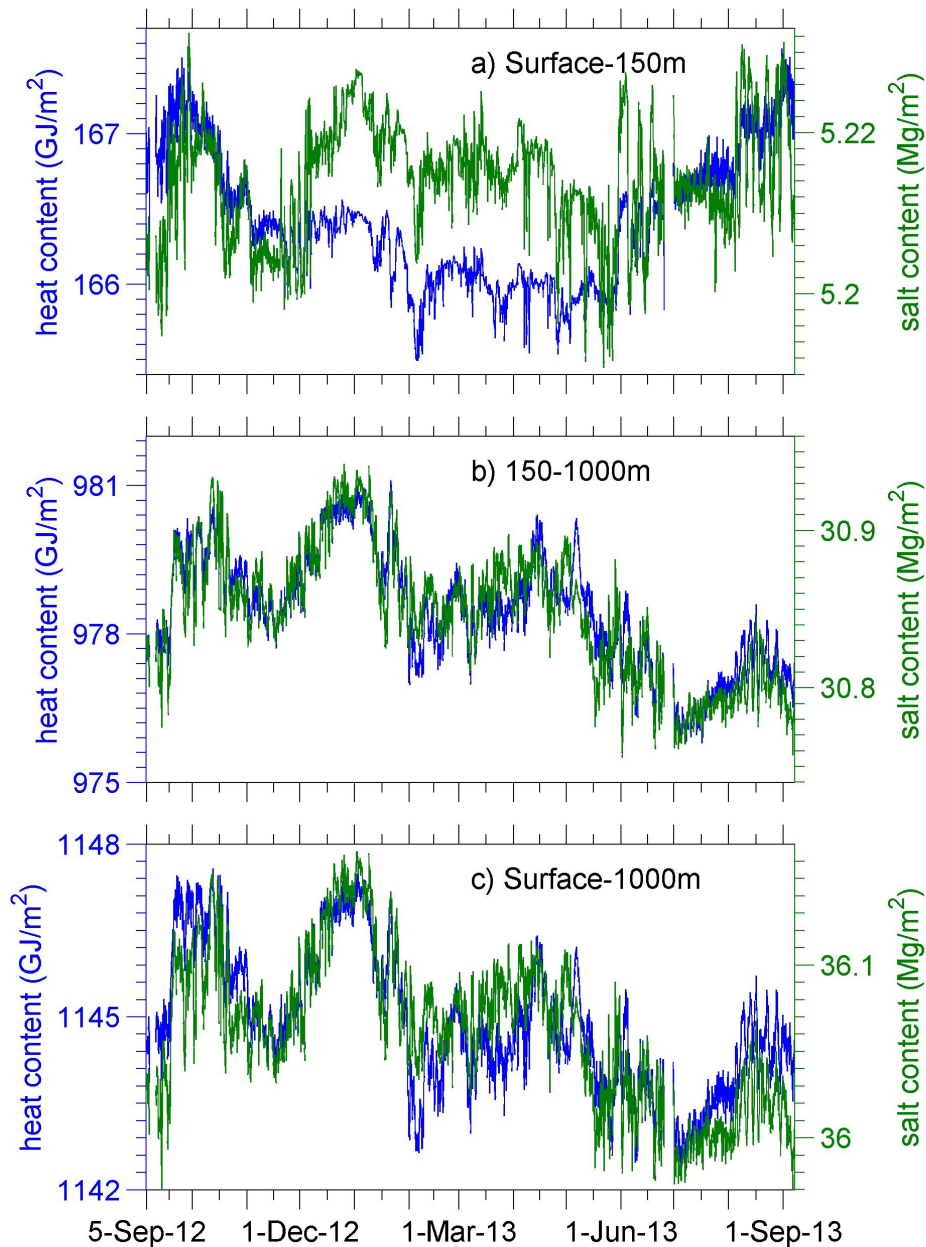


**Figure 9.** Time series of heat content ( $\text{GJ m}^{-2}$ ) (blue) and salt content ( $\text{Mg m}^{-2}$ ) summed over (a) the top 150 m, (b) 150-1000 m, and (c) the top 1000 m.

profiles at approximately 3 month intervals, those of *Prieto et al.* [2013] on CTD profiles at approximately 6 month intervals, those of *Machin et al.* [2010] on only 2 depths on a single mooring, and those of *Chidichimo et al.* [2010] on a composite profile obtained by combining observations from a moored array spread over approximately 1250 km. Our glider-based observations, with full temporal coverage and resolution alongside good vertical resolution, provide new insights into the intraseasonal variability at all depths to 1000 m.

Below 150 m, we observe significant intraseasonal variability in temperature and salinity on a timescale of about 3 months (Figs. 2, 5 and 9b). The studies described above [*Bray,*

1982; *Chidichimo et al.*, 2010; *Prieto et al.*, 2013] were unable to resolve this intraseasonal variability and therefore ascribed it to a seasonal cycle. The variability of the heat and salt content of the upper 1000 m (Fig. 9c) is dominated by gyre-scale and/or mesoscale variability below 150 m and not by the surface forcing. We suggest that other processes such as latitudinal variability in wind stress curl should be investigated using numerical models. The intraseasonal variability in the heat and salt content is not obviously related to the state of the North Atlantic Oscillation [*Barnston and Livezey*, 1987], the RAPID MOC volume transport time series [*Smeed et al.*, 2015] or the local wind stress (Figure S2). This intraseasonal variability is also seen in the dissolved oxygen content below 700 m (not shown). Above 700 m, oxygen concentration variations are uncoupled from the intraseasonal variability in temperature and salinity, presumably due to horizontal or vertical entrainment of water with elevated oxygen concentrations which developed when the water was closer to the surface.

A peak in variability at intraseasonal periods (40-100 days) could be due to Rossby waves [*Price and Rossby*, 1982]. This peak is still present in spectra calculated on density levels instead of depth (Fig. 10) so Rossby waves are unlikely as the source of this variability since they would cause variability by heaving of the density surfaces. The intraseasonal variability is much more pronounced in the zonal component than the meridional component of the dive-average currents, which might be associated with drifting quasi-zonal jets [*van Sebille et al.*, 2011].

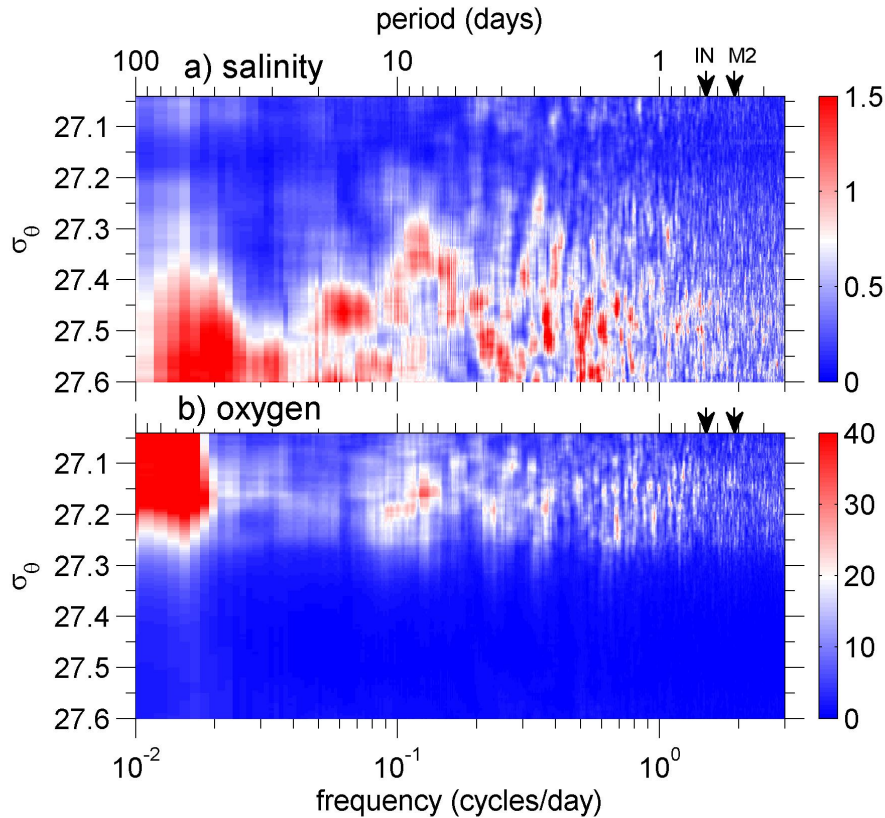


**Figure 10.** Variance preserving spectra for (a) salinity ( $\times 10^{-3}$ ) and (b) dissolved oxygen concentration calculated on density surfaces. In each panel the colors show the power spectral density  $\times$  frequency. The inertial frequency (IN) and M2 tidal frequency are marked as black arrows on the upper axis. Spectra are shown for  $\sigma_\theta$  in the range 27.04 - 27.6. This is the range over which we have data for the complete year, as shown by the density contours on Figure 2.

### 3.4 Tidal and inertial frequencies

The spectra of the dive average currents show a very large peak in energy precisely at the M2 semi-diurnal tidal frequency (Fig. 5d-e). There is no evidence of significant variability at diurnal tidal frequencies. This semi-diurnal signal is also noticeable in temperature (Fig. 5a), where its energy increases with depth. This is present in salinity and oxygen but is less pronounced (Fig. 5b-c). A barotropic tide would produce the greatest spectral energy where horizontal property gradients are greatest, near the surface. Since the tidal signal observed here increases with depth, we ascribe this to an internal tide. The OSMOSIS site lies in an abyssal plain far from the continental slope where internal tides are generated ( $\sim 350$  km to the nearest point of the continental slope), so we would expect predominantly mode-1 internal tides since higher modes would have dissipated before reaching the OSMOSIS site. Predicted mode-1 isopycnal displacement (based on full-depth profiles of the buoyancy frequency from OSMOSIS CTD surveys) would increase from zero at the surface to a maximum at depth of 1750 m, consistent with the glider-based observations of an increased tidal signal from the surface to 1000 m. This peak is not visible in power spectra calculated on density surfaces (Fig. 10), supporting the hypothesis that it is an internal tide. Spectra computed from moored instruments deployed between 50 m and 500 m depth as part of OSMOSIS also show a significant peak at the M2 tidal frequency (Figure S1).

At the inertial frequency ( $1.1 \times 10^{-4}$  rad s $^{-1}$ , a period of 15.9 hours), spectra of both the zonal and meridional dive-average velocities show a small increase in energy (Fig. 5d-e). The upper 100 m also displays slightly increased energy at near-inertial frequencies in both temperature and density. This is consistent with wind-generated near-inertial waves propagating downwards [Pollard, 1970; Alford, 2001, 2003].

## 4 Conclusions

A year-long time series of temperature, salinity and dissolved oxygen concentration at 2-hourly intervals in the uppermost 1000 m of the ocean was obtained from gliders. This provides an ideal data set for validation of process or regional models. The ENACW shows evidence of warming since the 1950s/60s. There is a strong seasonal cycle in near-surface temperature and mixed layer depth, as expected, consistent with net surface heat flux. The shoaling of the ML in spring is intermittent and interspersed with deepening events. Variations in ML salinity are not explained by local freshwater fluxes and must therefore be influenced by horizontal advection of different water masses associated with changes in local gyre-scale circulation, and/or mesoscale eddies. A strong peak in variability is observed at the M2 tidal frequency due to a mode-1 baroclinic internal tide. In terms of mixing processes, the ENACW is susceptible to salt fingering for much of the year. Gravitational instabilities are seen in winter, associated with rapid deepening of the mixed layer. At about 700-900 m, the depth of the dissolved oxygen minimum, the water column is susceptible to diffusive layering, particularly when MW is present. The deep variability is dominated by the intermittent appearance of patches of MW, and this variability in temperature and salinity is present at all time scales due to the filamented nature of these patches. Below  $\sim 150$  m we see intraseasonal variability (on time periods of 2-5 months) which dominates the variability in heat and salt content variability in the entire upper 1000 m. The unique ability of ocean gliders to resolve both high vertical and temporal resolution highlights the importance of intraseasonal variability in upper ocean heat and salt content, variations that may be aliased by traditional observing techniques.

### Acknowledgments

We would like to thank the scientists, technicians, officers and crew of the *RRS Discovery* cruise D381, the *RV Celtic Explorer* cruise CE13001, and the *RRS James Cook* cruises JC085, JC087 and JC090, especially those which were not primarily OSMOSIS cruises and so went out of their way to accommodate our glider deployments. We would also like to thank, in particular, the many people involved in CTD data collection, processing, water mass sampling

and calibration, without which the glider data would be uncalibrated. The data presented in this study are the result of five research cruises and a full year of glider piloting and involved many contributions not represented in the author list. This work was supported by NERC grants NE/I019905/1, NE/I020083/1 and NSF award OCE 1155676. Additional funding was provided by the EU Framework 7 project EuroBASIN (FP7-ENV-2010). We also thank Noel Pelland and an anonymous reviewer for insightful comments that improved the paper. Data are held at the British Oceanographic Data Centre (<http://bodc.ac.uk/>).

The ERA-Interim data were obtained from the European Centre for Medium-Range Weather Forecasts (downloaded from <http://www.ecmwf.int/en/research/climate-reanalysis/era-interim> on 17/6/2014). The NAO index data were obtained from the National Weather Service Climate Prediction Center (downloaded from <http://www.cpc.ncep.noaa.gov/products/precip/CWlink/pna/nao.shtml> on 2/10/2014). The Aquarius sea surface salinity mission is a joint effort between NASA and the Argentinian Space Agency, CONAE (Comisin Nacional de Actividades Espaciales), data downloaded from <http://aquarius.nasa.gov> on 19/6/2014. Data from the RAPID-WATCH MOC monitoring project are funded by the Natural Environment Research Council and are freely available from [www.rapid.ac.uk/rapidmoc](http://www.rapid.ac.uk/rapidmoc) (data downloaded 11/9/2015).

## References

- Alford, M. H. (2001), Internal swell generation: The spatial distribution of energy flux from the wind to mixed layer near-inertial motions, *J. Phys. Oceanogr.*, *31*(8), 2359–2368.
- Alford, M. H. (2003), Improved global maps and 54-year history of wind-work on ocean inertial motions, *Geophys. Res. Lett.*, *30*(8), 1424.
- Anis, A., and J. N. Moum (1992), The superadiabatic surface layer of the ocean during convection, *J. Phys. Oceanogr.*, *22*(10), 1221–1227.
- Arhan, M. (1990), The North Atlantic Current and Subarctic Intermediate Water, *J. Mar. Res.*, *48*(1), 109–144, doi:10.1357/002224090784984605.
- Barnston, A. G., and R. E. Livezey (1987), Classification, seasonality and persistence of low-frequency atmospheric circulation patterns, *Mon. Wea. Rev.*, *115*, 1083–1126.
- Bray, N. A. (1982), Seasonal variability in the Intermediate Waters of the Eastern North Atlantic, *J. Phys. Oceanogr.*, *12*(9), 972–983.
- Chidichimo, M. P., T. Kanzow, S. A. Cunningham, W. E. Johns, and J. Marotzke (2010), The contribution of eastern-boundary density variations to the Atlantic meridional overturning circulation at 26.5 degrees N, *Ocean Science*, *6*(2), 475–490, doi:10.5194/os-6-475-2010.
- Cronin, M., N. Pelland, W. Crawford, and S. Emerson (2015), Estimating diffusivity from the mixed layer heat and salt balances in the North Pacific, *J. Geophys. Res.*, *120*, 7346–7362, doi:10.1002/2015JC011010.
- de Boyer Montegut, C., G. Madec, A. S. Fischer, A. Lazar, and D. Iudicone (2004), Mixed layer depth over the global ocean: An examination of profile data and a profile-based climatology, *J. Geophys. Res.*, *109*(C12), C12,003, doi:10.1029/2004JC002378.
- Dee, D. P., S. M. Uppala, A. J. Simmons, P. Berrisford, P. Poli, S. Kobayashi, U. Andrae, M. A. Balmaseda, G. Balsamo, P. Bauer, P. Bechtold, A. C. M. Beljaars, L. van de Berg, J. Bidlot, N. Bormann, C. Delsol, R. Dragani, M. Fuentes, A. J. Geer, L. Haimberger, S. B. Healy, H. Hersbach, E. V. Holm, L. Isaksen, P. Kallberg, M. Koehler, M. Matricardi, A. P. McNally, B. M. Monge-Sanz, J. . J. Morcrette, B. . K. Park, C. Peubey, P. de Rosnay, C. Tavolato, J. . N. Thepaut, and F. Vitart (2011), The ERA-Interim reanalysis: configuration and performance of the data assimilation system, *Quart. J. Roy. Meteor. Soc.*, *137*(656), 553–597, doi:10.1002/qj.828.
- Emerson, S. (1987), Seasonal oxygen cycles and biological new production in surface waters of the Subarctic Pacific Ocean, *J. Geophys. Res.*, *92*(C6), 6535–6544, doi:10.1029/JC092iC06p06535.
- Eriksen, C. C., T. J. Osse, R. D. Light, T. Wen, T. W. Lehman, P. L. Sabin, J. W. Ballard, and A. M. Chiodi (2001), Seaglider: A long-range autonomous underwater vehicle

- for oceanographic research, *IEEE Journal of Oceanic Engineering*, 26(4), 424–436, doi: 10.1109/48.972073.
- Flament, P. (2002), A state variable for characterizing water masses and their diffusive stability: spiciness, *Progress In Oceanography*, 54(1-4), PII S0079–6611(02)00,065–4, doi: 10.1016/S0079-6611(02)00065-4.
- Frajka-Williams, E., C. C. Eriksen, P. B. Rhines, and R. R. Harcourt (2011), Determining vertical water velocities from Seaglider, *J. Atmos. Oceanic Technol.*, 28(12), 1641–1656, doi:10.1175/2011JTECH0830.1.
- Garau, B., S. Ruiz, W. G. Zhang, A. Pascual, E. Heslop, J. Kerfoot, and J. Tintore (2011), Thermal lag correction on Slocum CTD glider data, *J. Atmos. Oceanic Technol.*, 28(9), 1065–1071, doi:10.1175/JTECH-D-10-05030.1.
- Hartman, S. E., K. E. Larkin, R. S. Lampitt, M. Lankhorst, and D. J. Hydes (2010), Seasonal and inter-annual biogeochemical variations in the Porcupine Abyssal Plain 2003-2005 associated with winter mixing and surface circulation, *Deep-Sea Res.*, 57(15), 1303–1312, doi:10.1016/j.dsr2.2010.01.007.
- Hartman, S. E., R. S. Lampitt, K. E. Larkin, M. Pagnani, J. Campbell, T. Gkritzalis, Z.-P. Jiang, C. A. Pebody, H. A. Ruhl, A. J. Gooday, B. J. Bett, D. S. M. Billett, P. Provost, R. McLachlan, J. D. Turton, and S. Lankester (2012), The Porcupine Abyssal Plain fixed-point sustained observatory (PAP-SO): variations and trends from the Northeast Atlantic fixed-point time-series, *ICES Journal of Marine Science*, 69(5), 776–783, doi:10.1093/icesjms/fss077.
- Harvey, J. (1982), Theta-S relationships and water masses in the eastern North Atlantic, *Deep-Sea Res.*, 29(8), 1021–1033, doi:10.1016/0198-0149(82)90025-5.
- IOC, SCOR, and IAPSO (2010), *The international thermodynamic equation of seawater - 2010: Calculations and use of thermodynamic properties.*, Intergovernmental Oceanographic Commission, Manuals and Guides No. 56, UNESCO (English).
- Lampitt, R. S., D. S. M. Billett, and A. P. Martin (2010), The sustained observatory over the Porcupine Abyssal Plain (PAP): Insights from time series observations and process studies, *Deep-Sea Res.*, 57(15), 1267–1271, doi:10.1016/j.dsr2.2010.01.003.
- Lee, E., Y. Noh, B. Qiu, and S.-W. Yeh (2015), Seasonal variation of the upper ocean responding to surface heating in the North Pacific, *J. Geophys. Res.*, 120(8), 5631–5647, doi: 10.1002/2015JC010800.
- Lee, T., G. Lagerloef, M. Gierach, H.-Y. Kao, S. Yueh, and K. Dohan (2012), Aquarius reveals salinity structure of tropical instability waves, *Geophys. Res. Lett.*, 39, L12,610, doi: 10.1029/2012GL052232.
- Machin, F., J. L. Pelegri, E. Fraile-Nuez, P. Velez-Belchi, F. Lopez-Laatzten, and A. Hernandez-Guerra (2010), Seasonal flow reversals of Intermediate Waters in the Canary Current System east of the Canary Islands, *J. Phys. Oceanogr.*, 40(8), 1902–1909, doi:10.1175/2010JPO4320.1.
- Mauritzen, C., Y. Morel, and J. Paillet (2001), On the influence of Mediterranean Water on the Central waters of the North Atlantic Ocean, *Deep-Sea Res.*, 48(2), 347–381, doi: 10.1016/S0967-0637(00)00043-1.
- Najjar, R. G., and R. F. Keeling (1997), Analysis of the mean annual cycle of the dissolved oxygen anomaly in the World Ocean, *J. Mar. Res.*, 55(1), 117–151, doi: 10.1357/0022240973224481.
- Painter, S. C., R. E. Pidcock, and J. T. Allen (2010), A mesoscale eddy driving spatial and temporal heterogeneity in the productivity of the euphotic zone of the northeast Atlantic, *Deep-Sea Res.*, 57(15), 1281–1292, doi:10.1016/j.dsr2.2010.01.005.
- Percival, D., and A. Walden (1993), *Spectral Analysis for Physical Applications: Multitaper and Conventional Univariate Techniques*, Cambridge University Press.
- Pollard, R. T. (1970), On generation by winds of inertial waves in ocean, *Deep-Sea Res.*, 17(4), 795.
- Pollard, R. T., and S. Pu (1985), Structure and circulation of the Upper Atlantic Ocean northeast of the Azores, *Progress In Oceanography*, 14(1-4), 443–462, doi:10.1016/0079-6611(85)90022-9.

- Pollard, R. T., M. J. Griffiths, S. A. Cunningham, J. F. Read, F. F. Perez, and A. F. Rios (1996), Vivaldi 1991-A study of the formation, circulation and ventilation of Eastern North Atlantic Central Water, *Progress In Oceanography*, 37(2), PII S0079-6611(96)0008.0, doi:10.1016/S0079-6611(96)00008-0.
- Price, J. F., and H. T. Rossby (1982), Observations of a barotropic planetary wave in the western North Atlantic, *J. Mar. Res. Suppl.*, 40, 543-558.
- Prieto, E., C. Gonzalez-Pola, A. Lavin, R. F. Sanchez, and M. Ruiz-Villarreal (2013), Seasonality of intermediate waters hydrography west of the Iberian Peninsula from an 8 yr semiannual time series of an oceanographic section, *Ocean Science*, 9(2), 411-429, doi: 10.5194/os-9-411-2013.
- Rios, A. F., F. F. Perez, and F. Fraga (1992), Water masses in the upper and middle North Atlantic Ocean east of the Azores, *Deep-Sea Res.*, 39(3-4A), 645-658, doi:10.1016/0198-0149(92)90093-9.
- Rudnick, D. L., and S. T. Cole (2011), On sampling the ocean using underwater gliders, *J. Geophys. Res.*, 116, C08,010, doi:10.1029/2010JC006849.
- Smeed, D., G. McCarthy, D. Rayner, B. I. Moat, W. E. Johns, M. O. Baringer, and C. S. Meinen (2015), Atlantic meridional overturning circulation observed by the RAPID-MOCHA-WBTS (RAPID-Meridional Overturning Circulation and Heatflux Array-Western Boundary Time Series) array at 26N from 2004 to 2014, *British Oceanographic Data Centre - Natural Environment Research Council, UK.*, doi:10/6qb.
- Thompson, A. F., A. Lazar, C. Buckingham, A. C. Naveira Garabato, G. M. Damerell, and K. J. Heywood (2016), Open-ocean submesoscale motions: A full seasonal cycle of mixed layer instabilities from gliders, *J. Phys. Oceanogr.*, 46, 1285-1307, doi:10.1175/JPO-D-15-0170.1.
- Thomson, D. J. (1982), Spectrum estimation and harmonic-analysis, *J. Proc. IEEE*, 70(9), 1055-1096.
- Ullgren, J. E., and M. White (2010), Water mass interaction at intermediate depths in the southern Rockall Trough, northeastern North Atlantic, *Deep-Sea Res.*, 57(2), 248-257, doi: 10.1016/j.dsr.2009.11.005.
- Ullgren, J. E., and M. White (2012), Observations of mesoscale variability in the Rockall Trough, *Deep-Sea Res.*, 64, 1-8, doi:10.1016/j.dsr.2012.01.015.
- van Sebille, E., I. Kamenkovich, and J. K. Willis (2011), Quasi-zonal jets in 3-D Argo data of the northeast Atlantic, *Geophys. Res. Lett.*, 38, L02,606, doi:10.1029/2010GL046267.

# APPENDIX III

## Oxygen data collection and calibration

### Best practice protocol

#### III.1 CTD Data collection

In case of studies that include several platform and/or cruises operating together, it is highly recommendable to fix a common unit of measure to use in all steps of the survey in order to avoid time-consuming transformations of the data. These transformations can in fact also increase the noise in the dataset due to the intrinsic variability of the density data or because of spikes in the salinity and temperature profiles. The unit of  $\mu\text{mol kg}^{-1}$  is here suggested.

CTD profiles should be observed on their descendent phase to determine depths with constant oxygen concentration  $c(\text{O}_2)$ . On the ascendant phase, the CTD frame should be stopped at these depths to collect water through Niskin bottles. It is suggested firing at least two bottles per depth. Maximum and minimum  $c(\text{O}_2)$  in the profile should also be sampled to consider the whole range of values in the calibration. A selection of five to seven depths should be considered.  $c(\text{O}_2)$  measured by the CTD at the moment of firing should be recorded in the unit of measure fixed at the beginning of the survey.

Once the frame is aboard, water should be sampled at least in three replicates for each depth. In order to analyse the variability of  $c(\text{O}_2)$  among the Niskin replicates, it is suggested that replicates of water are taken for both the Niskin fired for one or two depths. The temperature of the water should be recorded as soon as the Niskin is opened for the sampling. If the temperature is significantly different from the one recorded in the CTD profile, the Niskin should be flagged as leaking and not used for the calibration.

After the Winkler titration (for protocol, see WOCE protocol as described by Culberson (1991) and Dickson (1996)), the mean oxygen concentration measured per each Niskin should be compared with the value recorded at the firing time in the CTD profile. The linear regression between the values obtained through titration and the ones obtained by the CTD profiles throughout the whole cruise has to be applied as calibration equation to the raw CTD values.

### III.2 Glider data calibration

The calibration is based on the comparison between CTD profiles and the relative closest glider profiles. These profiles should be close each other in time and space to avoid bias due to the geographical and temporal heterogeneity. One calibration should be done at the beginning of the mission and one at its end to correct for drifts in the sensor. For long missions (> 3 months), a third calibration is recommendable halfway through. Before the calibration, the  $\phi_{TC}$  profiles of the glider should have been corrected for the lag  $\tau$  in the optode.

Each calibration is done comparing the  $\phi_{TC}$  phase of the glider profiles with the backcalculated  $\phi_{cal}$  of the CTD profiles (for this calculation, see 2.3.3). The regression between the CTD  $\phi_{cal}$  profiles and the nearby glider  $\phi_{TC}$  profiles provides the calibrated values  $TPhaseCoef_0$  and  $TPhaseCoef_1$  to apply in the transformation of  $\phi_{TC}$  profiles in  $\phi_{cal}$  profiles in gliders. If there is a drift,  $TPhaseCoef_0$  and  $TPhaseCoef_1$  are significantly different for the calibrations at the beginning and at the end of the mission. In this case, the calculated  $TPhaseCoef_0$  and  $TPhaseCoef_1$  have to be considered valid only for the glider casts used for the calibrations. For the rest of the mission,  $TPhaseCoef_0$  and  $TPhaseCoef_1$  values have to be calculated assuming a linear shift between the initial and final values and temporally interpolating the values.

Once the  $\phi_{cal}$  profiles are transformed in  $c(O_2)$ , the  $c(O_2)$  profiles of the glider and the CTD used for the calibrations should be plotted together to confirm the quality of the calibration. In case of portion of the water column where the profiles mismatch obviously, it is suggested to repeat the calculation of  $TPhaseCoef_0$  and  $TPhaseCoef_1$  not considering the portion of the profiles at these depths.